Numerical resolution of turbulent flows on complex geometries

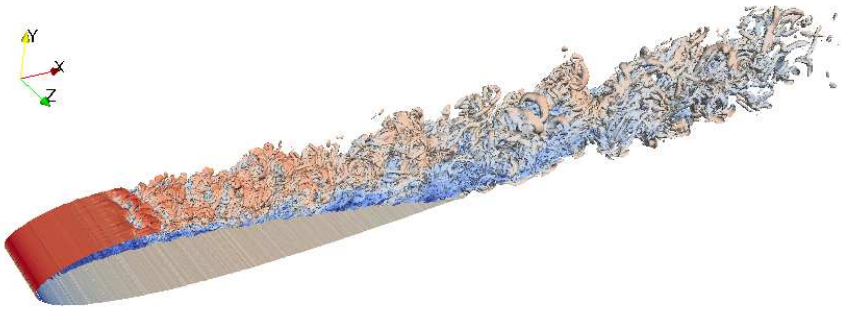

Centre Tecnològic de Transferència de Calor
Departament de Màquines i Motors Tèrmics
Universitat Politècnica de Catalunya

Oriol Lehmkuhl Barba
Doctoral Thesis

Numerical resolution of turbulent flows on complex geometries

Oriol Lehmkuhl Barba

TESI DOCTORAL

presentada al

Departament de Màquines i Motors Tèrmics
E.T.S.E.I.A.T.
Universitat Politècnica de Catalunya

per a l'obtenció del grau de

Doctor per la Universitat Politècnica de Catalunya

Terrassa, July, 2012

Numerical resolution of turbulent flows on complex geometries

Oriol Lehmkuhl Barba

Directors de la Tesi

Dr. Assensi Oliva Llena
Dr. Carlos D. Pérez-Segarra

Tribunal Qualificador

Dr. Pedro J. Coelho
University of Lisbon

Dr. Antonio Lecuona Neumann
Universidad Carlos III de Madrid

Dr. Jesús Castro González
Universitat Politècnica de Catalunya

more gg, more skill.
White-Ra

Acknowledgements

I would like to thanks to my fathers for the unconditional support given in all my live. To my uncle for be my first reference to the research community and for always trying to push my curiosity to the wild life world, unfortunately for him computers were more attractive. Finally I want to thank my wife and Brego for making this world much more interesting.

From the professional point of view, I must thank all the old and new blood of the CTTC and Termo Fluids S.L. crew to be receptive to my ideas and for trying to help me to overcome my drawbacks. Moreover, I would like to thank more specifically some researchers:

My first memory of Assensi is in a lecture about Heat and Mass Transfer, he was the professor and I was an average student. The funny issue was that Assensi was using a napkin with the Navier Stokes (NS) equation written in order to remember all the terms of these famous equations. I was pumped, since Assensi was not able to remember the NS equations but he was talking of some ridiculous crazy Direct Numerical Simulations (DNS) techniques in order to solve numerically all the turbulent staff using parallel computers. My conclusion was that either Assensi was a crazy man or a genius. A week after this lecture I was at the CTTC talking with Assensi about Computational Fluid Dynamics (CFD). At some degree this was the beginning of my Ph.D. and my current live. During these years Assensi has been my PhD director at full time. We talked each day about all the different problems involved on my activities, and his magnificent intuition has been usefully for the modelling, software design and of course in order to push my limits. Assensi it is seen by a lot of people like one of the most successfully research managers of our University. But the reality is that Assensi is one of the more brilliant researchers of the country that in order to have a consolidated research group has quit the basic research activities. The reality is that the genius is still there and in my Ph.D. thesis all the tips and intuitions of Assensi have been fundamental in order to succeed. In that sense the use of Object Oriented Techniques, go for LES and forget RANS, push the parallelisation limits of the code, forget unstructured corrections, go to conservative schemes, etc., are decisions were Assensi has been one of the key actors. It has been super fun to work with a man like Assensi and at the end, I think that the bad things of his personality are below of the good things. I owe you a lot Assensi.

My other Ph.D. director is David. He is the canonical professor and if my formulation and explanations have some sense is thanks to him. David has been a devoted mentor always trying to make order of my chaos and writing all the things that I have tried. This is a lot of work because I like to try new things and I don't specifically like to write. With David we are always trying to find the thermodynamic equilibrium state since I am an intuitionist and he has a phenomenal theoretical capacity and a

amazing need to understand the details. This relationship it is not easy but has been very beneficial to the Ph.D. since at the end of the day, David has proved the majority of my ideas (in the process he usually find a better approximations to the problem), where my work has been to be focused on the implementation and test of all that stuff.

All these years Ricard has been my partner. It is difficult to understand my Ph.D. thesis and more extensible the TermoFluids CFD package without Ricard. Seven years ago Ricard started with me to think on how to make a CFD code general enough to allow 3D unstructured meshes on parallel computers. At that time, the experience on C++ at the CTTC was very reduced. With the help of Manel and Ricard, we started to try different techniques in order to implement mesh iterators, to encapsulate all the parallelisation staff, to look for parallel containers and sparse matrix implementations, etc. From all that experience and knowing all the excellent previous work on Cartesian parallel CFD done before in the center we started the TermoFluids CFD code. Now all that basic Object Oriented libraries of geometry, parallelisation, solvers are used by a lot of researchers of the CTTC and Termo Fluids S.L. like a black box. And without all that previous work, the presented DNS and LES simulations of profiles using 20 to 50 M CV and hundreds of CPUs would be impossible. On the other hand, Ricard has an ability to find the correct algorithm for each specific model and methodology. My work has been greatly beneficed of Ricard's capacity and all that effort is not reflected on the Ph.D. document. It is a pity that we can not present a unified document where the reader can look to both, the algorithmic and model side of our work as a whole.

Finally I would like to thank the rest of the DNS crew: Ivette, Xavi and Andrey. Your help on discussions about that crazy intersection between turbulence, numerical methods and parallel computers, called DNS, have been very usefully and fun!

Oriol Lehmkuhl

Contents

Abstract

This thesis aims at developing a numerical methodology suitable for the direct numerical simulation (DNS) and large-eddy simulation (LES) of turbulent flows in order to be used in complex flows, currently encountered in industrial application. At the same time, the study of such turbulent flows can be an opportunity for gaining insight into the complex physics associated with them.

To accomplish these goals, the mathematical formulation, conservative spatial discretization on unstructured grids and time- integration scheme for solving the Navier-Stokes equations are presented. The spatial discretization proposed preserves the symmetry properties of the continuous differential operator and ensure both, stability and conservation of the global kinetic energy balance on any grid. Furthermore, the time-integration technique proposed is an efficient self-adaptive strategy, based on a one-parameter second-order-explicit scheme, which has been successfully tested on both Cartesian staggered and unstructured collocated codes, leading to CPU cost reductions of up to 2.9 and 4.3, respectively.

After presenting the general methodology for computing flows in complex geometries with unstructured grids, different LES models and regularization models suitable for these kind of meshes are presented and assessed by means of the analysis of different flows. First, regularization models are tested by means of the simulation of different cases with different level of complexity of the mesh. From a structured grid to a very complex mesh, with zones composed of prism and tetrahedral control volumes. It has been shown, that regularization models are very dependent on the quality of the filtering process. Although good results can be obtained with structured or smooth unstructured meshes, their performance is affected under fully irregular unstructured grids. A possible remedy to circumvent this issue is also presented. The main idea is to formulate the $\mathcal{C}_4$ model within a LES template. Although preliminary results are promising, further testing is still required.

After regularization model assessment, LES models are also tested in a natural convection flow. It is shown that, although first order statistics are well solved for most of the models tested (with the exception of the Smagorinsky model), QR- and dynamic-Smagorinsky models present a better prediction of the second-order statistics. However, if CPU time is considered, then QR model is the best alternative as it is essentially not more complicated to implement in a LES-code than the standard Smagorinsky model (with $\mathcal{C}_s$ constant) and is faster than the dynamic-Smagorinsky model.

The second part of the thesis is devoted to the study of turbulent flows past bluff bodies. The cases studied are: the flow past a sphere, the flow past a circular cylinder and the flow past a NACA 0012 airfoil. All these cases shares some characteristics encountered in turbulent flows with massive separations, i.e., flow separation, tran-

sition to turbulence in the separated shear-layers and turbulent wakes with periodic shedding of vortices. However there are intrinsic characteristics of the turbulence in each of them, which make them interesting for the studying of the turbulence. Furthermore, the results presented for the flow past a sphere at $Re = 3700$ and 10000, together with the flow past a NACA 0012 at Re=50000 and $AoA = 8°$ are the first DNS results presented in the literature for both flows.

The study of these cases contributed to shed some light into physics present in flows with massive separation. For instance, computations of the sphere wake at $Re = 3700$ and 10000 allowed to analyse the influence of shear-layer vortices and vortex shedding process in the wake configuration at these subcritical Reynolds numbers. The instantaneous analysis of the wake revealed that its structure is quite similar at both Reynolds numbers, i.e. they exhibit a helical-like configuration due to the instabilities in the shear layer which occur at random azimuthal positions. In addition, in the analysis of the spectra at different locations a mechanism through which low-frequency large-scale flow affects the underlying turbulence and consequently, the wake characteristics is identified. This mechanism is related to the modulation of the near wake behind the sphere, which causes it shrinkage and enlargement of the vortex formation region with a very low-frequency.

A similar mechanism is also studied in the flow past a circular cylinder, although differences between both flows are also observed. Regarding the low-frequency modulation of the wake of the cylinder, it is measured its value being of $f_m = 0.0064$. Also two different wakes configurations, as a result of this modulation, are identified: i) a high-energy mode with larger fluctuations in the shear-layer (Mode H) and ii) a low-energy mode with weaker fluctuations in the shear layer (Mode L). Furthermore, by means of cross-correlation between the base pressure and the stream-wise velocity in the wake centerline, it is shown that both variables are negative correlated. As the suction base pressure gets more negative, the stream-wise velocity increases and as a consequence, the vortex formation zone decreases.

In the last chapter of this thesis, the DNS of the flow past a NACA 0012 airfoil at $Re = 5 \times 10^4$ and angles of attack of $AOA = 5°,\ 8°$ are computed. In addition to the identification of the coherent structures of the flow and the computation of the flow statistics, the results obtained are used to assess the capabilities of two LES models for the prediction of flows with massive separation characteristic of many industrial flows. It is shown that, both models perform quite well being capable of predicting separation and transition to turbulence, as well as the fully developed turbulence in the wake. Yet, in coarser grids the VMS-WALE presents a better behaviour than QR-model. To close the study of suitability of LES modeling of industrial flows, two more challenging cases at higher Reynolds numbers up to $Re = 3 \times 10^6$ and different AOA are computed. Conclusions drawn from the good results obtained point out that the use of the conservative formulation presented in this thesis, is one of the

keys for the success of the SGS models used. This formulation, together with the use of unstructured grids might be a step towards the use of LES models for solving industrial flows on complex geometries at high Reynolds numbers.

Chapter 1

Introduction

1.1 Prologue

Turbulence is the underlying phenomena in many applications in engineering, geophysics, astro-physics, weather prediction, etc. Indeed, it is one of the key problems of classical physics and has been the object of intense research in the last decades. According to physicist Richard Feynman, it is the most important " unsolved problem of classical physics“.

In a flow at high Reynolds numbers the non-linearity of the convection process leads to instabilities which makes the flow unsteady and three-dimensional (even when subject to two-dimensional and steady boundary conditions). Under these situations the flow is called turbulent. Some of its properties are: disorder - random character (the flow is never reproduced in detail); turbulence is a continuum phenomenon (the smallest turbulent scales are much larger than molecular scales); turbulence is diffusive (efficient mixing and efficient transport of mass and momentum) and dissipative (dissipation occurs due to fluid viscosity at the smallest scales); the motion is always rotational (presence of vorticity distributed continuously but irregularly).

Turbulent flows are characterised by the wide range of scales, which (roughly speaking) can be divided into large and small scales. At sufficient high Reynolds numbers, inertial range scales can also be identified. Large scales contains most of the energy of the flow and dominate the transport phenomena (momentum, mass, heat). Contrary to large scales, which are their size is of the order of the flow domain, small scales are responsible of the energy dissipation. As aforementioned, if Reynolds numbers is high enough, inertial scales of a size in between of both range of scales are also observed.

Turbulence and Kolmogorov theory

Kolmogorov theory of the inertial subrange is one of the most important contributions in turbulence physics. Kolmogorov theory (K41) [1] is based on two premises. The former is that at sufficiently high Reynolds number, the turbulent flow is locally homogeneous and the latter is that small scale turbulent motions are statistically isotropic. That is, in isotropic turbulence the average value of any function of the velocity components and their derivatives, defined in relation to a particular reference system, is unaltered if the reference system is rotated in any manner or reflected in any plane. This definition of isotropic turbulence as is specified in K41 is somewhat different than the definition of Taylor [2], in the sense that it is independent of time (sadistically speaking) and involves also velocity components derivatives.

Under these premises, the first similarity hypothesis of K41 states that: *for locally isotropic turbulence, dissipation scales are uniquely determined by the energy dissipation rate ϵ and the fluid viscosity ν*. From this first similarity hypothesis, Kolmogorov scales can be derived: the Kolmogorov length scale $\eta \equiv (\nu^3/\epsilon)^{1/4}$; the velocity scale $u_\eta \equiv (\epsilon\nu)^{1/4}$ and time scale $\tau_\eta \equiv (\nu/\epsilon)^{1/2}$.

The second similarity hypothesis reads (approximately): *at sufficient high Reynolds number, the statistics motions in the inertial subrange are uniquely determined by the quantity of ϵ, and do not depend on ν.* From this hypothesis is derived the relation for the second moment of velocity increments, as

$$\mathcal{D}_{LL}(r) \sim C\,(\epsilon\, r)^{2/3} \tag{1.1}$$

Kolmogorov [3] also derived the *so-called* Kolmogorov's $4/5$th law for the third-order structure functions in decaying homogeneous and isotropic turbulence from:

$$\mathcal{D}_{LLL}(r) = -\frac{4}{5}\epsilon\, r + 6\nu\frac{\partial \mathcal{D}_{LL}}{\partial r} \tag{1.2}$$

Kolmogorov argued that in the inertial range the viscous term of equation 1.2 is negligible, yielding:

$$\mathcal{D}_{LLL}(r) = -\frac{4}{5}\epsilon\, r \tag{1.3}$$

The classical interpretation of this non-vanishing third moment is that the energy flux from large to small scales is uni-directional on average [4].

It follows from the second similarity hypothesis that, in the inertial subrange the one-dimensional spectrum of energy in the wave number component κ_1 is

$$\mathcal{E}(\kappa_1) = C_\kappa\, \epsilon^{2/3}\kappa_1^{-5/3} \tag{1.4}$$

This is the well known Kolmogorov $-5/3$ spectrum, where C_κ named after Kolmogorov, is a universal constant which value determined experimentally is $C_\kappa =$

0.53 ± 0.055 [5]. Note that for K41 similarity ideas to be applied it is necessary the existence of an inertial range. The obvious question here is, which is the condition for the inertial range to exist? Bradshaw [6], from a compilation of several works, estimated that for $Re_\lambda > 100$ inertial range might be detected. Here, Re_λ is the Reynolds number defined as a function of the Taylor micro-scale, λ, [2], which in isotropic turbulence it is derived from:

$$\epsilon = 15\nu \, \overline{u'^2}/\lambda \tag{1.5}$$

Later, Dimotakis[7] supported that issue, arguing that a necessary condition for fully-developed turbulence and the K41 inertial-range existence is the uncoupling of a range of scales from the large scales, which is accomplished at about $Re_\lambda > 100$.

1.2 Objectives of this thesis

The numerical simulation of turbulent flows is a powerful tool for investigating and understanding the turbulence phenomena and shed some light on the physics of turbulent flows such as transitional flows with massive separation, natural and mixed convection, atmospheric turbulence, among others. The advances in computational fluid dynamics (CFD) together with the increasing capacity of parallel computers have made possible to tackle such complex problems by using high performance numerical techniques such as direct numerical simulation (DNS).

DNS is an important research area in modern CFD. In this sense, DNS has a key role for improving the understanding of the turbulence phenomena and for using this technique for the simulation of flows in complex geometries. On the other hand, results from DNS can be very useful for developing better turbulence models or for fine tuning existing ones. However, one of the limitations of DNS is that it can require the use of very large computational resources which increase rapidly with Reynolds numbers (Re). Hence, DNS is still limited to low-to-moderate Re numbers and relative simple geometries. An alternative to DNS is large-eddy simulation (LES), which are based on computing the large-scales of the flow while modelling of the smallest ones. In this context, LES models have been proven to yield accurate results in different kind of flows.

Since now most of the DNSs performed have been restricted to very simple geometries and academic configurations. The reasons are mainly due to the limited computational resources and because the standards algorithms used for the largest DNSs are based on spectral methods that, although they are very efficient, they are restricted to very simple domains and grid spacings. Considering the actual state-of-the-art in turbulence modelling and numerical simulations, the main objectives of this thesis are:

- To develop a suitable formulation for the DNS of turbulent flows on complex geometries using unstructured grids
- The use of this formulation might allow the advance in the understanding of the physics of turbulent flows by means of the numerical simulations of turbulent natural and forced convection
- To contribute to the improvement of these CFD tools and in special subgrid-scale and regularization modelling of complex flows, by the assessment of the performance of models suitable for unstructured grids and complex geometries at high Reynolds numbers. This is of importance as modelling of turbulent flows constitute an step towards the simulation of flows encountered in industrial applications.

To do so, the symmetry preserving discretization formulation proposed by Verstappen and Veldman [8] has been extended to non-structured collocated meshes and an efficient time-advancement algorithm has been developed. The resulting code allows the high-performance computing of turbulent problems using millions of control volumes on parallel computers. Taking in account the ability of unstructured meshes to create grids around complex geometries, this code is used to simulate complex fluid dynamics and heat and mass transfer problems of industrial interest .

1.3 First implementation of the unstructured CFD code

This thesis has been developed within the framework of the collaboration project between Termo Fluids S.L. and the Heat and Mass Transfer Technological Center (CTTC).

The Heat and Mass Transfer Technological Center (CTTC) of the Technical University of Catalonia (UPC) is a research group dedicated to academic, research, innovation and technology transfer in the heat and mass transfer and fluid dynamic field, together with their application to thermal systems and equipments. The laboratory is composed by 47 professors and researchers, with all the members of the staff working full time. CTTC is one of the first research groups member of Technological Innovation Centers Network by the Spanish Government, and is considered as a Consolidated Center by the Catalan Government.

Termo Fluids S.L. is a spin-off which was born 6 years ago from members of the CTTC and, together with CTTC, have a high capacity of simulating thermal systems and equipment.

The CTTC research activities are focused on one basic research line dedicated to the mathematical formulation, numerical resolution and experimental validation of

heat and mass transfer phenomena. Some issues in this line are: natural and forced convection, turbulence modelling (RANS, LES and DNS), combustion, two-phase flow, solid-liquid phase change, radiation, porous media, numerical algorithms and solvers, general purpose CFD codes, high performance computing HPC (parallelisation), aerodynamics, etc.

A second research line involves the application of the acquired know-how from the basic studies mentioned above to the thermal and fluid dynamic optimization of thermal system and equipment (maximum efficiency with a minimum environmental impact).

Based on the previous experience with CFD modelling (for cite some of them [9, 10, 11, 12, 13, 14]) and unstructured grids [15, 16] existing at CTTC, an unstructured methodology was developed. Previous to the actual structure and form of the present methodology, as described throughout this thesis, a first implementation was carried out during the first year of this Ph.D.. Although in many aspects it has been changed and evolved into a more efficient and accurate methodology, it is the intention of the present section of describing the main features of this *early beta version* of the actual methodology.

The main characteristics of this first implementation of the unstructured code were:

- Full parallel CFD code (automated algebraic domain partitioning) for solving three-dimensional domains.
- Unstructured mesh (solution on any mixture of tetrahedral, hexahedral, prism and/or pyramid elements).
- First and second order spatial discretizations
- Finite volume method.
- Steady state or transient laminar and turbulent flows
- Implicit and explicit transient solvers.
- Conjugate heat transfer with a loosely coupled algorithm (possibility of different time integration step fluid/solid).
- Local refinement and Laplacian smoother post-processing tools.

In addition to the aforementioned characteristics of the code, different RANS turbulent models were implemented. The use of these models was based on the previous experiences acquired at CTTC with the use of [9, 10, 13]. The main models implemented at that time were:

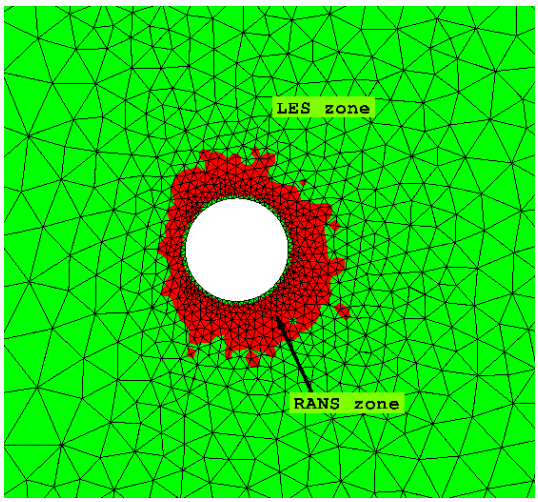

Figure 1.1: Example of an hybrid RANS/LES mesh for calculating the near-wall flow

- $k-\omega$ **models**: i) Wilcox [17]; ii) Peng, Davidson and Holmberg [18]; iii) Bredberg, Davidson and Peng [19]

- $k-\epsilon$ **models**: i) Ince and Lauder with standard Yap correction [20]; ii)Abe, Kondoh and Nagano [21]; iii) Goldberg, Peroomian and Chakravarthy [22] ; iv) RNG-Based $k-\epsilon$ (Speziale, Gatski and Fitzaurice) [23].

- **Hybrid** $k-\omega/k-\epsilon$ **models**: i) Menter Standard SST Model and Low Reynolds version of Menter SST Model (Langley) [24]

As an alternative to RANS models, hybrid LES/RANS models were also implemented. The main idea behind this was to take advantage of the RANS models for approximating the near-wall behaviour, in order to save computational resources, whereas in the regions off the wall LES models were used (see figure 1.1). The implemented LES/RANS models were:

- Spalart Detached Eddy Simulation Model (One equation Spalart-Allmaras RANS model [25] coupled with Smagorinsky SGS model [26]) [*continuous model*]

- Menter Detached Eddy Simulation Model (Menter Standard SST Model coupled with Smagorinsky SGS model) [*continuous model*]

- One-Equation SGS Model Yoshizawa [27] with possibility of hybrid LES/RANS using all linear RANS models [*zonal model*]

Hybrid LES/RANS models implementation details

The turbulent kinetic energy (k) and vorticity (ω) transport equations read,

$$\frac{\partial k}{\partial t} + \frac{\partial}{\partial x_i}(\rho u_i k) = \frac{\partial}{\partial x_i}(\mu_{eff}\frac{\partial k}{\partial x_i}) + P_k - \rho\beta_k\frac{k^{\frac{3}{2}}}{\ell} \tag{1.6}$$

$$\frac{\partial \omega}{\partial t} + \frac{\partial}{\partial x_i}(\rho u_i \omega) = \frac{\partial}{\partial x_i}(\mu_{eff}\frac{\partial \omega}{\partial x_i}) + P_\omega - \rho\beta_\omega\omega^2 + C_D \tag{1.7}$$

$$\mu_t = \rho C_\mu \ell\sqrt{k} \tag{1.8}$$

The turbulence length scale ℓ depending if the equations works in RANS or LES mode is evaluated as $\ell = \sqrt{\frac{k}{\omega}}$ for RANS mode or as $\ell = C_{LES}\triangle$ for LES mode. To change any generic model from LES to RANS mode it is only required the definition of a function that switches the turbulence length scale. The standard LES/RANS switch function are,

$$\ell = min(\sqrt{\frac{k}{\omega}}, C_{LES}\triangle) \tag{1.9}$$

$$\ell = \sqrt{\frac{k}{\omega}}\cdot(F_2) - (1-F_2)\cdot(C_{LES}\triangle) \tag{1.10}$$

being $F_2 = \tanh(max(2\frac{\sqrt{k}}{0.09\omega y}, \frac{400\nu}{y^2\omega})^2)$

The first switch function (equation 1.9) is quite efficient but its main drawback is that it must be used in a well designed grid. On the contrary, switch function (equation 1.10) is independent of the mesh design but not as efficient as equation 1.9.

These techniques were used for simulating different industrial applications such as the air flow in a refrigerated chamber. Different cases were considered. As an example, an sketch of one of the cases is depicted in figure 1.2.

In addition, the results of the formulation was compared against a published test in a refrigerated truck container. The experimental and RANS data was obtained from Moureh & Flick [28]. As indicated in the publication, RANS models are not capable of predicting the complex flow pattern of this case, specially the rear part recirculation. The main objective in this case was to detect how these models were capable of predicting this kind of flow, very usual in refrigerated chambers/enclosures (air jets within closed spaces).

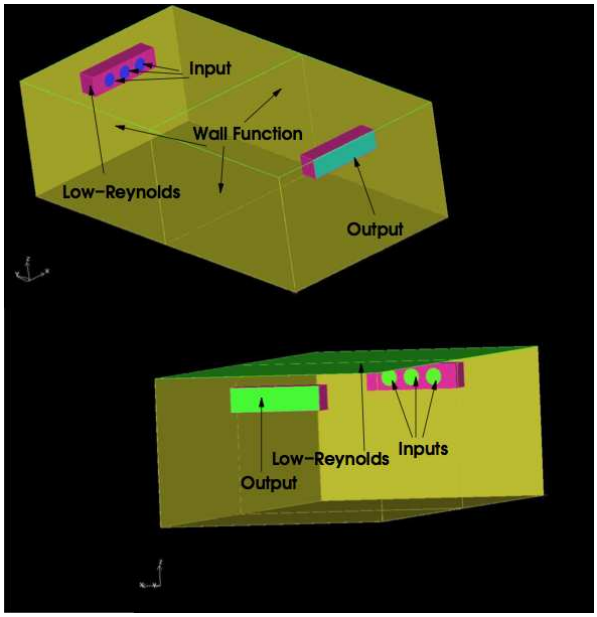

Figure 1.2: Sketch of one of the refrigeration chambers

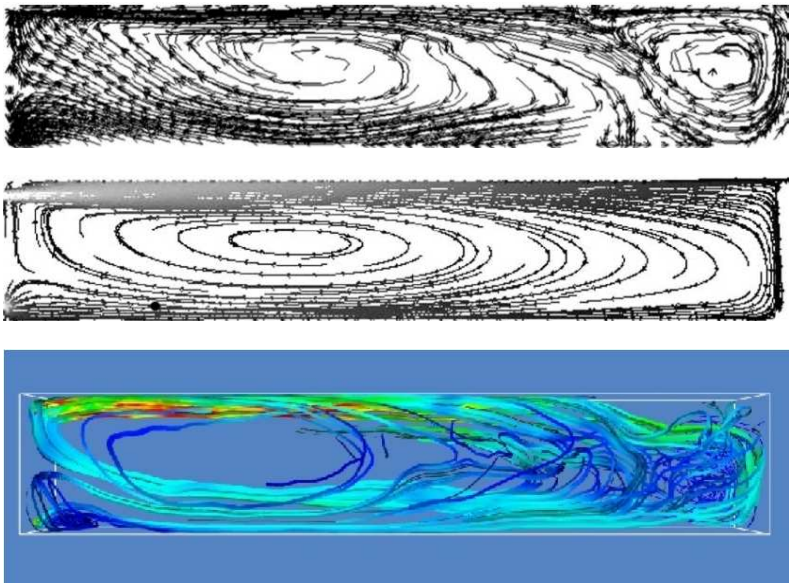

Figure 1.3: Flow pattern of the flow in the truck chamber. (top) Experimental results; (middle) RANS results; (bottom) LES results

The test case defined was a long slot-ventilated enclosure, which was simulated with a over 0.7M CV using 10 CPUs. For turbulence modelling, the Dynamic Smagorinsky SGS Mode was used. The flow pattern obtained and the comparison with the results of the reference work is plotted in figure 1.3. The comparison shows how the RANS models do not follow correctly the flow pattern found in experiments. Conversely, the LES models used predicts in a very good manner the flow behaviour. Moreover, the picture for LES is instantaneous (not an averaged one), so the flow characteristics can be much better understood and studied than using RANS models, where the variables used are temporal-means. In this particular case, RANS model were not capable of capturing the recirculation region, while LES reproduced correctly the flow pattern observed in experiments.

Although these previous results obtained with the unstructured formulation and turbulence models implemented were very encouraging, deficiencies also emerged. At that point, and considering other experiences at CTTC with structured grids and using a symmetry-preserving formulation [29], a new strategy was depicted. That is, the implementation of a symmetry-preserving formulation in collocated unstructured grids to be used for the direct numerical simulation (when possible) and large-

eddy simulation of the turbulent flow encountered in engineering applications.

1.4 Outline of the thesis

As aforementioned, this thesis aims at developing numerical tools suitable for the direct numerical simulation and large-eddy simulation of turbulent flows in order to be used in complex flows currently encountered in industrial application. At the same time, the study of such turbulent flows can be an opportunity for gaining insight into the complex physics associated with them.

To accomplish these goals, the next Chapter is devoted to present the mathematical formulation, spatial discretization on unstructured grids and time-integration of for solving the Navier-Stokes equations. The spatial discretization proposed preserves the symmetry properties of the continuous differential operator and ensure both, stability and conservation of the global kinetic energy balance on any grid. Furthermore, the time-integration technique proposed is efficient self-adaptive strategy, based on a one-parameter second-order-explicit scheme, which is proven to work well on both, Cartesian and unstructured grids.

The following Chapter (Chapter 3) is devoted to the detailed description of the LES and regularization models used throughout this thesis. These models are: the Smagorinsky model, the dynamic eddy-viscosity model, the wall-adapting eddy diffusivity model, the the wall-adapting eddy diffusivity model within a variational multi-scale framework, the QR-eddy diffusivity model and $\mathcal{C}_q$ regularization models. After this Chapter, the validity of regularization models is assessed by means of the study of three different flows: the impinging jet at, the flow past a circular cylinder and the ahmed car flow in Chapter 4.

After the assessment of the regularization models, in Chapter 5 LES models have been assessed in a natural convection case: the Rayleigh-Benard convection in a cylindrical enclosure at $Ra = 2 \times 10^9$. This case has been selected as it is a canonical case, in which it is well-known the fluid behaves as a quasi-homogeneous turbulent fluid, specially in the zone near the center of the cavity.

Since now, all the Chapters of this thesis have been dedicated to the description of the methodology used for the resolution of turbulent flows by means of DNS and LES and the further assessment of the LES models. The last part of the present thesis (Chapters 6 to 8) will be devoted to the study of turbulent flows past bluff bodies. The cases studied are: the flow past a sphere, the flow past a circular cylinder and the flow past a NACA 0012 airfoil. All these cases shares some characteristics encountered in turbulent flows with massive separations, i.e., flow separation, transition to turbulence in the separated shear-layers and turbulent wakes with periodic shedding of vortices. However there are intrinsic characteristics of the turbulence in each of them, which makes them interesting for the studying of the turbulence.

In Chapter 6, the turbulent flow past a sphere at two Reynolds numbers in the sub-critical regime at $Re = 3700$ and $Re = 10000$ has been studied. These cases are of interest, as the wake developed behind the sphere is completely three dimensional and present a helical-like configuration, which has been the object of many studies and conjectures about the way it is originated. Thus, particular attention has been devoted to investigate the shear-layer instabilities and its influence in the vortical structures, as well as the wake configuration.

In Chapter 7, the flow past circular cylinder at $Re_D = 3900$ is solved by means of DNS. This case has been object of several experimental and numerical investigations, but still nowadays there is a large scattering in the average statistics in the near wake. Thus, attention has been focused on investigate the possible cause of such different results. To do this, long-term computations of this flow have been performed, which is by far, as far as the author knowledge is concerned, the largest time integration statistics computed for this case.

The flow past a NACA 0012 airfoil is studied by means of DNS and LES in Chapter 8. The flow past aerodynamics structures is of interest for many industrial applications, and it is a quite challenging case. Two angles of attack have been investigated, and the results of the DNS have been used for the assessment of two promising LES models for computing flows with massive separation. In the reminder of the chapter, these LES models have been used for computing flows at challenging Reynolds numbers up to $Re = 3 \times 10^6$. Closing this thesis, conclusions and further research work are highlighted.

References

[1] A. N. Kolmogorov. The local structure of turbulence in incompressible viscous fluid for very large reynolds numbers. *Proceedings of the Royal Society of London. Series A: Mathematical and Physical Sciences*, 434(1890):9–13, 1991.

[2] GI Taylor. Statistical theory of turbulence. *Proceedings of the Royal Society of London. Series A,*, pages 421–444, 1935.

[3] A. N. Kolmogorov. Dissipation of energy in the locally isotropic turbulence. *Proceedings of the Royal Society of London. Series A: Mathematical and Physical Sciences*, 434(1890):15–17, 1991.

[4] A.S. Monin and A.M. Yaglom. *Statistical fluid mechanics: mechanics of turbulence*. Statistical Fluid Mechanics: Mechanics of Turbulence. MIT Press, 1975.

[5] Katepalli R. Sreenivasan. On the universality of the kolmogorov constant. *Physics of Fluids*, 7(11):2778–2784, 1995.

[6] P. Bradshaw. *Conditions for the Existence of an Inertial Subrange in Turbulent Flow*. Reports and memoranda. H.M. Stationery Office, 1969.

[7] Paul E. Dimotakis. The mixing transition in turbulent flows. *Journal of Fluid Mechanics*, 409:69–98, April 2000.

[8] Verzicco R. and R. Camussi. Numerical experimenrs on strongly turbulent thermal convection in a slender cylindrical cell. *Journal of Fluid Mechanics*, 477:19–49, 2003.

[9] J.E. Jaramillo, K. Claramunt, C.D. Perez-Segarra, R. Consul, and J. Cadafalch. Numerical study of different RANS models applied to turbulent forced convection. In *Proceedings of the IV International Symposium on Turbulence, Heat and Mass Transfer*, pages 671–680, 2003.

[10] X. Albets, C.D. Perez-Segarra, J. Cadafalch, C. Lifante, and K. Claramunt. Numerical experiments in turbulent natural convection using two-equation eddy-viscosity models. In *Proceedings of the IV International Symposium on Turbulence, Heat and Mass Transfer*, pages 853–860, 2003.

[11] M. Soria, F.X. Trias, C.D. Pérez-Segarra, and A. Oliva. Direct numerical simulation of a three-dimensional natural convection flow in a differentially heated cavity of aspect ratio 4. *Numerical Heat Transfer*, 45:649–673, 2004.

[12] F.X. Trias, M. Soria, C.D. Pï¿½ez-Segarra, and A. Oliva. A Direct Schur-Fourier Decomposition for the Efficient Solution of High-Order Poisson Equations on Loosely Coupled Parallel Computers. *Numerical Linear Algebra with Applications*, 2005.

[13] J.E. Jaramillo, C.D. Pérez-Segarra, A. Oliva, and K. Claramunt. Analysis of different rans models applied to turbulent forced convection. *International Journal of Heat and Mass Transfer*, 50(19):3749 – 3766, 2007.

[14] J. E. Jaramillo, C. D. Pérez-Segarra, I. Rodríguez, and A. Oliva. Numerical Study of Plane and Round Impinging Jets Using RANS Models. *Numerical Heat Transfer, Part B*, 54(3):213–237, 2008.

[15] C. D. Perez-Segarra, C. Farre, J. Cadafalch, and A. Oliva. Analysis of different numerical schemes for the resolution of convection-diffusion equations using finite-volume methods on three-dimensional unstructured grids. part i: Discretization schemes. *Numerical Heat Transfer, Part B: Fundamentals*, 46(4):333–350, 2007.

[16] C. Farre, C. D. Perez-Segarra, M. Soria, and A. Oliva. Analysis of different numerical schemes for the resolution of convection-diffusion equations using finite-volume methods on three-dimensional unstructured grids. part ii: Numerical analysis. *Numerical Heat Transfer, Part B: Fundamentals*, 49(4):351–375, 2006.

[17] D. C. Wilcox. Simulation of Transition with a Two-Equation Turbulence Model. *AIAA Journal*, 32:247–255, 1994.

[18] S.H. Peng, L. Davidson, and S. Holmberg. The two-equations turbulence k-ω model applied to recirculating ventilation flows. Technical Report 96/13, almers University of Technology, 1996.

[19] J Bredberg and L Davidson. Prediction of flow and heat transfer in a stationary two-dimensional rib roughened passage using low-Re turbulent models. In *Third Eupopean Conference on Turbomachinery, IMECHE*, page C557/074/99, 1999.

[20] N.Z. Ince and B.E. Launder. Computation of Buoyancy-Driven Turbulent Flows in Rectangular Enclosures. *International Journal of Heat and Fluid Flow*, 10(1):110–117, 1989.

[21] Abe K., Kondoh T., and Nagano Y. On Reynolds-Stress expresions and near-wall scaling parameters for predicting wall and homogeneous turbulent shear flows. *International Journal of Heat and Fluid Flow*, 18:266–282, 1997.

[22] U. Goldberg, O. Peroomian, and S. Chakravarthy. A wall-distance-free k-ϵ model with enhanced near-wall treatment. *Journal of Fluids Engineering*, 120:457–462, 1998.

[23] Speziale C.G., Sarkar S., and Gatski T.B. Modelling the Pressure-Strain Correlation of Turbulence: an Invariant Dynamical systems Approach. *Journal of Fluid Mechanics*, 227:245–272, 1991.

[24] Menter F.R. Two-Equation Eddy-Viscosity Turbulence Models for Engineering Applications. *AIAA Journal*, 32(8):1598–2005, 1994.

[25] P.R. Spalart and S.R. Allmaras. A one equation turbulence model for aerodynamic flows. In *AIAA 30th Aerospace Sciences Meeting and Exhibig*, 1992.

[26] J. Smagorinsky. General circulation experiments with the primitive equations, part. I: the basic experiment. *Monthly Weather Rev.*, 91:99–164, 1963.

[27] Akira Yoshizawa. Statistical theory for compressible turbulent shear flows, with the application to subgrid modeling. *Physics of Fluids*, 29(7):2152–2164, 1986.

[28] J. Moureh and D. Flick. Airflow pattern and temperature distribution in a typical refrigerated truck configuration loaded with pallets. *International Journal of Refrigeration*, 27(5):464 – 474, 2004.

[29] X. Trias. *Direct numerical simulation and regularization modelling of turbulent flows on loosely coupled parallel computers using symmetry-preserving discretizations*. PhD thesis, Universitat Politecnica de Catalunya, 2006.

Chapter 2

Mathematical formulation and conservative discretization for unstructured meshes

Part of the contents of this chapter have been published as:

F. X. Trias and O. Lehmkuhl. A self-adaptive strategy for the time-integration of Navier-Stokes equations. *Numerical Heat Transfer. Part B. Fundamentals*

Abstract.

A conservative discretization for unstructured meshes together with an efficient self-adaptive strategy for the explicit time-integration of Navier-Stokes equations are presented. The spatial discretization preserves the symmetry properties of the continuous differential operator and ensure both, stability and conservation of the global kinetic energy balance on any grid. In addition, the time-integration scheme proposed is not based on a standard CFL condition as most of the conventional methods found in the literature. Instead, the eigenvalues of the dynamical system are analytically bounded and the linear stability domain of the time-integration scheme is adapted in order to maximize the time-step. The method works independently of the underlying spatial mesh; therefore, it can be easily integrated into structured or unstructured codes. The additional computational cost is minimal and a significant increase of the time-step is achieved without losing accuracy. The effectiveness and robustness of the method are demonstrated on both a Cartesian staggered and an unstructured collocated formulation. In practice, CPU cost reductions up to more than 4 respect to the conventional approach have been measured.

2.1 Introduction

The incompressible Navier-Stokes equations form an excellent mathematical model of turbulent flows. Unfortunately, attempts at performing Direct Numerical Simulations (DNS) with the available computational resources and numerical methods are limited to relatively low-Reynolds numbers. Regarding the numerical algorithms, cost reductions can be achieved by one or more of the following issues: (i) decreasing the number of grid points using high-order schemes [1, 2, 3], (ii) reducing the computational cost per iteration or (iii) using larger time-steps; all without affecting the quality of the numerical solution. Hereafter, the mathematical formulation, spatial discretization and time integration scheme used throughout this thesis are described in detail.

2.2 Finite-volume discretization of the convection-diffusion equation on general meshes

Tradicionally in CFD&HT community, transport equations are all summarized in the general convection-diffusion equation [4]. If the dependent variable is denoted by ϕ, the general differential equation is

$$\frac{\partial(\rho\phi)}{\partial t} + \nabla \cdot (\rho\vec{v}\phi) = \nabla \cdot (\Gamma\nabla\phi) + S \tag{2.1}$$

where Γ is the diffusion coefficient, and S is the source term.

The four terms in the general convection-diffusion equation are the unsteady term, the convection term, the diffusion term, and the source term.

Integrating Eq. (2.1) over a general cell volume, and using a first-order time discretization gives

$$\int_{V_c} \frac{(\rho\phi)^{n+1} - (\rho\phi)^n}{\Delta t}\, dV + \int_{V_c} \nabla \cdot (\rho\vec{v}\phi)^n\, dV = \int_{V_c} \nabla \cdot (\Gamma\nabla\phi)^n\, dV + \int_{V_c} S^n\, dV \tag{2.2}$$

where superscript n refers to time instant, Δt is the time step and V_c is the volume of the cell under consideration.

Assuming the finite-volume hypothesis [5] and the divergence theorem, Eq. (2.2) can be discretizated as

$$\frac{(\rho\phi)^{n+1} - (\rho\phi)^n}{\Delta t} V_c + \sum_f (\rho_f \vec{v}_f \phi_f)^n \cdot \vec{n}_f A_f = \sum_f (\Gamma_f \nabla\phi_f)^n \cdot \vec{n}_f A_f + S^n\, V_c \tag{2.3}$$

where subscript f refers to cell face, and $\vec{n}_f$ and A_f are the outward-normal vector and surface of face f, respectively.

In the next sections a summary of the numerical approximations used in this thesis in order to solve equation 2.3 are discussed.

2.2.1 Evaluation of the convection term

The unstructured finite-volume discretization of the convection term, see Eq. (2.3), is

$$C = \sum_f \rho_f \vec{v}_f \phi_f \cdot \vec{n}_f A_f = \sum_f \dot{m}_f \phi_f \tag{2.4}$$

where the mass flow $\dot{m}_f$ is interpolated, if a cell-centered formulation is used (collocated mesh), and ϕ_f is calculated using a numerical scheme.

There are many different numerical schemes [6]. The simplest numerical scheme which has good numerical stability properties is the upwind difference scheme (UDS) that can be evaluated, see Fig. (2.1), by different criterions:

- Criterion UDSa:

$$\begin{aligned} \phi_f &= \phi_P \qquad \dot{m}_f \geq 0 \\ \phi_f &= \phi_F \qquad \dot{m}_f < 0 \end{aligned} \tag{2.5}$$

- Criterion UDSb:

$$\begin{aligned} \phi_f &= \phi_P + \nabla\phi_P \cdot \vec{Pf} \qquad \dot{m}_f \geq 0 \\ \phi_f &= \phi_F + \nabla\phi_F \cdot \vec{Ff} \qquad \dot{m}_f < 0 \end{aligned} \tag{2.6}$$

- Criterion UDSc:

$$\begin{aligned} \phi_f &= \phi_P + \nabla\phi_P \cdot \vec{PP''} \qquad \dot{m}_f \geq 0 \\ \phi_f &= \phi_F + \nabla\phi_F \cdot \vec{FF''} \qquad \dot{m}_f < 0 \end{aligned} \tag{2.7}$$

All these criterions can can be straightforward extended to other traditional Upwind-based schemes used in Cartesian meshes (i.e. QUICK, SMART, etc.). For more details the reader is referred to Pérez-Segarra [6].

Furthermore, similar to the above presented UDS schemes extensions to unstructured meshes of the classical second order skew-symmetric scheme (SSS) can be also derived:

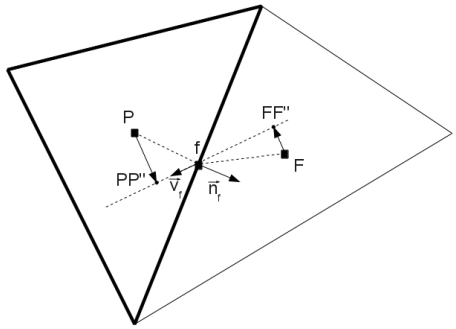

Figure 2.1: Node location for convective criterions.

- Criterion SSSa:

$$\phi_f = 0.5 \cdot (\phi_P + \phi_F) \tag{2.8}$$

- Criterion SSSb:

$$\phi_f = 0.5 \cdot (\phi_P + \phi_F) + 0.5 \cdot (\nabla\phi_P \cdot + \nabla\phi_F \cdot) \cdot \vec{d_f} \tag{2.9}$$

where vector $\vec{d_f}$ has to be numerical determined for each control volume by the means of a Least Squares technique in order to minimize the symetric part of this the convective criteria.

2.2.2 Evaluation of the diffusion term

The discretization of the diffusion term using a finite-volume approach, see Eq. (2.3), is

$$D = \sum_f \Gamma_f \nabla\phi_f \cdot \vec{n}_f A_f \tag{2.10}$$

Different approaches of the diffusion fluxes are given by Pérez-Segarra [6] for a generic internal face f of an arbitrary unstructured mesh.

The Direct Gradient Evaluation (Criterion D1), see Fig. (2.2), evaluates the gradients directly at the desired cell face

$$D = \sum_f \Gamma_f \left(\frac{\partial\phi}{\partial n}\right)_f A_f \approx \sum_f \Gamma_f \frac{\phi_{F'} - \phi_{P'}}{\vec{PF} \cdot \vec{n}_f} A_f = \sum_f \Gamma_f \frac{\phi_{F'} - \phi_{P'}}{d_{PF}} A_f^s \tag{2.11}$$

where d_{PF} is the distance between node P and node F, $\vec{s}_f$ is a unit vector on the $\vec{PF}$ direction, A_f is the cell-face area, $A_f^s = A_f / \vec{s}_f \cdot \vec{n}_f$ represents the surface vector component on the $\vec{s}_f$ direction, and $\phi_{P'}$ and $\phi_{F'}$ are the projections of the nodal values on the normal surface vector direction $\vec{n}_f$. These values can be estimated using the gradient at the nodal position

$$\phi_{P'} \approx \phi_P + \nabla\phi_P \cdot \vec{PP'} \qquad and \qquad \phi_{F'} \approx \phi_F + \nabla\phi_F \cdot \vec{FF'} \tag{2.12}$$

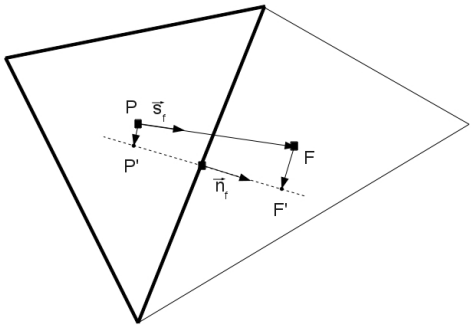

Figure 2.2: Detail of the geometric parameters for the diffusion evaluation.

2.2.3 Gradient evaluation

Gradient evaluation at the cell centers is required for the discretization of convective and diffusive terms. Most methods in the literature are based on the Green-Gauss theorem and least-squares method [6].

Using the Green-Gauss theorem and the midpoint-rule approximation, the gradient at cell P is

$$\nabla\phi_P \approx \frac{1}{V_c}\int_{V_c} \nabla\phi \, dV = \frac{1}{V_c}\int_{S_c} \phi \, d\mathbf{S} = \frac{1}{V_c}\sum_f \phi_f A_f \vec{n}_f \tag{2.13}$$

where the cell-face values of the dependent variable ϕ should be evaluated based on some kind of interpolation of the nodal values. This method results in a symmetric gradient operator if the effects of the volume normalization are neglected.

The least-squares method is unrelated to mesh topology, and it is distance weighted. The gradient is calculated by minimizing the sum of the squares of the differences of the variable values at a stencil of points and the values obtained at these points

with linear extrapolation from actual node. The stencil of points usually chosen is the neighbors of the node where the gradient is evaluated. For more details of the standard method see Haselbacher [7]. The main down-break of this method is the lack of symmetry of the resulting gradient operator.

2.3 Discrete Navier-Stokes equations

The divergence form of the incompressible Navier-Stokes equations is

$$\nabla \cdot \mathbf{u} = 0, \tag{2.14}$$

$$\frac{\partial \mathbf{u}}{\partial t} + \nabla \cdot (\mathbf{u}\mathbf{u}) = -\frac{1}{\rho}\nabla p + \nu \Delta \mathbf{u}, \tag{2.15}$$

where $\mathbf{u}$ is the velocity, p the pressure and ρ and ν the constant density and kinematic viscosity, respectively. The finite-volume spatial discretization of these equations on an general arbitrary mesh scheme, using discrete matrix operators, is written as

$$\mathbf{M}\mathbf{u} = \mathbf{0}, \tag{2.16}$$

$$\mathbf{\Omega}\frac{d\mathbf{u}}{dt} + \mathbf{C}(\mathbf{u})\mathbf{u} + \nu\mathbf{D}\mathbf{u} + \frac{1}{\rho}\mathbf{G}\mathbf{p} = \mathbf{0}, \tag{2.17}$$

where $\mathbf{u}$ and $\mathbf{p}$ are the vectors of velocities and pressures. The diagonal matrix $\mathbf{\Omega}$ describes the volume of the cells, matrices $\mathbf{C}(\mathbf{u})$ and $\mathbf{D}$ are the convective and diffusive operators and matrices $\mathbf{G}$ and $\mathbf{M}$ represent the gradient and divergence operators.

The discrete conservation properties are related to the symmetries of these matrices as studied in detail by Verstappen and Veldman [8]. Hence, the kinetic energy is conserved if and only if the discrete convective operator is skew-symmetric, i.e. the transpose of the matrix is also its negative $\mathbf{C}(\mathbf{u}) = -\mathbf{C}(\mathbf{u})^*$, and if the negative conjugate transpose of the discrete gradient operator is equal to the divergence operator, $\mathbf{M} = -\mathbf{G}^*$. On the other hand, since the diffusive terms must be dissipative, the diffusive operator must be symmetric and positive-definite, i.e. the matrix is equal to its transpose $\mathbf{D}_c = \mathbf{D}_c^*$ and $\mathbf{z}^*\mathbf{D}_c\mathbf{z} > \mathbf{0}$ for all non-zero $\mathbf{z}$.

2.3.1 Collocated mesh scheme

The collocated mesh scheme calculates the velocity and pressure fields at the centroids of the cells, while needs particular interpolations and special velocity fluxes at faces, in order to minimize the kinetic energy error and conserve mass exactly, respectively.

The velocity-pressure coupling of the momentum equation, Eq. 2.15, is solved by means of a classical fractional step projection method along with explicit time-advancement, written as

$$\mathbf{u}^{n+1} - \mathbf{u}^{p} = -\frac{\Delta t}{\rho}\nabla p^{n+1}, \tag{2.18}$$

$$\mathbf{u}^{p} = \mathbf{u}^{n} + \Delta t\left[\nabla\cdot(\mathbf{u}^{n}\mathbf{u}^{n}) - \nu\Delta\mathbf{u}^{n}\right], \tag{2.19}$$

where superscript n refers to time instant, $\mathbf{u}^p$ is the predictor velocity and Δt is the time step.

First, the predictor velocity is discretizated by integrating Eq. 2.19 over a cell k and applying the divergence theorem to its bordering faces, $f \in F(k)$, giving

$$\mathbf{u}_k^p = \mathbf{u}_k^n + \frac{\Delta t}{V_k}\left[\sum_{f\in F(k)} \boldsymbol{\phi}_f^n \hat{U}_f^n A_f - \nu \sum_{f\in F(k)} (\mathbf{u}_{nb}^n - \mathbf{u}_k^n)\frac{A_f}{\delta d_f}\right], \tag{2.20}$$

where V_k is the volume of cell k, $\boldsymbol{\phi}_f$ is the convected face velocity, $\hat{U}_f = \mathbf{u}_f\cdot\hat{\mathbf{n}}_f$ is the normal face velocity evaluated by taking the dot product of the mass-conserving face velocity, $\mathbf{u}_f$, and the outward-unit face normal, $\hat{\mathbf{n}}_f$, A_f is the face surface, subscripts k and nb refer to the cell itself and the face-neighbor one, and the length δd_f is the normal-projected distance between the centroids of cells k and nb.

Next, taking the divergence of Eq. 2.18, applying the incompressibility condition, Eq. 2.14, and discretizating over cell k, yields a discrete Poisson equation

$$\sum_{f\in F(k)} \hat{U}_f^p A_f = \frac{\Delta t}{\rho}\sum_{f\in F(k)} (p_{nb}^{n+1} - p_k^{n+1})\frac{A_f}{\delta d_f}, \tag{2.21}$$

which solves the pressure field. Then, when the solution of p^{n+1} is obtained, $\mathbf{u}^{n+1}$ results from discretizating Eq. 2.18 over cell k as

$$\mathbf{u}_k^{n+1} = \mathbf{u}_k^p - \frac{\Delta t}{\rho V_k}\sum_{f\in F(k)} p_f^{n+1}\hat{\mathbf{n}}_f A_f, \tag{2.22}$$

where p_f is the pressure interpolated to face f.

Notice that no specific interpolations for $\boldsymbol{\phi}_f^n$, $\hat{U}_f^p$ and p_f^{n+1} have been explained yet. In order to fulfill the skew-symmetric conservation requirement of the discrete convective operator, the convected face velocity is evaluated as $\boldsymbol{\phi}_f^n = \frac{1}{2}(\mathbf{u}_k^n + \mathbf{u}_{nb}^n)$ [8]. On the other hand, the normal face predictor velocity and face pressure are calculated as $\hat{U}_f^p = \frac{1}{2}(\mathbf{u}_k^p + \mathbf{u}_{nb}^p)\cdot\hat{\mathbf{n}}_f$ and $p_f^{n+1} = \frac{1}{2}(p_k^{n+1} + p_{nb}^{n+1})$, respectively, to minimize the kinetic energy conservation error as analyzed by Felten and Lund [9].

Finally, the evaluation of the normal face velocity, $\hat{U}_f^{n+1}$ needs to be studied in detail in order to exactly conserve mass. Taking again the divergence of Eq. 2.18 and discretizating over cell k, gives

$$\sum_{f\in F(k)} \hat{U}_f^{n+1} A_f - \sum_{f\in F(k)} \hat{U}_f^{p} A_f = -\frac{\Delta t}{\rho} \sum_{f\in F(k)} (p_{nb}^{n+1} - p_k^{n+1}) \frac{A_f}{\delta d_f}, \tag{2.23}$$

which can be arranged in the following form

$$\sum_{f\in F(k)} \left[\hat{U}_f^{n+1} A_f - \hat{U}_f^{p} A_f + \frac{\Delta t}{\rho} (p_{nb}^{n+1} - p_k^{n+1}) \frac{A_f}{\delta d_f} \right] = 0. \tag{2.24}$$

Imposing a more restrictive but easier condition that asks for each face to equal zero, the following equation is obtained

$$\hat{U}_f^{n+1} = \hat{U}_f^{p} - \frac{\Delta t}{\rho} \frac{(p_{nb}^{n+1} - p_k^{n+1})}{\delta d_f}, \tag{2.25}$$

if the predictor normal face velocity is evaluated as the semi-sum $\hat{U}_f^p = \frac{1}{2}(\mathbf{u}_k^p + \mathbf{u}_{nb}^p)\cdot \hat{\mathbf{n}}_f$, as commented before, and $\mathbf{u}^p$ is substituted using Eq. 2.22, Eq. 2.25 is rewritten as

$$\begin{aligned} \hat{U}_f^{n+1} =& \frac{1}{2}(\mathbf{u}_k^{n+1} + \mathbf{u}_{nb}^{n+1})\cdot \hat{\mathbf{n}}_f - \frac{\Delta t}{\rho} \left[\frac{(p_{nb}^{n+1} - p_k^{n+1})}{\delta d_f} \right] \\ &+ \frac{\Delta t}{\rho} \left[\frac{1}{2} \left(\frac{1}{V_k} \sum_{f\in F(k)} p_f^{n+1} \hat{\mathbf{n}}_f A_f + \frac{1}{V_{nb}} \sum_{f\in F(nb)} p_f^{n+1} \hat{\mathbf{n}}_f A_f \right) \right] \cdot \hat{\mathbf{n}}_f, \end{aligned} \tag{2.26}$$

which is similar to the mass-conserving normal face velocity proposed by Felten and Lund [9].

2.3.2 Conservation properties

Collocated momentum conservation

Total conservation of momentum is obtained by integrating Eq. 2.15 over the whole domain, which is transformed to a summation of integrals for each control volume that form the domain and converted to surface integrals by applying the divergence

theorem, as previously done for mass conservation, giving

$$\sum_{k\in\Omega}\frac{d\mathbf{u}_k}{dt}V_k+\sum_{k\in\Omega}\sum_{f\in F(k)}\boldsymbol{\phi}_f\hat{U}_f A_f \tag{2.27}$$
$$=-\frac{1}{\rho}\sum_{k\in\Omega}\sum_{f\in F(k)}p_f\hat{\mathbf{n}}_f A_f+\nu\sum_{k\in\Omega}\sum_{f\in F(k)}(\mathbf{u}_{nb}-\mathbf{u}_k)\frac{A_f}{\delta d_f}.$$

Notice that $\hat{U}_f$, $\hat{\mathbf{n}}_f$ and $(\mathbf{u}_{nb}-\mathbf{u}_k)$ are quantities that present equal values but with different sign when evaluating them at a face f from two adjacent interior cells. Hence, interior fluxes cancel out and Eq. 2.27 is evaluated as the summation over boundary faces, $f\in F(\partial\Omega)$, written as

$$\sum_{k\in\Omega}\frac{d\mathbf{u}_k}{dt}V_k+\sum_{f\in F(\partial\Omega)}\boldsymbol{\phi}_f\hat{U}_f A_f \tag{2.28}$$
$$=-\frac{1}{\rho}\sum_{f\in F(\partial\Omega)}p_f\hat{\mathbf{n}}_f A_f+\nu\sum_{f\in F(\partial\Omega)}(\mathbf{u}_f-\mathbf{u}_a)\frac{A_f}{\delta d_f},$$

which is a proof of momentum conservation for collocated meshes since it states that the change in momentum is due only to the fluxes through the boundary of the domain.

Collocated kinetic energy conservation

In order to investigate the collocated conservation of kinetic energy, the momentum equation, Eq. 2.15, is discretizated over the whole domain and multiplied by the velocity vector, $\mathbf{u}$. Then, the resulting equation can be transformed to a summation of surface integrals for each cell k, written as

$$\sum_{k\in\Omega}\mathbf{u}_k\cdot\frac{d\mathbf{u}_k}{dt}V_k+\sum_{k\in\Omega}\mathbf{u}_k\cdot\sum_{f\in F(k)}\boldsymbol{\phi}_f\hat{U}_f A_f \tag{2.29}$$
$$=-\frac{1}{\rho}\sum_{k\in\Omega}\mathbf{u}_k\cdot\sum_{f\in F(k)}p_f\hat{\mathbf{n}}_f A_f+\nu\sum_{k\in\Omega}\mathbf{u}_k\cdot\sum_{f\in F(k)}(\mathbf{u}_{nb}-\mathbf{u}_k)\frac{A_f}{\delta d_f},$$

where the terms from left to right correspond to the time derivative, convection, pressure and diffusion contributions to the kinetic energy equation.

The detailed analysis of Eq. 2.29 is easier if an important identity involving combinations of interpolation and differentiation operators is introduced. The identity

was first presented by Morinishi et al. [2] and restated in finite-volume form by Felten and Lund [9]. The relation reads

$$\varphi_k \sum_{f\in F(k)} \bar{\psi}_f Q_f + \psi_k \sum_{f\in F(k)} \bar{\varphi}_f Q_f = \sum_{f\in F(k)} \bar{\varphi}_f \bar{\psi}_f Q_f + (\varphi_k \psi_k) \sum_{f\in F(k)} Q_f, \tag{2.30}$$

where φ and ψ are two general variables, Q_f is a general quantity known on the cell face (i.e. no interpolation needed) and the upper bars refer to interpolated values.

First, the convective term of Eq. 2.29 is developed by specializing Eq. 2.30 by taking $\varphi = \mathbf{u}$, $\psi = \boldsymbol{\phi}$ and $Q_f = \hat{U}_f A_f$, evaluating interpolations as semi-summed variables and using the continuity equation, Eq. 2.14, then, the convective term can be rewritten as

$$\sum_{k\in\Omega} \mathbf{u}_k \cdot \sum_{f\in F(k)} \boldsymbol{\phi}_f \hat{U}_f A_f = \sum_{k\in\Omega} \sum_{f\in F(k)} \frac{1}{2} \mathbf{u}_f \cdot \boldsymbol{\phi}_f \hat{U}_f A_f, \tag{2.31}$$

where $\mathbf{u}_f$ and $\boldsymbol{\phi}_f$ are both evaluated as semi-summed adjacent cell velocities, but the first one is the interpolated face velocity while the second one is the symmetry-preserving convective scheme.

Second, if the pressure term in Eq. 2.29 is analyzed in a similar fashion by taking $\varphi = \mathbf{u}$, $\psi = p$ and $Q_f = \hat{\mathbf{n}}_f A_f$, and Eq. 2.26 is used to simplify the expression, the following relation results

$$\begin{aligned}\sum_{k\in\Omega} \mathbf{u}_k \cdot \sum_{f\in F(k)} p_f \hat{\mathbf{n}}_f A_f = \sum_{k\in\Omega} \sum_{f\in F(k)} p_f \mathbf{u}_f \cdot \hat{\mathbf{n}}_f A_f - \frac{\delta t}{\rho} \sum_{k\in\Omega} p_k \sum_{f\in F(k)} \left[(p_{nb} - p_k) \frac{A_f}{\delta d_f} \right] \\ + \frac{\delta t}{\rho} \sum_{k\in\Omega} p_k \sum_{f\in F(k)} \frac{1}{2} \left[\frac{1}{V_k} \sum_{f\in F(k)} p_f \hat{\mathbf{n}}_f A_f + \frac{1}{V_{nb}} \sum_{f\in F(nb)} p_f \hat{\mathbf{n}}_f A_f \right] \cdot \hat{\mathbf{n}}_f A_f.\end{aligned} \tag{2.32}$$

Finally, noticing that the interior fluxes in Eq. 2.31 and Eq. 2.32 cancel out, Eq. 2.29 can be rewritten as

$$\begin{aligned}\sum_{k\in\Omega} \frac{d(\frac{1}{2}\mathbf{u}_k \cdot \mathbf{u}_k)}{dt} V_k + \sum_{f\in F(\partial\Omega)} \frac{1}{2} \mathbf{u}_f \cdot \boldsymbol{\phi}_f \hat{U}_f A_f = -\frac{1}{\rho} \sum_{f\in F(\partial\Omega)} p_f \mathbf{u}_f \cdot \hat{\mathbf{n}}_f A_f \\ - \frac{\delta t}{\rho^2} \sum_{k\in\Omega} p_k \sum_{f\in F(k)} \frac{1}{2} \left[\frac{1}{V_k} \sum_{f\in F(k)} p_f \hat{\mathbf{n}}_f A_f + \frac{1}{V_{nb}} \sum_{f\in F(nb)} p_f \hat{\mathbf{n}}_f A_f \right] \cdot \hat{\mathbf{n}}_f A_f \\ + \frac{\delta t}{\rho^2} \sum_{k\in\Omega} p_k \sum_{f\in F(k)} \left[(p_{nb} - p_k) \frac{A_f}{\delta d_f} \right] + \nu \sum_{k\in\Omega} \mathbf{u}_k \cdot \sum_{f\in F(k)} (\mathbf{u}_{nb} - \mathbf{u}_k) \frac{A_f}{\delta d_f},\end{aligned} \tag{2.33}$$

which states that in the absence of viscosity ($\nu = 0$) the change in kinetic energy is due to the fluxes through the boundary of the domain and a kinetic energy error from the pressure term. This pressure error term arises from the special definition for the normal face velocity, Eq. 2.26, needed to exactly conserve mass in collocated schemes. Notice that when using first-order interpolations (semi-summed variables from adjacent cells) and a symmetry-preserving convection scheme, the kinetic energy conservation error is minimized.

It is of great interest to evaluate the scaling order of the kinetic energy pressure error since it can not be eliminated. Looking in detail at Eq. 2.33, it can be shown that the spatial pressure error scales like $\mathcal{O}(\Delta x^2)$, as deduced by Felten and Lund [9], while the time pressure error scales as $\mathcal{O}(\Delta t)$, but can be reduced through the use of gear like time integration schemes, as studied by Fishpool and Leschziner [10] or by strategies such as those explained in the next section.

This result can be related to the symmetries of discrete operators in the following way: i) the convective term in Eq. 2.33 presents no kinetic energy error since the convection scheme has been chosen to make the convective operator skew-symmetric, ii) the need of a special definition for the normal face velocity in order to conserve mass, Eq. 2.26, makes the divergence-gradient relation, $\mathbf{M} = -\mathbf{G}^*$, not true, therefore, a pressure gradient error term arises in Eq. 2.33.

2.4 A self-adaptive strategy for the time-integration of Navier-Stokes equations

Since the pioneering channel flow simulations by Kim et al.[11, 12], DNS simulations of incompressible flows have been usually carried out by means of fractional step methods together with explicit or semi-implicit time-integration methods. In their work, they proposed to use a second-order-explicit Adams-Bashforth (AB2) method for the non-linear convective terms whereas the viscous terms were advanced in time by a second-order-implicit Crank-Nicolson scheme. Later, a three-step third-order semi-implicit Runge-Kutta (RK3) scheme was proposed by Le & Moin [13]. The non-linearity was again treated explicitly, and the Poisson equation was solved only at the final step to project the velocity vector onto a divergence-free space. Slightly different variants of the method can be found in [14, 15, 16], for instance. In short, the RK3 algorithm has three steps and, therefore, it requires three times more operations (except for the Poisson equation that is solved only in the last step) to advance to a new time level. To compensate this, stability analysis leads to significantly larger CFL-numbers [17], that is larger time-steps, compared with the AB2 method; therefore, RK3 method is often the favorite option (see [18, 19, 20, 21, 22, 23], for example). However, Verstappen and Veldman [1, 3]

showed that a minor modification respect the original AB2 method may lead to similar computational cost than the RK3 method proposed in [13] without affecting the accuracy. It must be noted that the RK3-based schemes use second-order accurate implicit methods for the viscous term and, therefore, their overall accuracy is second-order in time like the AB2-based schemes. Despite the most widespread schemes are the above-mentioned AB2 (see [24, 25, 26, 27, 28], for instance) and RK3 methods, other schemes (or variants) have also been used in the context of the numerical simulation of the unsteady Navier-Stokes equations. In [29], a six-step fourth-order-implicit Runge-Kutta method in conjunction with several non-linear solvers was presented. A semi-implicit third-order accurate in time Runge-Kutta scheme was proposed in [30]; it is based on the original three-step RK3 scheme with one additional sub-step to achieve a higher-order of accuracy. More recently, in the context of collocated spatial formulations, a third-order-explicit Gear-based scheme was proposed to mitigate the unwanted spatial oscillations [10].

The performance of an explicit time-integration method basically depends on three issues: (i) the ability to determine (or bound) the eigenvalues of our dynamical system in a relatively inexpensive manner, (ii) how this information is used to choose the 'optimal' time-step, and (iii) the capability of the time-integration scheme to self-adapt the stability domain. In this context, an efficient self-adaptive strategy for the explicit time-integration of Navier-Stokes equations is presented in the framework of a one-parameter second-order-explicit scheme. Unlike the conventional explicit integration schemes, it is not based on a standard CFL condition. Instead, the eigenvalues of our dynamical system are analytically bounded and the linear stability domain of the time-integration scheme is adapted in order to maximize the time-step. The method works independently of the underlying spatial mesh; therefore, it can be easily integrated into structured and unstructured codes. The additional computational cost is minimal and a significant increase of the time-step is achieved without losing accuracy. The effectiveness and robustness of the method are demonstrated on both a Cartesian staggered and an unstructured collocated formulation. In practice, CPU cost reductions up to more than 4 respect the conventional approach have been measured on unstructured grids.

2.4.1 Explicit versus (semi-)implicit methods

In the context of DNS of turbulent flows, the computational costs of using an implicit time-integration method are rather high compared to those of explicit methods [1]. In the latter case, stability condition is always given by a CFL-like criterion; in dimensionless variables, it reads

$$\Delta t < Re\Delta x^2 \qquad \text{(diffusion)}, \tag{2.34}$$
$$U_{max}\Delta t < \Delta x \qquad \text{(convection)}. \tag{2.35}$$

If we then compare the CFL-condition with accuracy requirements, assuming that the ratios of the smallest length scales, η, (also the smallest time scale, τ_η) in the flow to the largest are given by the Kolmogorov scaling law,

$$1/\eta \sim Re_{le}^{3/4} \qquad \text{and} \qquad 1/\tau_\eta \sim Re_{le}^{1/2}, \tag{2.36}$$

where Re_{le} is based on the velocity U_{le} and length of large eddies, we find that

$$\Delta t/\tau_\eta < (\Delta x/\eta)^2 \qquad \text{(diffusion)}, \tag{2.37}$$
$$\Delta t/\tau_\eta < (U_{le}/U_{max})Re_{le}^{-1/4}(\Delta x/\eta) \qquad \text{(convection)}. \tag{2.38}$$

Since for DNS applications $(\Delta x/\eta) \sim 1$, the time-step of explicit time-integration methods is usually limited by the convective stability. In general, this discards the use of implicit schemes for the diffusive terms. Then, the main reasons to rule out an implicit treatment of the non-linearity are twofold: (i) firstly, for DNS the $\Delta t/\tau_\eta$ must be kept close to unity, so Δt cannot be arbitrarily large and (ii) a computationally expensive non-linear solver would be needed. Hence, in the view of lower costs, a fully-explicit time-integration scheme has been adopted.

2.4.2 One-parameter second-order-explicit method (κ1L2)

We consider the following one-leg second-order-explicit time-integration scheme

$$\Omega\frac{\boldsymbol{u}_h^{n+\kappa+1/2} - \boldsymbol{u}_h^{n+\kappa-1/2}}{\Delta t} + \mathsf{C}\left(\boldsymbol{u}_h^{n+\kappa}\right)\boldsymbol{u}_h^{n+\kappa} + \mathsf{D}\boldsymbol{u}_h^{n+\kappa} - \mathsf{M}^*\boldsymbol{p}_h^{n+1} = \mathbf{0}_h, \tag{2.39}$$

where the off-step velocities are given by

$$\boldsymbol{u}_h^{n+\kappa+1/2} = (\kappa + 1/2)\,\boldsymbol{u}_h^{n+1} - (\kappa - 1/2)\,\boldsymbol{u}_h^{n}, \tag{2.40}$$
$$\boldsymbol{u}_h^{n+\kappa} = (1+\kappa)\,\boldsymbol{u}_h^{n} - \kappa\boldsymbol{u}_h^{n-1}. \tag{2.41}$$

This time-integration scheme can be viewed as a minor modification of the classical second-order Adams-Bashforth (AB2) scheme ($\kappa = 1/2$). This was already proposed in [1, 3] in the context of DNS simulations of incompressible flows. The pressure-velocity coupling is then solved by means of a classical fractional step projection

method [31]. Shortly, a predictor velocity, $\boldsymbol{u}_h^p$, is explicitly evaluated without considering the contribution of the pressure gradient. Then, by imposing the incompressibility constraint, $\mathsf{M}\boldsymbol{u}_h^{n+1} = \mathbf{0}_h$, it leads to a Poisson equation for $\boldsymbol{p}_h^{n+1}$,

$$-\mathsf{M}\Omega^{-1}\mathsf{M}^*\boldsymbol{p}_h^{n+1} = \mathsf{M}\boldsymbol{u}_h^p, \tag{2.42}$$

that must be solved once each time-step. For further details about the Poisson solver the reader is referred to [32]. Then, substituting the linear inter/extrapolations for the off-step velocities into (2.39) yields a family of one-leg methods (so-called because it uses just one evaluation of the flux per time-step). Hence, the proposed scheme is controlled by one parameter, κ, that allows to adapt the linear stability domain to the instantaneous flow conditions in order to maximize the time-step, Δt. Hereafter this method is referred as κ1L2.

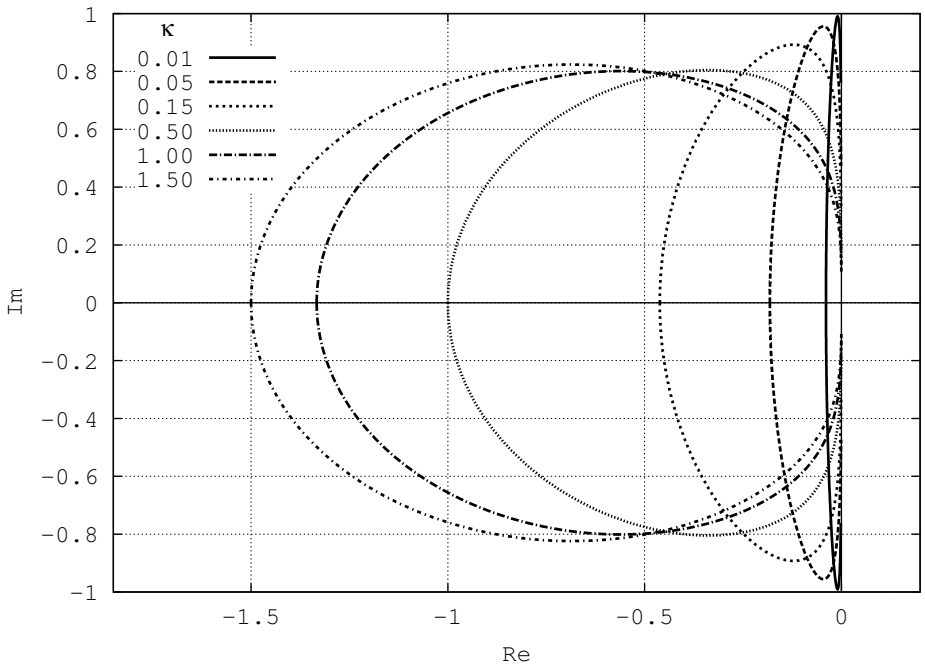

Figure 2.3: Stability domain of the one-leg method κ1L2 (2.43) for different values of κ from 0.01 to 1.5. The stability domain is pressed against the imaginary axis when κ goes to zero

2.4.3 One-dimensional test problem

Our aim is now to determine κ such that the resulting method possesses the optimal region of stability. Since incompressibility constraint is treated implicitly, it can be discarded from the stability analysis. Thus, we focus on the one-leg scheme for the simplified, one-dimensional Cauchy problem $\delta_t u = f(u)$. In this case, the κ1L2 method reads

$$\left(\kappa + \frac{1}{2}\right) u^{n+1} - 2\kappa u^n + \left(\kappa - \frac{1}{2}\right) u^{n-1} = \Delta t f\left((1+\kappa)u^n - \kappa u^{n-1}\right). \tag{2.43}$$

Then, it is possible to numerically investigate how the stability region of $f(\cdot)$ depends on the value of the parameter control, κ. Illustrative results are shown in Figure 2.3 for values of κ from 0.05 to 2.0. Note that when κ goes to zero the stability domain is pressed against the imaginary axis. In the limit $\kappa = 0$ (leapfrog scheme), the stability domain lies in the interval $[-i, i]$. Moreover, the stability domain also includes the interval $[-4\kappa/(2\kappa+1), 0]$ on the real axis. Hence, in the limit $\kappa = +\infty$, this interval becomes $(-2, 0]$. Here, we restrict the method to values $\kappa \leq 1$. In this way, (i) we keep the function $K_{opt}(\varphi)$ continuous for the whole range of $\varphi \in [0, \pi/2]$ (see Appendix 8.4), (ii) the extrapolation of the off-step velocities in (2.41) do not fall out of the range $[n, n+1]$ and (iii) from a practical point-of-view, recalling that convection usually dominates diffusion in DNS simulations (see Section 2.4.1), the choice of κ_{max} has no effect on the proposed scheme for the working range of the phase angle, φ (see Figure A.1 in Appendix 8.4).

Thus, knowing the exact location of the eigenvalues (in the stable half-plane) of our dynamical system, we can choose the optimal value of κ that results with the stability region that fits better. This allows to use of the largest Δt possible maintaining all the eigenvalues inside the stability region. For details, the reader is referred to the Appendix 8.4. However, to apply this method for our problem (2.39), we need to know (or bound) the eigenvalues of our dynamical system.

2.5 Time-integration of Navier-Stokes equations

A fully-explicit second-order accurate method has been proposed in the previous section. This method, named κ1L2, makes uses of the eigenvalues of the dynamical system. Then, to apply this method to our problem (2.39), we need to know (or bound) the eigenvalues of the matrix $-(\mathsf{C}+\mathsf{D})$ in a relatively inexpensive manner. It must be recalled that the diffusive operator, D, remains constant during the simulation; therefore, it needs to be computed only once. On the contrary, the convective operator, $\mathsf{C}(\boldsymbol{u}_h)$, depends on the velocity field and needs to be recomputed during the simulation.

2.5.1 Eigenvalues of C and D operators

In the Section 2.3.2, we showed that for a proper symmetry-preserving discretization, the convective, C, and the diffusive, D, operators must possess the following properties

$$\mathsf{C} = -\mathsf{C}^* \qquad \text{for any } \boldsymbol{u}_h, \text{ provided } \mathsf{M}\boldsymbol{u}_h = \mathbf{0}_h, \tag{2.44}$$

$$\mathsf{D} = \mathsf{D}^* \qquad \text{and positive-definite matrix.} \tag{2.45}$$

Thus, their eigenvalues lie on the imaginary and the positive-real axis respectively,

$$\lambda_k^{\mathsf{C}} \in \mathbb{I} \quad \text{and} \quad \lambda_k^{\mathsf{D}} \in \mathbb{R}^+, \qquad \forall k = 1 \dots m, \tag{2.46}$$

where m is the dimension of the discrete velocity vector, *i.e.* $\boldsymbol{u}_h \in \mathbb{R}^m$. Note that the matrix $-(\mathsf{C}+\mathsf{D})$ is regular, because all the eigenvalues lie on the stable half-plane. Then, the eigenvalues of C and D can be bound by means of the Gershgorin circle theorem,

$$\left|\lambda_k^{\mathsf{C}} - c_{ii}\right| \leq \sum_{j \neq i} |c_{ij}| \quad \text{and} \quad \left|\lambda_k^{\mathsf{D}} - d_{ii}\right| \leq \sum_{j \neq i} |d_{ij}|, \qquad \forall i, k = 1 \dots m. \tag{2.47}$$

Then, recalling the skew-symmetry of C ($c_{ii} = 0$, $c_{ij} = -c_{ji}$) and the symmetry ($d_{ij} = d_{ji}$) and positive-definiteness ($\lambda_k^{\mathsf{D}} > 0$, $d_{ii} > 0$ and $d_{ii} \geq \sum_{j \neq i} |d_{ij}|$) of D in conjunction with momentum conservation ($d_{ii} = -\sum_{j \neq i} d_{ij}$ and $\sum_{j \neq i} c_{ij} = 0$) the previous expressions simplify

$$\left|\lambda_k^{\mathsf{C}}\right| \leq \sum_{j \neq i} |c_{ij}| \qquad \text{and} \qquad \lambda_k^{\mathsf{D}} \leq 2d_{ii}, \qquad \forall i, k = 1 \dots m. \tag{2.48}$$

2.5.2 Applying the method to our problem ($EigenCD$ method)

Our dynamical system is governed by the matrix $-(\mathsf{C}+\mathsf{D})$. As the numerical computation of its eigenvalues is not viable in our context we need to bound them. From the expressions (2.46) follows

$$max\left(Re(\lambda_k^{\mathsf{C}+\mathsf{D}})\right) \leq \max\left(\lambda_k^{\mathsf{D}}\right) = a, \qquad \forall k = 1 \dots m, \tag{2.49}$$

$$max\left(Im(\lambda_k^{\mathsf{C}+\mathsf{D}})\right) \leq \max\left(\left|\lambda_k^{\mathsf{C}}\right|\right) = b, \qquad \forall k = 1 \dots m, \tag{2.50}$$

where the eigenvalues of C and D operators are bound by the expressions (2.48). In conclusion, the latter expressions bound all the eigenvalues of the matrix $-(\mathsf{C}+\mathsf{D})$

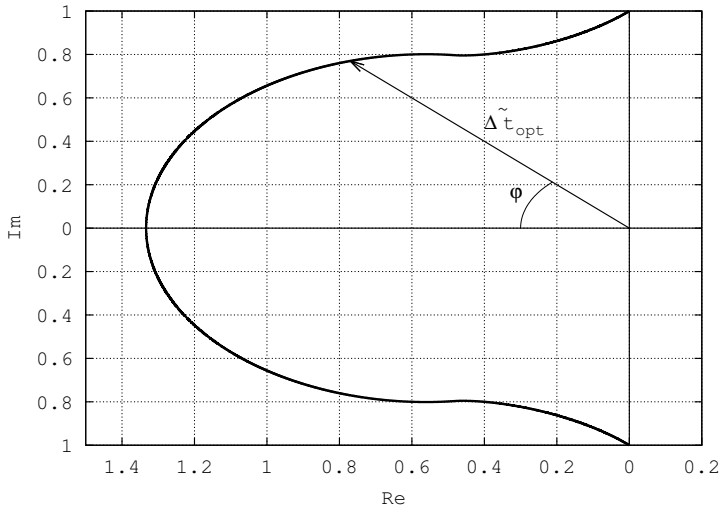

Figure 2.4: Stability domain of the one-leg κ1L2 method (2.43) for the optimal $\kappa = K_{opt}(\varphi)$.

in the stable half-plane. Hereafter, this method to bound the eigenvalues of our dynamical system is referred as $EigenCD$.

Therefore, we look for stability domains which includes eigenvalues

$$\lambda = -\widetilde{\Delta t} e^{-i\varphi} = \Delta t \left(-a + ib\right), \tag{2.51}$$

that lie on the line $x/y = -a/b$. Under these conditions we need to solve a maximum optimization problem for $\widetilde{\Delta t}$ as a function of parameter κ. The idea of the method is depicted in Figure 2.4. For details see the Appendix 8.4.

This dynamic time-integration method has already been successfully used to perform DNS simulations on a Cartesian staggered code [33, 34]. In the previous version of the code [25], a standard second-order Adams-Bashforth ($\kappa = 1/2$) scheme together with a classical CFL-based method was being used. In such configurations, the alternative method proposed here leads to time-steps more than two times greater, that is twice cheaper, without affecting the quality of the numerical results. However, the benefits of the proposed approach became even more relevant when the method is applied to an unstructured formulation where CPU cost reductions up to more than 4 respect the convectional approach have been measured. For a detailed analysis the reader is referred to Section 2.6. At this point, to understand better the benefits of the proposed method a further analysis is necessary.

2.5.3 Comparison with a classical CFL method

Roughly speaking, standard CFL-based methods consist on bounding the time-step, Δt, by means of expressions (2.34) and (2.35). In practice, to keep them stable a restrictive criterion is usually imposed, *i.e.*

$$\Delta t_{CFL} = min\left(C_{\mathsf{D}} Re \Delta x^2, C_{\mathsf{C}} \Delta x / U_{max}\right) \tag{2.52}$$

where $C_{\mathsf{D}}, C_{\mathsf{C}} \lesssim 1$ have to be prescribed in advance and a characteristic length, Δx, of the control volume needs to be estimated. For moderately skewed grids, such a method can provide proper bounds. However, for highly skewed grids the time-step can be clearly under-predicted. It must be recalled that the presence of highly skewed control volumes is, in general, a common feature for wall-bounded flows.

The main drawbacks of these kinds of methods are twofold. Firstly, the eigenvalues of our dynamical system are not properly bounded by (2.52). Secondly, the diffusive and convective terms give their bounds for the time-step, Δt, irrespective of each other; instead of using the ratio between convection and diffusion to obtain a better estimation of Δt (the basic idea is depicted in Figure 2.4). Furthermore, the method proposed here also adapts the stability domain in order to optimize the Δt. Altogether, provides a substantial computational cost reduction compared with the standard methods.

This can be further analyzed by comparing the performance of both methods as estimators of the maximum eigenvalues of our dynamical system. Let us consider first the diffusive terms. In this case, a CFL-based method provides the following bounds

$$\lambda^{\mathsf{D}}_{CFL} \leq \frac{1}{C_{\mathsf{D}} Re} \max_k \left\{ \frac{1}{\Delta x_k^2} \right\}, \tag{2.53}$$

whereas the approximation given by (2.48) reads

$$\lambda^{\mathsf{D}}_{EigenCD} \leq -2 \max_k \left\{ \frac{d_{k,k}}{[\Omega]_{k,k}} \right\} \qquad \text{with} \qquad d_{k,k} = -\frac{1}{Re} \sum_{f \in F_c(k)} \frac{A_f}{\delta n_f}, \tag{2.54}$$

where $F_c(k)$ is the set of faces bordering the cell k. A_f and δn_f are the area of the face f and the length between the centroids of adjacent cells c_1 and c_2, respectively (see Figure 2.5). A CFL-based method (2.53) makes use of the distance Δx. In order to keep the method on the safe side, this is usually set equal to the minimum distance δn_f, *i.e.* $\Delta x_k = min_{f \in F_c(k)}\{\delta n_f\}$ (*e.g.* [35]). As expected, for non-skewed meshes both approximations provide similar results. To exemplify this, two canonical cases are compared: a cubical control volume and a regular tetrahedron of edge length

h. For these cases Δx becomes $\Delta x^{cube} = h$ and $\Delta x^{tetra} = h/\sqrt{6}$; therefore, the eigenvalues are bounded by

$$\lambda_{CFL}^{\mathsf{D},cube} \leq \frac{1}{C_{\mathsf{D}} Re} \frac{1}{h^2} \qquad \text{and} \qquad \lambda_{CFL}^{\mathsf{D},tetra} \leq \frac{1}{C_{\mathsf{D}} Re} \frac{6}{h^2}, \tag{2.55}$$

whereas using the approximation given by (2.48) leads to

$$\lambda_{EigenCD}^{\mathsf{D},cube} \leq \frac{12}{Re} \frac{1}{h^2} \qquad \text{and} \qquad \lambda_{EigenCD}^{\mathsf{D},tetra} \leq \frac{72}{Re} \frac{1}{h^2}. \tag{2.56}$$

Hence, the values for C_{D} that would give the same bounds are the same ($C_{\mathsf{D}} = 1/12$), meaning that both methods perform alike on non-skewed meshes. However, for highly skewed meshes it can differ substantially. Let us consider a cuboid of dimensions $h \times h \times \xi h$. The two limiting situations are $\xi \ll 1$ and $\xi \gg 1$. In such cases, the CFL-based method would provide the following bounds

$$\lambda_{CFL}^{\mathsf{D},\xi \ll 1} \leq \frac{1}{C_{\mathsf{D}} Re} \frac{1}{\xi^2 h^2} \qquad \text{and} \qquad \lambda_{CFL}^{\mathsf{D},\xi \gg 1} \leq \frac{1}{C_{\mathsf{D}} Re} \frac{1}{h^2}, \tag{2.57}$$

whereas for the proposed method they read

$$\lambda_{EigenCD}^{\mathsf{D},\xi \ll 1} \lesssim \frac{4}{Re} \frac{1}{\xi^2 h^2} \qquad \text{and} \qquad \lambda_{EigenCD}^{\mathsf{D},\xi \gg 1} \lesssim \frac{8}{Re} \frac{1}{h^2}, \tag{2.58}$$

leading to equivalent C_{D} values of $1/4$ and $1/8$, respectively. Hence, a wide range of values for C_{D} has been obtained (from $1/12$ to $1/4$). Since in real-world applications all kinds of control volumes usually co-exits on the same mesh, we conclude that a CFL-based criterion is not the most appropriate approach to bound the eigenvalues of the diffusive operator.

The convective terms can be analyzed in the same vein. In this case, the bounds given by CFL-based method usually read

$$\lambda_{CFL}^{\mathsf{C}} \leq \frac{1}{C_{\mathsf{C}}} \max_k \left\{ \sum_{i=1}^{3} \frac{|U_i|}{\Delta x_i} \right\}, \tag{2.59}$$

where the sub-index k has been dropped for simplicity. On the other hand, the approximation given by (2.48) leads to

$$\lambda_{EigenCD}^{\mathsf{C}} \leq \frac{1}{2} \max_k \left\{ \frac{1}{[\Omega]_{k,k}} \sum_{f \in F_c(k)} |U_f| A_f \right\}. \tag{2.60}$$

In the case of Cartesian meshes both approximations provide very similar results. However, for unstructured meshes the distances Δx_i need to be estimated and,

therefore, the expression given in (2.59) may become inaccurate. Hence, for the sake of generality it is preferable to use the expression (2.60).

At this point, it must be noted that the proposed method could also be used for other discretizations of the convective term. For instance, upwind-like schemes are also very popular because they are very stable: the convective term introduces artificial numerical dissipation that systematically damps kinetic energy. In this case, the non-constant additional dissipation should be added to the viscous dissipation to bound the eigenvalues of our dynamical system in (2.51). Then, the rest of the method would remain exactly the same.

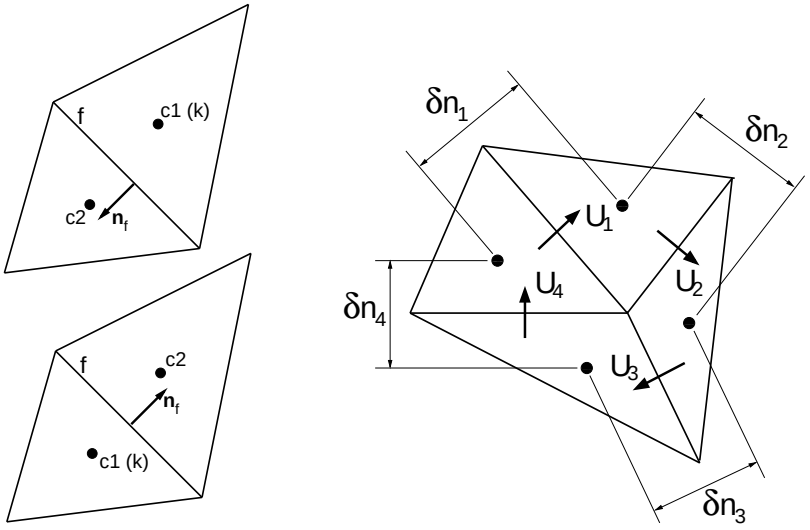

Figure 2.5: Left: face normal and neighbor labeling criteria. Right: definition of volumes of the face-normal velocity cell.

2.6 Numerical experiments

In this section the performance of the κ1L2 time-integration algorithm (see Section 2.4) in conjunction with the analytical method $EigenCD$ (see Section 2.5) to bound the eigenvalues of our dynamical system is tested by direct comparison with a standard AB2 scheme together with a CFL criterion. Hereafter, these two methods are referred as $EigenCD + \kappa$1L2 and CFL $+$ AB2, respectively. For the CFL criterion, values of C_{D} and C_{C} are set to 0.2 and 0.35, respectively. These are the values that were used in the previous version of the code [25].

	N_x	N_y	N_z	$\overline{\varphi}/(\pi/2)$	$\overline{\delta t}_{\text{CFL+AB2}}$	$\overline{\delta t}_{EigenCD+\kappa\text{1L2}}$	$\overline{\delta t}_{EigenCD+\kappa\text{1L2}}/\overline{\delta t}_{\text{CFL+AB2}}$
MeshA	128	338	778	0.072	1.04×10^{-4}	3.02×10^{-4}	2.90
MeshB	64	168	338	0.158	4.31×10^{-4}	1.21×10^{-3}	2.80
MeshC	32	84	168	0.252	1.80×10^{-3}	4.69×10^{-3}	2.59
MeshD	32	56	112	0.408	4.21×10^{-3}	8.75×10^{-3}	2.08
MeshE	16	42	84	0.504	6.88×10^{-3}	1.35×10^{-3}	1.96

Table 2.1: Tests for the air-filled ($Pr = 0.71$) differentially heated cavity at Rayleigh number $Ra = 3 \times 10^{10}$ and height aspect ratio 4. Averaged results correspond to the statistically steady state.

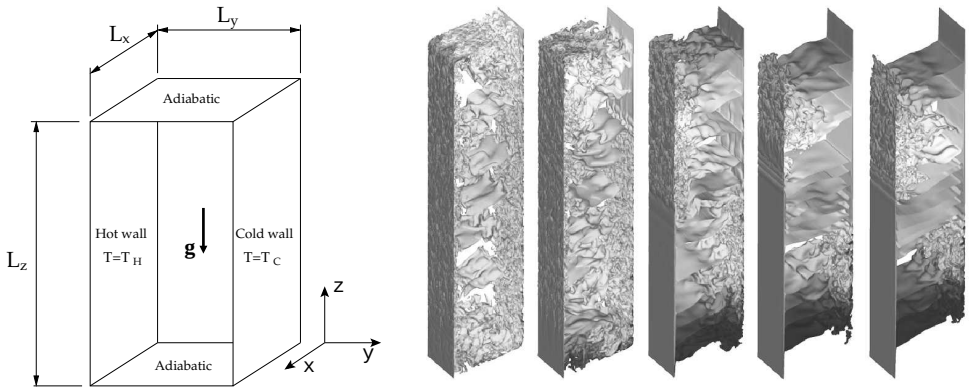

Figure 2.6: Differentially heated cavity problem. Left: general schema. Right: Several instantaneous temperature fields. This sequence illustrates the time-evolution from the initial conditions to the statistically steady-state.

To test the performance of the $EigenCD + \kappa$1L2 method two problems models have been considered. Firstly, a DNS of a buoyancy-driven turbulent flow in an air-filled ($Pr = 0.71$) differentially heated cavity has been used (see Figure 2.6, left) to test the method on a structured Cartesian staggered mesh. The cavity is subjected to a temperature difference, $\Delta T = T_H - T_C$, across the vertical isothermal walls while the top and bottom horizontal walls are adiabatic. Periodic boundary conditions are imposed in the span-wise x-direction. Finally, the no-slip boundary condition is imposed on the velocity field at the four closing walls. In Figure 2.6 (right) several instantaneous temperature maps corresponding to the DNS at Rayleigh number $Ra = 3 \times 10^{10}$ (based on the cavity height, L_z) and height aspect ratio $L_z/L_y = 4$ are displayed. For this case, the reference time is $(L_z^2/\alpha)Ra^{-0.5}$ where α is the thermal diffusivity. This simulation has been carried out using 128 processors on the MareNostrum supercomputer and a symmetry-preserving fourth-order spatial discretization [3] on a $\approx 33.7 \times 10^6$ points mesh ($128 \times 338 \times 778$). This mesh is labeled MeshA in Table B.1. These new DNS results have provided new insights into the physics of turbulence and indispensable data for the progress on turbulence modeling [36]. Further details and results for this configuration can be found in [33, 34]. Apart from the MeshA, the performance of the method has also been tested on four coarser meshes (see Table B.1). Notice that these cases are not fine enough to be considered DNS in the sense that not all relevant turbulent scales can be captured. Figure 2.7 shows a comparison between the $EigenCD + \kappa$1L2 and the CFL + AB2 method. The time-integration method is basically governed by the ratio between convection and diffusion, $\tan(\varphi)$. The initial velocity field is null and therefore, φ

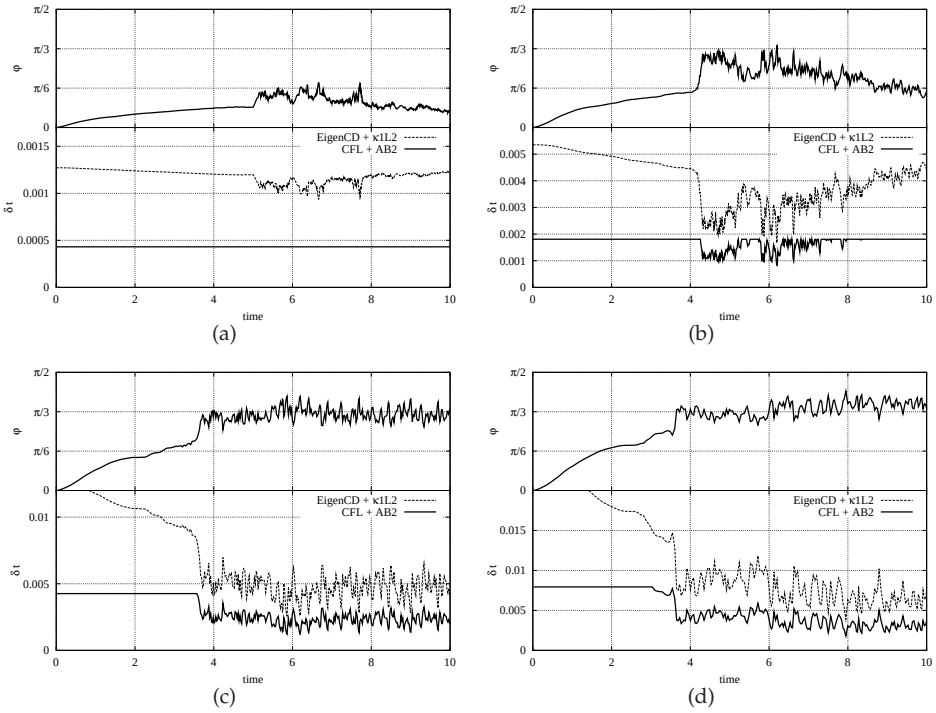

Figure 2.7: Comparison between self-adaptive $EigenCD + \kappa$1L2 method and the standard CFL + AB2 method. Results correspond to a turbulent differentially heated cavity at $Ra = 3 \times 10^{10}$, $Pr = 0.71$ using meshes MeshA (top left), MeshB (top right), MeshC (bottom left) and Mesh D (bottom right).

is zero (pure diffusion) at the beginning of the simulations. Then, during the start-up period diffusion still dominates convection. Eventually, an statistically steady state is reached and the balance between convection and diffusion depends on the mesh resolution. In Table B.1, the averaged values of φ are shown. Here, $\overline{(\cdot)}$ represents the time-averaging within the statistically steady state period. For this test-case, $\overline{\varphi}$ ranges from 0.072 (MeshA) to 0.504 (MeshE). For all meshes, the proposed method clearly outperforms the previous CFL + AB2 method. As expected, the ratio $\overline{\delta t}_{EigenCD+\kappa\text{1L2}}/\overline{\delta t}_{\text{CFL+AB2}}$ tends to increase for diffusion-dominated simulations reaching an acceleration of 2.90 for the finest mesh (MeshA).

A second test-case on an unstructured collocated mesh has also been considered. Namely, a turbulent flow around a NACA 0012 airfoil at Reynolds number 5×10^4

(based on the free-stream velocity, v_{in}, and the chord length, C) and an angle of attack of 5°. The computational domain is $0.2C \times 20C \times 10C$ in the span-wise, stream-wise and cross-stream directions, respectively. The airfoil is located at the center of the domain. At the inflow, a constant velocity profile is prescribed and pressure-based condition is used at the outflow. Periodic boundary conditions are imposed in the span-wise direction. Finally, no-slip boundary conditions are imposed at the surface of the airfoil. Here, the reference time is C/v_{in}. In Figure 2.8 (right) an illustrative instantaneous span-wise vorticity field is displayed. This simulation has been carried out on a $\approx 17 \times 10^6$ points unstructured mesh using 152 processors. It consists on a 2D unstructured mesh (Mesh2D in Table 2.2) with triangular elements extruded in the span-wise direction (see Figure 2.8, left). The number of mesh points in the span-wise direction is denoted by N_x. The ANSYS ICEM CFD package has been used to generate it. Most of the grid points are clustered around the airfoil in the region from $1C$ in front of the leading edge until $5C$ behind the trailing edge. This mesh is labeled UMeshA in Table 2.2 and it has been used to computed a DNS simulation [37]. Moreover, a coarser mesh with $\approx 1.5 \times 10^6$ grid points has also been considered (labeled UMeshB in Table 2.2). Figure 2.9 shows a comparison between the $EigenCD + \kappa$1L2 and the CFL + AB2 method for these two meshes. Again, the proposed method clearly improve the performance of the standard CFL method. However, it is important to note that in this case the ratio $\overline{\delta t}_{EigenCD+\kappa 1L2}/\overline{\delta t}_{\text{CFL+AB2}}$ do not increase for the finest mesh. Apparently, this is in contradiction with the behavior observed for the structured Cartesian mesh. However, for unstructured meshes the quality of the grid plays an important role for the performance of the standard CFL methods where bounds given by (2.53) and (2.59) may be very inaccurate for highly skewed elements. Since the quality of the grid improves when refining, it justifies the observed behavior. It must be also noted that the performance of the method ultimately depends on the spatial mesh and the configuration of the flow. Therefore, these gain factors must be taken as indicative.

2.7 Concluding remarks

An efficient self-adaptive strategy for the explicit time-integration of the Navier-Stokes equations has been presented. It is based on a one-parameter second-order-explicit scheme. Firstly, the eigenvalues of our dynamical system are bounded by means of an 'almost' inexpensive method. Secondly, the linear stability domain of the time-integration method is adapted in order to maximize the time-step. To do so, the control parameter is automatically tuned. The method works independently of the underlying spatial mesh and, therefore, it is suitable for both structured and unstructured codes.

The computational cost benefits respect the standard approach have been ana-

	N_x	Mesh2D	$\overline{\varphi}/(\pi/2)$	$\overline{\delta t}_{\text{CFL+AB2}}$	$\overline{\delta t}_{EigenCD+\kappa\text{1L2}}$	$\overline{\delta t}_{EigenCD+\kappa\text{1L2}}/\overline{\delta t}_{\text{CFL+AB2}}$
UMeshA	64	$\approx 2.65 \times 10^5$	0.593	4.69×10^{-5}	1.30×10^{-4}	2.77
UMeshB	32	$\approx 4.69 \times 10^4$	0.956	1.61×10^{-4}	6.86×10^{-4}	4.27

Table 2.2: Tests for the flow around a NACA 0012 airfoil at Reynolds number 5×10^4 and an angle of attack of 5^o. Averaged results correspond to the statistically steady state.

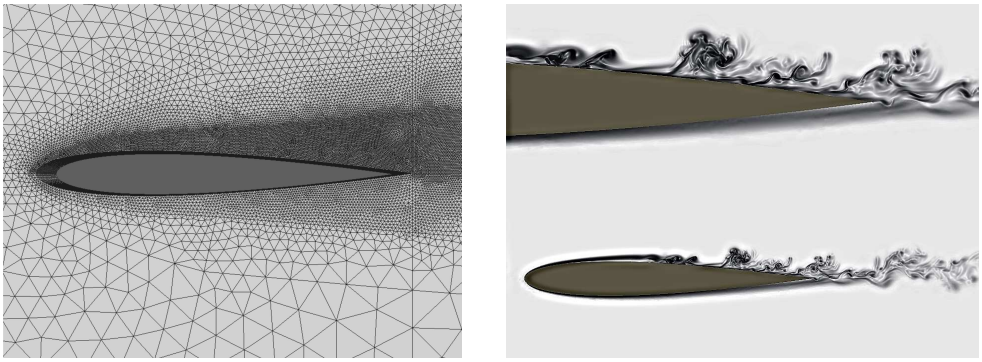

Figure 2.8: NACA 0012 airfoil. Left: zoom around the airfoil of the unstructured mesh UMeshB. Right: instantaneous span-wise vorticity field corresponding to the DNS simulation computed with UMeshA.

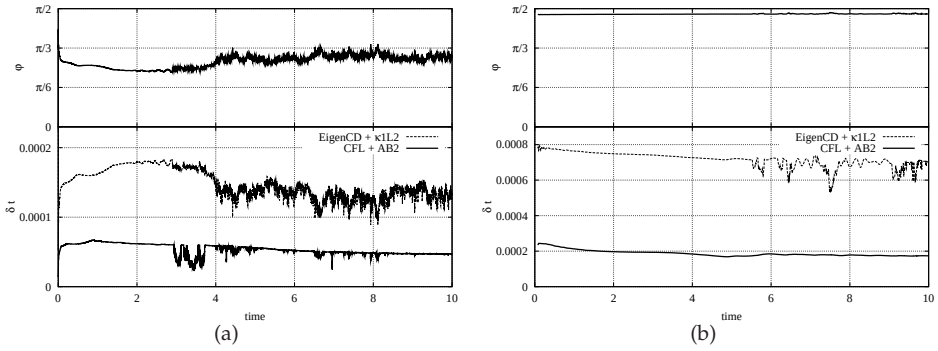

Figure 2.9: Comparison between self-adaptive $EigenCD + \kappa$1L2 method and the standard CFL + AB2 method. Results correspond to the NACA 0012 airfoil at $Re = 5 \times 10^4$ and an angle of attack of 5° using meshes UMeshA (left) and UMeshB (right).

lyzed. Since the additional computational cost is minimal, the CPU cost reduction can be measured in terms of the resulting time-step. The advantage of the proposed method becomes more significant for highly skewed meshes where the CFL-based criteria tend to under-predict the eigenvalues of the dynamical system. Such effect becomes even more relevant on unstructured formulations. In practice, the method has been successfully tested on both a Cartesian staggered and an unstructured collocated codes leading to CPU cost reductions of up to $\approx$ 2.9 and $\approx$ 4.3, respec-

tively. Therefore, it constitutes a robust and easy-to-implement approach for the time-integration of incompressible turbulent flows.

The proposed one-parameter self-adaptive approach can be extended to a multiparameter method. The essential ideas would remain exactly the same. In this way, it may lead to larger stability domains and, therefore, larger time-steps without affecting the quality of the numerical solutions. This is part of our future research plans.

References

[1] R. W. C. P. Verstappen and A. E. P. Veldman. Direct Numerical simulation of turbulence at lower costs. *Journal of Engineering Mathematics*, 32:143–159, 1997.

[2] Y. Morinishi, T.S. Lund, O.V. Vasilyev, and P. Moin. Fully conservative higher order finite difference schemes for incompressible flow. *Journal of Computational Physics*, 143(1):90–124, 1998.

[3] R. W. C. P. Verstappen and A. E. P. Veldman. Symmetry-Preserving Discretization of Turbulent Flow. *Journal of Computational Physics*, 187:343–368, May 2003.

[4] S.V. Patankar. *Numerical heat transfer and fluid flow*. Hemisphere Publishing Corporation, 1980.

[5] J.H. Ferziger and M. Peric. *Computational methods for fluid dynamics*. Springer-Berlag, 1996.

[6] C. D. Perez-Segarra, C. Farre, J. Cadafalch, and A. Oliva. Analysis of different numerical schemes for the resolution of convection-diffusion equations using finite-volume methods on three-dimensional unstructured grids. part i: Discretization schemes. *Numerical Heat Transfer, Part B: Fundamentals*, 46(4):333–350, 2007.

[7] A Haselbacher and Oleg V. Vasilyev. Commutative discrete filtering on unstructured grids based on least-squares techniques. *Journal of Computational Physics*, 187(1):197–211, 2003.

[8] Verzicco R. and R. Camussi. Numerical experimenrs on strongly turbulent thermal convection in a slender cylindrical cell. *Journal of Fluid Mechanics*, 477:19–49, 2003.

[9] F.N. Felten and T.S. Lund. Kinetic energy conservation issues associated with the collocated mesh scheme for incompressible flow. *Journal of Computational Physics*, 215(2):465–484, 2006.

[10] G.M. Fishpool and M.A. Leschziner. Stability bounds for explicit fractional-step schemes for the Navier-Stokes equations at high Reynolds number. *Computers and Fluids*, 38:1289–1298, 2009.

[11] J. Kim and P. Moin. Application of a fractional-step method to incompressible navier-stokes equations. *Journal of Computational Physics*, pages 308–323, 1985.

[12] J. Kim, P. Moin, and R. Moser. Turbulence statistics in fully developed channel flow at low Reynolds number. *Journal of Fluid Mechanics*, 177:133–166, 1987.

[13] Hung Le and Parviz Moin. An Improvement of Fractional Step Methods for the Incompressible Navier-Stokes Equations. *Journal of Computational Physics*, 92:369–379, 1991.

[14] R. Vezicco and Orlandi P. A finite-difference scheme for three dimensional incompressible flows in cylindrical coordinates. *Journal of Computational Physics*, 123:402–414, 1996.

[15] P. R. Spalart, R. D. Moser, and M. M. Rogers. Spectral methods for the navier-stokes equations with one infinite and two periodic directions. *Journal of Computational Physics*, 96(2):297–324, 1991.

[16] M. M. Rai and P. Moin. Direct simulations of turbulent flow using finite-difference schemes. *Journal of Computational Physics*, 96(1):15–53, 1991.

[17] R. Courant, K. Friedrichs, and H. Lewy. Über die partiellen Differenzengleichungen der mathematischen Physik. *Mathematische Annalen*, 100:32–74, 1928.

[18] Moser R., Kim J., and Mansour N.N. Direct Numerical Simulation of Turbulent Channel Flow up to $Re_\tau = 590$. *Physics of Fluids*, 11:943–945, 1999.

[19] J. Kim, D. Kim, and H. Choi. An immersed-boundary finite-volume method for simulations of flow in complex geometries. *Journal of Computational Physics*, 171(1):132–150, 2001.

[20] Y. Morinishi, S. Tamano, and K. Nakayashi. Direct numerical simulation of compressible turbulent channel flow between adiabatic and isothermal walls. *Journal of Fluid Mechanics*, 502:273–308, 2004.

[21] Juan C. del Álamo, Javier Jiménez, Paulo Zandonade, and Robert D. Moser. Scaling of the energy spectra of turbulent channels. *Journal of Fluid Mechanics*, 500:135–144, 2004.

[22] A. Yakhot, H. Liu, and N. Nikitin. Turbulent flow around a wall-mounted cube: A direct numerical simulation. *International Journal of Heat and Fluid Flow*, 27:994–1009, 2006.

[23] C. Zhang and W. Zhang andG. Xi. A pseudospectral multidomain method for conjugate conduction-convection in enclosures. *Numerical Heat Transfer, Part B: Fundamentals*, 57(4):260–282, 2010.

[24] S. Xin and P. Le Queré. Direct numerical simulations of two-dimensional chaotic natural convection in a differentially heated cavity of aspect ratio 4. *Journal of Fluid Mechanics*, 304:87–118, 1995.

[25] M. Soria, F.X. Trias, C.D. Pérez-Segarra, and A. Oliva. Direct numerical simulation of a three-dimensional natural convection flow in a differentially heated cavity of aspect ratio 4. *Numerical Heat Transfer*, 45:649–673, 2004.

[26] H. Hattori and Y. Nagano. Direct numerical simulation of the turbulent heat transfer in plane impinging jet. *International Journal of Heat and Fluid Flow*, 25:749–758, 2004.

[27] H. Xu. Direct numerical simulation of turbulence in a square annular duct. *Journal of Fluid Mechanics*, 621:23–57, 2009.

[28] K. Noto. Direct numerical simulation of isothermal wake: Dns noise, strong anisotropy turbulence, and vortex dislocation generation mechanism. *Numerical Heat Transfer, Part B: Fundamentals*, 56(2):167–189, 2009.

[29] G. Jothiprasad, D. J. Mavriplis, and D. A. Caughey. Higher-order time integration schemes for the unsteady navier-stokes equations on unstructured meshes. *Journal of Computational Physics*, 191(2):542–566, 2003.

[30] N. Nikitin. Third-order-accurate semi-implicit runge-kutta scheme for incompressible navier-stokes equations. *International Journal for Numerical Methods in Fluids*, 51(2):221–233, 2006.

[31] A. J. Chorin. Numerical Solution of the Navier-Stokes Equations. *Journal of Computational Physics*, 22:745–762, 1968.

[32] A. Gorobets, F. X. Trias, M. Soria, and A. Oliva. A scalable Krylov-Schur-Fourier Decomposition for the efficient solution of high-order Poisson equation on parallel systems from small clusters to supercomputers. *Computers and Fluids*, (submitted).

[33] F. X. Trias, A. Gorobets, M. Soria, and A. Oliva. Direct numerical simulation of a differentially heated cavity of aspect ratio 4 with ra-number up to 10^{11} - part i: Numerical methods and time-averaged flow. *International Journal of Heat and Mass Transfer*, 53:665–673, 2010.

[34] F. X. Trias, A. Gorobets, M. Soria, and A. Oliva. Direct numerical simulation of a differentially heated cavity of aspect ratio 4 with Ra-number up to 10^{11} - part ii: Heat transfer and flow dynamics. *International Journal of Heat and Mass Transfer*, 53:674–683, 2010.

[35] R. Lewis, I. Masters, and J. Cross. Automatic timestep selection for the super-time-stepping acceleration on unstructured grids using object-oriented programming. *Communications in Numerical Methods in Engineering*, 13(4):249–260, 1997.

[36] F. X. Trias, R. W. C. P. Verstappen, A. Gorobets, M. Soria, and A. Oliva. Parameter-free symmetry-preserving regularization modeling of a turbulent differentially heated cavity. *Computers & Fluids*, 39:1815–1831, 2010.

[37] O. Lehmkuhl, A. Baez, I. Rodríguez, and C. D. Perez-Segarra. Direct numerical simulation and Large-Eddy simulations of the turbulent flow around a NACA-0012 airfoil. In *7th International Conference on Computational Heat and Mass Transfer*, pages 1–8, 2011.

Chapter 3

LES and Regularization models

Abstract. Turbulence is present in most engineering flows, and thus is important to be able to predict the effects of turbulent motion in the design process. Hence, the simulation of turbulence plays an essential part in most CFD calculations. Due to its complexity, the direct numerical simulation of most of these flows is far beyond the computer capabilities nowadays and therefore, some level of modelization is required. In this sense, Large-Eddy Simulations (LES) and regularization models are different approaches which are playing an important role in the modelization and understanding of complex industrial flows. In this chapter, the mathematical description of the main models used in this thesis is described.

3.1 Introduction

The direct resolution of the Navier-Stokes equations for most of the industrial problems demand a large amount of computational resources, due to the requirement of solving the smallest scales of the turbulent flow. Thus, Direct Numerical Simulations (DNS) are still limited to low Reynolds numbers and relatively simple geometries. Traditionally, turbulence modelling of industrial flows in complex geometries have been solved using RANS models and unstructured meshes based solvers. The lack of precision of RANS models in these situations and the increase of computational power, together with the emergence of new high-efficiency sparse parallel algorithms, have made possible the use of more accurate turbulent models such as Large Eddy Simulation (LES). In LES, the largest-scales of the flow are solved while the small-scale motions are modeled by means of a subgrid-scale (SGS) model.

Recently, relevant improvements on turbulence modelling based on symmetry-preserving regularization techniques for the convective (non-linear) terms have been developed [14]. They basically alter the convective terms to reduce the production of small scales of motion by means of vortex-stretching and preserving exactly all inviscid invariants. To do so, symmetry and conservation properties of the convective terms must be preserved. These requirements yield a novel class of regularizations which restrains the convective production of small scales in an unconditional stable manner, meaning that the velocity cannot blow up in the energy-norm (enstrophy norm in 2D). The numerical algorithm used to solve the governing equations must preserve the symmetry and conservation properties too. At this stage, results using regularization models at relatively complex geometries and configurations are of extreme importance for further progress.

In the present chapter, the mathematical description of the SGS and regularization models used in this thesis is presented. These models used are suitable for unstructured grids as they do not require of any special near-wall treatment.

3.2 Large-eddy Simulation models

The discretised Navier-Stokes and energy equations can be written as

$$\mathsf{M}\boldsymbol{u} = \mathbf{0} \tag{3.1}$$

$$\Omega\frac{\partial \boldsymbol{u}}{\partial t} + \mathsf{C}\left(\boldsymbol{u}\right)\boldsymbol{u} + \mathsf{D}\boldsymbol{u} + \rho^{-1}\Omega\mathsf{G}\boldsymbol{p} - \boldsymbol{f} = \mathbf{0} \tag{3.2}$$

$$\Omega\frac{\partial \boldsymbol{T}}{\partial t} + \mathsf{C}\left(\boldsymbol{u}\right)\boldsymbol{T} + \alpha\mathsf{D}\boldsymbol{T} = \mathbf{0} \tag{3.3}$$

where $\boldsymbol{u} \in \mathbb{R}^{3m}$ and $\boldsymbol{p} \in \mathbb{R}^{m}$ are the velocity vector and pressure, respectively

(here m applies for the total number of control volumes (CV) of the discretised domain). $\boldsymbol{f} = \beta(\boldsymbol{T} - \boldsymbol{T}_0)\boldsymbol{g} \in \mathbb{R}^{3m}$, ν is the kinematic viscosity, ρ the density, β is the thermal expansion coefficient and α the thermal difussivity. Convective and diffusive operators in the momentum equation for the velocity field are given by $\mathsf{C}(\boldsymbol{u}) = (\boldsymbol{u} \cdot \nabla) \in \mathbb{R}^{3m\times 3m}$, $\mathsf{D} = -\nabla^2 \in \mathbb{R}^{3m\times 3m}$ respectively. Gradient and divergence (of a vector) operators are given by $\mathsf{G} = \nabla \in \mathbb{R}^{3m\times m}$ and $\mathsf{M} = \boldsymbol{\nabla}\cdot \in \mathbb{R}^{m\times 3m}$ respectively.

In the quest for a correct modelling of Navier-Stokes equations (Eqn. 3.1), they can be filtered spatially as in Large-Eddy Simulations (LES),

$$\begin{aligned} \Omega\frac{\partial\overline{\boldsymbol{u}}}{\partial t} + \mathsf{C}(\overline{\boldsymbol{u}})\,\overline{\boldsymbol{u}} + \nu\mathsf{D}\overline{\boldsymbol{u}} + \rho^{-1}\Omega\mathsf{G}\overline{\boldsymbol{p}} - \overline{f} &= \mathsf{C}(\overline{\boldsymbol{u}})\,\overline{\boldsymbol{u}} - \overline{\mathsf{C}(\boldsymbol{u})\,\boldsymbol{u}} \\ &\approx -\mathcal{M}\mathcal{T} \end{aligned} \tag{3.4}$$

$$\begin{aligned} \Omega\frac{\partial\overline{T}}{\partial t} + \mathsf{C}(\overline{\boldsymbol{u}})\,\overline{T} + \frac{\nu}{Pr}\mathsf{D}\overline{T} - \overline{\nabla\cdot q_{rad}} &= \mathsf{C}(\overline{\boldsymbol{u}})\,\overline{T} - \overline{\mathsf{C}(\boldsymbol{u})\,T} \\ &\approx -\mathcal{M}\mathcal{T}_T \end{aligned} \tag{3.5}$$

where the last term in both equations indicates some modelisation of the filtered non-linear convective term. $\overline{\boldsymbol{u}}$ and $\overline{T}$ are the filtered velocity and temperature, $\mathcal{M}$ represents the divergence operator of a tensor, and $\mathcal{T}$ is the SGS stress tensor, which is defined as [1],

$$\mathcal{T} = -2\nu_{sgs}\overline{\mathcal{S}} + (\mathcal{T} : \mathsf{I})\mathsf{I}/3 \tag{3.6}$$

where $\overline{\mathcal{S}} = \frac{1}{2}[\mathsf{G}(\overline{\boldsymbol{u}}) + \mathsf{G}^*(\overline{\boldsymbol{u}})]$, where G^* is the transpose of the gradient operator. $\mathcal{T}_T$ term is evaluated as in $\mathcal{T}$ term, but ν_{sgs} is substituted by ν_{sgs}/Pr_t, where Pr_t is the turbulent Prandtl (0.4 in this thesis). To close the formulation, a suitable expression for the subgrid-scale (SGS) viscosity, ν_{sgs}, must be introduced.

3.2.1 Smagorinsky model

Smagorinsky [2] proposed the following approach which is an adaptation of Prandtl's mixing length theory to subgrid-scale modelling, i.e. eddy viscosity arising in RANS equations is proportional to a turbulence characteristic scale (the mixing length) multiplied by a turbulence characteristic velocity. In the same way, Smagorinsky supposed that eddy viscosity is proportional to a subgrid-scale characteristic length l, and to a characteristic subgrid-scale velocity [3]. Then,

$$\begin{aligned} \nu_{sgs} &= (\mathcal{C}_s l)^2 \mid \overline{\mathcal{S}} \mid \\ \mid \overline{\mathcal{S}} \mid &= (2\overline{\mathcal{S}} : \overline{\mathcal{S}})^{1/2} \end{aligned} \tag{3.7}$$

where l is the grid cutting length and $\mathcal{C}_s$ is the Smagorinsky coefficient, which may be tuned so as the model reproduces the energy cascade when simulating isotropic decay. As it is well known, the value of this coefficient lies in the range between 0.1 and 0.24, depending on the numerical method used to solve the equations. However, this model is not appropriate in the close vicinity of a solid wall subject to dominant molecular-viscosity effects. Thus, a near-wall correction is also required. Traditionally, the well-known Van Driest damping function [4], $f_{VD} = 1-\exp(-\frac{y^+}{25})$, is introduced substituting the length scale in Eq. 3.7, i.e.

$$l \rightarrow f_{VD} l \equiv (1 - \exp(-\frac{y^+}{25}))l \tag{3.8}$$

where $y^+ = \frac{u_\tau y}{\nu}$ is the non-dimensional distance to the wall, y is the wall normal coordinate and u_τ is the wall friction velocity.

The use of Van Driests damping function is a strong constraint on the applicability of the model to a wide range of engineering flows, because the function is written using wall-unit coordinates. The identification of the normal distance to the wall (y) is straightforward in the case of a plane wall and structured meshes, but it is quite ambiguous near highly curved walls or sharp corners with unstructured meshes.

The other main limitation of this damping function lies in the use of the friction velocity (u_τ). Near a separation point, the friction velocity vanishes or becomes very small. This results in inaccurate evaluation of the SGS-viscosity effect, which leads the model to perform inadequately in these situations.

Thus, in order to widen the applicability of LES to various types of engineering flows, and for using them on unstructured meshes, it is advisable to look for SGS models that do not use the wall-unit coordinates. Different proposals can be found in the literature, e.g. the dynamic subgrid-scale eddy viscosity model [5], the Variational Multiscale Method (VMS [6]), the wall-adapting local eddy-viscosity method (WALE [7]), among others. In what follows, a brief mathematical description of some of these models is given.

3.2.2 Dynamic Eddy-viscosity model

Germano et. al. [5] proposed a methodology to improve the Smagorinsky model by automatically adjusting the empirical constant $\mathcal{C}_s$ at each point in space and time. This dynamic procedure is based on Germano's identity, which can be formulated as follows,

$$\mathcal{L} = \hat{\mathcal{T}} - \mathcal{T} \tag{3.9}$$

where,

$$
\begin{aligned}
-\mathcal{M}\mathcal{T} &= \mathsf{C}\left(\overline{\boldsymbol{u}}\right)\overline{\boldsymbol{u}} - \overline{\mathsf{C}\left(\boldsymbol{u}\right)\boldsymbol{u}} \\
-\mathcal{M}\hat{\mathcal{T}} &= \mathsf{C}\left(\overline{\overline{\boldsymbol{u}}}\right)\overline{\overline{\boldsymbol{u}}} - \overline{\overline{\mathsf{C}\left(\boldsymbol{u}\right)\boldsymbol{u}}} \\
-\mathcal{M}\mathcal{L} &= \mathsf{C}\left(\overline{\overline{\boldsymbol{u}}}\right)\overline{\overline{\boldsymbol{u}}} - \overline{\overline{\mathsf{C}\left(\overline{\boldsymbol{u}}\right)\overline{\boldsymbol{u}}}}
\end{aligned}
\tag{3.10}
$$

The $\mathcal{L}$ tensor can be directly computed from the resolved field. The tensors $\hat{\mathcal{T}}$ and $\mathcal{T}$ and are the subgrid scale tensors corresponding to the first and second filtering levels respectively. A major assumption is made for the two SGS tensors, which are modelled using the same constant $\mathcal{C}_d$, i.e.

$$
\begin{aligned}
\mathcal{T} &= -2\,\mathcal{C}_d\,l^2|\overline{\mathcal{S}}|\,\overline{\mathcal{S}} + (\mathcal{T}:\mathsf{I})\mathsf{I}/3 \\
\hat{\mathcal{T}} &= -2\,\mathcal{C}_d\,\hat{l}^2|\overline{\overline{\mathcal{S}}}|\,\overline{\overline{\mathcal{S}}} + (\hat{\mathcal{T}}:\mathsf{I})\mathsf{I}/3
\end{aligned}
$$

Substituting these expressions into Germano's identity, Eqn 3.9, six independent equations for the unknown Smagorinsky constant are obtained. The standard method to solve this over-determined set of equations is to calculate the constant using a least-squares method, as proposed by Lilly [8]. Thus, could also take negative or arbitrarily high values. Negative values could be associated with backscatter, but numerical tests have shown that, unless a special treatment is provided, they can produce stability problems. Many different procedures have been proposed to guarantee stable behaviour. In general, they involve averaging the constant of the subgrid-scale viscosity in space and/or time. When homogeneous direction exists, space averaging can also be done. In many cases a clipping of the constant is also performed in order to guarantee a bounded value.

3.2.3 QR eddy-viscosity model

It was proposed by Verstappen [9] and is a SGS model based on the invariants of the rate-of-strain tensor which is proposed with the following advantages compared to the classical Smagorinsky formulation:

i) $\nu_{sgs} = 0$ in any laminar flow,

ii) $\nu_{sgs} = 0$ in any 2D flow,

iii) $\nu_{sgs} \propto y^3$ near a wall and,

iv) $\nu_{sgs} \to 0$ when $l \propto Re^{-4/3}$.

It may be emphasized that the QR eddy-viscosity model is essentially not more complicated to implement in a LES-code than the standard Smagorinsky model (with $\mathcal{C}_s$ constant). Indeed, the QR-model is expressed in terms of the invariants of the rate-of-strain tensor and does not involve explicit filtering:

$$\begin{aligned} \nu_{sgs} &= (\mathcal{C}_{qr} l)^2 \frac{r^+}{q} \\ \mathcal{C}_{\mathrm{II}\nabla} &= \frac{1}{\pi} + \frac{1}{24} \\ \overline{\mathcal{S}} &= \frac{1}{2}[\mathsf{G}(\overline{\boldsymbol{u}_c}) + \mathsf{G}^*(\overline{\boldsymbol{u}_c})] \\ |\,\overline{\mathcal{S}}\,| &= (2\overline{\mathcal{S}\mathcal{S}})^{1/2} \\ q &= \frac{1}{4}\,|\,\overline{\mathcal{S}}\,|^2 \\ r &= -det\,\overline{\mathcal{S}} \end{aligned} \tag{3.11}$$

3.2.4 Wall-adapting eddy viscosity model (WALE)

This model proposed by Nicaud and Ducros [10], is based on the square of the velocity gradient tensor. In its formulation the SGS viscosity accounts for the effects of both, the strain and the rotation rate of the smallest resolved turbulent fluctuations. In addition, the proporcionality of the eddy viscosity near walls ($\nu_{sgs} \propto y^3$) is recovered without any dynamic procedure,

$$\begin{aligned} \nu_{sgs} &= (\mathcal{C}_w \Delta)^2 \frac{(\mathcal{V}_{\mathsf{ij}}{}' : \mathcal{V}_{\mathsf{ij}}{}')^{\frac{3}{2}}}{(\mathcal{S}_{\mathsf{ij}}{}' : \mathcal{S}_{\mathsf{ij}}{}')^{\frac{5}{2}} + (\mathcal{V}_{\mathsf{ij}}{}' : \mathcal{V}_{\mathsf{ij}}{}')^{\frac{5}{4}}} \\ \mathcal{S}_{\mathsf{ij}}{}' &= \frac{1}{2}[\mathsf{G}(\overline{\boldsymbol{u}_c'}) + \mathsf{G}^*(\overline{\boldsymbol{u}_c'})] \\ \mathcal{V}_{\mathsf{ij}}{}' &= \frac{1}{2}[\mathsf{G}(\overline{\boldsymbol{u}_c'})^2 + \mathsf{G}^*(\overline{\boldsymbol{u}_c'})^2] - \frac{1}{3}(\mathsf{G}(\overline{\boldsymbol{u}_c'})^2 \mathsf{I}) \end{aligned} \tag{3.12}$$

In our studies a value of $\mathcal{C}_w = 0.325$ is used.

3.2.5 WALE model within a variational multiscale framework (VMS-WALE)

The variational multiscale (VMS) approach was originally formulated for the Smagorinsky model by Hughes [6] in the Fourier space, and is a promising approach for LES of turbulent flows. In VMS three classes of scales are considered: large, small

and unresolved scales. If a second filter with filter length $\hat{l}$ is introduced (usually called test filter), a splitting of the scales can be performed,

$$f^{'} = \overline{f} - \hat{f} \tag{3.13}$$

where following Vreman [11] notation, $f^{'}$ is called the small-scale component, $\hat{f}$ the large-scale component and $\overline{f}$ is the original resolved quantity. Thus, for the large-scale parts of the resolved $\overline{\boldsymbol{u}}$ a general governing equation can be derived,

$$\Omega\frac{\partial\overline{\boldsymbol{u}}}{\partial t} + \mathsf{C}\left(\overline{\boldsymbol{u}}\right)\overline{\boldsymbol{u}} + \nu\mathsf{D}\overline{\boldsymbol{u}} + \rho^{-1}\Omega\mathsf{G}\overline{\boldsymbol{p}} - \overline{f} \;=\; -\frac{\partial\widehat{\mathcal{T}}}{\partial x_j} - \frac{\partial\mathcal{T}^{'}}{\partial x_j} \tag{3.14}$$

Inspecting Eqn. 3.14 it is possible to identify $\widehat{\mathcal{T}}$ as the subgrid term in the large-scale equation and $\mathcal{T}^{'}$ as the subgrid small-scale term. Now, neglecting the effect of unresolved scales in the large-scale equation ($\widehat{\mathcal{T}} \approx 0$), we only need to model the $\mathcal{T}^{'}$. In our implementation the *small-small* strategy is used in conjunction with the WALE model:

$$\begin{aligned} \mathcal{T}^{'} &= -2\nu_{sgs}\mathcal{S}_{\mathrm{ij}}{}^{'} + \frac{1}{3}\mathcal{T}^{'}\delta_{ij} \\ \nu_{sgs} &= (C_w^{vms}\Delta)^2\frac{(\mathcal{V}_{\mathrm{ij}}{}^{'} : \mathcal{V}_{\mathrm{ij}}{}^{'})^{\frac{3}{2}}}{(\mathcal{S}_{\mathrm{ij}}{}^{'} : \mathcal{S}_{\mathrm{ij}}{}^{'})^{\frac{5}{2}} + (\mathcal{V}_{\mathrm{ij}}{}^{'} : \mathcal{V}_{\mathrm{ij}}{}^{'})^{\frac{5}{4}}} \end{aligned} \tag{3.15}$$

where $\mathcal{C}_w^{vms}$ is the equivalent of the WALE coefficient for the *small-small* VMS approach and in the finite volume context its value lies in the range between 0.3 and 0.5.

3.3 Regularization models

Geurts and Holm [12] regularization approach involves the introduction of a filter pair $(\mathcal{F}, \mathcal{F}^{-1})$ to fully specify the subgrid model. This modelling strategy has a number of important benefits, addressing directly the non-linear convective contributions and requiring no additional external information such as model coefficients.

To illustrate this approach, the pioneering Leray regularization model [13] is considered. The model replaces convective terms in Eqn. 3.1 by $\mathsf{C}\left(\overline{\boldsymbol{u}_c}\right)\boldsymbol{u}$. Thus, the solution is convected with a smoothed velocity. Taking into account this approach, the model can be written as,

$$\frac{\partial\boldsymbol{u}}{\partial t} + \mathsf{C}\left(\overline{\boldsymbol{u}_c}\right)\boldsymbol{u} + \nu\mathsf{D}\boldsymbol{u} + \rho^{-1}\mathsf{G}\boldsymbol{p} \;=\; \boldsymbol{0} \tag{3.16}$$

At this point, Geurts and Holm introduced the inversion operator, $\boldsymbol{u} = \mathcal{F}^{-1}\overline{\boldsymbol{u}}$, in the Eqn. 3.16, obtaining the following expression analogous to the LES concept (see Eqn. 3.4),

$$\frac{\partial \overline{\boldsymbol{u}}}{\partial t} + \mathsf{C}\left(\overline{\boldsymbol{u}_c}\right)\overline{\boldsymbol{u}} + \nu \mathsf{D}\overline{\boldsymbol{u}} + \rho^{-1}\mathsf{G}\overline{\boldsymbol{p}} \;=\; \mathsf{C}\left(\overline{\boldsymbol{u}_c}\right)\overline{\boldsymbol{u}} - \mathcal{F}(\mathsf{C}\left(\overline{\boldsymbol{u}_c}\right)\mathcal{F}^{-1}\overline{\boldsymbol{u}}) \tag{3.17}$$

Thus, an equivalent SGS stress ($\mathcal{T}$) can be obtained from,

$$-\mathcal{M}\mathcal{T} = \mathsf{C}\left(\overline{\boldsymbol{u}_c}\right)\overline{\boldsymbol{u}} - \mathcal{F}(\mathsf{C}\left(\overline{\boldsymbol{u}_c}\right)\mathcal{F}^{-1}\overline{\boldsymbol{u}}) \tag{3.18}$$

This model requires the explicit application of both $\mathcal{F}$ and $\mathcal{F}^{-1}$. As a consequence, some technical difficulties arising from the reconstruction of an accurate inverse operator $\mathcal{F}^{-1}$ appear. In addition to this problem, Geurts and Holm also reported that the model does not provide sufficient smoothing and leads to unstable LES on coarse grids at high Reynolds numbers.

A solution to these problems has been raised recently by Verstappen [14]. First, the use of the $\mathcal{F}^{-1}$ is not necessary if Eqn. 3.16 is solved directly. On the other hand, the unstable behaviour of the Leray model may be related with the fact that this model does not conserve all the inviscid invariants (kinetic energy, enstrophy in 2D and helicity in 3D). Verstappen proposed to approximate the convective nonlinearity in such a manner that the symmetry properties that form the basis for the conservation of the inviscid invariants are preserved and, at the same time, the production of small scales is restrained.

These criteria yield the following class of regularizations [14],

$$\mathcal{C}_2(\boldsymbol{u},\boldsymbol{v}) \;=\; \overline{\mathsf{C}\left(\overline{\boldsymbol{u}}\right)\overline{\boldsymbol{v}}} \tag{3.19}$$

$$\mathcal{C}_4(\boldsymbol{u},\boldsymbol{v}) \;=\; \mathsf{C}\left(\overline{\boldsymbol{u}}\right)\overline{\boldsymbol{v}} + \overline{\mathsf{C}\left(\overline{\boldsymbol{u}}\right)\boldsymbol{v}'} + \overline{\mathsf{C}\left(\boldsymbol{u}'\right)\overline{\boldsymbol{v}}} \tag{3.20}$$

where the prime indicates the residual of the filter, i.e. $\boldsymbol{u}' = \boldsymbol{u} - \overline{\boldsymbol{u}}$, which can be explicitly evaluated, and $\overline{(\cdot)}$ represents a normalised self-adjoint linear filter. The difference between $\mathcal{C}_q(\boldsymbol{u},\boldsymbol{u})$ and the original $\mathsf{C}\left(\boldsymbol{u}\right)\boldsymbol{u}$ is of the order ϵ^q (where $q = 2, 4, ...$) for symmetric filters with filter length ϵ.

The approximations $\mathcal{C}_q(\boldsymbol{u},\boldsymbol{v})$ are stable by construction, meaning that convective terms do not contribute to the evolution of $|\boldsymbol{u}_\epsilon|^2$. Hence, the evolution of $|\boldsymbol{u}_\epsilon|^2$ is governed by a dissipative process. Therefore, replacing the convective term in the Navier-Stokes equations by the $\mathcal{O}(\epsilon^q)$-accurate smooth approximation, the partial differential equations to be solved are,

$$\mathsf{M}\boldsymbol{u} \;=\; \boldsymbol{0} \tag{3.21}$$

$$\frac{\partial \boldsymbol{u}}{\partial t} + \mathcal{C}_q(\boldsymbol{u},\boldsymbol{u}) + \nu \mathsf{D}\boldsymbol{u} + \rho^{-1}\mathsf{G}\boldsymbol{p} \;=\; \boldsymbol{0} \tag{3.22}$$

Note that $\mathcal{C}_q$ approximations are also skew-symmetric operators, as the original convective operator. Therefore, the same inviscid invariants characteristics of the original Navier-Stokes equations (kinetic energy, enstrophy in 2D and helicity) are preserved for the new set of partial differential equations [14].

3.4 Choice of the filter type

Since $\mathcal{C}_q$-regularization governing equations, Eqn. 3.22, are formally derived applying a low-pass filter to Navier-Stokes equations, it can be argued that its performance will be directly dependent of this filtering procedure. Furthermore, the properties of discrete filters can significantly differ from those of continuous filters, which are the basis of the theoretical analysis. In this section, the main properties of the filters for unstructured meshes for preserving both, the symmetry and the conservation properties (inviscid invariants).

3.4.1 Discrete filters

In order to ensure all the symmetry and conservation properties, the $\mathcal{C}_q$-regularization needs a normalised self-adjoint filter, thus

$$\Omega\mathcal{F} = (\Omega\mathcal{F})^* \tag{3.23}$$

$$\mathcal{F}1 = 1 \tag{3.24}$$

where Ω is the volume. In other words, it is assumed that the filter has the following properties: (i) symmetry (see Eqn. 3.23), (ii) a constant velocity vector is unaffected by the filter (see Eqn. 3.24), and (iii) it reduces the high-frequency components of the discrete velocity vector $\boldsymbol{u}$.

On the other hand, and similar to LES, the filter needs some extra properties for a correct treatment of the modified Navier-Stokes equations. In general terms, a suitable $\mathcal{C}_q$-regularization filter has to commutate with the addition. Given two functions φ and ω, this means that $\overline{\varphi+\omega} = \overline{\varphi} + \overline{\omega}$. The filter has also to commutate with the differentiation, i.e. $\overline{\dfrac{\partial\varphi}{\partial x_i}} = \dfrac{\partial\overline{\varphi}}{\partial x_i}$. Commutation with the addition property is automatically verified independently of the choice of the filter kernel, as the filters are linear operators. Unfortunately, this is not true for the differentiation operations when the filter width is not uniform. Since unstructured meshes rarely satisfy smoothness constrains on the grid spacing, the assumptions that the operations of filtering and differentiation commute may be violated even away from the walls.

Haselbacher and Vasilyev [15], proposed a methodology that allows to construct commutative discrete filters on unstructured meshes. Its key concept is that the filter

weights exhibit vanishing moments. The larger the number of vanishing moments, the higher the order of commutation error. The filter is based on the classical least-squares gradient reconstruction method developed by Barth [16]. This method is based on approximating the variation of the dependent variable ϕ along an edge linking points 0 and i by truncated Taylor series. That is, for a 1D linear approximation,

$$\phi_i = \phi_0 + \Delta x_{0i} \frac{\partial \phi}{\partial x}, \qquad i = 1, ..., n \tag{3.25}$$

where n is the number of neighbours of the point 0. The application of Eqn. 3.25 to a set of selected points gives a linear system of equations for the derivatives at point 0. Finally this set of equations can be written as an overdetermined system of linear equations,

$$\mathsf{A}\boldsymbol{x} = \boldsymbol{b} \tag{3.26}$$

The algebraic solution of Eqn 3.26 can be obtained evaluating the Moore-Penrose pseudo-inverse of A,

$$\hat{\boldsymbol{x}} = (\mathsf{A}^*\mathsf{A})^{-1}\mathsf{A}^*\boldsymbol{b} = \mathsf{A}^+\boldsymbol{b} \tag{3.27}$$

where A^* is the transpose of A and A^+ is the pseudo inverse. Since this system of equations is relatively small, a direct method can be used. The advantage of this filter is that it is truly constructed in three dimensions and no transformation from physical to computational space is required.

The least-squares gradient reconstruction method can be turned into a filtering method by modifying Eqn. 3.25. Thus, in one dimension, the general reconstruction equation for a second-order filter is,

$$\phi_i = \overline{\phi_0} + \Delta x_{0i} \frac{\partial \phi}{\partial x} + \frac{\Delta x_{0i}^2}{2!} \frac{\partial^2 \phi}{\partial x^2}, \qquad i = 1, ..., n \tag{3.28}$$

where n is the number of points of the stencil used by the filtering method and $\overline{\phi_0}$ is the filtered value at point 0. In three dimensions the number of terms in the Taylor expansion for this second-order filter grows rapidly,

$$\begin{aligned} \phi_i = \overline{\phi_0} \quad &+ \quad \Delta x_{0i} \frac{\partial \phi}{\partial x} + \Delta y_{0i} \frac{\partial \phi}{\partial y} + \Delta z_{0i} \frac{\partial \phi}{\partial z} \\ &+ \quad \frac{1}{2!} \Delta x_{0i}^2 \frac{\partial^2 \phi}{\partial x^2} + \frac{1}{2!} \Delta y_{0i}^2 \frac{\partial^2 \phi}{\partial y^2} + \frac{1}{2!} \Delta z_{0i}^2 \frac{\partial^2 \phi}{\partial z^2} \\ &+ \quad \frac{2}{2!} \Delta x_{0i} \Delta y_{0i} \frac{\partial^2 \phi}{\partial x \partial y} + \frac{2}{2!} \Delta x_{0i} \Delta z_{0i} \frac{\partial^2 \phi}{\partial x \partial z} \\ &+ \quad \frac{2}{2!} \Delta y_{0i} \Delta z_{0i} \frac{\partial^2 \phi}{\partial y \partial z}, \qquad i = 1, ..., n \end{aligned} \tag{3.29}$$

Then, $\overline{\phi_0}$ can be written in terms of ϕ_i. Therefore, it is possible to evaluate the least-squares reconstruction filter as any other standard convolution filter,

$$\overline{\phi_0} = \sum_{i=1}^{n} w_i \phi_i \tag{3.30}$$

where the discrete filter weights, w_i, can be evaluated from the first row of the pseudo inverse matrix A^{+}. More algebraically, Eqn 3.30 can be written as,

$$\overline{\boldsymbol{\phi}} = \mathcal{F}\boldsymbol{\phi} \tag{3.31}$$

where $\mathcal{F}$ is the filter matrix, $\boldsymbol{\phi}$ the original scalar field, and $\overline{\boldsymbol{\phi}}$ the filtered field. Thus, only a matrix-vector product is needed to evaluate the filtered field (see Eqn. 3.31). Note, that the evaluation of the filter weights, w_i, is a pre-processing step and its influence on the global computational time is minimum.

The least-squares reconstruction filter proposed by Haselbacher and Vasilyev [15], conserves the commutative property, but unfortunately, it is not a self-adjoint filter, i.e. the filter is not symmetric. Thus, it is not a good candidate to be used in conjunction with the $\mathcal{C}_q$-regularization approximations, since the skew-symmetric property of the convective operator may be lost. A possible solution to this problem is to force numerically the properties described in Eqns 3.23 and 3.24. This can be easily achieved, since the symmetry of the filter matrix can be forced algebraically,

$$\mathcal{F}_{sym} = \frac{1}{2}(\mathcal{F}^{*} + \mathcal{F}) \tag{3.32}$$

And the normalisation of $\mathcal{F}_{sym}$ can be forced altering its diagonal.

The method of manufactured solutions (MMS) has been applied to test the least-squares reconstruction filter (LSRF) and its symmetrical variant (Symmetric LSRF). The ANSYS ICEM CFD package has been used to randomly generate 500 unstructured grids, in a hexahedral domain, with tetrahedral elements of a minimum aspect ratio of 0.3. The selected average mesh size, h, goes from $0.02L$ up to $0.5L$ (where L is a side of the hexahedral domain). On each of these meshes, the truncation error on the filtering stage has been evaluated for the two filters as

$$E = \| \overline{\phi_{ref}} - \overline{\phi} \|_{\infty} \tag{3.33}$$

where $\overline{\phi_{ref}}$ is the analytical result.

In Fig. 3.1, the truncation error versus the average mesh size is plotted. The lines of slope 3.09 and 1.67 are the least-squares fitting of the truncation error for the LSRF and the Symmetric LSRF filters, respectively. Evaluating the order of accuracy of both filters, it is clear that the Symmetric LSRF is not working as expected. This behaviour may be related to the aforementioned method of forcing the symmetry

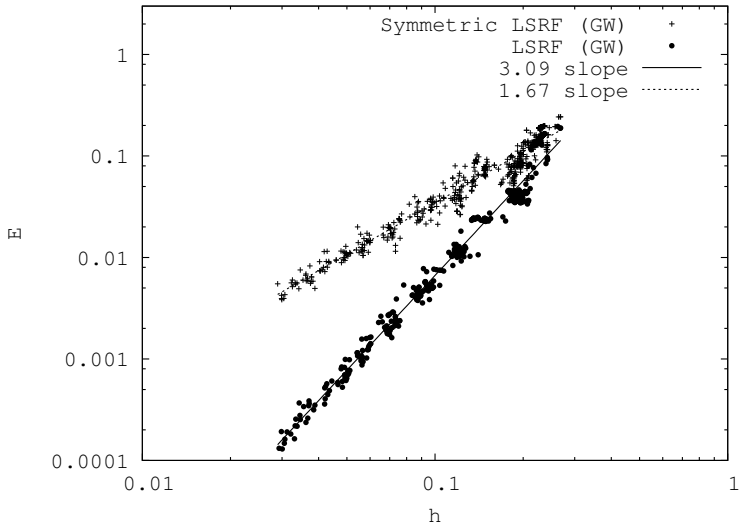

Figure 3.1: Truncation error, $E = \| \overline{\phi_{ref}} - \overline{\phi} \|_\infty$, versus average mesh size, for the LSRF and the Symmetric LSRF. Results are plotted in a log-log scale.

of the filter *a-posteriori*. This global operation breaks all the local properties of the original LSRF filter (note that the original LSRF has an approximate order of accuracy of 3).

This study shows the difficulties of constructing an accurate symmetric filter, i.e. minimising both, the local truncation and commutative errors, using Taylor series. Commutative and symmetry properties are strongly related but they act differently. While the first one is a local relationship, the second one is a global property. Thus, it is difficult to change a filter focused at the local character of the commutative property such as the LSRF, in order to became symmetric. It is more advisable to seek a filter that takes this two properties as a whole from the scratch. Furthermore, in the $\mathcal{C}_q$-regularization context, the symmetry property seems to be more important than the commutative property. Thus, in this work, the LSRF and its symmetric version are not used. The first one because it is not symmetrical and the second one due to its lack of precision.

3.4.2 Differential filters

Another class of well-known LES filters are the differential filters [17, 18]. The subset of differential filters are obtained when the convolution kernel is taken equal to the

Green's function associated to an inverse linear differential operator. These filters are symmetric can be used with unstructured meshes. In this work, two of them are used: a differential Helmholtz filter and a second order Gaussian filter.

The Helmholtz filter is based on the elliptic differential operator:

$$\mathcal{F}^{-1}\overline{\boldsymbol{u}} = (\mathsf{I} - \alpha_k^2 \mathsf{L_c})\overline{\boldsymbol{u}} = \boldsymbol{u} \tag{3.34}$$

where $\mathcal{F}^{-1}$ is the inverse of the filter transfer function and $\mathsf{L_c}$ is the Laplace operator. Fixing α_k as an isotropic case ($\alpha_k = \alpha$), Eqn. (3.34) becomes the inverse operator of the differential (or Helmholtz) filter proposed by Germano [17].

The second filter is a non-uniform Laplace filter based on a Gaussian filter, which is always self-adjoint. The second-order term in the Taylor expansion of $\mathcal{F}\boldsymbol{u}$ for a Gaussian convolution filter is the Laplace operator [19]:

$$\mathcal{F}\boldsymbol{u} = (\mathsf{I} + \frac{\epsilon^2}{24}\mathsf{L_c})\boldsymbol{u} = \overline{\boldsymbol{u}} \tag{3.35}$$

These filters are normalised, conservative and also self-adjoint. However, the commutation property is not guaranteed (for general meshes). Notice that both, the elliptic filter and the Gaussian filter can be discretised in an identical manner than the diffusive term in Navier-Stokes equations. In both filters, the grid cutting length is evaluated using Deardorff's proposal [20]. This method is the most widely used today. It consists of evaluating the grid cut-off length as the cube root of the volume Ω of the cell. Thus, if the ratio of the filter cut-off length ϵ, to the grid cutting length l ($e = \epsilon/l$) is fixed, it is possible to evaluate the volume of the filtering cell.

3.5 Concluding remarks

Different LES model which might be suitable for unstructured grids have been presented. The performance of these models will be discussed in further chapters. In addition, regularization models have been also presented. This kind of models are directly dependent on the filtering procedure, i.e. in order to preserve symmetry and conservation properties the C_q-regularization models need normalised self-adjoint filters. Thus, special attention to the different filters to be used has been paid.

The influence of the filter on the modelling has been analysed by means of a detailed study of the properties of standard filters for unstructured grids. It has been shown, that filters based on least-squares minimization procedures are not suitable for regularization models since they are not symmetrical. Furthermore, it has also been proven that it is not possible to force their symmetry because this operation breaks the local properties of the original least-squares reconstruction filter.

References

[1] P. Sagaut and M. Germano. *Large Eddy Simulation for Incompressible Flows*. Springer-Berlag, 2001.

[2] J. Smagorinsky. General circulation experiments with the primitive equations, part. I: the basic experiment. *Monthly Weather Rev.*, 91:99–164, 1963.

[3] S.B. Pope. *Turbulent Flows*. Cambridge University Press, 2000.

[4] D. C. Wilcox. Simulation of Transition with a Two-Equation Turbulence Model. *AIAA Journal*, 32:247–255, 1994.

[5] M. Germano, U. Piomelli, P. Moin, and W. Cabot. A Dynamic Subgrid-Scale Eddy Viscosity Model. *Physics of Fluids A*, 7(3):1760–1765, 1991.

[6] T.J.R. Hughes, L. Mazzei, and K.E. Jansen. Large eddy simulation and the variational multiscale method. *Computing and Visualization in Science*, 3:47–59, 2000.

[7] F. Nicoud and F. Ducros. Subgrid-scale stress modelling based on the square of the velocity gradient tensor. *Flow, Turbulence and Combustion*, 62:183–200, 1999.

[8] D. K. Lilly. A proposed modification of the Germano subgrid-scale closure method. *Physics of Fluids A: Fluid Dynamics*, 4(3):633, 1992.

[9] R. Verstappen. When does eddy viscosity damp subfilter scales sufficiently? In M.V. Salvetti, B. Geurts, J. Meyers, and P. Sagaut, editors, *Quality and Reliability of Large-Eddy Simulations II*, volume 16 of *Ercoftac Series*, pages 421–430. Springer, 2010.

[10] F. Nicoud and F. Ducros. Subgrid-Scale Stress Modelling Based on the Square of the Velocity Gradient Tensor. *Flow, Turbulence and Combustion*, 62:183–200, 1999.

[11] A. W. Vreman. The adjoint filter operator in large-eddy simulation of turbulent flow. *Physics of Fluids*, 16(6):2012, 2004.

[12] B. J. Geurts and D. D. Holm. Regularization modeling for large-eddy simulation. *Physics of Fluids*, 15:L13–L16, 2003.

[13] J. Leray. Sur le movement d'un liquide visqueaux emplissant l'espace. *Acta Mathematica*, 63:193–248, 1934.

[14] Roel Verstappen. On restraining the production of small scales of motion in a turbulent channel flow. *Computers and Fluids*, Vol. 37(7):887–897, 2008.

[15] A. Haselbacher and O. V. Vasilyev. Commutative discrete filtering on unstructured grids based on least-squares techniques. *Journal of Computational Physics*, 187:197–211, 2003.

[16] T.J. Barth. A 3-D upwind Euler solver for unstructured meshes. *AIAA Computational Fluids Dynamics Conference. AIAA paper 1991-1548*, pages 228–238, 1991.

[17] M. Germano. Differential filters for large eddy numerical simulation of turbulent flows. *Physics of Fluids*, 29(6):1755–1757, 1986.

[18] M. Germano. Differential filters of elliptic type. *Physics of Fluids*, 29(6):1757–1758, 1986.

[19] A. W. Vreman. The adjoint filter operator in large-eddy simulation of turbulent flow. *Physics of Fluids*, 16:2012–2022, 2004.

[20] P. Sagaut. *Large Eddy Simulation for Incompressible Flows*. Springer-Verlag, 2001.

Chapter 4

Assessment of the Symmetry-Preserving Regularization model on complex flows using unstructured grids

Most of the contents of this chapter have been published as:

O. Lehmkuhl, R. Borrell, I. Rodríguez, C.D. Pérez-Segarra and A. Oliva. Assessment of the Symmetry-Preserving Regularization model on complex flows using unstructured grids. *Computer & Fluids*, 60:108–116. 2012. doi:10.1016/j.compfluid.2012.02.030.

Abstract. The assessment of regularization models on unstructured meshes is carried out by means of three different test cases. The cases are: the impinging jet flow, the flow past a circular cylinder and a simplified Ahmed car. The properties of the filters and their performance on general unstructured meshes have also been considered. A detailed analysis considering the Gaussian and the Helmholtz differential filters is presented. It has been shown that the model degrades as the meshes used are less homogeneous due to the loss of quality in the filtering process.

4.1 Introduction

Traditionally, turbulence modelling of industrial flows in complex geometries have been solved using RANS models and unstructured meshes based solvers. The lack of precision of RANS models in these situations and the increase of computational power, together with the emergence of new high-efficiency sparse parallel algorithms, have made possible the use of more accurate turbulent models such as Large Eddy Simulation (LES). Recently, relevant improvements on turbulence modelling based on symmetry-preserving regularization techniques for the convective (non-linear) terms have been developed. They basically alter the convective terms to reduce the production of small scales of motion by means of vortex-stretching and preserving exactly all inviscid invariants. To do so, symmetry and conservation properties of the convective terms must be preserved. These requirements yield a novel class of regularizations which restrains the convective production of small scales in an unconditional stable manner, meaning that the velocity cannot blow up in the energy-norm (enstrophy norm in 2D). The numerical algorithm used to solve the governing equations must preserve the symmetry and conservation properties too. At this stage, results using regularization models at relatively complex geometries and configurations are of extreme importance for further progress.

The main objective of the present paper is the assessment of regularization models on unstructured meshes. Three different test cases have been studied: the impinging jet flow, the flow past a circular cylinder and a simplified Ahmed car. The properties of the filters and their performance on general unstructured meshes have also been considered. A detailed analysis considering the Gaussian and the Helmholtz differential filters is presented. Hereafter, the performance of the presented regularization methodology on unstructured meshes is investigated by means of three different test cases: i) the impinging jet flow at $Re_B = 2 \times 10^4$, ii) the flow past a circular cylinder at $Re_D = 3900$, and iii) the flow over an Ahmed car at $Re_H = 7.68 \times 10^5$. All the results presented have been obtained with the $\mathcal{C}_4$ approximation.

4.2 Numerical results

4.2.1 Impinging Jet Flow at $Re_B = 2 \times 10^4$

Turbulent impinging jets have been the subject of many experimental research works [1, 2] and numerical investigations using RANS based models [3, 4]. However, they have been less studied by means of DNS or LES models [5]. The test case here presented consists of a plane turbulent impinging jet in a confined space. Numerical computations are carried out for a moderate Reynolds number of 2×10^4 (defined in terms of the nozzle width B) and an aspect ratio $H/B = 4$, where H is the height of

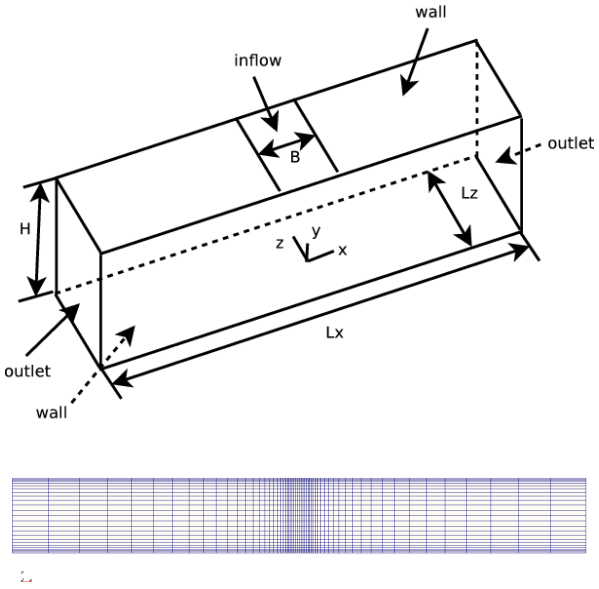

Figure 4.1: (top) Impinging jet geometry. (bottom) Mesh of the plane for m1.

the domain (see Fig. 4.1).

The computational domain is a rectangular box of dimensions $L_x \times H \times L_z$. The nozzle is centred in the upper boundary of the computational domain. The inlet vertical velocity (U_{ref}) is obtained from the Reynolds number value. No-slip conditions are imposed at solid walls. At the outflow, a pressure-based boundary condition is prescribed. Periodic boundary conditions are used in the spanwise direction.

Considering the geometry of the computational domain, an hexahedral unstructured mesh is used, being more concentrated in the region near the impingement wall and coarse toward the exit and the center of the channel. In order to evaluate the accuracy of the symmetry-preserving formulation, two different grids are used. The first one is a coarse grid (m1) of 11136 control volumes (CV) ($50 \times 24 \times 8$ nodes in x-,y- and z-directions respectively), while the second one is a medium sized grid (m2) of 94080 CV ($120 \times 49 \times 16$ nodes in x-,y- and z-directions, respectively). Both meshes are non-homogeneous in the (x,y) planes following an hyperbolic distribution, with a concentration factor at the walls and at the axis of $\gamma = 2$. For the mesh m1, the minimum distance in the wall normal direction has been of $\Delta y_{min}/B = 1.25 \times 10^{-2}$, whereas for m2 has been of $\Delta y_{min}/B = 1.75 \times 10^{-3}$ (see Fig. 4.1 bottom).

The numerical predictions of the mean flow and fluctuation quantities are compared with experimental data from Ashforth-Frost et al. [6] and Zhe and Modi [2]. All the results here presented have been obtained using the Helmholtz filter. However, the same study (not shown here) with the Gaussian filter has been also carried out. It has been observed that there is no influence in the results between both filters for a filter ratio $e > 3$. In Fig. 4.2(a), streamwise velocity at three different locations ($x/B = 2,\ 4,\ 7$) at the impingement plate is plotted together with experimental data. Very good agreement is obtained between numerical results using m2 mesh and experimental data. In fact, even for the simulation with the coarse mesh, m1, the results are reasonably good.

In addition to the mean flow features, flow fluctuations are also important. In Fig. 4.2(b) comparison of streamwise velocity fluctuations u_{rms}/U_{ref} at the same locations in the impingement plate, between the two meshes and the experimental data is shown. There is also a quite good agreement with experimental data for the m2 grid. This mesh is capable of fully describe the velocity fluctuations profile, except the peak in the stresses in the region close to the stagnation point where this quantity is slightly over-predicted. In general, the results obtained with this mesh are within the error range of both experimental studies. However, major discrepancies are obtained with the coarse grid. These differences are the largest in the region close to the impingement wall, where the mesh is not enough to predict accurately the peak in the turbulent intensities.

Based on the foregoing, $\mathcal{C}_4$-regularization model seems to perform quite well for this kind of turbulent flows and on hexahedral grids. For a relative coarse grid of

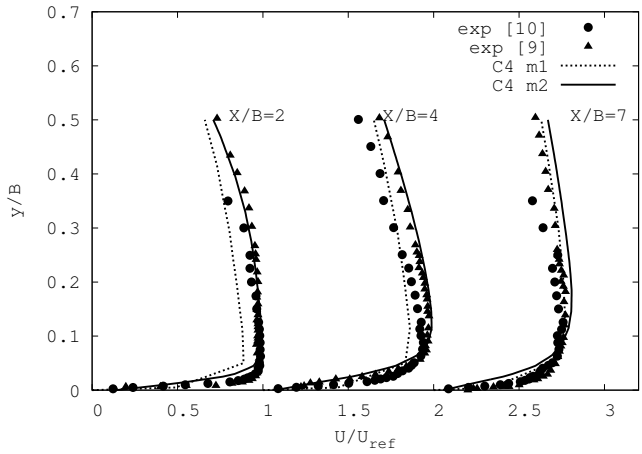

(a)

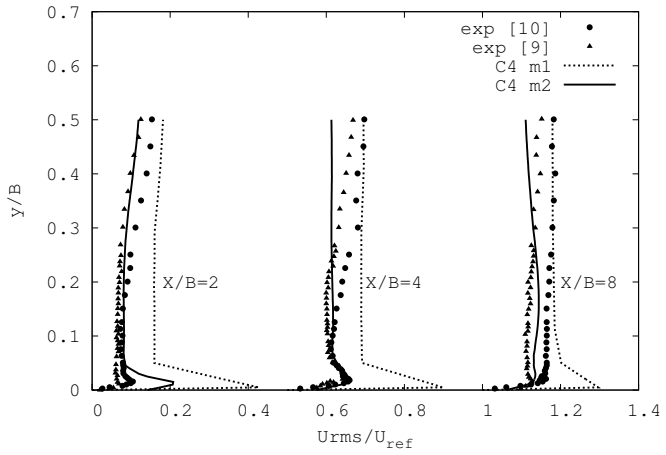

(b)

Figure 4.2: Streamwise velocity (a) and Reynolds stresses (b) at three different locations in the impingement plate. Lines: numerical solutions using two meshes; symbols: experimental data from Ashforth-Frost et al. [6] and Zhe and Modi [2].

94080 CVs, it is capable of reproducing the mean flow and its fluctuations within experimental accuracy.

4.2.2 Flow Around a Circular Cylinder at $Re_D = 3900$

As it is well known from experimental observations, the flow around a cylinder exhibits different behaviours depending on the Reynolds number [7]. At relatively high Reynolds numbers, the laminar to turbulent flow transition is not induced by the geometrical topology but due to instabilities in the separated shear layers. The unstable regions of the flow (where the turbulence is generated) can be roughly divided into three different zones: the boundary layer on the cylinder, the two shear layers, and the wake. In this section, attention is focussed on the flow at Reynolds number 3900 (defined in terms of the cylinder diameter D and free-stream velocity U_{ref}).

Numerical solutions have been obtained in a rectangular computational domain of dimensions $x = [-4D, 20D]$, $y = [-8D, 8D]$, $z = [0, L_z]$ with a circular cylinder located at (0,0,0). A spanwise length of $L_z = \pi D$ has been considered in this study. The boundary conditions at the inflow consist of a uniform velocity, $(u, v, w) = (1, 0, 0)$. At top and bottom walls, symmetry boundary conditions are imposed. At the outlet boundary, pressure-based condition is used. Periodic boundary conditions are prescribed for the spanwise direction, being this direction Fourier transformed. No-slip conditions on the cylinder surface are set. The computational mesh used is an unstructured grid with prisms of 349408 CV (21838×16 planes). The use of the unstructured grid has allowed to cluster more control volumes near the circular cylinder boundary layer, in the shear layers and in the near wake. Near the cylinder wall, as the flow is laminar until the drag crisis ($Re = 3.7 \times 10^5$ [8]), the boundary layer thickness can be estimated and about 3 grid points within the boundary layer have been placed. In the near wake zone, up to a distance from the cylinder of about $x/D = 5$ and a zone of $y/D = \pm D$, mesh sizes compared to the DNS grid for the plane are about $\overline{h}/\overline{h}_{DNS} \approx 2.2 - 2.7$ (the mesh size for the DNS grid has been obtained from [9] and [10]). The mesh used for the $\mathcal{C}_4$ calculation is about 3.3 times coarse regarding the number of control volumes in the plane and with 8 times few planes in the homogeneous direction. All in all, the grid used in the present study is about 27 times coarser than the DNS grid. A detail of the grid of the plane used in the present calculations is depicted in figure 4.3.

In order to test the regularization modelling on general unstructured meshes, two different simulations have been performed. The first one using the Gaussian filter (see Eqn. 3.35) with a filter ratio $e = 1$, and the second one using the Helmholtz filter (see Eqn. 3.34) with a filter ratio $e = 4$. At this point, it is important to remark that the stability of the Gaussian filter is restricted by the filter ratio. On the contrary, the

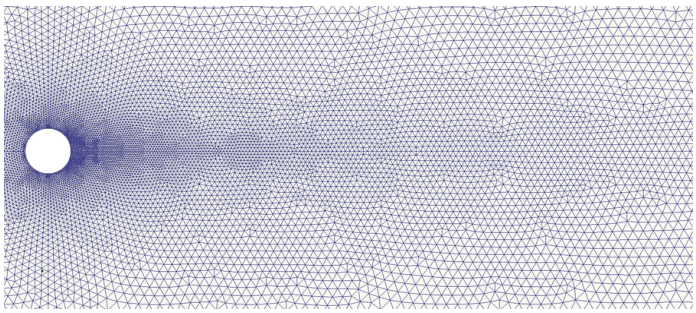

Figure 4.3: Detail of the mesh used near the cylinder surface and in the near-wake.

Helmholtz filter seems to be less dependent on this quantity. This is the reason for the lower value of the filter ratio used with the Gaussian filter.

Numerical results obtained with the two filters are given in Fig. 4.4. In the figure, the streamwise and cross-flow velocities profiles of the time-average flow at three different locations in the wake of the circular cylinder are plotted (see Fig. 4.4(a) and Fig. 4.4(c)). Turbulence intensities $< u'u' > /U_{ref}$ and $< v'v' > /U_{ref}$ at $x/D = 1.54$ are also depicted (Fig. 4.4(b) and Fig. 4.4(d)). Results are compared with DNS data by [9]. The mean flow solution obtained with the Helmholtz filter is in very good agreement with the reference data from DNS. Although the simulation using the Gaussian filter does not perform inadequately, the agreement with DNS data is not as good as the obtained with the Helmholtz filter.

Regarding to second-order statistics, the simulation using the Helmholtz filter is in correspondence with the DNS data, predicting very well the peak in the stresses. On the other hand, the results with the Gaussian filter are less satisfactory and, although it predicts the shape of the Reynolds stresses distribution and the position of the peak in the stresses, clearly under-predict their magnitude.

Therefore, the solution obtained with the $\mathcal{C}_4$-regularization model is affected by the performance of the filter. In this case, the simulation using Helmholtz filter shows better agreement with DNS data than the one obtained with the Gaussian filter. Moreover, the results with the Helmholtz filter are excellent taking into account that traditionally LES of this case have been solved using meshes of 1.5-2.5 million CV. For example, the numerical studies by Kravchenko and Moin [11] were performed using 1.5 million CV and a dynamic LES model.

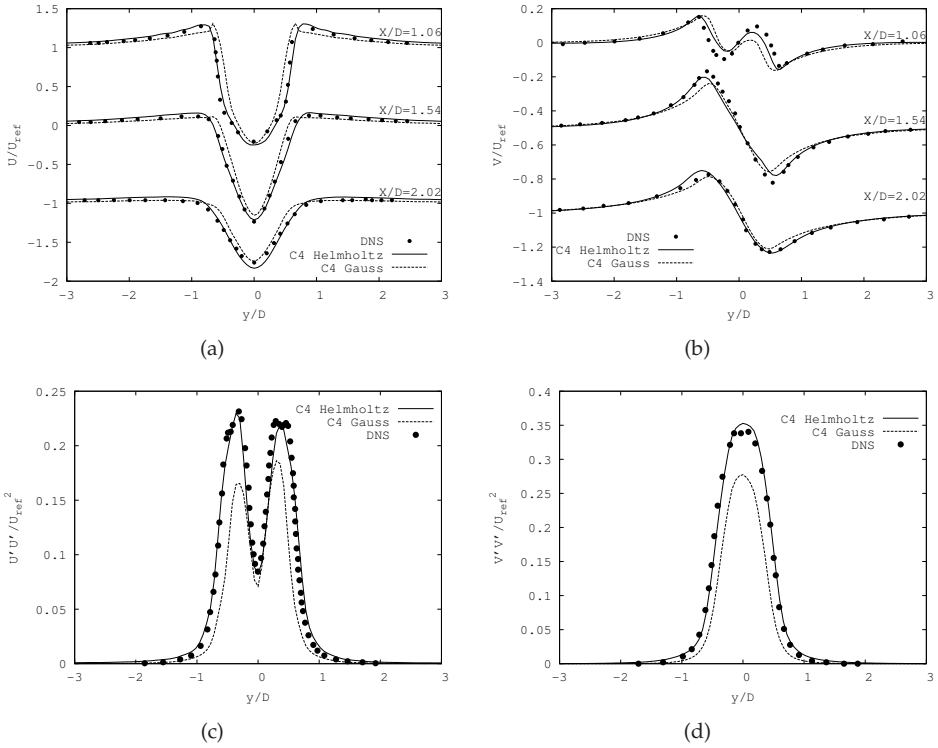

Figure 4.4: Results obtained at three locations in the wake of a circular cylinder. Comparison with DNS [9] data. (a) Streamwise velocity $< u > /U_{ref}$, (b) cross-flow velocity $< v > /U_{ref}$, (c) streamwise velocity fluctuations $< u'u' > /U_{ref}^2$ and (d) cross-flow velocity fluctuations $< v'v' > /U_{ref}^2$.

4.2.3 Turbulent flow over an Ahmed car at $Re_H = 7.68 \times 10^5$

The Ahmed body car is a semi-rectangular vehicle with a rounded front part and a slant back. Flow over this generic body reproduces the basic fluid-dynamics features of real cars with a typical fastback geometry. Furthermore, its simplified topology allows easy comparisons between experimental and numerical works.

Ahmed *et al.* [12] have carried out experiments of this vehicle with several slant angles (α). In their work, the main characteristics of the flow for various angles have also described. Their conclusions were that the flow is fully unsteady, three-dimensional and shows separations than can be followed by reattachments, depend-

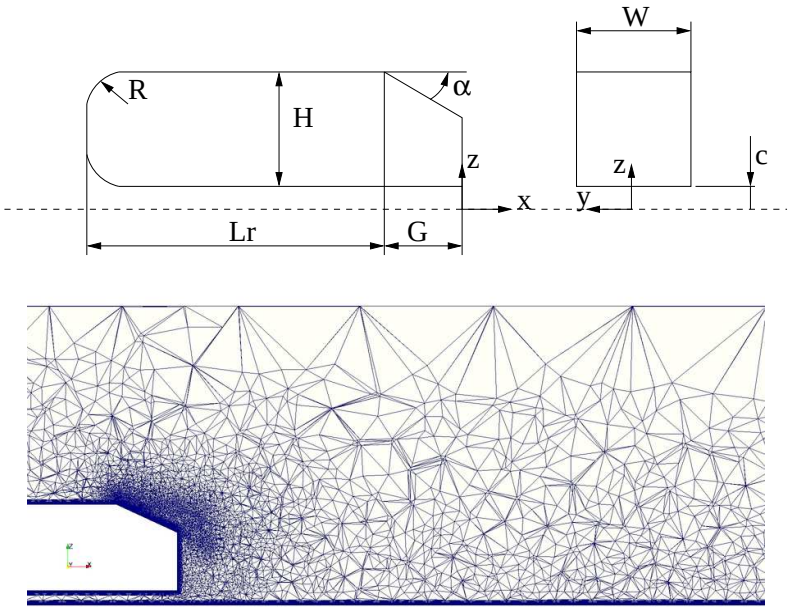

Figure 4.5: (top) Ahmed body car geometry. (bottom) A detail of the unstructured mesh projected onto a 2D plane

ing on α. The flow also shows large unsteady phenomena coming from interactions between recirculation bubbles and vortices. Moreover, a critical $\alpha \sim 30^o$ was found to lead an abrupt decrease in drag associated with the merging of separation regions and vortex breakdown.

This test case was selected for the 9^{th} ERCOFTAC Workshop since the complex features of the flow make computations a challenging task from both the modelling and the numerical point of view. It was concluded that the unsteady simulation methods such as URANS and LES have a stronger potential to accurately capture the details of the flow than the standard RANS techniques. However, the case was still not considered to be satisfactorily predicted for the subcritical angle ($\alpha = 25^o$).

All these difficulties are mainly related to the partial detachment of the flow at the beginning of the slant. As Krajnovic *et al.* [13] have proved, the shear related to the small-scale structures generated by the detachment significantly increases the turbulent stresses. Experimental measurements by Lienhart *et al.* [14] have also shown that, at the slant mixing layer, the turbulent kinetic energy is much higher than in the canonical self-similar mixing cases.

Due to its complexity, this case has been selected in this paper to study the performance of the $\mathcal{C}_4$-regularization model. The geometry has been defined as in the experiments by Ahmed *et al.* [12] (see Fig. 4.5). The value of the body height is $H = 0.288m$. The other main geometric values are $L_r = 0.8428m$, $G = 0.2012m$, $W = 0.389m$ and $C = 0.05m$. The considered slant angle is $\alpha = 25°$. The computational domain is a rectangular channel of dimensions $9.1944 \times 1.87 \times 1.4$, with the front of the body located at a distance from the inlet of 2.1024m. The downstream region has a length of 6.048m measured from the rear end of the car. The Reynolds number based on the inlet velocity, U_{ref}, and the car height, H, is of $Re_H = 7.68 \times 10^5$. At the inflow, uniform axial velocity profile is imposed. At the lateral and top walls, slip boundary conditions are prescribed. At the outflow of the domain, a pressure-based boundary condition is applied. In addition, a buffer zone is defined at $x > 5$ in order to suppress non-physical waves which are reflected by the outflow boundary. No-slip conditions at the bottom surface are considered.

The calculations have been performed on an hybrid prism-hexahedral unstructured grid of 662282 CV. A prism-layer to capture the body boundary layer is constructed around the car surface. The height of the prism layer is of $H_{prism}/H = 0.0403$ with 10 nodes located within this layer and the first-one located at a non-dimensional distance of 1.736×10^{-3} off the car surface. Outside this layer, the mesh is composed of hexahedral-dominant elements and the size of these elements increases rapidly as it moves off the car. Thus, in the slant region, the relative size of a typical control-volume (respect of the size within the prism layer) at a wall normal distance of $\xi/H = 0.0562$ is 1.5 times, whereas at $\xi/H = 0.41$ this size has grown up to 6.5 times. A detail of the mesh projected onto a 2D plane is depicted in Fig. 4.5.

Results obtained have been compared with the experimental data by Leinhart *et al.* [14] and also with numerical results obtained using Large Eddy Simulations with the wall adapting local eddy viscosity (WALE)[15] model for the subgrid scale stresses.

In Fig. 4.6 the mean streamwise profiles of the velocity for the symmetry plane ($y = 0$) at the rear end of the body and at the near wake are shown. As can be seen, there are significant differences concerning the prediction of the mean flow behaviour in the slant back. In the results with the regularization model, the flow separates in the slant corner and forms a large recirculation zone. Furthermore, the flow does not reattaches the slant as in the experiments. As expected, larger discrepancies are obtained in the prediction of the Reynolds stresses as can be seen in Fig. 4.7. The $\mathcal{C}_4$-regularization model is not capable of well capture the behaviour of the flow. Although, *a-priori* it is possible to attribute this behaviour to a poor resolution near the wall, when comparing with the performance of the WALE model on the same grid, it can be observed that the WALE model shows a good agreement with the experiments even for this coarse grid. In fact, this behaviour might be attributed to the quality of the filtering procedure, which is more relevant in the zone of the slant near the wall. In this region the mesh is composed of prism and tetrahedral control volumes which rarely satisfy smoothness constrains on the grid spacing. Since the used differential filters have been discretised in an identical manner as the diffusive term in the Navier-Stokes equations, it can be argued that the filter truncation errors are affecting the high-frequency components of the discrete filtered velocity vector. Thus, to avoid the numerical interaction between the filter and the modelled scales, it may be interesting to discretise the differential filter with high order schemes but further investigation is required.

Another possible remedy to avoid such undesired effects can be to introduce the $\mathcal{C}_4$-approximation within a LES template. Being the spatially filtered Navier-Stokes equations as written in Eq. 3.4, the evaluation of the turbulent stress tensor can be made by using the $\mathcal{C}_4$ approximation (Eq. 3.20), similar to the implementation of Geurts and Holm [16] for the Leray model (see Eqs. 3.16 and 3.17), such as

$$
\begin{aligned}
-\mathcal{MT} &= \mathbf{C}\left(\overline{\boldsymbol{u}}\right)\overline{\boldsymbol{u}} - \mathcal{C}_4(\boldsymbol{u},\boldsymbol{v}) && (4.1)\\
-\mathcal{MT} &= \mathsf{C}\left(\overline{\boldsymbol{u}}\right)\overline{\boldsymbol{u}} - \mathcal{F}^{-1}(\mathsf{C}(\overline{\boldsymbol{u}})\overline{\boldsymbol{u}} - \mathcal{F}(\mathsf{C}\left(\overline{\boldsymbol{u}}\right)(\mathcal{F}^{-1}\overline{\boldsymbol{u}} - \overline{\boldsymbol{u}})) && (4.2)\\
&+ \mathcal{F}(\mathsf{C}(\mathcal{F}^{-1}\overline{\boldsymbol{u}} - \overline{\boldsymbol{u}})\overline{\boldsymbol{u}})
\end{aligned}
$$

From the above expression, the subgrid-scale viscosity ν_{sgs} can be evaluated adopting a Helmholtz filter by means of a least-square method. With this approximation, we have computed the above case with the same computational grid [17]. The results for the $\mathcal{C}_4$ within the LES template are shown in figures 4.8(a) and 4.8(b).

As can be observed, the $\mathcal{C}_4$ within the LES template performs better than the

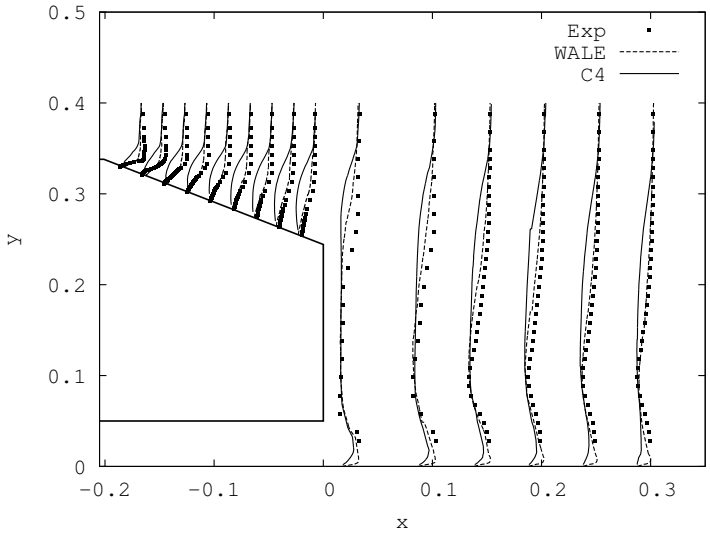

Figure 4.6: Mean streamwise velocity profiles in the symmetry plane: solid line $\mathcal{C}_4$, dashed line WALE model, dots experiments [14]

direct regularization of the convective flux ($\mathcal{C}_4$). In fact, it also outperforms the results obtained with the WALE model and seems that the quality of the filtering procedure is not significative. Although the use of this approximation is very promising, the computational cost increases more than a 50 % if it is compared with the cost needed for solving the same grid with the $\mathcal{C}_4$ model, as it implies the filtering operations of the direct $\mathcal{C}_4$ and the least-square resolution of the SGS viscosity. The extension of these results to different flow configurations and geometries still requires further research.

4.3 Conclusions

An assessment of regularization models on unstructured meshes has been presented. Considering the discussion presented in Chapter 3 regarding the influence of the different filters, two differential filters have been considered: a differential Helmholtz filter and a second-order Gaussian filter. Both filters are normalised, conservative and self-adjoint. Differential filters are a better alternative because they are symmetrical by construction.

Based on this modelling, three different test cases have been studied: i) the im-

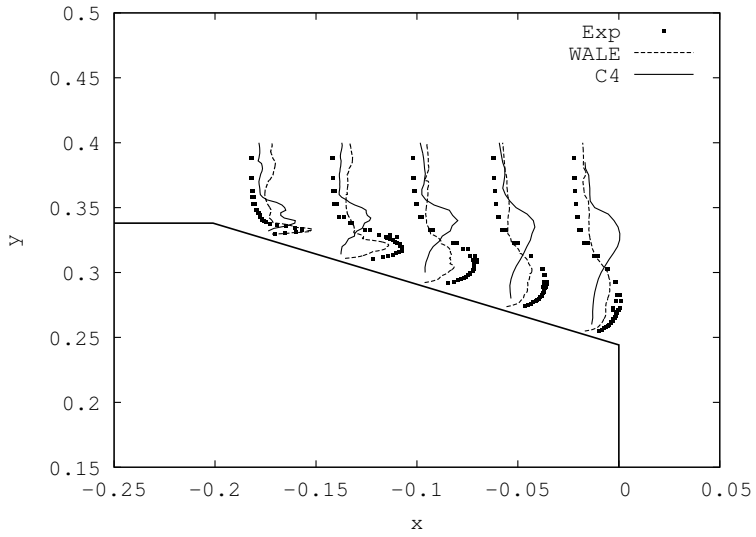

Figure 4.7: Root mean square of the streamwise velocity fluctuations u_{rms} profiles in the symmetry plane: solid line $\mathcal{C}_4$, dashed line WALE model, dots experiments [14]

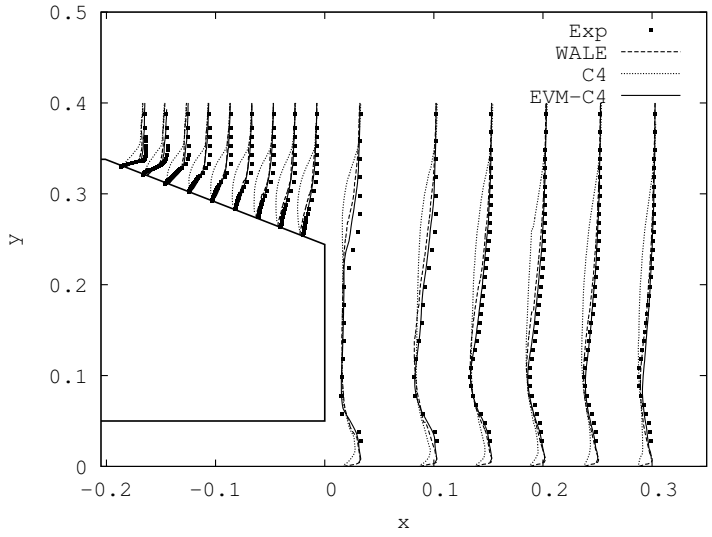

(a)

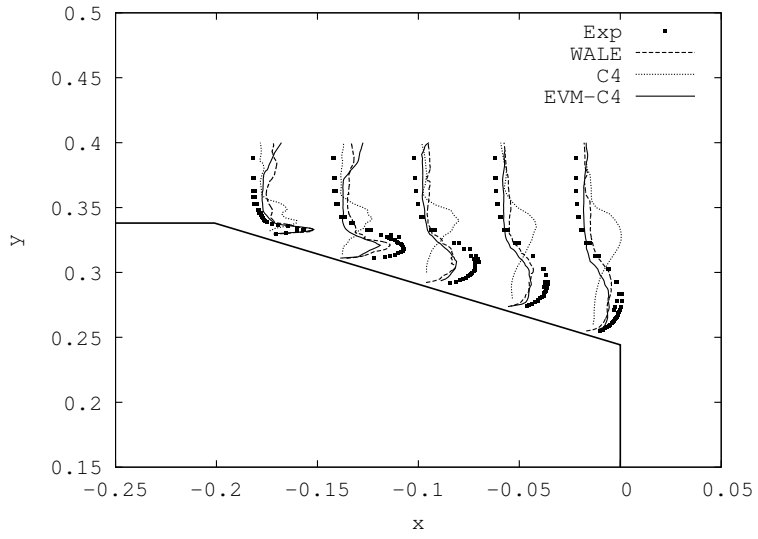

(b)

Figure 4.8: (a)Streamwise and (b) root mean square streamwise velocity profiles in the symmetry plane. Comparison of the $\mathcal{C}_4$-approximation within a LES template with previous results. solid line $\mathcal{C}_4$-approximation within a LES template, dotted line $\mathcal{C}_4$, dashed line WALE model, squares experiments [14]

pinging jet flow, ii) the flow past a circular cylinder and iii) a simplified Ahmed car. The results have shown that for structured meshes or smooth unstructured meshes differential filters are very effective. This can be observed in the results presented for the impinging jet and the flow over a circular cylinder. Taking into account traditionally LES results for the same type flow, the $\mathcal{C}_4$-regularization simulations behave as good as LES models but using coarser meshes. Thus, $\mathcal{C}_4$-regularization modelling proves to be an accurate approximation of the Navier-Stokes equations even in relative complex flows.

The flow over an Ahmed car has been selected to test the behaviour of the aforementioned methodology under fully irregular unstructured grids. The results obtained here have shown significant differences concerning the prediction of the mean flow behaviour in the slant back of the car. In this case, the performance of the model is strongly affected by the filtering quality. This is more relevant in the zone of the slant near the wall, where a hybrid mesh of prism and tetrahedral control volumes is used. As in this zone the mesh rarely satisfy smoothness constrains on the grid spacing, the filter truncation errors are affecting the high-frequency components of the discrete filtered velocity vector. As a possible remedy to this issue, the $\mathcal{C}_4$ model has been formulated within a LES template. Results obtained with this new approach seems very promising but further research is still required. Another method in order to avoid the numerical interaction between the filter and the modelled scales, might be to discretise the differential filter with high-order schemes. This aspect will be studied in future works, together with the use of powers of Laplacian filters as Trias and Verstappen have recently pointed out [18].

References

[1] Ashrae. *ASHRAE HANDBOOK Fundamentals*. 1997.

[2] Zhe J. and Modi V. Near Wall Measurements for a Turbulent Impinging Slot Jet. *Journal of Fluids Engineering*, 123(1):112–120, 2001.

[3] J. E. Jaramillo, C. D. Pérez-Segarra, I. Rodríguez, and A. Oliva. Numerical Study of Plane and Round Impinging Jets Using RANS Models. *Numerical Heat Transfer, Part B*, 54(3):213–237, 2008.

[4] M. K. Isman, E. Pulat, A. B. Etemoglu, and M. Can. Numerical Investigation of Turbulent Impinging Jet Cooling of a Constant Heat Flux Surface. *Numerical Heat Transfer, Part A*, 53(10):1109–1132, 2008.

[5] H. Hattori and Y. Nagano. Direct numerical simulation of the turbulent heat transfer in plane impinging jet. *International Journal of Heat and Fluid Flow*, 25:749–758, 2004.

[6] S. Ashforth-Frost, K. Jambunathan, and C. F. Whitney. Velocity and Turbulence Characteristics of a Semiconfined Orthogonally Impinging. *Exp. Thermal and Fluid Science*, 14:60–67, 1997.

[7] A. Prasad and C. H. K. Williamson. The instability of the separated shear layer from a bluff body. *Phys. Fluids*, 8:1347, 1996.

[8] H. Schlichting. *Boundary Layer Theory*. McGraw-Hill, Inc., Seventh Ed, 1979.

[9] O. Lehmkuhl, R. Borrell, C. D. Pérez-Segarra, J. Chiva, and A. Oliva. Direct Numerical Simulations and Symmetry-Preserving Regularization Simulations of the flow around a circular cylinder at Reynolds number 3900. In *Turbulence, Heat and Mass Transfer 6*, Rome, Italy, September 2009.

[10] I. Rodríguez, O. Lehmkuhl, R. Borrell, C.D. Pérez-Segarra, and A. Oliva. Low-frequency variations in the wake of a circular cylinder at $Re = 3900$. In *Proceedings of the 13th European Turbulence Conference*, 2011.

[11] A.G. Kravchenko and P. Moin. Numerical studies of flow over a circular cylinder at $Re_D = 3900$. *Physics of fluids*, 12(2):403–417, 2000.

[12] S. R. Ahmed, G. Ramm, and G. Faltin. Salient features of the time-averaged ground vehicle wake. *SAE Paper*.

[13] S. Krajnović and L. Davidson. Flow Around a Simplified Car, Part 1: Large Eddy Simulation. *Journal of Fluids Engineering*, 127:907–918, 2005.

[14] H. Lienhart and S. Becker. Flow and Turbulent Structure in the Wake of a Simplified Car Model. *SAE Paper*, (2003-01-0656), 2003.

[15] F. Nicoud and F. Ducros. Subgrid-Scale Stress Modelling Based on the Square of the Velocity Gradient Tensor. *Flow, Turbulence and Combustion*, 62:183–200, 1999.

[16] B. J. Geurts and D. D. Holm. Regularization modeling for large-eddy simulation. *Physics of Fluids*, 15:L13–L16, 2003.

[17] V. C. Wong and D. K. Lilly. A comparison of two dynamic subgrid closure methods for turbulent thermal convection. *Physics of Fluids*, 6(2):1016, 1994.

[18] F.X.Trias and R.W.C.P.Verstappen. On the construction of discrete filters for symmetry-preserving regularization models. *Computers and Fluids*, 40(1):139–148, 2011.

Chapter 5

On DNS and LES of natural convection of wall-confined flows: Rayleigh-Bénard convection

Most of the contents of this chapter have been published as:

I. Rodríguez, O. Lehmkuhl, R. Borrell and C.D. Pérez-Segarra. On DNS and LES of natural convection of wall-confined flows: Rayleigh-Bénard convection. *Direct and Large-Eddy Simulations 8* Eindhoven. 2010.

I Rodríguez, O Lehmkuhl, R Borrell and C.D. Pérez-Segarra. Assessment of LES models for solving turbulent natural convection in enclosures. *6th European Thermal Sciences Conference, Eurotherm 2012*. Poitiers, 2012

Abstract. The turbulent natural convection of a fluid inside an enclosure heated from below (Rayleigh-Benard convection), has been object of many theoretical and experimental investigations. Regarding to numerical simulations, in recent years Large-Eddy Simulations (LESs) have become an important tool for the resolution of flows, specially at high Rayleigh and Reynolds numbers, where direct numerical simulations are not affordable. However, as LES models the smallest scales of the fluid results are not only dependent on the grid resolution and the spatial and temporal discretizations, but also on the selection of the appropriate subgrid scale stress (SGS) model for describing the flow behaviour. Thus, this work aims at the assessment of different SGS models for simulating the turbulent natural convection within a cylindrical enclosure of aspect ratio D/H = 0.5 at Ra = 2×10^9. Results are compared in terms of first and second order statistics against well-solved long-term direct numerical simulations.

5.1 Introduction

Turbulent natural convection of a fluid inside an enclosure heated from below (Rayleigh-Bénard convection), has been object of many theoretical and experimental investigations [1, 2]. It has been long considered as a canonical case for the understanding of thermal convection problems encountered in the atmosphere, oceans and in many engineering applications (e.g. solar energy, crystal growth, micro-electronics). A major focus of previous works has been the study of the global heat transport and scaling relations of the Nusselt number with Rayleigh and Prandlt numbers [3], as well as gaining insight in the coherent Large-Scale Circulation (LSC) presented in the background of fluctuations of the flow, which is characterised by reorientations of the flow, by azimuthal rotations of the flow structure or by reversals of its direction (cessations). These flow reversals occur at times scales much more larger than the convective turnover time. In spite of the numerous numerical and experimental studies carried out, there are details in the behaviour and dynamics of the LSC that remains not well understood.

Another unsolved question is the existence of the ultimate state of convection [4]. In this state, it is supposed that convective heat transport is dominated only by the turbulence in the bulk while boundary layers are negligible. It has been suggested that for $Pr \sim 1$ the transition to this state might occur at $Ra \sim 10^{14}$. Even though the experimental efforts made, its existence still is an unknown. Furthermore, such experiments have to deal with many difficulties in order to maintain constant the laboratory conditions. Regarding to numerical simulations, over the past decades they have become a powerful tool for providing extensive data in turbulence structures and flow dynamics, but flow statistics for Direct Numerical Simulations (DNS) at relative high Ra numbers are still limited by an insufficient time integration [5]. In this sense, Large-Eddy Simulations (LES) can be an attractive alternative for the resolution of natural convection problems at high Ra numbers. As LES models the smallest scales of the fluid their results are not only dependent on the grid resolution and the spatial and temporal discretizations but also on the selection of the appropriate subgrid scale stresses (SGS) model for describing the flow behaviour. There are scarce long-term first and second order statistics results in the literature for comparing LES results. Furthermore, time integration for most of the statistical data available does not guarantee their independence with the LSC reversals.

Thus, the objectives of this chapter are twofold: i) to provide useful long-term accurate statistical data by means of DNS of a cylindrical enclosure of aspect ratio ($\Gamma = D/H$) 0.5 at $Ra = 2 \times 10^9$ and $Pr = 0.7$ and, ii) to assess the behaviour of different LES models by direct comparison with our DNS results. LES studies have been performed using different SGS models: i) the Smagorinsky (SMG), ii) the dynamic eddy viscosity model (DEV), iii) the wall-adapting local-eddy viscosity (WALE) [6], iv) the WALE model within a variational multiscale framework (VMS-WALE)[7] and

v) the QR-model [8]. In order to analyse the influence of the SGS models, a coarse DNS (no-model) has also been computed on the same grids where LES have been used.

5.2 Definition of the cases

The numerical computations have been performed at a Rayleigh number ($Ra = g\beta\Delta T H^3/\nu\alpha$) $Ra = 2 \times 10^9$ and a Prandlt number ($Pr = \nu/\alpha$) of $Pr = 0.7$ in a cylindrical cavity of aspect ratio $\Gamma = D/H = 0.5$. In order to assess the behaviour of LES models, first- and second-order statistics should be compared against experimental or well-solved DNS data. However, there are scarce long-term first and second order statistics results in the literature for comparing LES results. Furthermore, time integration for most of the statistical data available is not sufficient for guaranteeing their independence with the LSC reversals. Thus, we have first performed DNS and statistical data obtained for LES have been compared with that of DNS at different locations. In addition, in order to analyse the influence of the SGS models, a coarse DNS (no-model) has also been computed on the same grids where LES have been used.

For DNS, the mesh has been constructed considering that the smallest flow scales must be well solved. The smallest scales at the hot and cold walls are imposed by viscous and thermal boundary layers while grid size at the bulk must be lesser than Kolmogorov scale. According to Grötzbach estimates [1], the thickness of the thermal boundary layer is $\delta_\theta = H/2Nu$ while Kolmogorov length scale for $Pr \leq 1$ is of the order of $\eta/H \leq \pi\sqrt{Pr}/(NuRa)^{1/4}$, where H is the height of the cylinder. The estimates for δ_θ and η have been used to select an optimal grid for DNS, with grid-points clustered near the walls. Using Niemela [2] scaling relation ($Nu = 0.124Ra^{0.309}$), an a priori estimate of Kolmogorov scale yielded $\eta/H = 4.787 \times 10^{-3}$ and the wall boundary layer thickness was on the order of $\delta_\theta/H = 5.39 \times 10^{-3}$. Since both constrains must be attained, the computational mesh has 20591×128planes (~ 2.63M CV) with 10 grid-points within the boundary layers. This should be enough to satisfy recent criteria about the number of grid points within the boundary layer [9].

LES and the coarse DNS have been performed in a set of refined grids where minimum of 6 of grid-points within the boundary layer has been imposed in all cases. Details of the computational meshes used are given in Table 5.1. Due to the conservative formulation it is expected to achieve good stability properties even with the coarse grid.

mesh	N_{2D}	N_{planes}	$NCV \times 10^6$	N_{BL}
$m1$	4321	32	0.138	6
$m2$	8756	32	0.280	8
$m3$	8756	64	0.560	8
m_{DNS}	20591	128	2.63	10

Table 5.1: Computational meshes used for LES and DNS. N_{2D}, number of grid-points in the 2D planes; N_{planes} number of planes in which the mesh is extruded; $NCV \times 10^6$, total number of control volumes; N_{BL}, number of grid-points within the boundary layer

5.3 DNS results

In order to obtain first and second order statistics for comparison with LES results it is important to guarantee that these results are statistically well converged. To do so, we have located numerical probes at different positions of the cavity where flow dynamics have different characteristic time. The location of each of these probes is given in Table 5.2. Measurements are taken simultaneously at all the azimuthal planes of the computational domain. These probes have provided instantaneous data of the velocity components and temperature over more than 1600 time units ($TU = t/t_0$). Here reference time ($t_0 = H/U_0$) has been defined as a function of the free-fall velocity ($U_0 = \sqrt{g\,\beta\,\Delta T\,H}$) and the height of the domain.

Probe	r/H	z/H
P0	0.0	0.5
P1	0.125	0.5
P2	0.2374	0.5
P3	0.1	0.25
P4	0.1	0.25
P5	0.125	0.95
P6	0.2375	0.95

Table 5.2: Location of the different measurement stations

Figure 5.1(a) and 5.1(a) show the sampled data for the axial velocity and temperature from two of these locations at $P2 \equiv [r/H = 0.2375;\ z/H = 0.5]$ and $P3 \equiv [r/H = 0.1;\ z/H = 0.25]$. The inspection of these instantaneous data shows that the flow seems to be alternating its circulation with a periodic behaviour.

In order to analyse this periodic motion, we have calculated autocorrelations

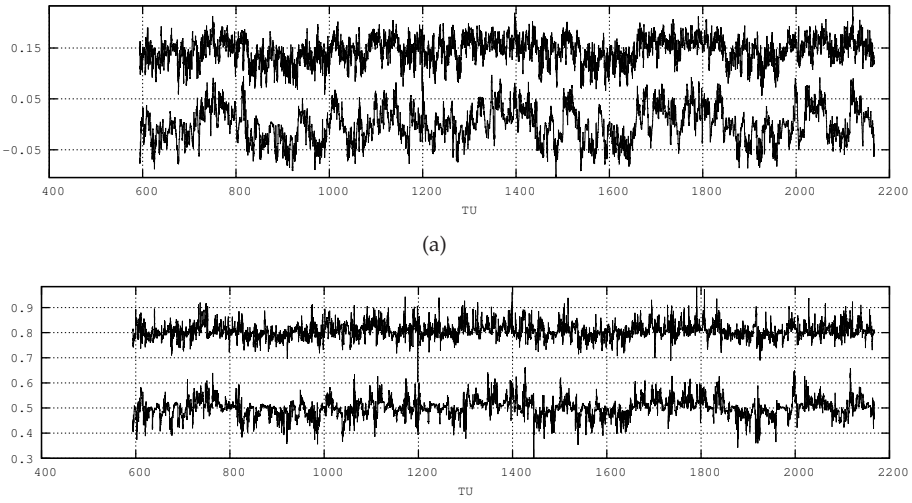

Figure 5.1: (a)Time series of axial velocity (v_z) and (b) temperature, at two different locations of the cavity. bottom: ($P2 \equiv [r/H = 0.2375;\ z/H = 0.5]$); top: ($P3 \equiv [r/H = 0.1;\ z/H = 0.25]$). For clarity, top time series has been displaced

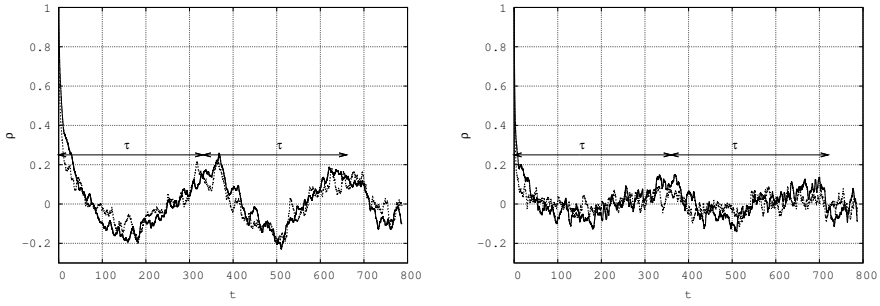

Figure 5.2: Time-series autocorrelation functions. Dotted line corresponds with series at $P3 \equiv [r/H = 0.1;\ z/H = 0.25]$ and solid line $P2 \equiv [r/H = 0.2375;\ z/H = 0.5]$. (a) Autocorrelation for axial velocity time-series; (b) autocorrelation for temperature time-series

from the time-series of the DNS data, for the different probes. Figures 5.2(a) and 5.2(b) show the autocorrelation for axial velocity and temperature fluctuations for the probes shown in figures 5.1(a) and 5.1(b).The autocorrelation, at τ time lag, of any time series can be defined as,

$$\rho(\tau) = \frac{\left\langle \phi'(t)\phi'(t+\tau) \right\rangle}{\left\langle \phi'(t)^2 \right\rangle} \tag{5.1}$$

where fluctuation are $\phi'(t) = \phi(t) - \overline{\phi}$, being $\overline{\phi}$ the mean value of the variable at the probe location.

In the figure, a well-defined periodic oscillation of the axial velocity fluctuations can be observed. These oscillations, which have a very-long time period of more than $\mathcal{T} = 300TU$, have been also observed in the temperature fluctuations (5.2(b)) and seem to be related with oscillations in the large-scale flow motion in the sense that it is alternating directions.

In order to clearly measure the frequency of this periodic oscillation, the frequency power spectra of these fluctuations have been calculated. In figure 5.3, the spectra of the temperature fluctuations at $P2$ and $P3$ are plotted. In the figure, a dominant peak at a very low frequency $f = 0.00302$ (here $f = t_0/t$) can be observed. This peak matches the frequency of the periodic oscillation observed in the autocorrelation functions with a period of about $\mathcal{T} = 331$ TU. It is important to remark that this peak in the spectra does not corresponds with one the observed by Qiu and Tong [11] related to the emission of plumes in the boundary layers. The frequency

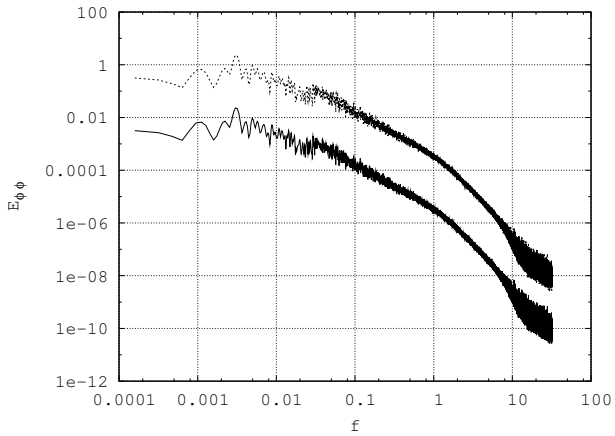

Figure 5.3: One-dimensional energy spectra for the axial velocity fluctuations. Dotted line corresponds with time-series at $P3 \equiv [r/H = 0.1;\ z/H = 0.25]$ and solid line $P2 \equiv [r/H = 0.2375;\ z/H = 0.5]$.

of this secondary peak is much more higher (about one magnitude order) and its contribution to the spectra can not be observed clearly from this figure, where the contribution of a much larger scale is more dominant. However, the behaviour of the thermal plumes and its influence in the large scale circulation is an important feature that deserves a specific analysis, but it is beyond the objective of the present work.

Furthermore, investigating the time series of the data collected, the same periodic behaviour is taking place at different locations within the cavity, thus providing evidence that this is not a local phenomenon but a global one. In fact, it seems to be related to oscillations in the large-scale flow motion in the sense that it is alternating directions.

Further investigation in this periodic behaviour are carried out calculating the histogram of the velocity at $P5 \equiv r/H = 0.125;\ z/H = 0.95$, which exhibits a bimodal shape with two probable peaks at opposite directions (see figure 5.3). This behaviour in the velocity histogram corroborates the above observations that the large scale circulation alternates directions with certain periodicity. This periodic behaviour has been reported before by Niemela et al. [2] for an aspect ratio $\Gamma = 1$ and Ra=6×10^{13} and by Verdoold et al. [10] in an aspect ration $\Gamma = 4$ cavity. As in previous observations, a large-scale flow survives to this alternating circulation, but its mean value is very small if it is compared to the value of the small-scale fluctuations.

The existence of this periodic oscillation with a very low frequency should affect

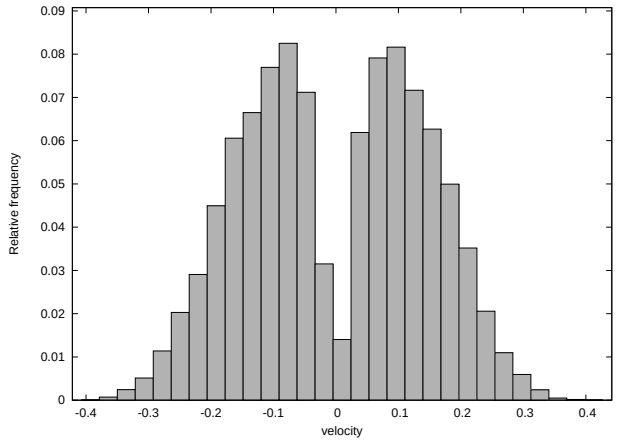

Figure 5.4: Velocity histogram at $P8 \equiv r/H = 0.125;\ z/H = 0.95$

converged statistics. In figure 5.5 the time series and cumulative average of axial velocity components and temperature are given at three different stations of in the cavity: i) at $P1$ near the center of the cavity; ii) at $P3$ neat the wall, but at mid-height and iii) at $P5$ near the top wall. It should be highlighted, that average statistics shown in the figure have been averaged not only in time but also in space, considering that time-series have been collected for every plane in the azimuthal direction. As can be seen from these cumulative averaged statistics, in order to obtain well-converged statistics a long integration time is required. Even after more than 1000 TU of time-integration oscillation in these quantities are still observed. This behaviour is not only obtained at these locations inside the cavity, but also it affects the convergence of the average Nusselt number.

According to the results obtained, the dynamics of the large scale circulation presents a periodic behaviour that occurs with a large temporal scale of about 331 TU. Thus, in order to ensure that statistics of DNS data are adequate and that all transients effects are washed out, statistical data have been collected starting from instant $600TU$. After that, the averaging of the first and second order statistics has been carried out for more than $1600TU$ which corresponds with almost 5 cycles of the periodic behaviour observed.

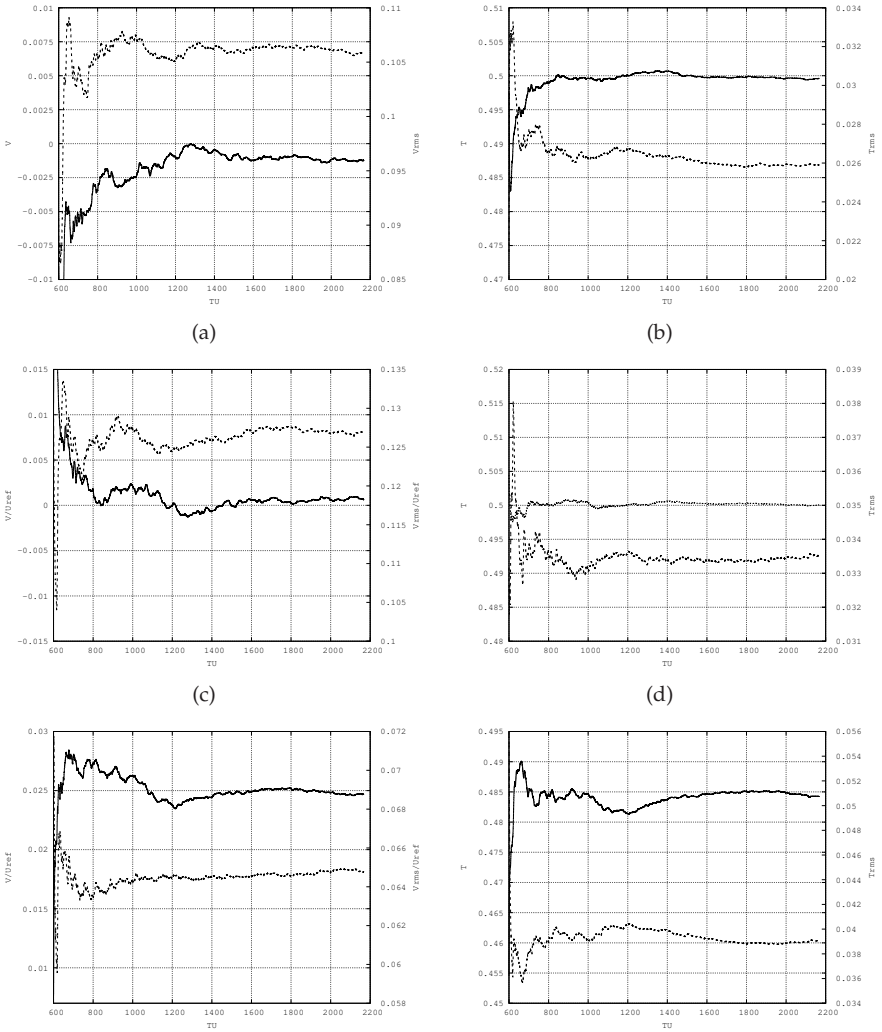

Figure 5.5: Cumulative average statistics for the (left) axial velocity component and its fluctuations and (right) temperature and its fluctuations, at different locations inside the cavity. (a,b) at $P1$; (c,d) at $P2$; (e,f) at $P5$. (solid line) first-order statistics; (dashed line) second-order statistics

5.4 LES results

5.4.1 First order statistics

The average Nusselt number at the horizontal walls have been calculated and is given in table 5.3. In the table it is shown that even for the coarse grid, there is quite good agreement with the reference DNS data. In fact, differences in the prediction of the Nusselt number for the coarse grid without any SGS model is quite good, being less than 3% in all cases. These good results can be attributed to the use of a conservative formulation, which preserves the kinetic-energy balance, together with the large integration time used, ensuring temporal converged statistics. The present results are in contradiction with recent findings of Stevens et al. [9] where it is argued that a very fine mesh is required for solving the plume dynamics. In their case, they used a mesh with ($129 \times 513 \times 513$) grid-points in the radial, axial and azimuthal directions respectively and with 17 control volumes within the boundary layer and about 100 TU of integration time. However, in the present work it has been shown the importance of a large integration time if the whole dynamics of the LSC is to be captured.

The present results obtained for the average Nusselt number are of special interest for practical applications, because with a minimum number of grid points within the boundary layer and a coarse grid it is possible to reproduce the results of the DNS for the average Nusselt number with less than a 3% of difference but with a huge saving in time and computational resources. It is important to highlight that in terms of CPU time QR model has the best performance (it is faster than DEV and VMS-WALE models). Thus, this feature can be of special interest if the resolution of industrial complex flows at high Rayleigh numbers is required. However, for the prediction of the maximum and minimum peaks in the heat flux, a SGS model and the largest mesh have been necessary. In this case, DEV, QR and VMS-WALE models predict quite well these quantities for the largest grid.

A close inspection to the first-order statistics in the center of the cavity is depicted in figure 7.1, where LES computations with the different grids are compared to the DNS results. As can be seen, small differences are observed in the temperature distribution for all the models and even with the coarse grid $m1$. However, larger differences are obtained in the axial velocity distribution for $m1$ and $m2$. In fact, for the coarse grid the models which perform better are DEV and QR, but differences between SGS models are reduced as the grid is refined. For the largest grid even the no-model solution approaches the DNS results.

Grid	Model	$\overline{Nu}$	$\epsilon[\%]$	Nu_{max}	$\epsilon[\%]$	Nu_{min}	$\epsilon[\%]$
m_{DNS}	DNS	84.97	-	100.14	-	44.78	-
	no model	85.73	0.89	112.39	12.2	33.15	25.9
	WALE	82.60	2.78	106.69	6.5	36.18	19.2
$m1$	DEV	81.84	3.7	104.64	4.5	35.25	21.2
	QR	83.75	1.43	109.12	8.9	31.84	28.8
	VMS-WALE	85.14	0.2	111.11	10.9	34.97	21.9
	no model	84.61	0.42	116.17	16.0	36.37	18.8
	WALE	82.02	3.5	110.51	10.3	36.75	17.9
$m2$	DEV	81.84	3.7	104.65	4.5	35.79	20.1
	QR	82.57	2.8	110.19	10.03	32.99	26.3
	VMS-WALE	84.27	0.82	104.93	4.7	35.15	21.5
	no model	87.3	2.7	104.04	3.9	42.92	4.1
	WALE	86.97	2.3	102.44	2.3	42.45	5.2
$m3$	DEV	84.29	0.8	100.4	0.26	43.08	3.7
	QR	84.48	0.57	100.29	0.15	41.19	8.01
	VMS-WALE	86.5	1.8	101.98	1.8	43.13	3.6

Table 5.3: Comparison of the average, maximum and minimum Nusselt numbers between LES and DNS results for the different grids solved.

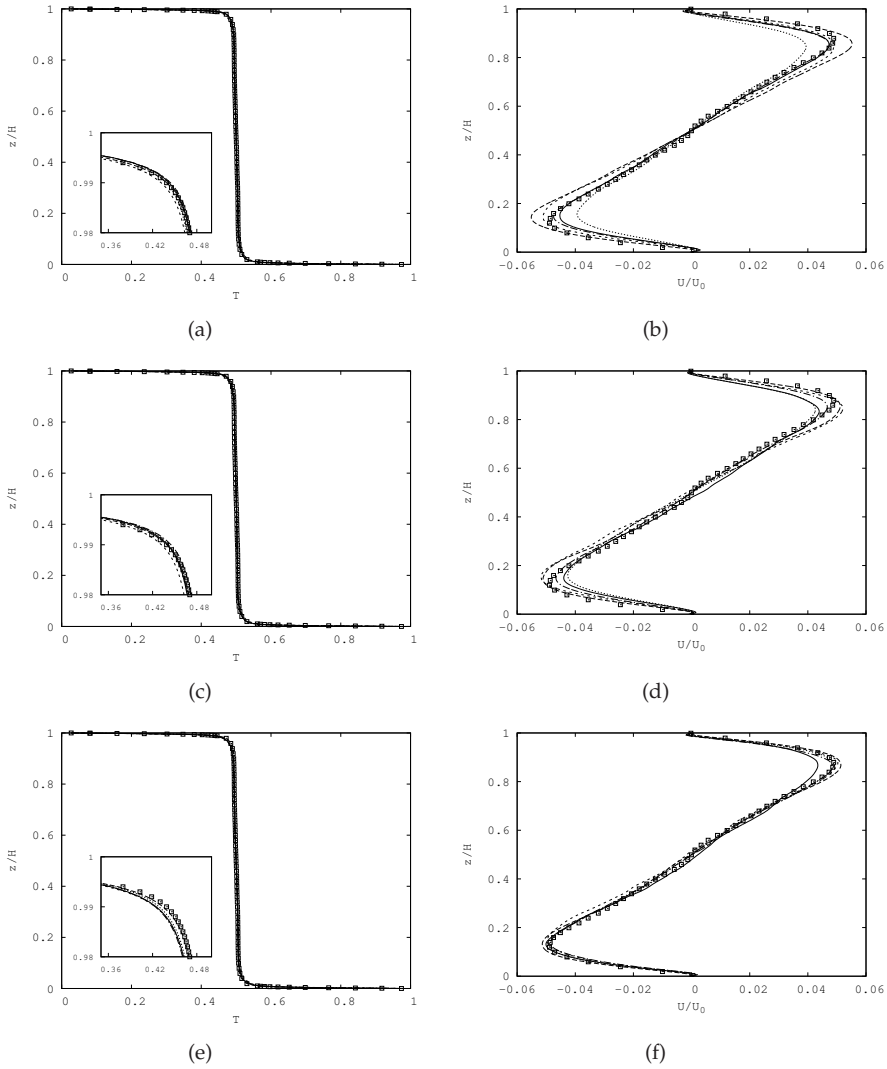

Figure 5.6: Comparison of vertical profiles at the axis of the cylinder for the three meshes studied (left) temperature; (right) axial velocity $\overline{v_z/U}$. (a,b) $m1$; (c,d) $m2$; (e,f) $m3$. squares, DNS; long-dashed line DEV; dashed line QR; dash-dotted line WALE; solid line VMS-WALE; dotted line no-model.

5.4.2 Second-order statistics

Although the results of comparison of first-order statistics is encouraging, it is important also to compare the second-order statistics. Figure 5.7 shows the vertical distributions of the root mean square time-averaged fluctuations of the temperature and radial velocity for the SGS models and also for the coarse DNS. As can be seen, larger differences are obtained in the peak in the stresses, specially for radial velocity fluctuations, where noticeable differences in the core of the cavity are observed for $m1$ and $m2$. However, with the finest grid $m3$, all the models behaves quite well.

The largest differences have been observed not in the axis of the cavity but off the center. For instance, if axial velocity and radial velocity fluctuations are plotted at $r/H = 0.125$, deviations from the DNS data in some models and with the finest grid are noticeable.

In general, DEV and QR models perform better. However, as can be seen as the grid is refined, even without model deviations from reference data is small. This can be attributed in part to the characteristics of this flow, which behaves similar to homogeneous turbulence, in special at the core of the cavity, and thus all models present a good behaviour. In addition, the use of a conservative formulation, which preserves the kinetic-energy balance, together with the large integration time used, ensuring converged temporal statistics, also contribute to enhance the performance of the SGS models.

5.5 Conclusions

DNS and LES of the Rayleigh-Benard convection at $Ra = 2 \times 10^9$ in a cylindrical cavity of aspect ratio $\Gamma = 0.5$ have been carried out using a symmetry-preserving formulation. The analysis of the DNS data for the velocity and temperature fluctuations has shown that LSC oscillates with a periodic behaviour of $t_0 = 331$TU, which affect the statistical convergence of the data. Thus, results presented have been integrated for more than 1800 TU in order to obtain well-converged statistical data for comparison with turbulence models.

Comparison with the different SGS models show that in general as the grid is refined all models behave quite well, in special at the core of the cavity where the turbulence is almost homogeneous. Largest differences are observed off the center of the cavity. Although even without model a good approach to reference data is observed, QR and DEV models predictions are in better agreement even with the coarser grid. However, if CPU time is considered, then QR model is the best alternative as it is essentially not more complicated to implement in a LES-code than the standard Smagorinsky model (with $\mathcal{C}_s$ constant) and is faster than DEV model.

The comparison of the average Nusselt number shows that this quantity is quite

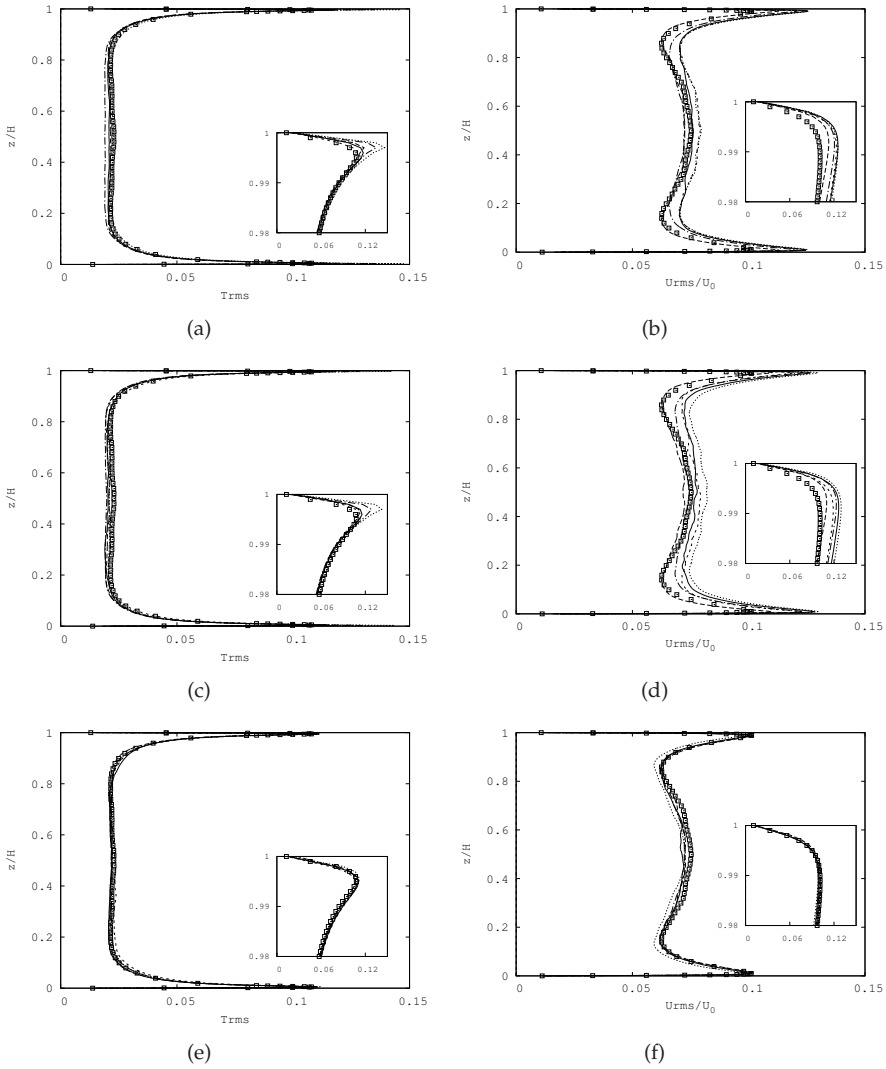

Figure 5.7: Comparison of vertical profiles at the axis of the cylinder for the three meshes studied (left) temperature fluctuations; (right) radial velocity fluctuations $\overline{v_r'}/U$. (a,b) $m1$; (c,d) $m2$; (e,f) $m3$. squares, DNS; long-dashed line DEV; dashed line QR; dash-dotted line WALE; solid line VMS-WALE; dotted line no-model.

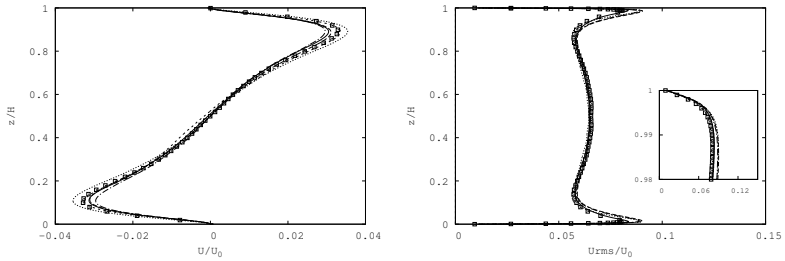

Figure 5.8: Comparison of vertical profiles at $r/H = 0.125$ with the $m3$ grid. (a) axial velocity $\overline{v_z/U}$.; (b) radial velocity fluctuations $\overline{v_r'/U}$. For more details about each line see fig. 5.7

well predicted even for the coarse grid and without model. These good results can be attributed to the use of a conservative formulation, which preserves the kinetic-energy balance, together with the large integration time used, ensuring converged temporal statistics. The present results are in contradiction with recent findings of Stevens et al. [9], as in this case it has been observed that for solving the plume dynamics it is more important a large integration time to consider all the dynamics of the LSC than an extremely fine computational mesh. These results are of special interest for practical applications, because with a minimum number of grid points within the boundary layer and a coarse grid it is possible to reproduce the results of the DNS for the average Nusselt number with less than a 3% of difference but with a huge saving in time and computational resources.

References

[1] G. Grötzbach. Spatial resolution requirements for direct numerical simulation of the Rayleigh-Bénard convection. *Journal of computational physics*, 49:241–264, 1983.

[2] J.J. Niemela, L. Skrbek, K.R. Sreenivasan, and R.J Donnelly. Turbulent convection at very high Rayleigh numbers. *Nature*, 404, 2000.

[3] S. Grossmann and D. Lohse. Scaling in thermal convection: a unifying theory. *Journal of Fluids Mechanics*, 407:27–56, 2000.

[4] D. Funfschilling, E. Bodenschatz, and G. Ahlers. Search for the "ultimate state" in turbulent Rayleigh-Benard convection. *Physical Review Letters*, 2009.

[5] G. Amati, K. Koal, F. Massaioli, K.R. Sreenivasan, and R. Verzicco. Turbulent thermal convection at high Rayleigh numbers for a Boussinesq fluid of constant Prandtl number. *Physics of fluids*, 17(121701), 2005.

[6] F. Nicoud and F. Ducros. Subgrid-scale stress modelling based on the square of the velocity gradient tensor. *Flow, Turbulence and Combustion*, 62:183–200, 1999.

[7] T.J.R. Hughes, L. Mazzei, and K.E. Jansen. Large eddy simulation and the variational multiscale method. *Computing and Visualization in Science*, 3:47–59, 2000.

[8] R. Verstappen. When does eddy viscosity damp subfilter scales sufficiently? In ERCOFTAC Series, editor, *Quality and Reliability of Large-Eddy Simulations II*, volume 16, pages 421–430, 2011.

[9] R.J.A.M Stevens, R. Verzicco, and D. Lohse. Radial boundary layer structure and nusselt number in Rayleigh-Benard convection. *Journal of Fluids Mechanics*, 649:495–507, 2010.

[10] J. Verdoold, M. J. Tummers, and K. Hanjalic. Oscillating large-scale circulation in turbulent Rayleigh-Bénard convection. *Physical Review E*, 73(056304), 2006.

[11] X.-L. Qiu and P. Tong. Temperature oscillations in turbulent Rayleigh-Bénard convection. *Physical Review E*, 66(026308), 2002.

[12] Verzicco R. and R. Camussi. Numerical experimenrs on strongly turbulent thermal convection in a slender cylindrical cell. *Journal of Fluid Mechanics*, 477:19–49, 2003.

Chapter 6

Direct numerical simulation of the turbulent flow past a sphere at subcritical Reynolds numbers

Most of the contents of this chapter have been published as:
I. Rodríguez, R. Borrell, O. Lehmkuhl, C.D. Pérez-Segarra and A. Oliva (2011). Direct numerical simulation of the flow over a sphere at Re = 3700. *Journal of Fluid Mechanics*, 679, pp 263-287
I. Rodríguez, O. Lehmkuhl, R. Borrell and A. Oliva (2012). Flow dynamics in the turbulent wake of a sphere at sub-critical Reynolds numbers. *Computer & Fluids*. doi:10.1016/j.compfluid.2012.02.030. 2012.

Abstract. Direct numerical simulations of the flow over a sphere have been performed. The computations have been carried out in the sub-critical regime at $Re = 3700$ and $Re = 10000$ (based on the free-stream velocity and the sphere diameter). A parallel unstructured conservative formulation has been used for simulating the flow. Computations have been carried out on unstructured grids obtained by the constant-step rotation about the axis of a two-dimensional grid. With this discretisation, the Poisson equation has been solved by means of a Fourier diagonalization method. Particular attention has been devoted to investigate the shear-layer instabilities and its influence in the vortical structures, as well as the wake configuration. The main features of the flow including power spectra of a set of selected monitoring probes at different positions have been described and discussed in detail. Detailed information about turbulent statistics have also been provided.

6.1 Introduction

The flow around bluff bodies is of great interest for a large number of engineering applications such as vehicle aerodynamics, wings at high angle of attack, interaction of the wind with buildings, cooling devices using forced convection, heat transfer enhancement using droplets, among others. Prediction of flows which exhibit massive separation, such as those mentioned before, remains nowadays one of the principal challenges to the computational fluids dynamics (CFD). In fact, the study of turbulent flows behind canonical geometries can be useful to investigate these complex flow structures as well as to provide useful information for validating CFD models (e.g. LES models). In this sense, the main interest of the present work is the study of the turbulent flow past a sphere at sub-critical Reynolds numbers.

The unsteady flow over a sphere at sub-critical Reynolds numbers has a complex nature characterized by the transition from laminar to turbulent flow in the detached shear layer, the existence of a turbulent wake behind the sphere and the unsteady shedding of vortices in the wake. This flow has been object of many experimental and numerical studies (see for instance [1, 2, 3, 4]), most of them providing flow visualization, distribution of the pressure coefficient and skin friction over the sphere, and integral parameters such as the shedding frequency and the drag coefficient, among others. In addition to the experimental techniques, in the last decades Direct Numerical Simulation (DNS) and Large-Eddy Simulation (LES) have become powerful tools for providing time-accurate useful information about the fluid behaviour. However, one of the major constraints to the simulation of complex turbulent flows is the large amount of computational resources needed to carry them out. By means of the modelisation of some of the turbulence scales (e.g. LES modelling), it is possible to reduce these costs and perform simulations of more complex turbulent flows. For this reason, most of the numerical simulations of the flow around a sphere have been carried out in the laminar regime, considering both, the steady and unsteady flows [5, 6]. However, there are few time-accurate calculations carried out in the turbulent regime [4, 7]. Moreover, most of the numerical works reported since now have been performed using different turbulent models, including Large Eddy Simulations (LES) [8, 9, 10] and Detached Eddy Simulations (DES) [11].

Even though the large amount of research works available, studies on the mechanism of transition in the shear-layer, wake structure and quantitative measurements of the wake characteristics are still scarce. There is a lack of detailed experimental or numerical data such as first and second order statistics, as well as wake parameters, e.g. detachment angle, recirculation length, drag coefficient, among others,at different Reynolds numbers. Considering this, the aim of this work is to investigate the characteristics of the wake of a sphere in order to provide an insight of the instantaneous and time-average near-wake flow in the subcritical regime by means of Direct Numerical Simulations (DNS) at Reynolds numbers of Re=3700 and Re=10000. To

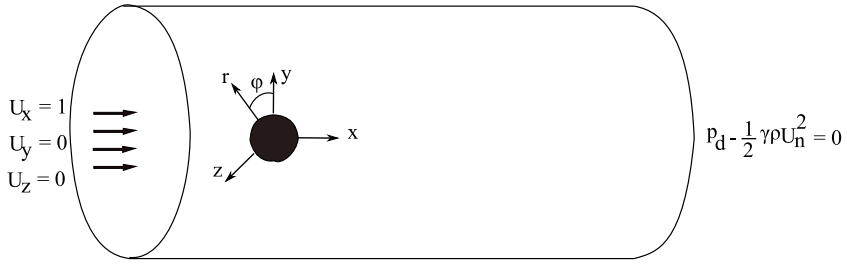

Figure 6.1: Computational domain and boundary conditions

do this, the computations have been performed by using a parallel unstructured conservative formulation for accurate solving complex geometries. The computational domain simulated is a cylindrical domain and the meshes used have been generated by the constant-step revolution in the azimuthal direction of a two-dimensional (2D) unstructured grid, being $2\pi/N_{planes}$ the step size (N_{planes} is the number of 2D planes in the azimuthal direction). Considering the grid generated by this method, the Poisson equation which arises from the incompressibility constrain is solved by means of a Fourier diagonalization method in the periodic direction.

6.2 Flow parameters overview

Numerical simulations of the flow over a sphere have been performed at two Reynolds numbers $Re = 3700$ and $Re = 10000$, where the Reynolds number ($Re = UD/\nu$) is defined in terms of the free-stream velocity U and the sphere diameter D. Solutions are obtained in a cylindrical computational domain of dimensions x=[-5D,20D]; r=[0,7D]; θ=[0,2π], where the sphere is located at (0,0,0) (see figure 6.1). The boundary conditions at the inflow consist of a uniform velocity (u,v,w)=(1,0,0). Constant velocity (u,v,w)=(1,0,0) is also prescribed at the other external boundaries except for the downstream one (outlet) where a pressure-based condition is used. No-slip conditions on the sphere surface are imposed.

6.3 Computational details

The governing equations are discretised on an unstructured mesh generated by the constant-step rotation around the axis of a two-dimensional unstructured grid. In this discretisation, the azimuthal direction is divided into N_{planes} identical planes. The use of an unstructured grid for the plane has allowed to cluster more control

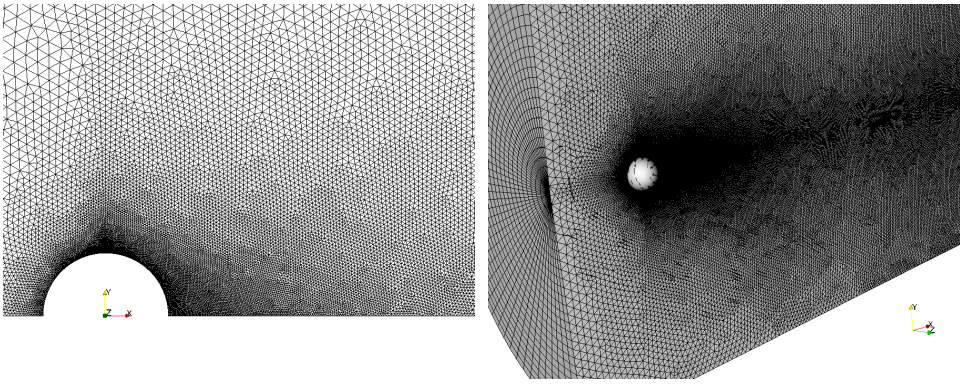

(a) (b)

Figure 6.2: a) Detail of the mesh of the 2D grid in the region near the sphere, b) 3D mesh

volumes around the sphere and in the near wake. An example of the 2D grid and its refinement around the sphere together with the 3D mesh are depicted in figures 6.2(a) and 6.2(b) respectively.

At each time step, the parallel algorithm used for the time integration can be divided into two parts: the implicit part, in which the Poisson equation is solved (this is the main bottleneck of the algorithm), and the explicit part, in which the rest of calculations are performed explicitly. In the explicit part, a point-to-point communication is needed between the different parallel processes involved in the simulation. The load of this communication depends on the size of the stencils used in the numerical schemes but, in general, it does not significantly degrade the parallelism unless the subdomains are too small. On the contrary, the implicit part (i.e. solving the Poisson equation) is costly in terms of parallelism, RAM memory requirements and CPU-time consumption.

In the discretisation used in this paper, the azimuthal direction has been uniformly divided into N_{planes} planes. Under these conditions, the azimuthal coupling of the discrete Poisson equation results into circulant sub-matrices that are diagonalizable in a Fourier space by means of a Fast Fourier Transform (FFT) based algorithm [12]. This diagonalization decouples the initial 3D system into a set of mutually uncoupled 2D subsystems which can be solved by means of a Direct Schur-complement based Decomposition method (DSD). For more details the reader is referred to Borrell et. al.[13].

Concerning the parallelisation strategy, each plane of the extrusion has been divided into P_{2d} parts while the azimuthal direction has been divided into P_{per} parts.

Therefore, the domain has been decomposed into $P = P_{per} \times P_{2d}$ subdomains. When considering the optimal values for P_{per} and P_{2d}, it must be taken into account that: i) the DSD method has not unlimited speed-up (P_{2d} should be within the linear speed-up region); ii) when the change-of-basis to the Fourier space is performed by means of the FFT, a global communication between each sub-group of P_{per} processors/subdomains aligned in the azimuthal direction is required. This global communication eventually degrades the parallelisation as the number of partitions in the azimuthal direction (P_{per}) increases.

Given a problem and a parallel computational architecture, some tests must be carried out in order to find out the optimal decomposition. Studies to determine the best option to solve the meshes used in the simulations have been performed. For the finest grids at both Reynolds numbers, 240 CPUs have been used in the simulation, and the optimum parallelisation strategy has been to divide the 2D plane into 60 subdomains ($P_{2d} = 60$) and the azimuthal direction into 4 parts ($P_{per} = 4$). For instance, the time required to solve the Poisson equation in a mesh of (74041×128 planes) is 0.067 seconds, which is about the 20% of the total time spend in a time-step (0.337 seconds).

The computations reported in this paper have been performed on a 76 nodes in-house cluster, each node has 2 AMD Opteron 2350 Quad Core processors linked with an infiniband DDR4 network, and on MareNostrum supercomputer at the Barcelona Supercomputing Center (BSC). At the moment when these computations have been performed, this was an IBM BladeCenter JS21 Cluster with 10 240 PowerPC 970MP processors at 2.3 GHz with 1MB cache per processor. Quad-core nodes with 8GB RAM were coupled by means of a high-performance Myrinet network.

6.4 Mesh resolution studies

In order to evaluate the adequacy of the spatial discretisation, computations have been performed on different meshes. Extensive grid refinement tests have been conducted. Table 6.1 shows the different grids considered for both Reynolds numbers. When performing DNS, it must be ensured that the grid size is enough to solve the smallest flow scales well and, that near the solid walls the viscous boundary layer is also well solved. This means that, within the boundary layer, a minimum number of grid points must be assured. Considering that the boundary layer is laminar until the drag crisis ($Re = 3.7 \times 10^5$), and its thickness can easily be estimated [14] and thus, the estimation of the number of control volumes within the boundary layer.

Details of the analysis for $Re = 3700$ can be found appendix 8.4. The finest grid has been about 9.48 million CVs (74041×128 planes) which covered the whole domain. For this mesh, a minimum of 12 grid-points within the boundary layer have been considered. In addition, taking advantage of the unstructured grid, control vol-

Case	$N_t[MCV]$	$N_{CVplane}$	N_{planes}	N_{BL}
		$Re = 3700$		
I	9.48	74041	128	12
II	5.45	56787	96	10
III	3.63	56787	64	10
IV	1.8	28168	64	4
		$Re = 10000$		
I	18.2	142254	128	12
II	4.6	72133	64	8

Table 6.1: Main parameters for the meshes used for $Re = 3700$ and $Re = 10000$. N_t total number of CVs; $N_{CVplane}$ number of CVs in the plane; N_{planes} number of planes in the azimuthal direction; N_{BL} number of points in the viscous boundary layer

umes have been clustered in the near wake region in order to ensure that the grid size is in the same order of magnitude that the smallest scales of the flow (Kolmogorov scales).

As for $Re = 10000$, following the same considerations, two different grids have been tested to evaluate the adequacy of the spatial discretisation. For the sake of brevity we are not presenting here the results obtained with the coarse grid, but a thorough comparison of the main parameters of the flow and first and second order statistics have been carried out. For instance, the relative difference in the magnitude of the drag coefficient between the two grids is only 2.7%, which is a fair good agreement considering that grid II is almost 4 times coarser than grid I. Although when comparing first-order statistics, results with the coarser grids show quite good agreement for both Reynolds numbers, for second-order statistics the finest grids are required in both cases. This is because only with the finest meshes all scales of the flow are solved as is it shown hereafter.

The quality of the grid resolution used in present computations has been further assessed by means of *a-posteriori* analysis of meshes used for DNS computations at both Reynolds numbers by comparing the grid size h ($h \equiv (\Delta x \times \Delta y \times \Delta z)^{1/3}$) to the Kolmogorov length scale η. Kolmogorov length scale has been obtained from the dissipation rate ϵ as,

$$\eta = (\nu^3/\epsilon)^{1/4} \tag{6.1}$$

Figure 8.3 shows profiles of the ratio of h/η at different positions in the near wake at both Reynolds numbers obtained with the finest grids. As can be seen, for $Re = 3700$, the average ratio between the grid size and the Kolmogorov length scales

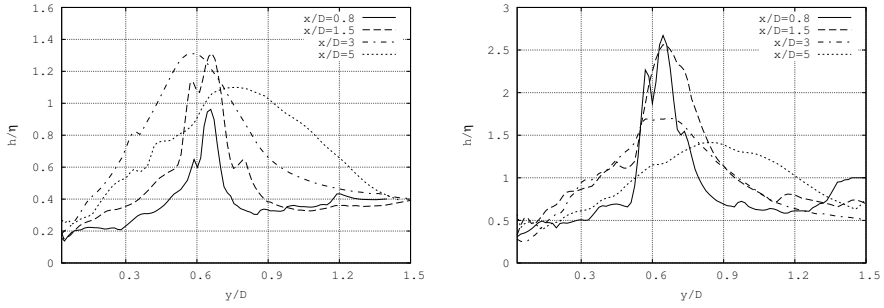

Figure 6.3: Ratio of h/η at different positions in the near wake. a) $Re = 3700$, b) $Re = 10000$

is of $\overline{h}/\eta = 0.642$ for the near wake zone up to a distance from the rear end of the sphere of $x/D = 5$. For $Re = 10000$, within the near wake region ($x/D < 5$), the average value of this ratio is $\overline{h}/\eta = 0.91$. It should be noted, that the peak value for $Re = 10000$ is about $h/\eta = 2.5$. However, according to Moin & Mahesh [15], the smallest length-scale to be resolved must be of $\mathcal{O}(\eta)$ (not equal to η), as it has been proven that the relevant requirement is to have a fine enough resolution to accurately capture the dissipation spectrum. This gives as a result that the smallest length-scale is typically greater than Kolmogorov length scale. In addition Pope [16] has shown that dissipation peak occurs at $h/\eta \sim 24$, being the motions responsible for the dissipation of a scale larger than that of the Kolmogorov and in the range $8 < h/\eta < 60$. Thus, considering the ratios obtained, the grid density used for both meshes should be fine enough for solving the smallest flow scales in the near wake zone.

6.5 Numerical simulations results

For obtaining the numerical results presented, small random disturbances have been introduced to the initially homogeneous flow field. At a certain time, the flow becomes three-dimensional and the transition to turbulence occurs in the wake of the sphere. Thus, simulation has been advanced in time until statistical stationary flow conditions have been achieved. Once the initial transient has been washed out, first and second order statistics have been obtained based on the integration of instantaneous data over a sufficiently long-time period. In order to guarantee that the solved quantities are statistically independent, the evolution of first and second or-

der statistics have been studied. A summary of these results is presented in figure 6.4 for $Re = 3700$. The figure illustrates the time history averaging for streamwise (v_x) and radial velocity components (v_r), respectively. These values have been sampled at the axis at a distance of $x/D = 3$. This point is located downstream the recirculation bubble and, at this station, streamwise velocity exhibits clearly large fluctuations due to the turbulent mixing between the convected fluid along the shear layer and the fluid in the recirculation bubble. In the figure can be observed how mean and turbulent statistics approach to converged values as time-averaging increases. Based on these results, statistical data have been obtained by means of the integration of the instantaneous quantities over a period of 350 D/U time-units for $Re = 3700$. For $Re = 10000$, 150 TU (about 30 vortex-sheddings) have been required for obtaining converged statistics. For this time integration period, the resolved turbulence statistics should be considered as statistically converged values. Furthermore, all statistical quantities have also been averaged in the azimuthal direction.

6.5.1 Power spectra analysis

In order to gain further insight in the turbulent structures in the wake of the sphere, the main frequencies dominating the flow have been computed via power spectra of the turbulent velocity fluctuations. The spectrum has been computed by means of the Lomb periodogram technique and the result has been averaged along the azimuthal direction. To do this, instantaneous velocities have been sampled at different locations in the shear-layer and in the near wake. For both Reynolds, instantaneous velocities are strongly unsteady and the flow is perturbed by intermittent high-frequency strong fluctuations in the transition region in the shear-layer and by the large-scale motion due to vortex shedding in the near wake. However, both contributions act at different time-scales and also at different zones.

For $Re = 3700$, the first of these probes is located at the axi-symmetric shear layer at $x/D = 1.0$, $r/D = 0.6$. The second one is placed at $x/D = 2.4$, $r/D = 0.6$, in the zone of the shear layer where transition to turbulence is supposed to occur. The third one at $x/D = 3$, $r/D = 0.6$ and, the last one, at $x/D = 5$, $r/D = 0.6$ further downstream in the turbulent wake.

One can notice that radial velocity fluctuations display different frequency contributions depending on the position of the probes in the shear layer and in the wake. Indeed, the spectrum of the probe located at $x/D = 2.4$, $r/D = 0.6$ exhibit a dominant peak in the energy at the large scale vortex shedding frequency $S_t = f_{vs}\ D/U = 0.215$ (see figure 6.5(d)). This peak is also detected at all stations downstream of the sphere (figures 6.6(b) and 6.6(d)). The magnitude of the peak decreases slightly with the distance from the sphere, but it is clearly seen at all monitored ports. In the figures, the $-5/3$ Kolmogorov's law is also represented. As can be seen from the figures, only at $x/D = 5$, the slope of the spectrum approximates the

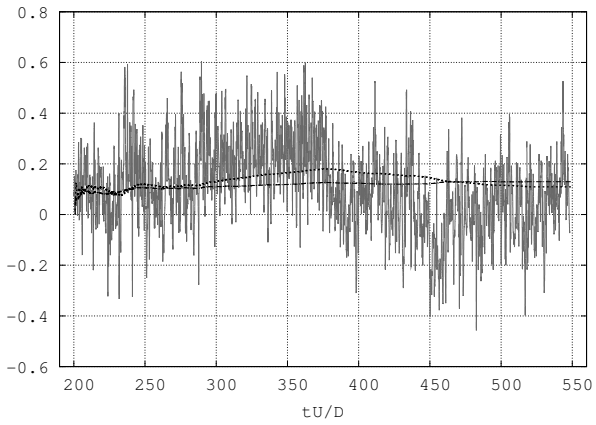

(a)

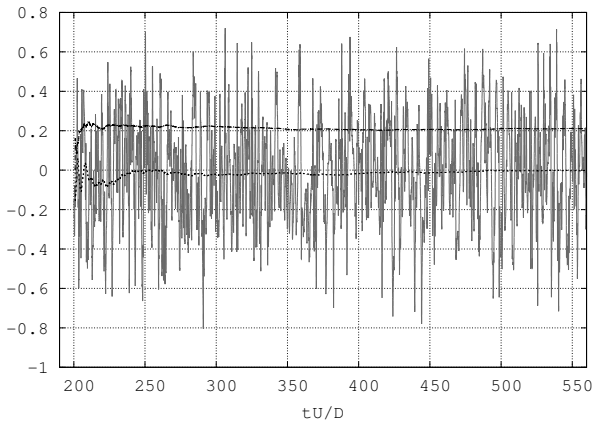

(b)

Figure 6.4: Time history for streamwise and radial velocity components and their time-averaging history (a) streamwise velocity v_x (solid line), its time-average $\overline{v_x}$ (dotted line) and its time-averaged fluctuation $\overline{v_x}_{rms}$ (dash-dotted line). (b)radial velocity v_r (solid line), its time-average $\overline{v_r}$ (dotted line) and its time-averaged fluctuation $\overline{v_r}_{rms}$ (dash-dotted line)

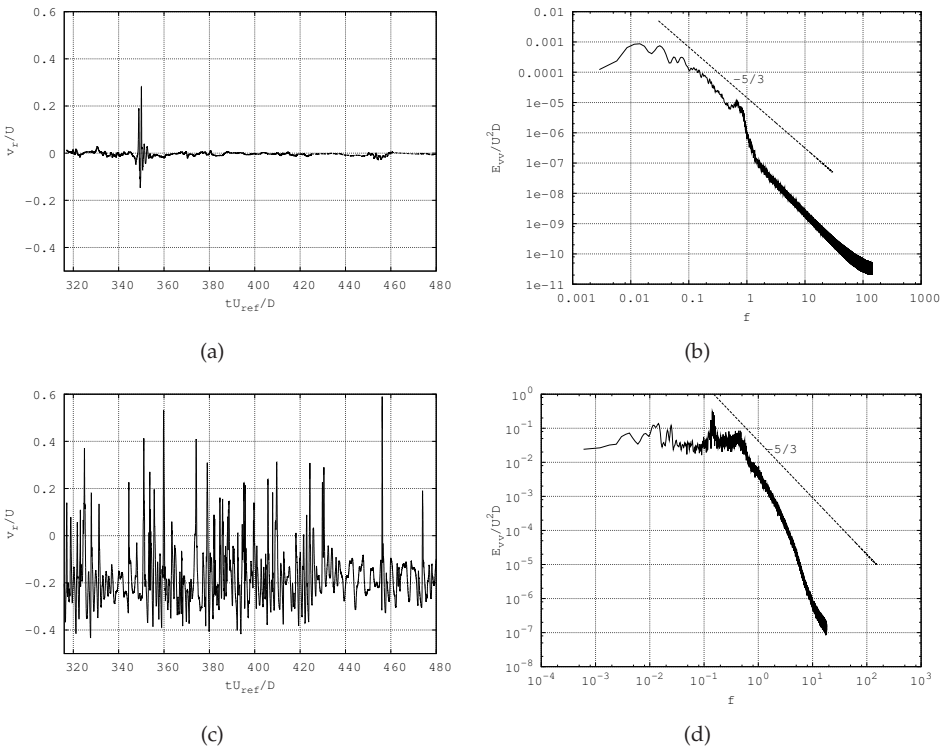

Figure 6.5: Time history and power spectrum at different locations (a,b) radial velocity v_r and power spectrum at $x/D = 1$, $r/D = 0.6$, (c,d) radial velocity v_r and power spectrum at $x/D = 2.4, r/D = 0.6$,

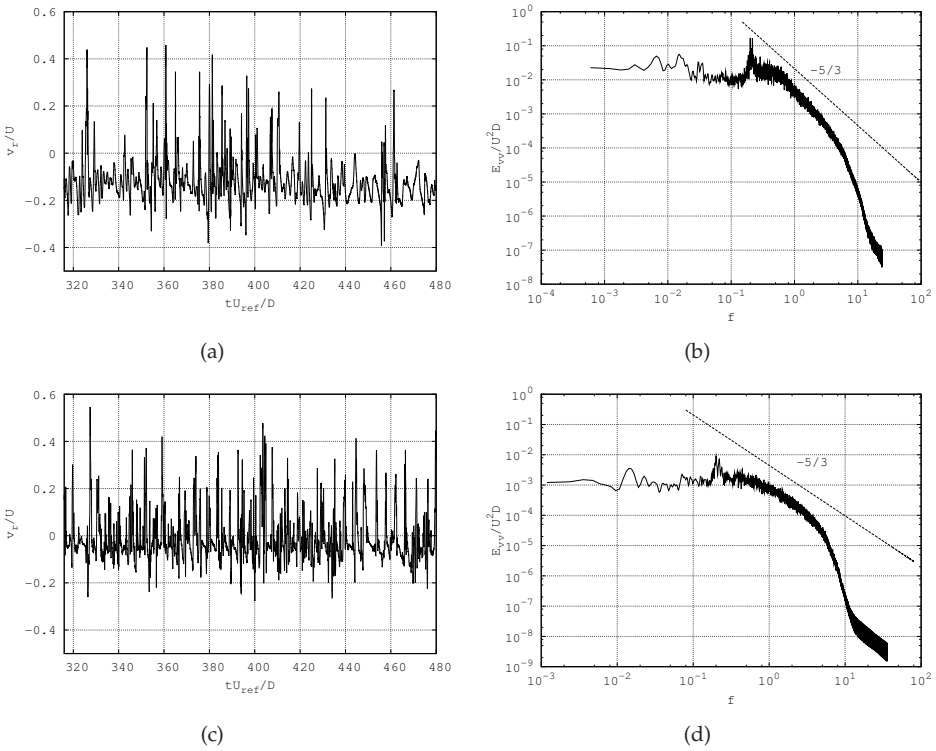

Figure 6.6: Time history and power spectrum at different locations (a,b) radial velocity v_r and power spectrum at $x/D = 3, r/D = 0.6$, (c,d) radial velocity v_r and power spectrum at $x/D = 5, r/D = 0.5$

$k^{-5/3}$ behaviour according to Kolmogorov's law for a narrow range of frequencies. However, at this low Reynolds, the power spectrum almost pass directly from the energy carrying scales to the dissipative range.

In addition to the large-scale vortex-shedding frequency, there is a secondary characteristic frequency associated with the Kelvin-Helmholtz instabilities of the separating shear layer at $f_{KH}\ D/U = 0.72$. This frequency has been detected only in the very near wake, just downstream of the sphere (see the spectrum for location $x/D = 2.4$, $r/D = 0.6$, figure 6.5(d)). In fact, the first probe located in the laminar region of the shear layer, closer to the separation point, also shows a broadband peak centred at f_{KH}. These instabilities can be observed as high frequency fluctuations of the radial velocity and they seem to grow in magnitude as the downstream distance

from the sphere increases (see figures 6.5(a), 6.5(c), see also figure 6.11). Such intermittency has been observed before for a circular cylinder by Prasad and Williansom [17], who studied the shear layer instabilities and, has also been captured by DNS of the flow past a sphere at $Re = 650$ [5] and at $Re = 1000$ [4]. In experiments of the flow behind a sphere, this frequency has also been reported previously. Kim and Durbin [18] reported a high frequency mode to be between 0.75 and 1.04, while Sakamoto and Haniu [3] measured a frequency value within $0.97 - 1.22$. The value obtained in this paper is more consistent with Kim and Durbin [18] measurements while there is little difference with the one reported by Sakamoto and Haniu[3].

A similar behaviour can be observed for $Re = 10000$. Yet, as the point of transition to turbulence moves upstream with the increase in the Reynolds number, shear-layer instabilities appear closer to the separation point. Figure 6.7(b) shows the energy spectrum of a probe located in a position where the passage of shear-layer vortices are meant to occur ($x/D = 1$, $r/D = 0.6$). The spectral peak of these structures appear to be broad as in the case of $Re = 3700$, but at a larger frequency $f_{KH} = 1.77\ D/U$ as expected. At this Reynolds, the shedding is weaker than at $Re = 3700$, i.e. the peak in the spectra is not as large as for $Re = 3700$ (see fig. 6.7(d)). Even though, the vortex-shedding signature is still observed at $f_{vs} = 0.195\ D/U$, which is slightly lower than for $Re = 3700$. This value is in agreement with experimental results [3, 18], where a decrease in the vortex-shedding frequency in the range of $Re = 6000 - 10000$ was measured. Beyond $Re = 10000$, experiments predict an asymptotic behaviour (with $f_{vs} = 0.2\ D/U$) of the main frequency up to the drag crisis at about $Re = 10^5$.

Besides the vortex shedding and the small-scale instabilities frequencies, another peak at a much lower frequency than that of the large-scale vortex shedding has been observed. The value of this low-frequency is $f_m\ D/U = 0.0178$ and it is captured at every position in the shear layer and the recirculation region, which denotes that is a phenomenon taking place within the formation region. Such low-frequency characteristics has been measured before in other bluff bodies such as in the flow past a circular disc, a normal flat-plate and a circular cylinder (see for instance [19, 20, 21] respectively). In the case of the sphere, it seems to be of less amplitude (i.e. less energetic) than for the other bluff bodies but still can be measured through energy spectra analysis. Tomboulides & Orszag [4], measured a value of $f_m = 0.045\ D/U$ at $Re = 500$, but they pointed out that it was insufficient temporal data to properly capture such low-frequency. Moreover, Constantinescu & Squire [22] observed a modulation in the drag coefficient signal for $Re = 10000$, but they could not solve its frequency due to the short statistical sampling (~ 10 vortex-shedding cycles). This low-frequency, usually reported as modulation frequency of the vortex-shedding, seems to be associated with a periodic shrinkage and enlargement of the vortex formation zone rather than to the rotation of the vortex separation point as it was su-

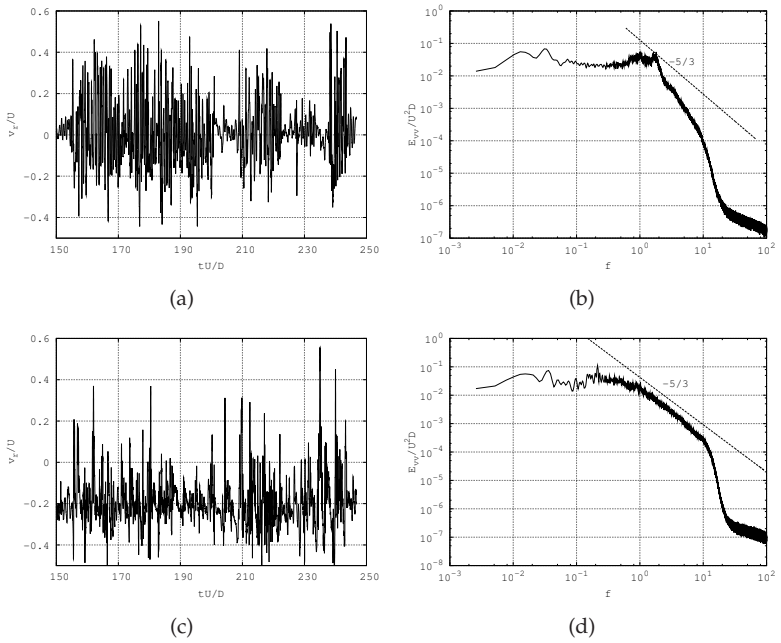

Figure 6.7: Radial velocity component and energy spectrum of its fluctuations at different locations behind the sphere at Reynolds number $Re = 10000$. a,b) At $x/D = 1.0$, $r/D = 0.6$, c,d) at $x/D = 2.0$, $r/D = 0.6$

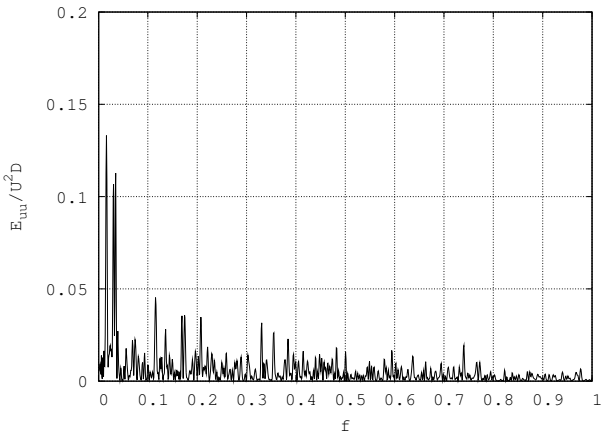

Figure 6.8: Power spectrum of the streamwise velocity fluctuations v'_x at $x/D = 3$, $r/D = 0$.

possed by Tomboulides & Orszag [4].

If the energy spectrum of streamwise velocity fluctuations at $x/D = 3$, $r/D = 0$ shown in figure 6.4(a) is analysed (see figure 6.8), it also exhibits a dominant peak at a very low frequency of $f_m\ D/U = 0.0178$. This is the same low-frequency found at locations of the shear layer, in especial at ($x/D = 2.4,\ r/D = 0.6$) and at ($x/D = 3, r/D = 0.6$). Just downstream the recirculation bubble at ($x/D = 3, r/D = 0.6$), it is expected to well capture this pumping motion of the recirculation zone. Thus, as the wake features are linked to this behaviour, special care must be taken when statistics in the recirculation region are computed. Hence, in order to include a few of these shrinkage/enlargement occurrences, statistical sampling might be a few times larger than $1/(f_m\ D/U)$ time units.

6.5.2 Coherent structures of the flow

An effective way to analyse the dynamics of the vortex formation region and the wake structure is to examine the instantaneous flow. There are several techniques for identifying coherent structures (see for instance [23, 24]). For the proper identification of the coherent structures of the flow the Q-criterion proposed by Hunt et al. [23] has been used. This method is based on the second invariant of the velocity gradient tensor $\nabla\mathbf{u}$. Definition and interpretations of the $\nabla\mathbf{u}$ invariants can be found in Chong et. al. [25]. The velocity gradient tensor can be decomposed into a symmetric (rate-of-strain, $\mathbf{S}$) and a skew-symmetric (rate-of-rotation, $\mathbf{\Omega}$) components. The

second invariant of $\nabla \mathbf{u}$ is,

$$Q = \frac{1}{2}(\| \mathbf{\Omega} \|^2 - \| \mathbf{S} \|^2) \tag{6.2}$$

where $\| \mathbf{\Omega} \|^2 = [Tr(\mathbf{\Omega}\mathbf{\Omega}^t)]$ and $\| \mathbf{S} \|^2 = [Tr(\mathbf{S}\mathbf{S}^t)]$, being $\mathbf{\Omega}$ and $\mathbf{S}$ the antisymmetric and symmetric components of the velocity gradient tensor $\nabla \mathbf{u}$. Positive values of Q means that vorticity prevails over strain, i.e. the strength of rotation overcomes the strain.

In order to explain the process of vortex-shedding, in figures 6.9 and 6.10, a sequence of four Q-iso-surface plots is presented for $Re = 3700$. This process is essencially the same as for $Re = 10000$, so for the sake of brevity it is only explained for $Re = 3700$. This sequence corresponds with the time evolution of the vortical structures in the wake of the sphere over a shedding cycle, viewed from two different azimuthal positions. Each panel of the figures depicts the wake of the sphere at each quarter period. Figure 6.9 corresponds to an arbitrary azimuthal position (e.g X-Y plane) and figure 6.10 is perpendicular to X-Y plane, viewed from the top.

An axisymmetric laminar boundary layer separates from the equator of the sphere, with a separation angle of $\varphi_s = 89.5°$ ($\varphi_s = 84.7°$ for $Re = 10000$). This separated shear layer remains laminar up to at a certain distance from the sphere where it becomes unstable. From the analysis of the instantaneous data, it has been observed that at about $x/D = 1 - 1.2$ the first instabilities in the shear layer appear. These instabilities occur, in first instance, as a consequence of the amplification of the small random disturbances introduced in the initial conditions. Due to these instabilities in the shear layer that appear randomly at any azimuthal location, the vortex sheet starts to roll-up, the flow becomes three-dimensional and results in a transition to turbulence. The zone where this transition occurs is located at about $x/D = 1.8 - 2.6$. The instabilities in the shear layer can be directly seen from the inspection of the time series of the radial velocity component in the laminar shear layer at $x/D = 1$, $r/D = 0.6$ at four azimuthal angles ($\theta = 0,\ \pi/2,\ \pi,\ 3\pi/2$) (see figure 6.11(a)). As can be observed, large velocity fluctuations occur randomly at all azimuthal position but at different time. These instabilities propagate in the shear layer and get amplified. As a consequence, in the zone where the transition to turbulence occurs, large velocity fluctuations are found at every azimuthal angle as shown in 6.11(b) ($x/D = 2.2$, $r/D = 0.6$). At $Re = 10000$ transition to turbulence occurs closer to the separation point at about $x/D = 1 - 1.2$, being in fair agreement with particle image velocimetry (PIV) observations of Jang & Lee [26] at $Re = 11000$. At this Reynolds number, although shear-layer instabilities also occurs at random azimuthal locations, they evolve into corrugated structures along the azimuthal direction at the end of the quasi-axialsymmetric shear-layer. These structures are formed by the interaction of the small-scales inside the recirculation bubble and the remnants of the

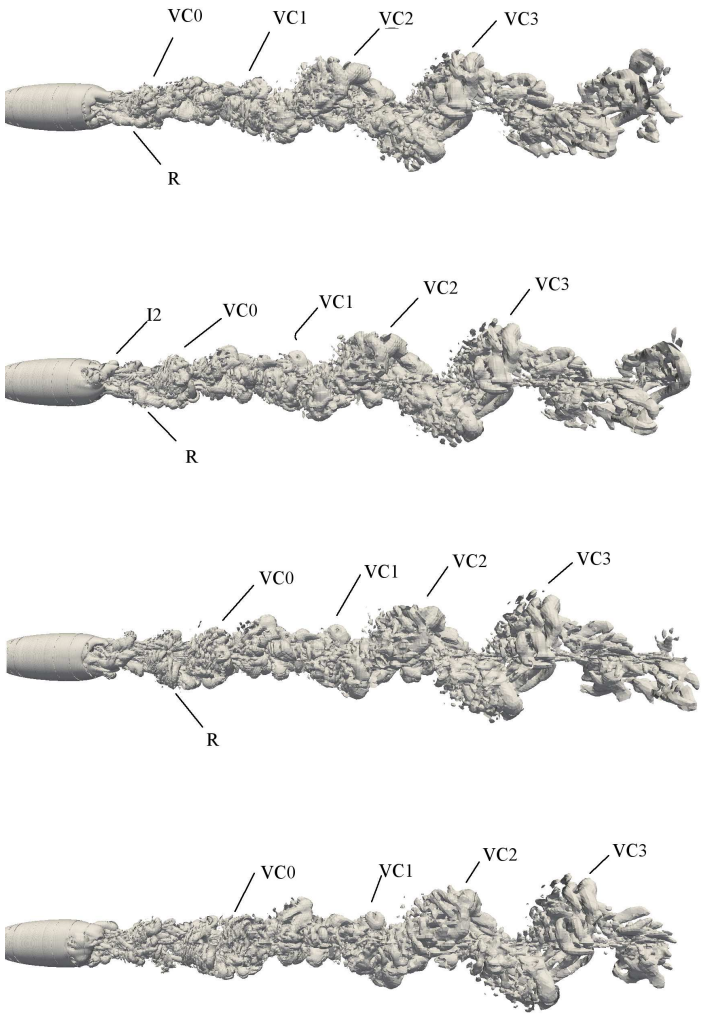

Figure 6.9: Vortical structures every quarter vortex shedding period (time advances from top to bottom). Plane X-Y

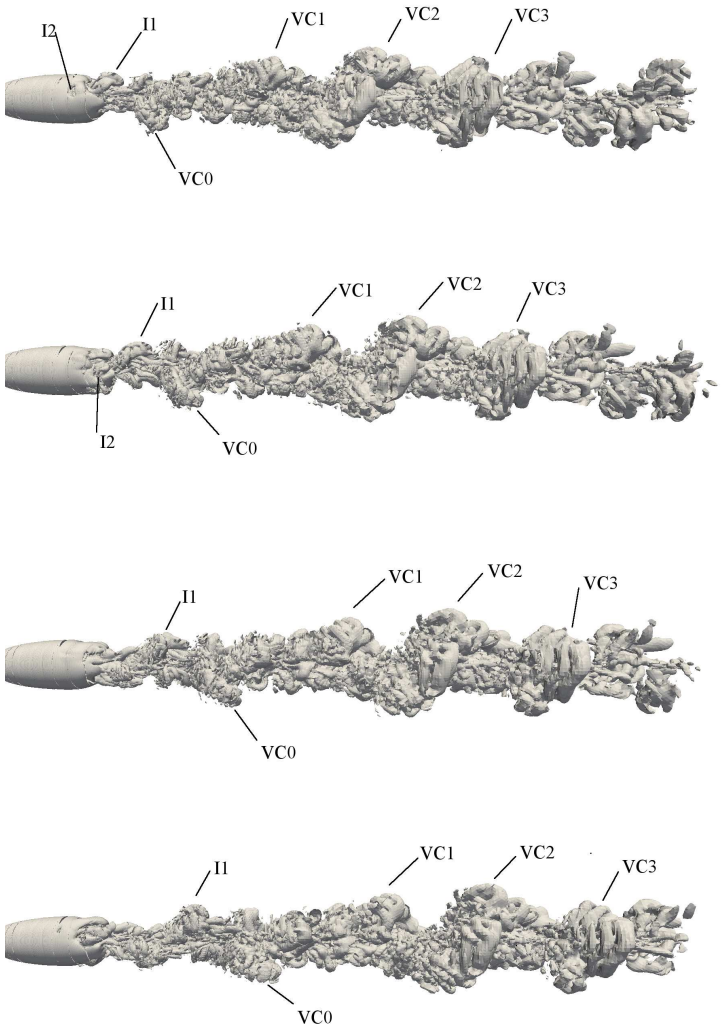

Figure 6.10: Vortical structures every quarter vortex shedding period (time advances from top to bottom). Plane perpendicular to X-Y plane, viewed from the top.

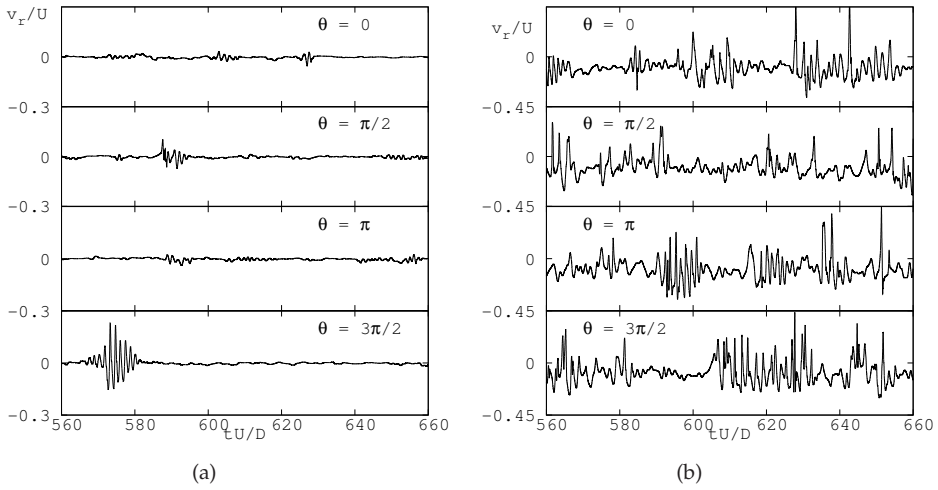

Figure 6.11: Time series of the radial velocity component at different locations in the shear layer and at four azimuthal angles ($\theta = 0,\ \pi/2\,\pi,\ 3\pi/2$) a) $x/D = 1$, $r/D = 0.6$; b) $x/D = 2.2$, $r/D = 0.6$

previous broken-off of the shear layer. As the flow moves downstream, these structures separate from the vortex sheet forming vortex rings.

As can be seen from the figures 6.9 and 6.10, there is a wide range of scales in the separated region, just behind the recirculation bubble and in the wake of the sphere. Vortex loops are detached from opposite positions, but they are not necessarily detached with 180° of separation. In the separated zone, the vortices formed break into small scale vortices which are drawn into the region behind the sphere (formation zone), but also they feed the turbulent wake. The large-scale vortices are not arranged in the same plane, but the wake exhibits a pronounced helical-like configuration as can also be observed from the general three-dimensional view of the wake in figure 6.12. This helical configuration was previously observed in experiments carried out by Achenbach [2] at $Re = 6000$ and by Taneda [27] at $Re = 10^4 - 3.8 \times 10^5$, and in numerical results at $Re = 10^4$ [22, 10]. In fact, in our results it can also be observed at $Re = 10000$ (see fig. 6.13). In the experimental observations of [2], he suggested that the vortex shedding occurs at a position around the sphere that rotates with the vortex shedding frequency. On the other hand, Taneda [27] observed an irregular rotation about the axis of the separation point and the wake. However, recent LES results from Yun et al. [10] showed that vortical structures travel downstream nearly straight, and they proposed that the helical-like structure might be

related to the wall-pressure changes in the sphere along the azimuthal direction.

From the examination of a large number of shedding cycles of the instantaneous data in the present simulation, it has been observed that shear layer instabilities occur at random position and the vortices are shed periodically in no particular azimuthal position. This gives the wake a helical appearance but the vortices move downstream without circulation in the azimuthal direction (see video). In fact, it can be argued that the observed helical pattern of the wake is due to the way the vortices are shed in time. At any shedding cycle, two anti-symmetric vortices are shed, but at the next shedding period, due to the randomness of the shear layer instabilities, the vortex shedding does not occur at the same azimuthal position of the previous one. Instead, these perturbations can produce vortices to be shed either to the left or to the right of the location of the previous vortex shedding. Thus, the handedness of the helical pattern is determined (in first instance) by the amplification of the random disturbances introduced in the initial conditions, but also the direction of the helix will vary in time due to the nature of the vortex shedding process.

Analysing the shedding cycle shown in the figures, the first panels depicts the shear layer in a stage just after the instability marked as I1 has grown and has broken off from the vortex sheet. Small instabilities in the axisymmetric shear layer are continuously appearing (e.g. the instability marked as I2). At the end of the axisymmetric bubble, corrugated structures along the azimuthal direction, can also be observed. These structures are induced by the action of the small-scales inside the recirculation bubble and the remnants of the previous broken off of the shear layer. A protruding structure (marked as VC0), which is the previous separated roller on the opposite side of the shear layer, and other vortices marked as VC1, VC2 and VC3 can also be noted. The second panels in the figures, correspond to a quarter period later, when the structure I1 has got amplified and has moved downstream. Of particular interest is the long rib structure (R) which is connected at one end with VC0 structure. The corrugated structures at the end of the vortex sheet are now more evident, as instability I2 has completely broken the shear layer in that azimuthal position. In the top view, small streamwise vortices which seem to be interlaced with vortex structure I1 can also be observed.

A quarter period later, which corresponds with third panels in figures 6.9 and 6.10, the vortex structure I1 has separated completely from the shear layer. The tail of the rib R has distorted in the azimuthal direction and has wrapped around itself, feeding the VC0 vortex, which has grown also fed by the small-scale vorticity from the recirculation bubble. The instability I2 has now separated from the shear layer and has grown as a new vortex structure opposite to I1. In the last quarter (bottom panels), the vortex structure I1 has moved downstream while the new vortex shed I2 is now in its final stage. Moreover, as a consequence of the pairing of vortices VC0 has become a larger structure.

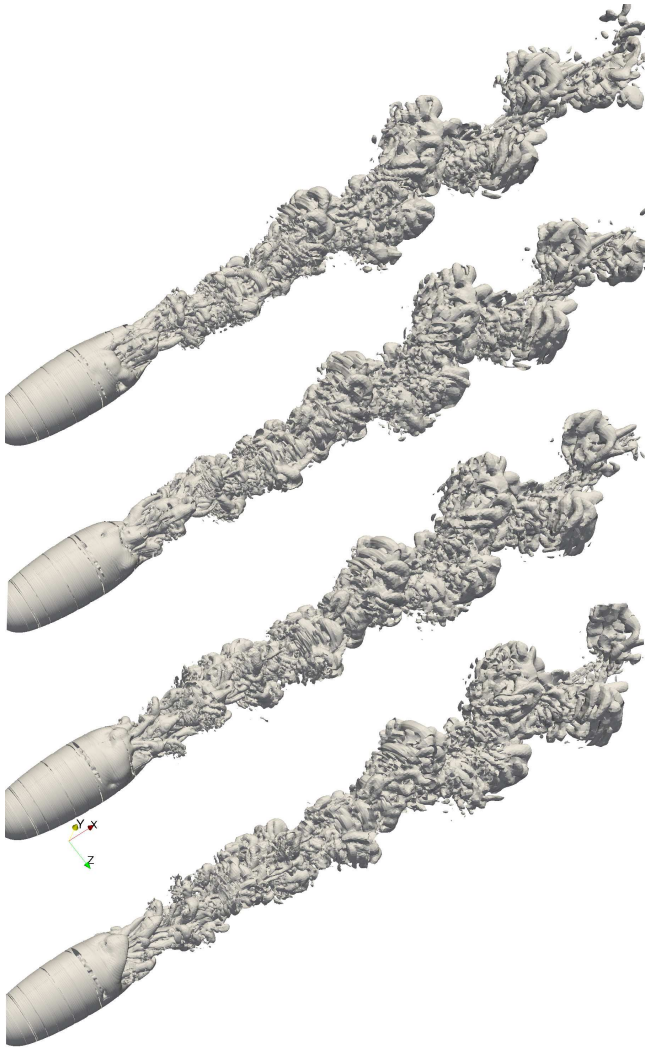

Figure 6.12: Visualisation of instantaneous vortical structures in the wake of the sphere (time advances from top to bottom).

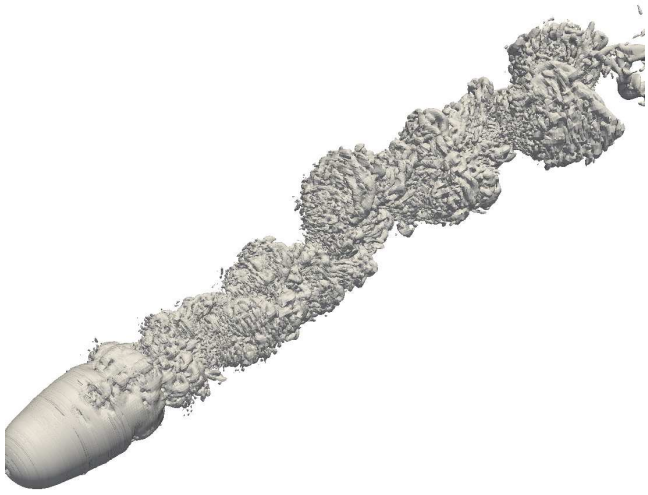

Figure 6.13: Visualisation of instantaneous vortical structures in the wake of the sphere by means of Q-iso-surfaces at Re=10000

The same shedding period shown in figures 6.9 and 6.10 is depicted in figure 6.12, but it offers a three-dimensional view of the helical pattern of the wake. Note also that large-scale structures are composed of about 3-4 azimuthal vortex rings, which is in agreement with the small-scale instability frequency f_{KH} measured. During the whole sequence, the large-scale structures such as VC1, VC2 and VC3 have moved uniformly downstream without change in their azimuthal position. As they travel downstream, the whole wake give the appearance of a wavy motion and, as has been commented before, it exhibits this helical-like configuration.

Due to the early transition in the shear-layer, recirculation bubble at $Re = 10000$ is shorter than for $Re = 3700$. In addition, turbulent structures become finer as the Reynolds number increases. If both figures are inspected in detail, one can observe that at $Re = 3700$ large-scale structures are formed by about 3-4 azimuthal vortex rings, while at $Re = 10000$ these structures are composed of about 9 of these azimuthal vortex rings. These observations are in fair agreement with the small-scale shear-layer instability frequency measured (see power spectra analysis section). That is, during a vortex-shedding period, instabilities at the separated shear-layer causes formation of vortex rings structures which are organised into large scale structures. As a consequence, the overall structure of the wake formed by the large-scale vortices is quite similar in both cases and exhibits a helical-like pattern. This is consistent

	St	φ_s (°)	$\overline{C_d}$	$\overline{C_{pb}}$	L_r/D	L_{SL}/D
	Re=3700					
Present work (DNS)	0.215	89.4	0.394	-0.207	2.28	2.75
Kim&Durbin [18] (exp)	0.225	-	-	-0.224	-	
Sakamoto&Haniu [3] (exp)	0.204	-	-	-	-	
Yun et al.[10] (LES)	0.21	90	0.355	-0.194	2.622	
Schlichting [14] (exp)	-	-	0.39	-	-	
	Re=10000					
Present	0.195	84.7	0.402	-0.272	1.657	1.8
Yun et. al. [10] (LES)	0.17	90	0.393	-0.274	1.364	
Constantinescu & Squires [11] (LES)	0.195	84-86	0.393	-	1.7	
Achenbach [1, 2] (exp)	0.195	82.5	0.4			

Table 6.2: Statistical flow features. DNS results compared with experimental measurements and numerical results from literature.

with previous experimental observations by Taneda [27] and Achenbach [1] among others.

6.6 Mean flow parameters

Table 6.2 summarises the results for the time-averaged integral parameters obtained and compared with experimental and numerical data available in the literature. In the table, the vortex-shedding frequency (Strouhal number) $St = f_{vs}\, U/D$, the separation angle φ_s (measured from the stagnation point), the drag coefficient Cp, the base-suction coefficient $-Cp_b$, the non-dimensional recirculation length L_r/D and the non-dimensional shear-layer length L_{SL} are presented. The recirculation length here is defined as the distance between the rear end of the sphere and the streamwise position along the axis where streamwise velocity changes sign. The length of the shear-layer has been defined, following the definition of Dong et al. [28], as the distance to the downstream location of a mean spanwise vorticity contour line at 8% of the maximum mean spanwise vorticity along the vertical line crossing $x/D = 0.0$.

There is a good agreement between computed flow parameters and previous results. As the Reynolds number increases, there is a shrinkage of the recirculation region. The recirculation bubble is about a 37% larger at Re=3700 than the value measured at Re=10000. This is an important shortening of this zone which clearly affects its configuration. The decrease in the recirculation zone (and thus, in the for-

mation length) is associated with the increase in the magnitude of the base-suction coefficient. The base-suction coefficient increases about 23 %, from $Cp_b = 0.207$ at $Re = 3700$ up to $Cp_b = 0.272$ at $Re = 10000$. This is also in agreement with the observations reported by Bearman [29] for the circular cylinder in the subcritical regime, i.e. the formation length is inversely proportional to the base-suction coefficient. The angular distribution of the mean pressure coefficient is plotted in figure D.1(a). In the figure, the mean pressure coefficient is compared with the experimental data by Kim and Durbin [18] at $Re = 4200$ and by Bakic [30] at $Re = 50000$. As can be seen, when comparing the DNS results a good agreement within experimental uncertainties have been obtained. The angular position of the pressure minimum has been well captured, being at $\varphi = 72^\circ$ for $Re = 3700$ and $\varphi = 71^\circ$ for $Re = 10000$. This value is also comparable with the position of the pressure minimum, $\varphi = 71^\circ$, reported by Seidl et al. [31] at $Re = 5000$. As observed, for both Reynolds numbers, the pressure distribution is quite similar except for the differences in the back region.

In contrast with the change in the base-suction coefficient, the average magnitude of the drag coefficient remains almost unaltered around $C_p = 0.4$ as in the subcritical regime ($Re < 3 \times 10^5$) the mean pressure coefficient is nearly independent of the Reynolds number [1]. The prediction of the average value of the drag coefficient for both Reynolds numbers is in fair agreement with the experimental measurements (see Table 6.2).

Also shown in the figure (see figure 6.14(b)) are the distribution of the non-dimensional skin-friction coefficient ($\tau_w/(\rho U^2 Re^{0.5})$) which is also compared with the DNS results of Seidl et al. [31]. Laminar separation occurs near at the equator of the sphere, but there is a slight displacement toward the stagnation point as the Reynolds increases of the detachment position ($\varphi_s = 90^\circ$ vs. $\varphi_s = 84^\circ$). This seems to be consistent with the experimental measurements of Achenbach [1], although there are no experimental measurements of this quantity for $Re = 3700$.

A further remark is about the value of the mean drag coefficient, $\overline{C_d} = 0.394$ is in correspondence with the value reported in experiments, $\overline{C_d} = 0.39$ (values summarised in [14]). This is also in agreement with observations that report a local minimum of the drag coefficient of $\overline{C_d} = 0.38$ at about $Re = 5000$ [31] with the further increase with the Reynolds number in the sub-critical regime approaching the drag crisis [14, 11]. However, when compared with the LES results by Yun et al. [10] some discrepancies are found. They predicted a lower value for the drag coefficient of $\overline{C_d} = 0.355$. It is important to highlight that computations performed with coarser grids of 3.63MCVs and 5.45 MCVs have shown little variation of the value of the mean drag coefficient $\overline{C_d}$ being of 0.39 and 0.399, respectively. Thus, differences with LES results might be attributed to the subgrid-scale model they have used.

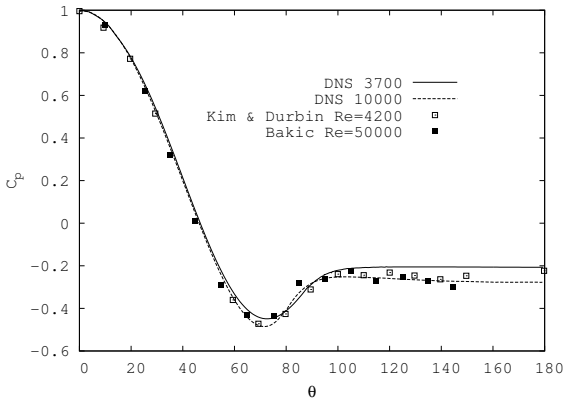

(a)

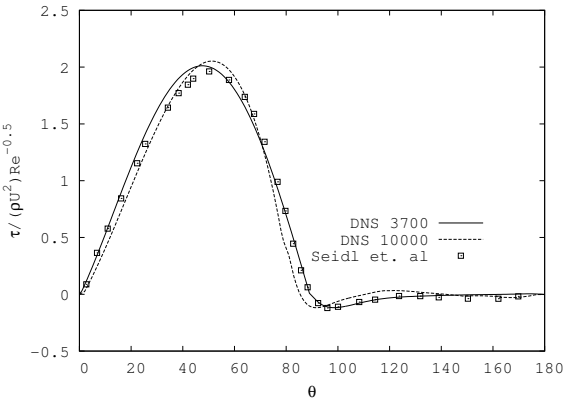

(b)

Figure 6.14: a) Angular distribution around the sphere of the mean pressure coefficient compared with experimental results of Kim and Durbin [18] at $Re = 4200$ and Bakic [30]. b) Angular distribution around the sphere of the skin-friction coefficient compared with experimental results of Seidl et al. [31] at $Re = 5000$.

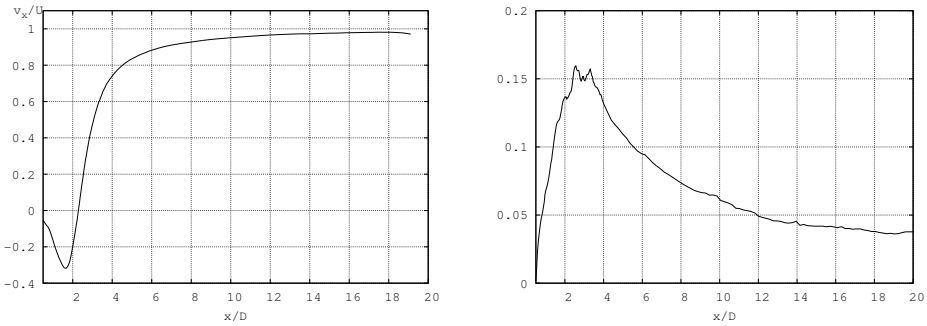

Figure 6.15: (a) Time-average streamwise velocity ($\overline{v_x}$) profile along the wake centreline. (b) Mean fluctuating streamwise velocity ($\overline{v_x'}$) along the wake centreline

6.6.1 Mean flow statistics

The average streamwise velocity ($\overline{v_x}$) normalised by the free-stream velocity U and its fluctuations ($\overline{v_x'}$) are given in figure 6.15 for $Re = 3700$. As can be seen from the figure 6.15(a) the length of the recirculation bubble, defined as the streamwise distance from the rear end of the sphere to the position where the mean streamwise velocity changes sign, is $L/D = 2.28$. This is nearly the same distance to the location where the fluctuations of the streamwise velocity reaches its maximum, i.e. the vortex formation zone, as [32] pointed out. In fact, figure 6.15(b) shows the presence two large peaks. The first one is more pronounced and its maximum occurs at $x/D = 1.98$ measured from the rear end of the sphere, while the second one takes place at $x/D = 2.81$. Some discrepancies with the previous LES modelling work by [10] are observed in the prediction of the recirculation length (see Table 6.2). These differences are also reflected when the profile of the mean streamwise velocity in the wake is compared with both experimental data of [18] and LES modelling [10] results (see figure 6.16). A good agreement between our DNS results and the experimental data is obtained. However, noticeable differences are observed when compared with the mentioned LES results. These discrepancies are more relevant at $x/D = 3$ where, according to our DNS and the experimental measurements, the flow is in the recovery zone (i.e. the region between the end of the recirculation bubble and the location where the flow accelerates in spite of the adverse pressure gradient). However, for LES results by [10] the profile shows that the flow is at the end of the recirculation bubble.

Time-averaged profiles of the streamwise and radial velocities at five different locations ($x/D = 1.6$, 2, 3, 5, 10) in the wake are plotted in figure 6.17 for $Re =$

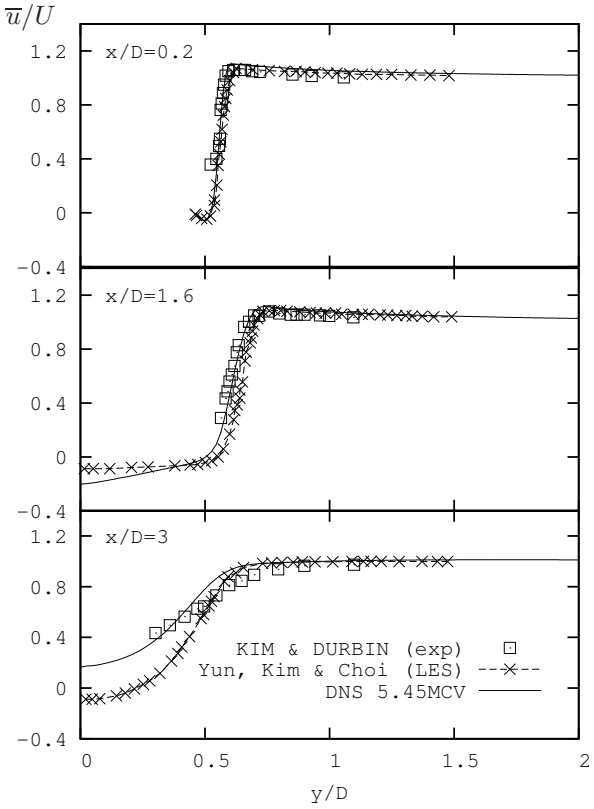

Figure 6.16: Streamwise velocity at three locations in the wake. Comparison of the DNS results with experiments of [18] and LES solution of [10].

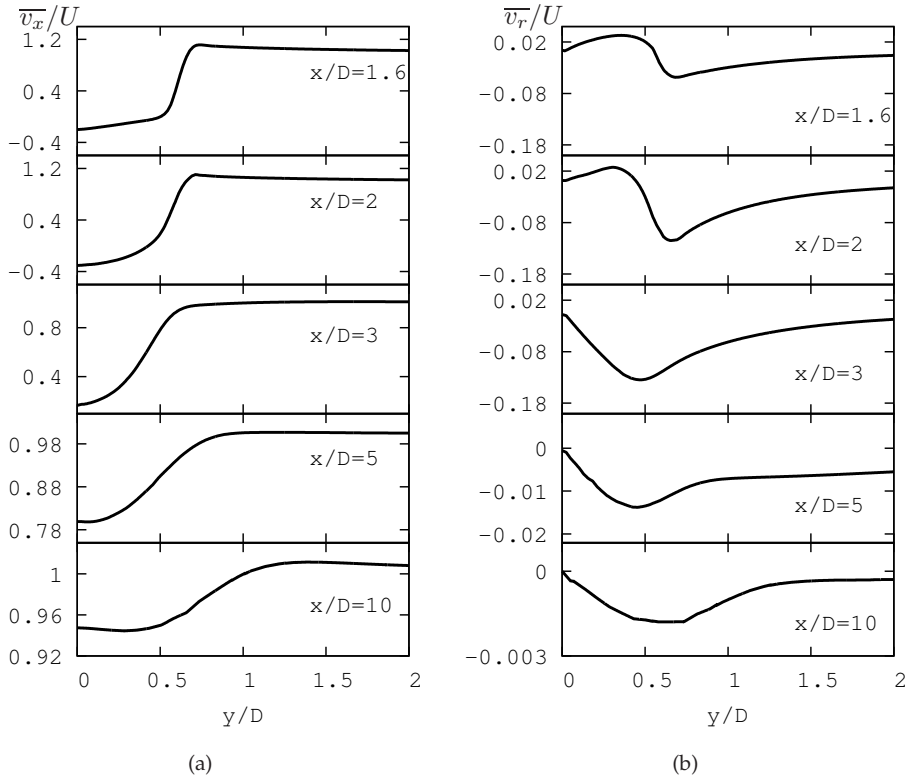

Figure 6.17: Mean velocity profiles at different positions in the wake behind the sphere at plane $[x/D, y/D, z = 0]$. a) streamwise velocity $\overline{v_x}/U$, b) radial velocity $\overline{v_r}/U$

3700. The negative streamwise velocity at $x/D = 1.6$ and $x/D = 2$ stems from the recirculation zone. In the wake behind the sphere, $\overline{v_x}$ is negative until the free-stagnation point. At $x/D = 3$ streamwise velocity is positive but near zero, since this position is very close to the end of the recirculation bubble. The minimum value of the radial velocity occurs on the side of the free-stagnation point and its value is $\overline{v_r} = -0.198\,U$. The largest backward velocity (minimum streamwise velocity) in the recirculation bubble is $\overline{v_x} = -0.321\,U$ according to figure 6.15(a).

In addition to these plots, time-average profiles of the streamwise velocity and its fluctuations at $x/D = 1.6$ and $x/D = 2.5$ are compared for both Reynolds numbers in figure 6.18. The negative values of the streamwise velocity stem for the recirculation bubble. Its minimum value $v_x = -0.321$ at $x/D = 2.13$ for $Re = 3700$ ($v_x = -0.404$

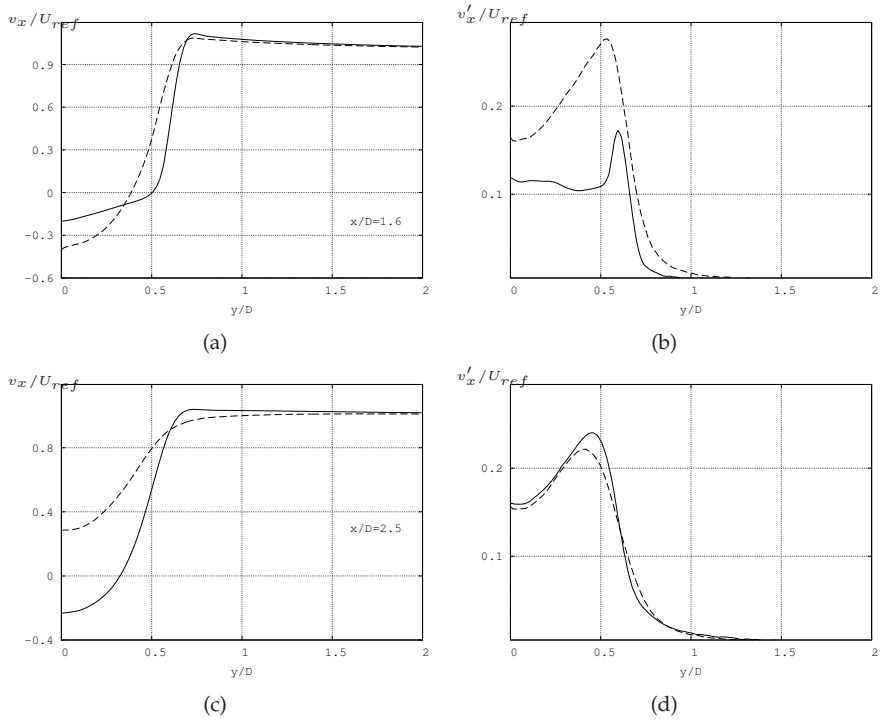

Figure 6.18: Flow statistics in the near wake at $x/D = 1.6$ and $x/D = 2.5$. (a, c) Mean streamwise velocity; (b, d) fluctuations of the mean streamwise velocity. (Solid line) $Re = 3700$, (dotted line) $Re = 10000$.

at $x/D = 1.56$ for $Re = 10000$) occurs at the wake axis. Note that the velocity deficit in the wake increases with the Reynolds number. As commented before, fluctuations for $Re = 10000$ are also larger within the recirculation zone. As there is a shrinkage of this zone, at $x/D = 2.5$ the flow at $Re = 10000$ is in the recovery region (the zone beyond the recirculation region where the flow accelerates in spite of the adverse pressure gradient) while for $Re = 3700$ it is still within the recirculation bubble.

The wake mean flow configuration for both Reynolds numbers is depicted in figure 6.19. In the figure, comparative contours of stream-wise ($\overline{v'_x v'_x}$), cross-flow ($\overline{v'_r v'_r}$) and shear stresses ($\overline{v'_x v'_r}$) are depicted. These representations of the Reynolds stresses distribution reveal the near wake structure associated with the changes in the base-suction coefficient. At $Re = 3700$, the recirculation region is relative large (see also table 6.2) while a shortening of this zone occurs with increasing Reynolds

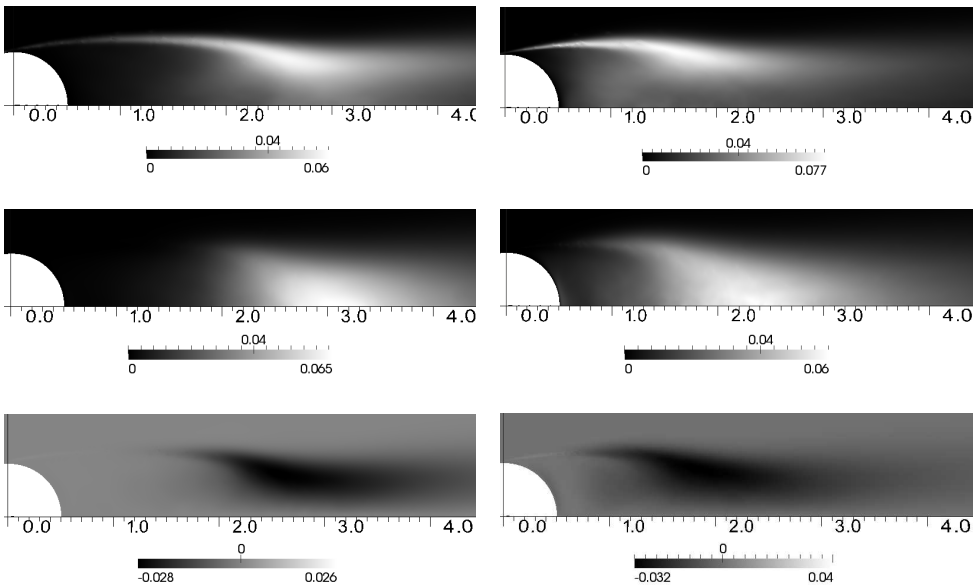

Figure 6.19: Topology of the Reynolds stresses in the near wake (left) $Re = 3700$ and (right) $Re = 10000$. From top to bottom: $\overline{v'_x v'_x}/U^2$; $\overline{v'_r v'_r}/U^2$; $\overline{v'_x v'_r}/U^2$. 10 contours levels from: (left) 0.00552-0.0555; 0.0068-0.068 and $-0.028 - -0.0032$, respectively; (right) 0.00552-0.0555; 0.0068-0.068 and $-0.028 - -0.0032$, respectively.

number up to $Re = 10000$. Indeed, peaks in the stresses are displaced upwards a distance between 0.75D - 1D, and their levels are found to be higher at $Re = 10000$. The streamwise turbulent stress peaks at the shear-layer at $x/D = 2.61$ for $Re = 3700$ (and $x/D = 1.64$ for $Re = 10000$) at the region where it began to curve towards the wake centreline, around the end of the vortex formation length. As for the cross-flow stress, its maximum is located at the wake centreline just after the closure of the recirculation bubble (at $x/D = 3.1$ for $Re = 3700$ and $x/D = 2.35$ for $Re = 10000$). On the other hand, the shear stress which exhibits a one-lobe structure off the axis peaks before the closure of the recirculation bubble ($\overline{v'_x v'_r} = -0.029$at $x/D = 2.56$ for $Re = 3700$ and $\overline{v'_x v'_r} = -0.033$ at $x/D = 1.78$ for $Re = 10000$). Furthermore, mean velocity fluctuations $\overline{v'_x}/U$ and $\overline{v'_r}/U$ are plotted in figure 6.20 for $Re = 3700$.

The variation of the mean turbulent kinetic energy and the energy dissipation rate are depicted in figures 6.21 and 6.22 for both Reynolds numbers. For comparison, both quantities are plotted at locations which are the same when normalised

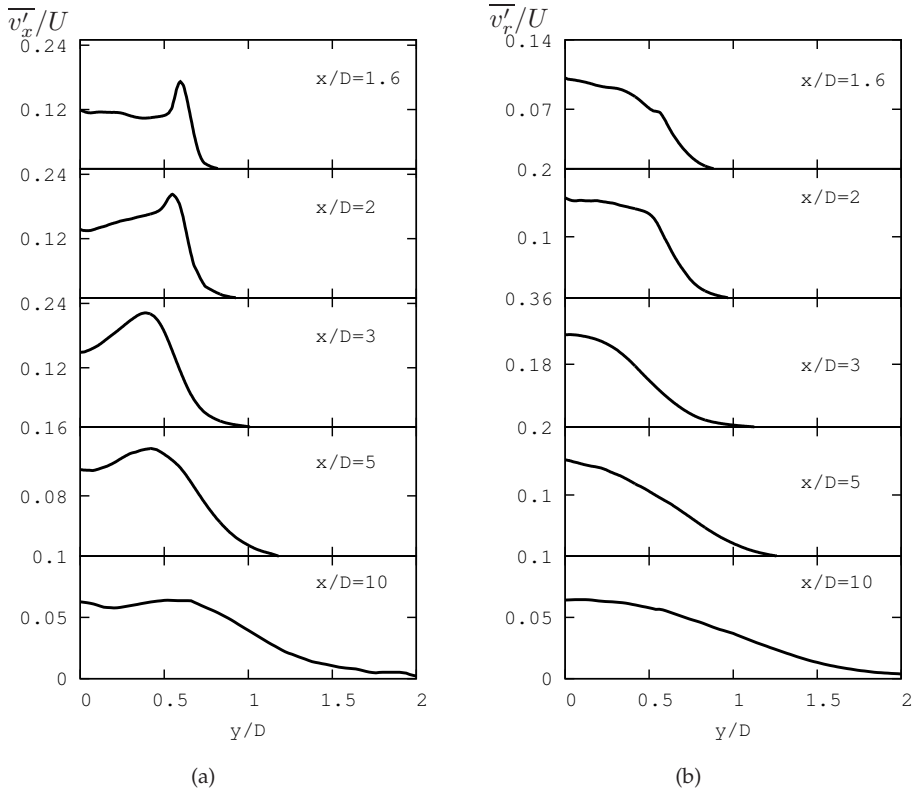

Figure 6.20: Mean velocity fluctuations at different positions in the wake behind the sphere at plane $[x/D, y/D, z = 0]$. a) streamwise velocity fluctuations $\overline{v'_x}/U$, b) radial velocity fluctuations $\overline{v'_r}/U$

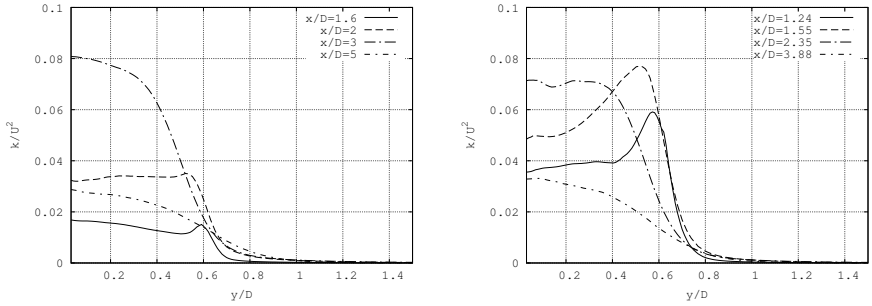

(a) (b)

Figure 6.21: Mean turbulent kinetic energy. a) $Re = 3700$, b) $Re = 10000$

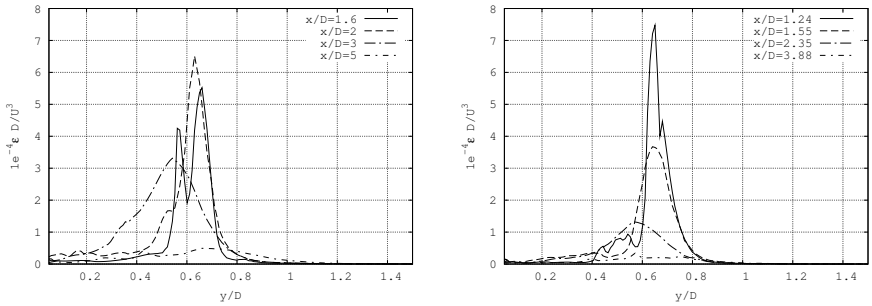

(a) (b)

Figure 6.22: Energy dissipation rate. a) $Re = 3700$, b) $Re = 10000$

with the recirculation length. Turbulent kinetic energy (tke) is mostly produced in the shear layers due to the contribution of the streamwise fluctuations and then, it is convected to the centre of the wake. However, the topology of the wake is slightly different at $Re = 3700$ and $Re = 10000$. At $Re = 3700$, tke peaks at the wake centreline just after the closure of the recirculation bubble, whereas at $Re = 10000$, tke maximum is displaced to a location off the wake centreline, near the position where the shear layer curves toward the axis.

The largest dissipation occurs in the shear layer (see figure 6.22) and then, it decays rapidly as the flows moves downstream. It is worth to mention, that most of the tke produced in the shear layer can be associated with the small-scale instabilities and thus, it contributes to dissipation. On the other hand, towards the wake centreline, tke produced is only partially dissipated but also it is advected downstream.

6.7 Conclusions

Direct numerical simulations of the turbulent flow past a sphere at Reynolds numbers of 3700 and 10000 have been carried out. Second-order conservative discretisation schemes on a collocated unstructured arrangement have been used. These schemes preserve the kinetic energy balance even on coarse grids ensuring good stability. The main features of the flow, including instantaneous and time-average flow structure, and energy spectra at selected locations in the near wake have been presented and compared.

Computations carried out have allowed to analyse the influence of shear-layer vortices and vortex shedding process in the wake configuration at these subcritical Reynolds numbers. The instantaneous analysis of the wake has revealed that its structure is quite similar at both Reynolds numbers, i.e. it exhibits a helical-like configuration due to the instabilities in the shear layer which occur at random azimuthal positions. However, significant differences in the flow dynamics have also been observed. At $Re = 3700$, the onset of the vortex roll-up due to instabilities in the shear layer occurs locally which determines the position where the vortex are shed, but at $Re = 10000$, shear-layer instabilities evolve as corrugated structures along the azimuthal direction which separate from the shear-layer as vortex rings. With the increase in the Reynolds number, these instabilities move closer to the separation point with the consequent shrinkage of the vortex formation region. It has been observed, that similar to the wake behind a cylinder, variations in the vortex formation region are related to the base-suction coefficient C_{pb}, i.e., as the base-suction increases the formation region is shortened.

It is shown how the wake is dominated by three instability mechanisms: the large-scale vortex-shedding at a frequency f_{vs}, the small-scale Kelvin-Helmholtz instabilities of the shear-layer at f_{KH} and the modulation of the recirculation region which occurs with a frequency f_m. The values of these characteristics frequencies have been discussed in the paper for both Reynolds numbers. Each of these mechanisms leave a clear footprint in the turbulent spectra of the different probes analysed. The latter of them can be identified as a mechanism through which low-frequency large-scale flow affects the underlying turbulence and consequently, the wake characteristics. As a result of the wake modulation, large integration times are required to capture properly the shrinkage and enlargement of the recirculation region and hence, to achieve well converged statistics in the wake zone. Although this modulation have been observed previously, there are still issues that remains unclear such as the wake configuration during the different stages of this process. Further investigations would be useful.

Furthermore, the topology of the near wake for both Reynolds numbers are compared in terms of the average second-order statistics. The average recirculation zone is decreased with increasing Reynolds number, as expected. As a result, maximum

values of the Reynolds stresses are displaced upwards a distance between 0.75 - 1 diameter, consistent with the variations in the magnitude of the base-pressure coefficient.

References

[1] E. Achenbach. Experiments on the flow past spheres at very high Reynolds numbers. *Journal of Fluid Mechanics*, 54:565–575, 1972.

[2] E. Achenbach. Vortex shedding from spheres. *Journal of Fluid Mechanics*, 62(2):209–221, 1974.

[3] H. Sakamoto and H. Haniu. A study on vortex sheding from spheres in an uniform flow. *Journal of Fluids Engineering*, 112:386–392, 1990.

[4] A. Tomboulides and S.A. Orszag. Numerical investigation of transitional and weak turbulent flow past a sphere. *Journal of Fluids Mechanics*, 416:45–73, 2000.

[5] R. Mittal and F.M. Najjar. Vortex dynamics in the sphere wake. *AIAA paper 99-3806*, 1999.

[6] T. A. Johnson and V. C. Patel. Flow past a sphere up to a Reynolds number of 300. *Journal of Fluid Mechanics*, 378:19–70, January 1999.

[7] I. Rodríguez, R. Borrell, O. Lehmkuhl, A. Oliva, and C.D. Pérez-Segarra. Direct numerical simulation of the flow over a sphere at Re = 3700. In *Turbulence, Heat and Mass Transfer*, 2009.

[8] Ananias G. Tomboulides, SA Orszag, and George Em Karniadakis. Direct and large-eddy simulations of axisymmetric wakes. *AIAA paper 93-0546*, 1993.

[9] M Torlak, G Jensen, and I. Hadžić. Large-eddy Simulation of Incompressible Flow Around a Sphere with Trip Wire at Re= 50 000. In *High Performance Computing in Science and Engineering*, pages 189–200. Springer, 2005.

[10] G. Yun, D. Kim, and H. Choi. Vortical structures behind a sphere at subcritical Reynolds numbers. *Physics of Fluids*, 18, 2006.

[11] G. Constantinescu, M. Chapelet, and K. Squires. Turbulence modeling applied to flow over a sphere. *AIAA Journal*, 41(9):1733–1741, 2003.

[12] M. Soria, C.D. Pérez-Segarra, and A. Oliva. A direct Schur-Fourier decomposition for the solution of three-dimensional Poisson equation of incompressible flow using loosely coupled parallel computers. *Numerical Heat Transfer, Part B*, 43(5):467–488, 2003.

[13] R. Borrell, O. Lehmkuhl, F.X. Trias, and A. Oliva. Parallel direct poisson solver for discretisations with one fourier diagonalisable direction. *Computational Physics*, 230(12):4723–4741, 2011.

[14] H. Schlichting. *Boundary Layer Theory*. McGraw-Hill, Inc., Seventh Ed, 1979.

[15] P. Moin and Krishnan Mahesh. DIRECT NUMERICAL SIMULATION: A Tool in Turbulence Research. *Annual Review of Fluid Mechanics*, 30(1):539–578, 1998.

[16] S.B. Pope. *Turbulent Flows*. Cambridge University Press, 2000.

[17] A. Prasad and C.H.K. Williamson. The instability of the shear layer separating from a bluff body. *Journal of Fluid Mechanics*, pages 375–492, 1997.

[18] H.J. Kim and P.A. Durbin. Observations of the frequencies in a sphere wake and of drag increase by acoustic excitation. *Physics of Fluids*, 31(11):3260–3265, 1988.

[19] E. Berger, D. Cholz, and M. Schumm. Coherent vortex structures in the wake of a sphere and a circular disk at rest and under forced vibrations. *Journal of Fluids and Structures*, 4(3):231–257, 1990.

[20] F M. Najjar and S. Balachandar. Low-frequency unsteadiness in the wake of a normal flat plate. *Journal of Fluid Mechanics*, 370:101–147, September 1998.

[21] J.J.Miau, J.T. Wang, J.H. Chou, and C.Y.Wei. Characteristics of the low-frequency variations embedded in vortex shedding process. *Journal of Fluids and Structures*, 13:339–359, 1999.

[22] G. Constantinescu and K. Squires. Numerical investigations of flow over a sphere in the subcritical and supercritical regimes. *Physics of fluids*, 16(5):1449–1466, 2004.

[23] J.C.R. Hunt, A.A. Wray, and P. Moin. Eddies, stream and convergence zones in turbulent flows. Technical Report CTR-S88, Center for turbulent research, 1988.

[24] J. Jeong and Hussain Fazle. On the identification of a vortex. *Journal of Fluids Mechanics*, 285(69–94), 1995.

[25] M. S. Chong, a. E. Perry, and B. J. Cantwell. A general classification of three-dimensional flow fields. *Physics of Fluids A: Fluid Dynamics*, 2(5):765, 1990.

[26] Y.I Jang and S.J Lee. Visualization of turbulent flow around a sphere at subcritical Reynolds numbers. *Journal of Visualization*, 10(4):359–366, 2007.

[27] S. Taneda. Visual observations of the flow past a sphere at Reynolds numbers between 10^4 and 10^6. *Journal of Fluids Mechanics*, 85(1):187–192, 1978.

[28] S. Dong, G. E. Karniadakis, a. Ekmekci, and D. Rockwell. A combined direct numerical simulation-particle image velocimetry study of the turbulent near wake. *Journal of Fluid Mechanics*, 569:185, 2006.

[29] P. W. Bearman. Investigation of the flow behind a two-dimensional model with a blunt trailing edge and fitted with splitter plates. *Journal of Fluid Mechanics*, 21:241–255, 1965.

[30] V. Bakic. *Experimental investigation of turbulent flows around a sphere*. PhD thesis, Technischen Universität Hamburg-Harburg, 2002.

[31] V. Seidl, S. Muzaferija, and M. Peric. Parallel DNS with local grid refinement. *Applied Scientific Reseach*, 59:379–394, 1998.

[32] C. Norberg. Ldv measurements in the near wake of a circular cylinder. In *Bearman PW, Williamson CHK (eds) Proceedings of the ASME conference on advances in the understanding of bluff body wakes and vortex induced vibration. Washington, DC*, 1998.

Chapter 7

Direct numerical simulation of the turbulent flow past a circular cylinder

Most of the contents of this chapter have been published as:

O. Lehmkuhl, I. Rodríguez, R. Borrell, C.D. Pérez-Segarra and A. Oliva. Low-frequency variations in the wake of a circular cylinder at $Re = 3900$. Journal of Physics: Conference Series. 318, 042038. doi:10.1088/1742-6596/318/4/042038.

Abstract. The presence of low-frequency fluctuations in the wake of bluff bodies have been observed in several investigations. Eventhough the flow past circular cylinder at $Re_D = 3900$ ($Re_D = U_{ref} D/\nu$) has been object of several experimental and numerical investigations, there is a large scattering in the average statistics in the near wake. In the present work, the flow-dynamics of the near-wake region behind a circular cylinder has been investigated by means of DNS and statistics have been computed for more than 858 shedding cycles. The analysis of instantaneous velocity signals of several probes located in the vortex formation region, point out the existence of a low-frequency fluctuation at $f_m = 0.0064$. This large-scale quasi-periodic motion registered seems to be related with the modulation of the recirculation bubble which causes its shrinking and enlargement over the time. Two different configurations have been identified: i) a high-energy mode with larger fluctuations in the shear-layer and in the vortex formation region (Mode H) and ii) a low-energy mode with weaker fluctuations in the shear layer (Mode L). The influence of such low-frequency in the wake topology has been studied by means of the phase-average flow field considering 10 cycles of vortex-shedding for each mode, but also by the analysis of the time-average first- and second-order statistics of each wake mode. The results are compared with the long-term averaged solution and with the literature available results.

7.1 Introduction

The flow over a circular cylinder has been subject of several numerical and experimental studies. From a theoretical point of view, this is a canonical case to perform studies of the turbulence behavior of these regions and to learn how they interact between them. On the other hand, from a practical point of view, this case is also of interest since flow around cylindrical structures is of relevance for many practical applications i.e. heat exchangers, bridge piers, chimneys, towers, antennae, wires... Knowledge about flow-related unsteady loading of such structures is crucial for hydro and aerodynamic control and design.

As it is well known from experimental observations, the flow around a cylinder exhibits different behaviors depending on the Reynolds number. Steady laminar flows exists at Reynolds numbers up to approximately 40 (based on the cylinder diameter and free-stream velocity) with a pair of steady dipole vortices forming behind the cylinder. The laminar vortex shedding, also known as the von-Karman vortex street, is observed at Reynolds numbers up to about 190. When the Reynolds number is approximately 260, the flow experiences transition to finer scale three dimensionality (also named as mode B instability) [1]. With increasing Reynolds number, the three dimensional cylinder wake becomes more chaotic. Finally, according to Prasad and Williamson [2], the shear layers separating from the cylinder become unstable at Reynolds number around 1200.

However, the value of this critical Reynolds number varies in the literature from 300 to 3000. It is believed that the separating shear layers are very sensitive to various experimental factors such as free-stream turbulence level, acoustic noise, cylinder vibrations, end boundary conditions and aspect ratio (spanwise direction length / cylinder diameter) [3]. A dramatic decrease in the base suction coefficient occurs between Reynolds numbers 2×10^5 and 3.5×10^6; this is associated with a complicated flow regime with laminar separation, transition to turbulence, reattachment, and another separation further downstream along the cylinder surface. At post-critical Reynolds numbers beyond 3.5×10^6, the boundary layer on the cylinder becomes turbulent before separation [4].

In the case of the flow past a circular cylinder at $Re_D = 3900$, it has been have been extensively investigated (see for instance [5, 6] and the citations therein). Even though the several studies carried out, there is a large scattering in the mean flow solutions in the near wake (see figure 7.1) which seems to converge into the same solution as the flow moves downstream. These differences in the near wake are also observed as different mean flow configurations of the stream-wise velocity usually referred as U-shape and V-shape profiles. According to Ma et al. [5], both states reflect the dynamics of the flow in the very near wake which is very sensitivity to disturbances and they concluded that U-shape profile emerges if the background fluctuations are relatively low or the span-wise extend the domain is small ($L_z/D =$

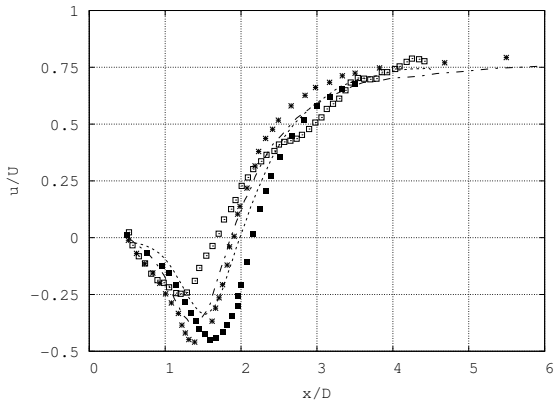

Figure 7.1: Stream-wise velocity at the wake centerline. (dotted line) Parnaudeau et al. [6]; (squares) Lourenco & Shih [7]; (dash-dotted line) Kravchenko & Moin [7]; (solid squares) Norberg $Re = 3000$; (stars) Norberg $Re = 5000$ [8].

π).

However, Ma et al. [5] observations are in disagreement with the results of other investigations in which a $L_z/D = \pi$ for the span-size were used. Franke & Frank [9], showed that average statistics in the wake of the cylinder would require a large integration time. They presented results for about 200 time-units but commented that it was not enough for obtaining converged statistics. Yet, they pointed out that their solution approached to that of Ma et al. [5] for the corresponding span-wise width ($L_z/D = \pi$). In addition, Tremblay et al. [10] by means of DNS and using an span-wise size of πD obtained the characteristic V-shape profile (with 300 time-units of time integration) contradicting the hypothesis of Ma et al. [5] about the span-wise size. Indeed, they observed that the shape of the stream-wise velocity profile developed from U towards V as longs as the recirculation length was not settled down to a stable state. More recently, [6] performed experimental and numerical studies and found that about 1200 time-units (250 shedding cycles) were required for obtaining a converged value but in their case the obtained solution shown a U-shaped stream-wise velocity profile.

All these studies pose the question about how the unsteady behaviour of the vortex formation region affects the near wake configuration. However, to the best of our knowledge, there is no a complete study of the convergence of flow statistics in the very near wake. On the other hand, low-frequency variations in the wake of bluff bodies have been observed by several investigations. Berger et al. [11] studied the formation of coherent structures in a wake of a disk and a sphere at Reynolds

numbers between $1.5 \times 10^4 < Re < 3 \times 10^5$, and found what they called a pumping mechanism of the recirculation bubble with a very low-frequency. Najjar & Balachandar [12] also observed a low-frequency unsteadiness in the wake of a normal flat plate, finding a high-drag regime with high coherence in the span-wise vortices and a low-mean drag regime where less coherent vortices were formed. Later, Miau et al. [13] found such variations in the wake of a trapezoidal cylinder and a circular cylinder at Reynolds numbers above 10^4 and shown that they were associated with the unsteady variations of the vortex formation length. Wu et al [14] studied the low-frequency fluctuations of the wake behind a normal plate confirming the existence of the two modes pointed out by Najjar & Balachandar [12], but at the Reynolds numbers of their experiments they found an asymmetry in the time where these modes occurred. In fact, they detect that the most energetic one, with a shorter vortex formation region, only occurred during the 5% of the total measured time. In the case of the sphere, the existence of such low frequency modulation has been recently measured by Rodriguez et al. [15] by means of DNS at $Re = 3700$.

This low-frequency behavior might be the responsible of the large scattering of the statistical data in the wake of the circular cylinder, but this issue appear to be still open. In this paper we report on detecting the low-frequency unsteadiness of the vortex formation region past a circular cylinder at $Re_D = UD/\nu = 3900$ (based on the free-stream velocity and the cylinder diameter). Thus, the main focus of this work is on the low-frequency modulation of the recirculation zone, to examine its possible influence on the wake configuration, as well as, to derive more time-accurate flow parameters and first- and second-order statistics. In this work we perform a comprehensive time series analysis by utilizing data from several probes located at different stations in the shear-layers and in the near wake. By means of the analysis of the power spectra of these probes, it has been found the co-existence of two different wake configurations which alternates with a very low-frequency. In order to study the influence of such low-frequency in the wake topology, the phase-average flow field considering 10 cycles of vortex-shedding for each mode has been computed. After that, time-average first- and second-order statistics of each wake mode have been compared with the long-term averaged solution (of about 4000 time-units) and with the literature available results.

7.2 Description of numerical method

The governing equations have been discretized on a collocated unstructured grid arrangement, by means of second-order spectro-consistent schemes [16]. Such schemes are conservatives, i.e., they preserve the symmetry properties of the continuous differential operators, and ensure both, stability and conservation of the global kinetic-energy balance on any grid. For the temporal discretisation of the momentum equa-

tion a two-steps linear explicit scheme on a fractional-step method has been used for the convective and diffusive terms [17], while for the pressure gradient term an implicit first- order scheme has been used. This methodology has been previously used with accurate results for solving the flow over bluff bodies with massive separation in [18] and [15].

The meshes used for solving the domain considered have been generated by a constant step extrusion of a two-dimensional (2D) unstructured grid. Under these conditions, the span-wise coupling of the discrete Poisson equation, which results from the incompressibility constrain, yields circulant sub-matrices that are diagonalizable in a Fourier space. This allows to solve the Poisson equation by means of a Fast Fourier Transform (FFT) method. The algorithm used is based on the explicit calculation and direct solution of a Schur Complement system for the independent 2D systems. For more details the reader is referred to [19].

7.3 Problem definition and computational domain

The methodology used for solving the flow over bluff bodies with massive separation is described in [18] and [15]. We consider here the DNS of the flow past a circular cylinder at $Re_D = 3900$. Although several computations have been carried out considering different domain sizes and computational grids, for the sake of brevity, the results presented in this paper have been obtained using a computational domain of dimensions [-8D,16D];[-10D,10D];[0,πD] in the stream-, cross- and span-wise directions respectively, with a circular cylinder of diameter D at (0,0,0). As for the span-wise size of the domain, in a previous study [18] it was shown than doubling the domain in the span-wise direction was not influence the statistical data. As the main concern of the present work is about the low-frequency variations in the near wake and on the time-dependence of turbulent statistics, it is required a large integration time. Hence, the computational effort has been focused on the long-term average statistics instead of a larger span-wise domain. Furthermore, although not for comparison, simulations with twice the span-wise size and twice the number of planes in the span-wise direction have also been considered. In all of them we have detected the low-frequency fluctuation of the recirculation bubble. Therefore, this phenomena is not dependent on the span-wise size of the domain, but it is an intrinsic characteristic of the recirculation zone.

The boundary conditions at the inflow consist of a uniform velocity (u,v,w)=(1,0,0), slip conditions in the top and bottom boundaries of the domain, while at the outlet a pressure-based condition is used. At the cylinder surface, no-slip conditions are prescribed. As for the span-wise direction, periodic boundary conditions are imposed. As mentioned before, the governing equations are discretised on an unstructured mesh generated by the constant-step extrusion of a two-dimensional un-

structured grid. The use of an unstructured grid for the plane has allowed to cluster more control volumes around the cylinder surface and in the near wake. As it has been commented, several grids have been considered, but for brevity the results presented here have been computed with a grid of about 9.3 M CVs (72700×128). In a-posteriori analysis of the grid sizes used, we have calculated the Kolmogorov length scale which gives ($x/D < 5$) $\overline{\eta}/D = 0.02$ on average in the near wake. In this zone, the average grid size is about $\overline{h}/D = 0.018$, yielding a ratio $\overline{h}/\overline{\eta} = 0.9$. With this ratio between grid-size and Kolmogorov scale, the resulting grid density obtained should be fine enough for solving the smallest flow scales in the near wake.

7.4 Results

The simulations have been started from homogeneous flow and initially some random perturbations have been introduced. In order to ensure temporal converged statistically steady state, the flow field has been advanced in time for an initial duration of about 100 tU/D. Once the initial transient has been washed out, statistics have been collected and averaged over approximately 3900 tU/D, which is about 836 shedding cycles. This time integration results in a long simulation time and is by far the largest numerical experiment carried out since now for this flow, but it ensure not only converged statistics but also a large time span to analyse low-frequency variations in the wake.

7.4.1 Coherent structures of the flow

Proper identification of the coherent structures of the flow is necessary in order to understand the dynamics of the vortex formation and the wake structure. In the present work, as in previous chapter, the Q-criterion proposed by Hunt et al. [20] has been used. In figure 7.2 a sequence of a vortex shedding is depicted. In the figure, each plot one eighth of cycle. Furthermore, in each of them side and top views are shown.

Starting from figure 7.2a, it corresponds with an instant in which the shedding of a counter clockwise roller is about to occur. Following Mittal and Balachandar [21], who conducted flow visualizations of the vortex-shedding process at $Re = 525$, it will be called CCR (counter clockwise roller). At the same time, in the top shear layer due to the presence of instabilities, an incipient clockwise roller (CR), which begins to roll-up, is being formed. Streamwise vorticity (ribs) connecting the span-wise vortices shed are also observed. Their core is also evident forming spanwise tubes. There are also small-scale structures in the recirculation region and in the wake. These small-scale structures seem to be constituted by the stretching of streamwise vortices.

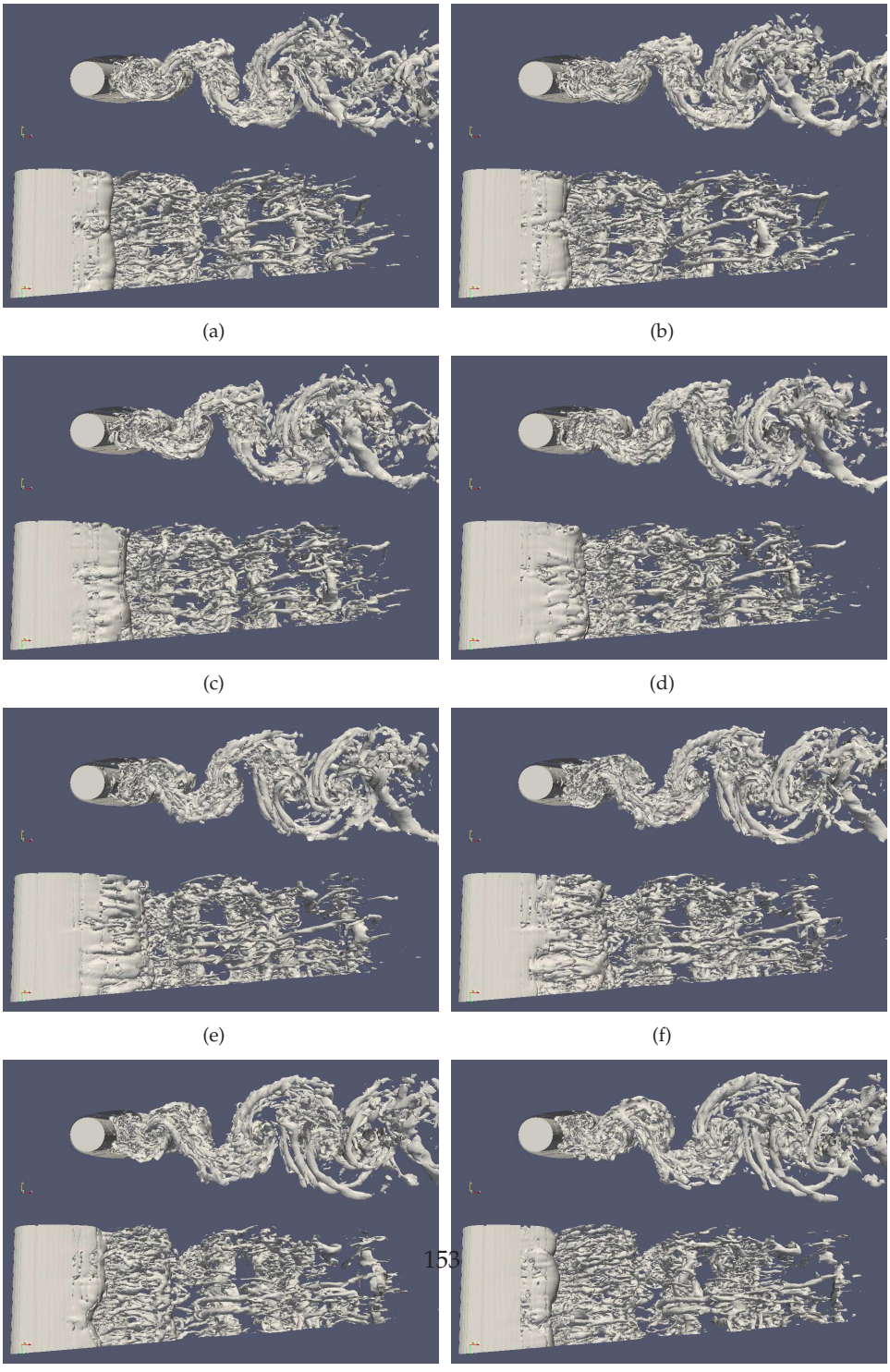

Figure 7.2: Visualization of the instantaneous flow. Sequence of a vortex shedding (each image represents $1/8th$ of the cycle).

An $1/8th$ of cycle later, CCR has almost separated from the bottom shear-layer and CR has grown in size. From the top view can be seen how spanwise vortices are distorted by the interaction with the ribs, which at the same time, are also deformed. The growth of instabilities in the shear-layer has provoked its broken off just by mid-span.

Advancing in time $1/8th$ of cycle, shear-layer instabilities continue to growth and new instabilities are continuously appearing. Although it is only shown the view of the top shear-layer, instabilities are also being developed in the bottom one. At this stage CCR has completely been separated and it is now moving downstream in the near wake, while CR has increased its size being fed by the instabilities arriving from the top shear-layer. Approaching to the half of the vortex-shedding period, CR is well-formed and a new counter clockwise roller (CCR1) is starting to be formed in the bottom shear-layer. At this instant, instabilities have a corrugated appearance just at the end of the shear-layer. These instabilities seem to be increased by the interaction with small vortices within the recirculation bubble. With this view (figure 7.2d), half vortex-shedding has occurred. The next four images (figure 7.2e to 7.2h) show the development and shedding of CCR1 in order to complete a full cycle. This can be described as follows.

Now CR is in process of separation from the vortex sheet (figure 7.2e) and in the top view the corrugated structures seem to break and form elongated structures, which finally broke-up when CR goes into the wake (figure 7.2f). These structures can now be identified as stream-wise vortices. Some of these vortices will grow and connect span-wise vortex tubes while they travel downstream. Part of these structures, due to the vortex stretching will also break up and feed the wake with small-scale structures.

As the cycle falls into its last quarter, CCR1 has grown in size due to new structures arriving from instabilities formed in the bottom shear-layer. Now, a small and incipient CR1 in the top vortex sheet can be seen. This sequence end-up with the view of CR completely surrounded by these streamwise structures and CCR1 about to be separated from bottom shear layer. This view is also interesting because 3 Kelvin-Helmholtz instabilities in the bottom shear layer are also well observed.

7.4.2 Energy spectrum

Single-points measurements have been carried out by positioning probes at different locations. Measurements at those ports have been taken over the whole simulation time. The location of these stations is as follows: $P1 \equiv [x/D = 0.71, y/D = 0.66]$ and $P2 \equiv [x/D = 1.3, y/D = 0.69]$ are located in one of the shear-layers, $P3 \equiv [x/D = 2.0, y/D = 0.0]$ and $P4 \equiv [x/D = 3.0, y/D = 0.0]$ are located in the wake centerline, $P5 \equiv [x/D = 2.0, y/D = 0.59]$ in the wake, $P6 \equiv [x/D = 0.5, y/D = 0.0]$ at the

cylinder base and $P7 \equiv [x/D = -0.465, y/D = 0.171]$ quite close to the laminar boundary layer at about 70° from the stagnation point.

The main frequencies corresponding to the large-scale vortex shedding (f_{vs}) and the small-scale Kelvin-Helmholtz (KH) instabilities of the shear-layers (f_{KH}) have been obtained from the power spectrum of the probes $P1,\ P2,\ P3$ and $P5$ by using the Lomb periodogram technique. The resulting spectra have also been averaged in the span-wise direction. A piece-wise of the stream-wise and cross-stream velocity components and their power spectra at the these stations are plotted in figures 7.3 and 7.4, respectively.

At all stations, the spectrum exhibits a dominant peak at $f_{vs} = 0.2145$, with the exception of the stream-wise spectrum of the probe located in the wake centreline ($P3$) in which its second-harmonic is visible ($f = 0.429$). The peak at f_{vs}, which corresponds with the large-scale vortex shedding frequency, is in agreement with the values reported in the literature (see Table 7.1 for more details). In addition, a broadband peak at a larger frequency and centred at $f_{KH} = 1.34$, which corresponds with the Kelvin-Helmholtz instabilities of the separating shear-layer, is also detected. This value is in fair agreement with Prasad & Williamson [22] predictions for this Reynolds number ($f_{KH} = 0.0235 Re^{0.67} f_{vs} = 1.29$). This secondary peak is only observed in the probes located at the shear-layers, and although at $P2$ ($x/D = 1.3$) is still visible in the cross-stream velocity fluctuations spectrum, its intensity diminishes as the flow moves downstream and is smeared out in the background of fluctuations of the turbulent flow.

On the top of both frequencies, i.e. the vortex-shedding and the KH instabilities frequencies, there is also a peak at a much lower frequency than that of the vortex shedding ($f_{vs}/f_m = 33.5$. This peak occurs on average at $f_m = 0.0064$ and is also observed at almost every station located in the vortex formation zone. In fact, if the time series of the stream-wise velocity component (see figure7.3(g)) is inspected, one can notice a quasi-periodic wave in the fluctuations of the variable with a frequency which is quite lower than that of the vortex shedding. This large-scale quasi-periodic motion registered seems to point out the existence of a modulation of the vortex formation zone which causes its shrinking and enlargement over the time.

In addition to these plots, the stream-wise and cross-flow velocity fluctuations spectra at the wake centreline (at probe $P4$, $x/D = 3$) are compared with the experimental data from Parnaudeau et al. [6]. The resulting comparison is depicted in figure 7.5. Note the good agreement between both results at all frequencies. It is very remarkable how the numerical data fit the experimental cross velocity spectra for the peaks of the fundamental frequency ($f/f_{vs} = 1$) and its third harmonic ($f/f_{vs} = 3$), which are very pronounced. Unfortunately for the spectra of stream-wise velocity the same level of consistency in the fundamental peak is no longer obtained. DNS data predict a pronounced peak at the second harmonic of the vortex-shedding fre-

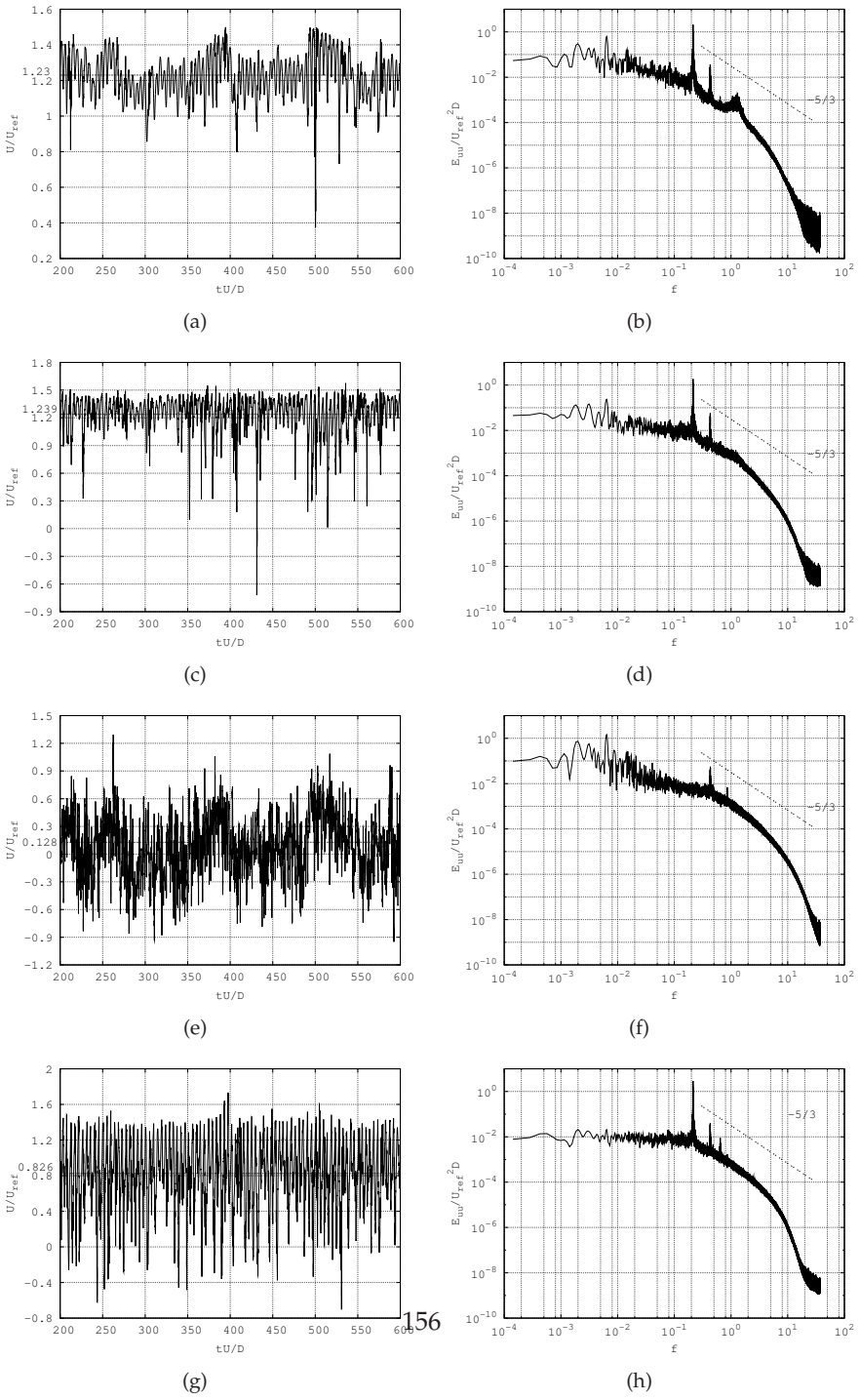

Figure 7.3: Time history of the stream-wise velocity and its power spectrum at different locations: (a,b) x/D=0.71, y/D=0.66, (c,d) x/D=1.3, y/D=0.69, (e,f) x/D=2.0, y/D=0.0, (g,h) x/D=2.0, y/D=0.59

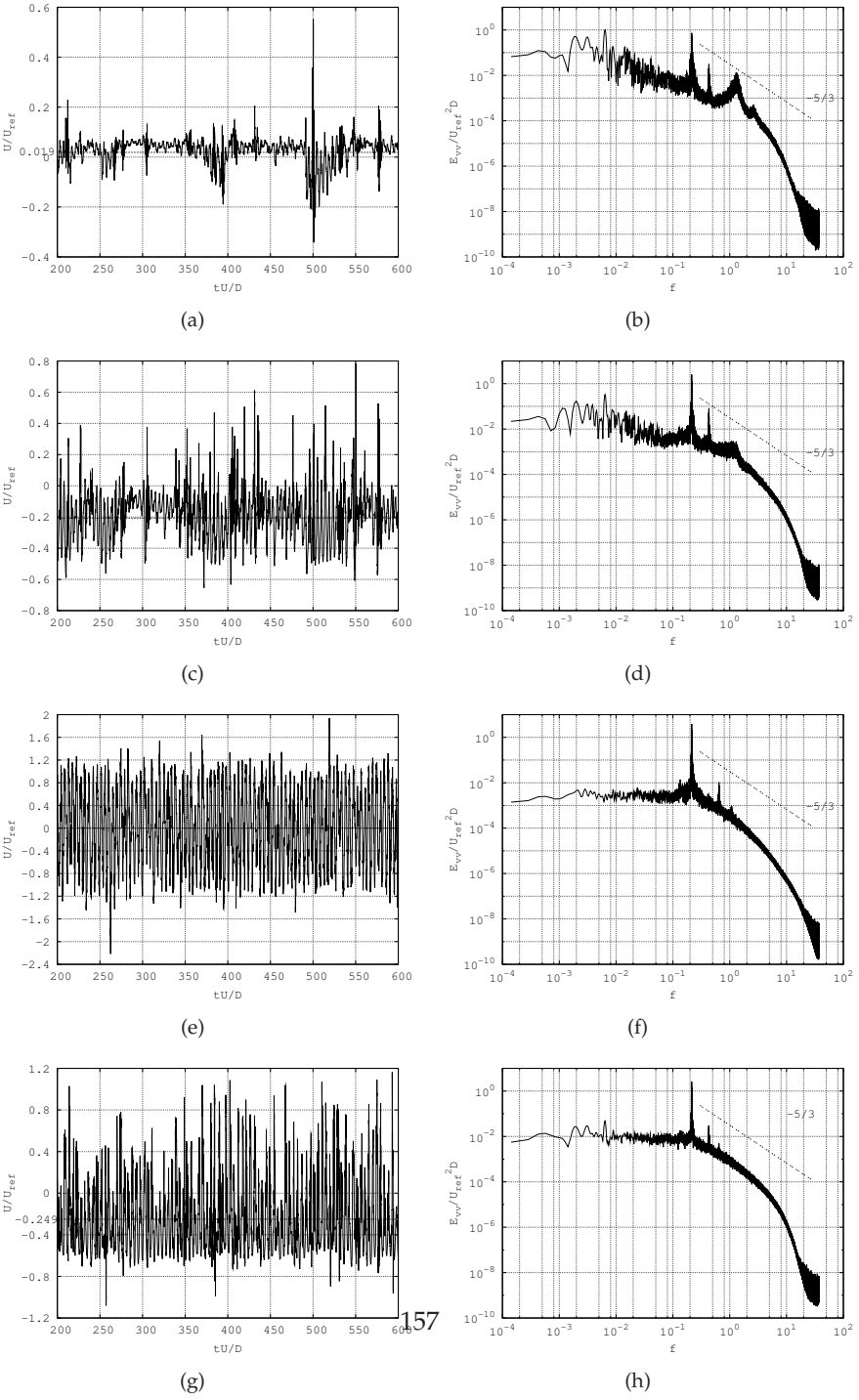

Figure 7.4: Time history of the cross-stream velocity and its power spectrum at different locations: (a,b) x/D=0.71, y/D=0.66, (c,d) x/D=1.3, y/D=0.69, (e,f) x/D=2.0, y/D=0.0, (g,h) x/D=2.0, y/D=0.59

	L_z/D	$St = f_{vs}U/D$	φ_s (°)	L_r/D	$\overline{C_d}$	$\overline{C_{pb}}$
Present work	π	0.215	87.8	1.36	1.015	0.935
Present work, Mode L	π	0.215	87.8	1.55	0.979	0.877
Present work, Mode S	π	0.215	87.8	1.26	1.043	0.98
Parnaudeau et al. (PIV) [6]	23	0.208	88	1.51	-	-
Norberg ($Re = 3000$) [8]	67	0.22	-	1.66	0.98*	0.88*
Lourenco& Shih†	21?	-	85	-	0.98	0.9
Dong et al. ($Re = 4000$)[23]	7.5	-	-	1.47	-	-
Ma et al. (Case I) (DNS) [5]	2π	0.203	-	1.12	0.96	0.96
Ma et al. (Case II) (DNS) [5]	π	0.219	-	1.59	0.84	0.88
Tremblay (DNS) [24]	π	0.22	85.7	1.3	1.03	0.93
Kravchenko&Moin (LES)[7]	π	0.21	88	1.35	1.04	0.94
Franke&Frank (LES) [9]	π	0.209	88.2	1.64	0.978	0.85
Mahesh et al. (LES) [25]	π	0.218	87.6	1.35	1.0	-

Table 7.1: Statistical flow features. DNS results compared with experimental measurements and numerical results from literature. (*) taken from [7] at $Re = 4020$; †Data summarised in [26]

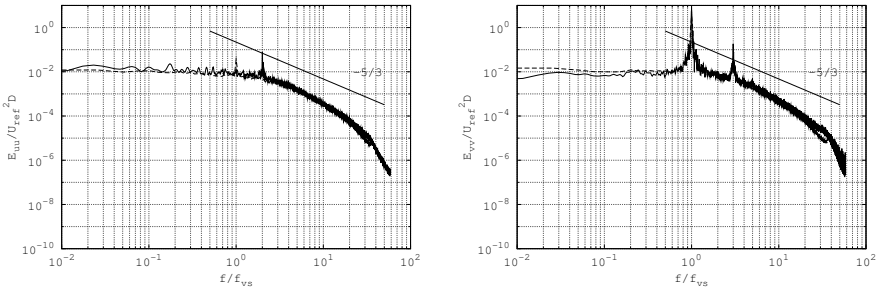

(a) (b)

Figure 7.5: Energy spectra of the stream-wise and cross-stream velocity fluctuations at probe $P4$ (solid line). Comparison with experimental measurements by Parnaudeau et al. [6] (dashed line).

quency for the stream-wise spectrum as expected for a probe located in the wake centreline. However, Parnaudeau et al. [6] indicated the occurrence of a peak in the u-spectra at the vortex shedding frequency due to the cosine law and calibration methods used in their Hot Wire Anemometry (HWA) measurements, which lead to slight contaminations of their results.

With the analysis of the power spectra at different locations in the formation zone, some questions arose: Is this low-frequency observed related with some modulation movement of the recirculation bubble? If is it the case, is there a relation between this movement and the base pressure? How this shrinking and enlargement of the recirculation zone affects the topology of the wake and thus, the statistics in the vortex formation zone? Hereafter, we will try to answer this questions by analysing the average and instantaneous flow in the wake.

One way to analyse if two signals are correlated is by computing the cross-correlation between them. This should provide a measure of the rate at which one signal is affected by the information of the other. Here, correlations have been used to quantify the relation between the base-pressure fluctuations (taken at $P5$) and the stream-wise velocity fluctuations in the wake centreline (taken at $P3$). If the signals are correlated one would expect high coherence for between them with some frequency. The correlation, at τ time lag, of two time series ($\phi_1(t)$ and $\phi_2(t)$) can be defined as,

$$\rho(\tau) = \frac{\left\langle \phi_1'(t)\phi_2'(t+\tau) \right\rangle}{\left\langle \phi_1'(t)^2 \right\rangle^2 \left\langle \phi_2'(t)^2 \right\rangle^2} \tag{7.1}$$

where fluctuations of the variables are defined as $\phi'(t) = \phi(t) - \overline{\phi}$, being $\overline{\phi}$ the mean value at the probe location.

The resulting cross-correlation coefficients are plotted in figure 7.6. In the figure, a well-defined periodic oscillation with a period (on average) of $\mathcal{T} = 156$ time-units can be observed. This period matches the frequency measured in the spectrum at different station of $f_m = 0.0064$, which seems to be the footprint of the quasi-periodic motion observed in the stream-wise velocity. The cross-correlation starts in a negative value, which might be interpreted as 180° phase angle between both signals. That is, as the base pressure gets more negative, the streamwise velocity at the wake centreline increases, which points out that there is a shrinking of the recirculation zone with a decrease in the vortex formation length. On the contrary, as the base pressure gets less negative, the streamwise velocity at $P3$ decreases meaning a lengthening in the recirculation zone.

The inverse correlation between the base pressure and the vortex formation length in the flow past bluff bodies as a function of the Reynolds number is a well known phenomena, which has been the object of different studies (see for instance [27]). However their correlation in the unsteady flow, has received lesser attention. For

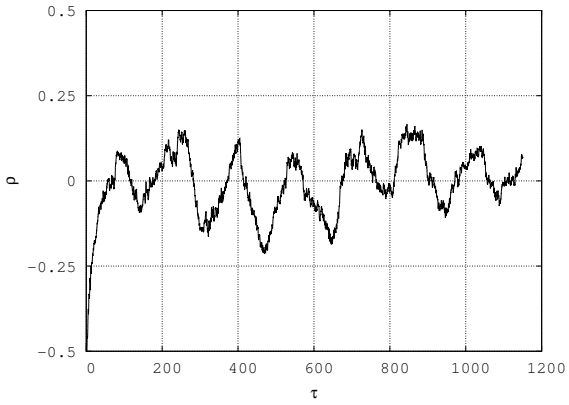

Figure 7.6: Cross-correlation between the base pressure and stream-wise velocity fluctuations at $P3$.

a higher Reynolds number $Re > 2 \times 10^4$, Miau et al. [13] measured a correlation with a time scale of just one order of magnitude larger that than of the vortex shedding. However, the implications of these low-frequency oscillations of the vortex formation zone in the wake topology have not yet been analysed.

7.4.3 Averaged statistics in the wake

The existence of different states in the near wake zone behind a normal flat plate was studied by Najjar & Balachandar [12]. Similar fluctuations in the recirculation zone behind bluff-bodies were also observed experimentally and numerically [11, 13, 15]. The low-frequency behaviour of the velocity fluctuations within the recirculation zone can be physically interpreted as the wake variation between two different modes: i) a high-energy mode dominated by strong fluctuations in the shear-layer, and in general, large-amplitude fluctuations in the vortex formation zone and, ii) a low-energy mode with weaker fluctuations in the shear layer. The large-amplitude fluctuations in the shear layers are accompanied with a shrinkage of the recirculation region, while when weaker fluctuations are observed there is also an enlargement of the recirculation region behind the cylinder. And, as has been previously shown, there is also a linkage with the suction base pressure: the higher the value of the suction base pressure, the larger the vortex formation zone.

In order to analyse the wake configuration we have computed the partial time-average statistics when there is a shortening in the vortex formation region and when this zone experiences a lengthening process. To do this, the low-pass filtered signal

of the stream-wise velocity at $P3$ station, with a cut-off frequency lower than of the vortex-shedding, has been used as reference. Positive values of the periodic component of the velocity ($\tilde{u}_i > 0$) are expected when fluctuations are the largest. On the contrary, negative values of this quantity ($\tilde{u}_i < 0$) are expected when the observed fluctuations are weaker. With this criteria, 10 consecutive vortex-shedding periods within each of these modes have been averaged and their statistics computed . Following the same nomenclature as in Najjar & Balachandar [12], the highest energetic mode (short recirculation) will be hereafter referred as Mode H, whereas Mode L will be used in reference to the lower energetic mode (larger recirculation zone). In addition to the statistics computed for each mode, statistics for the whole time integration period (4000 TU) have also been evaluated.

The resulting time-averaged flow parameters are summarised in table 7.1. Besides the vortex shedding frequency previously commented, the separation angle (φ_s), recirculation length (L_r/D), drag coefficient (C_D) and base-pressure coefficient (C_{pb}) are presented. For comparison, experimental and numerical (from DNS and LES) results from the literature are also given. The computed flow parameters are in good agreement with the ones published by other researchers. In fact, main different registered are in the length of the recirculation bubble as one could expect.

The angular distribution of the mean pressure coefficient (Cp) for both modes and for the long-term averaged solution is plotted in figure 7.7(a). Together with the present results, the pressure distribution measured by Norberg [28] at $Re = 3000$ is also shown. The result which better matches the experiments from Norberg is the solution corresponding with Mode L. All three solutions collapse in the into the same curve in the laminar boundary layer up to a location somewhat upstream the position where pressure reaches its minimum value ($\sim 70°$). After this location, the distribution corresponding with the lowest values of pressure occurs within Mode H, while long-term averaged solution is in between the two extreme modes. Note also the differences in the suction base pressure. Although the different behaviour in the pressure field, these changes have almost no effect in the skin-friction distribution (see figure 7.7(b)). There is only a slight difference in the peak value of this coefficient at about $58°$.

In figure 7.9 the stream-wise velocity profile and its fluctuation along the wake centreline is depicted. In the figure are plotted the averaged values for both modes together with the long-term averaged solution. As can be observed, the profiles of stream-wise velocity and its fluctuations are quite different. The recirculation zone goes from $L_r/D = 1.26$ during Mode H to a larger value of $L_r/D = 1.55$ in Mode L. The long-term average solution (with 4000 time-units) is within both modes yielding a length of the recirculation region of $L_r/D = 1.36$. It is interesting to remark that this result is in good agreement with the value calculated by Kravchenko&Moin [7] (see Table 7.1). In their LES, statistics were computed over 35 time-units which is a very

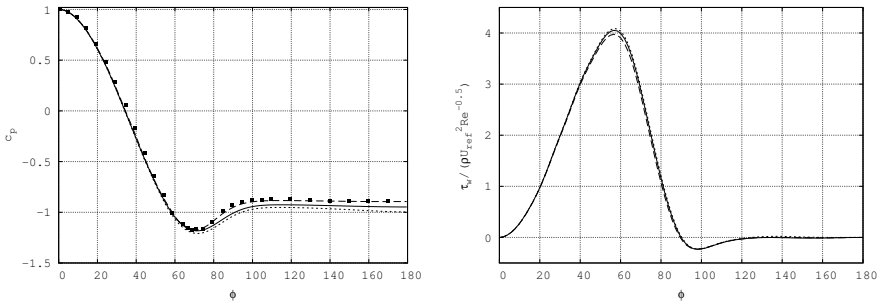

(a) (b)

Figure 7.7: Mean profiles distributions around the cylinder surface. (a) Mean pressure distribution in the cylinder surface compared with experimental results by Norberg at $Re = 3000$ [28]. (b) Mean skin-friction coefficient. Solid line, long-term averaged solution; dotted line, Mode S, dashed line, Mode L.

short time, considering the present results. One can conjecture that their averaging time was taken in the middle of both modes yielding a result quite close to the long-term averaged solution. This fact might be seen as fortuitous, as it could led to erroneous conclusions about the integration time required for obtaining converged statistics.

In Mode H the velocity deficit also is less than in Mode L. This value is of $u_{min}/U_{ref} = -0.23$ in mode H, while in model L stream-wise velocity in the wake centreline gets more negative ($u_{min}/U_{ref} = -0.32$). The position where this minimum occurs moves downstream, from $x/D = 1.35$ in mode H to $z/D = 1.59$ in mode L. However, it is remarkable the fact that this behaviour is just restricted to the vortex formation zone, as the wake recovers after $x/D > 4$. Indeed, further downstream the profile of the long-term averaged solution compares quite well with the experimental results by Ong&Wallace [29] (see figure 7.8).

Another striking fact is the profile of the stream-wise velocity fluctuations u_{rms}. In Mode L, it exhibits a two-lobed peak with maximums at $x/D = 1.45$ and $x/D = 1.9$. The second one occurs just upstream the location of the recirculation closure ($x/D = 1.95$), pointing the length of the vortex formation zone. This profile is similar to that observed by Norberg [8] for $Re_D = 3000$. In his work, two peaks at $x/D = 1.4$ and $x/D = 2.1$ in the u_{rms} profile were identified. On the contrary, u_{rms} along the wake centreline in Mode H is quite different with only one peak at $x/D = 1.62$. Furthermore, Mode H presents a higher level of fluctuation, suggesting that it is more energetic and turbulent than Mode L. Moreover, u_{rms} profile for the long-term averaged solution is similar to that described by Norberg [30] for $Re_D > 8000$. This

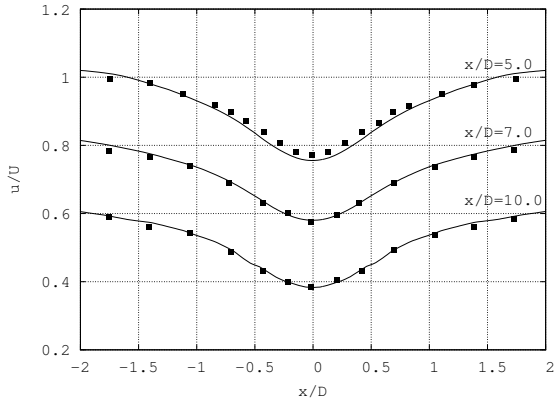

Figure 7.8: Stream-wise velocity profile at different locations in the wake. (solid line) long-term averaged solution, (solid squares) experimental results from Ong&Wallace [29]. For clearness, profiles has been shifted and are represented for increasing x/D from top to bottom.

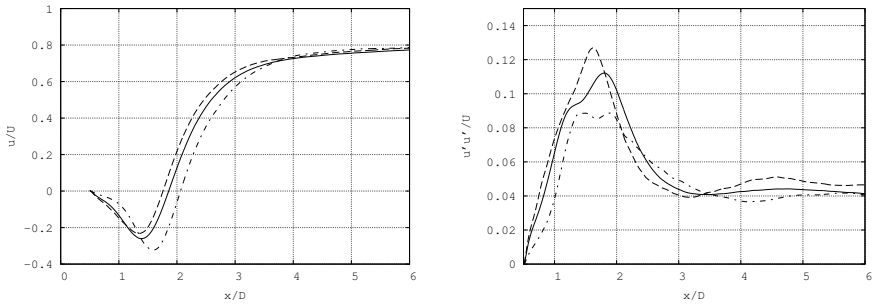

Figure 7.9: Effects of the recirculation in the wake configuration. (a) Averaged streamwise velocity and (b) its averaged fluctuation along the wake centreline. (solid line) long-term averaged solution; (dashed line) Mode H; (dash dotted line) Mode L.

solution presents a peak at $x/D = 1.8$ and (what Norberg called) an inflection point upstream this peak, between $1.2 < x/D < 1.4$.

As has been commented before, in the literature there is a large scattering in the mean flow solutions in the near wake which have observed as different mean flow configurations of the stream-wise velocity usually referred as U-shape and V-shape profiles. Different causes for these contradictory results have been indicated, such as insufficient span-size of the domain or dissipative numerical schemes (in the case of DNS or LES solutions). However, in the light of the results presented since now, one can argue that these differences registered are due to the quasi-periodic modulation of the recirculation bubble observed as an shrinking and enlargement of the recirculation. This unsteady long term motion of the near wake seems to be the cause zone of the different configurations in the wake.

In order to gain more insight into the behaviour of both modes, the stream-wise velocity profile and its fluctuations are plotted at different locations in the near wake (at $x/D = 1.06$, $x/D = 1.54$ and $x/D = 2.02$, figure 7.10). For comparison the experimental results from Parnaudeau et al. [6] and the numerical results of Case I from Ma et al. [5] (finer grid and larger span-wise domain) are also included. These reference solutions have been selected as both of them point out contradictory wake statistics due to their differences in the recirculation zone ($L_r/D = 1.51$ and $L_r/D = 1.12$, respectively). Also as reference, the long-term averaged solution is included (solid line). As can be seen, there is a good agreement for first- and second-order statistics with both data for each mode. Largest differences are observed with the solution from Ma et al. [5], as in their case a shorter recirculation region was obtained (than that of Mode H). The most energetic mode (Mode H) presents the largest fluctuations, specially in the region closest to the cylinder (at $x/D = 1.06$) where the stream-wise fluctuation peak at the shear layers is almost twice the value reached during Mode L. More differences between both modes are encountered if cross-flow velocity is compared at those locations (see figure 7.11. Cross-flow velocity fluctuations peak at the wake centreline. In all measurement stations, Mode H is registered as more energetic than Mode L. Similar to the stream-wise velocity fluctuations relative differences between both modes are attained in the closest location at $x/D = 1.06$, where fluctuations in Mode H doubled the peak value of Mode L. However, in terms of absolute quantities, the cross-flow fluctuations increases as the flow approaches the recirculation bubble closure.

It is clear, that along the time, the flow past the cylinder experiences changes in the vortex formation region which clearly affects the average statistics. Norberg [31], in his work, suggested that at $Re_D = 5000$ overcomes a change in the wake configuration. This transition was later confirmed by Prasad and Williamson [3], while Norberg [30] attributed this change to a transition between a high- and low-quality vortex shedding mode. The results here presented suggest that at $Re_D =$

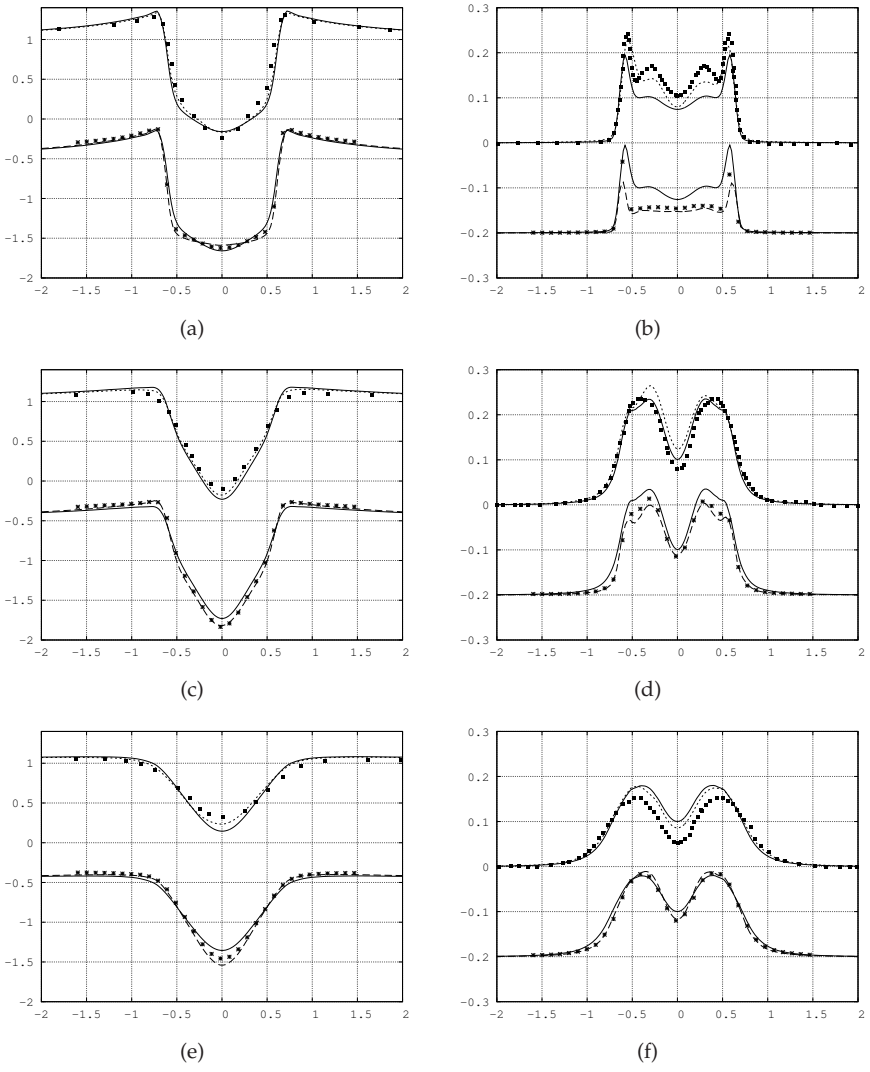

Figure 7.10: Effects of the recirculation in the wake configuration and comparison with literature results. (left) Averaged stream-wise velocity profile and (right) its fluctuation at different stream-wise locations. (a,b) $x/D = 1.06$; (c,d) $x/D = 1.54$ and; (e,f) $x/D = 2.02$. (solid line) long-term averaged solution, (dotted line) Mode H; (dashed line) Mode L; (■) C ase I from Ma et al. [5]; (*) Experimental results from Parnaudeau et al. [6]

3900 both modes co-exist and the wake is oscillating between them at a very low-frequency, and as has been shown this is the cause of the large scattering in the experimental and numerical results observed since now. Norberg [30] suggested that the low-quality mode was the consequence of the lost of coherence in the span-wise vortices, with vortex dislocations along the span. However, more study should be made in order to shed more light into the mechanism which triggers such oscillation.

7.4.4 Phase averaging

The unsteady mean flow of both modes is here analysed by means of the phase-average technique. The instantaneous flow can be represented by the contributions of a time-averaged component $\overline{\phi_i}$, a periodic fluctuation $\tilde{\phi}_i$ and a random fluctuation ϕ_i', i.e., $\phi_i = \overline{\phi_i} + \tilde{\phi}_i + \phi_i'$ [32]. The phase-average can be defined as the average value of the variable ϕ_i over an ensemble of signals which have the same phase with respect to a reference signal. It can be evaluated as: $\langle \phi_i \rangle = \overline{\phi_i} + \tilde{\phi}_i$. This decomposition opens the possibility of analysing the periodic motion of the flow by resolving the dominant frequency of the vortices (see appendix 8.4 for more details).

For the ensemble average, 10 phases have been used to generate each coherent component. To do this, the pressure signal on the cylinder surface at an angle $\theta = 70^\circ$ (measured from the stagnation point) has been used as the reference oscillator. In this position, the pressure signal varies in almost periodic manner with a period equal to the vortex shedding.

Streamlines and spanwise vorticity contours for both modes at phase angles of $\phi = 0^\circ,\ 90^\circ,\ 180^\circ,\ 270^\circ$ are represented in figures 7.12 and 7.13. In addition, normal and shear Reynolds stresses are also plotted for each wake mode in figures 7.14 and 7.15. The vortex-shedding process at both modes is clearly captured. Although, in both modes the vortex shedding occurs in a similar manner, there are also some important different between both wakes topologies. The first phase of the vortex shedding shows a saddle point which clearly marks the start of the new vortex. This saddle point can be located at $x/D = 1.6; y/D = 0.45$ in Mode H. However, its position for Mode L is located downstream and closest to the wake centreline at $x/D = 1.93; y/D = 0.35$. This is an important difference which points out the strength of the vortex shedding during Mode H if compared to Mode L. The strongest vortex shedding during Mode H produces the entrainment of the vortex core into the wake centreline, as can be seen by the position in of the shed vortex ($x/D = 1.4; y/D = 0.0$). This is in contrast with the location of the same vortex but during Mode L, which can be seen a slight downstream and off the wake centreline ($x/D = 1.75; y/D = -0.1$). Stream-wise normal and shear Reynolds stresses are maximum in the top shear layer near the position of the saddle point, whereas cross-stream normal Reynolds stress has two maximums near the position of the vortex

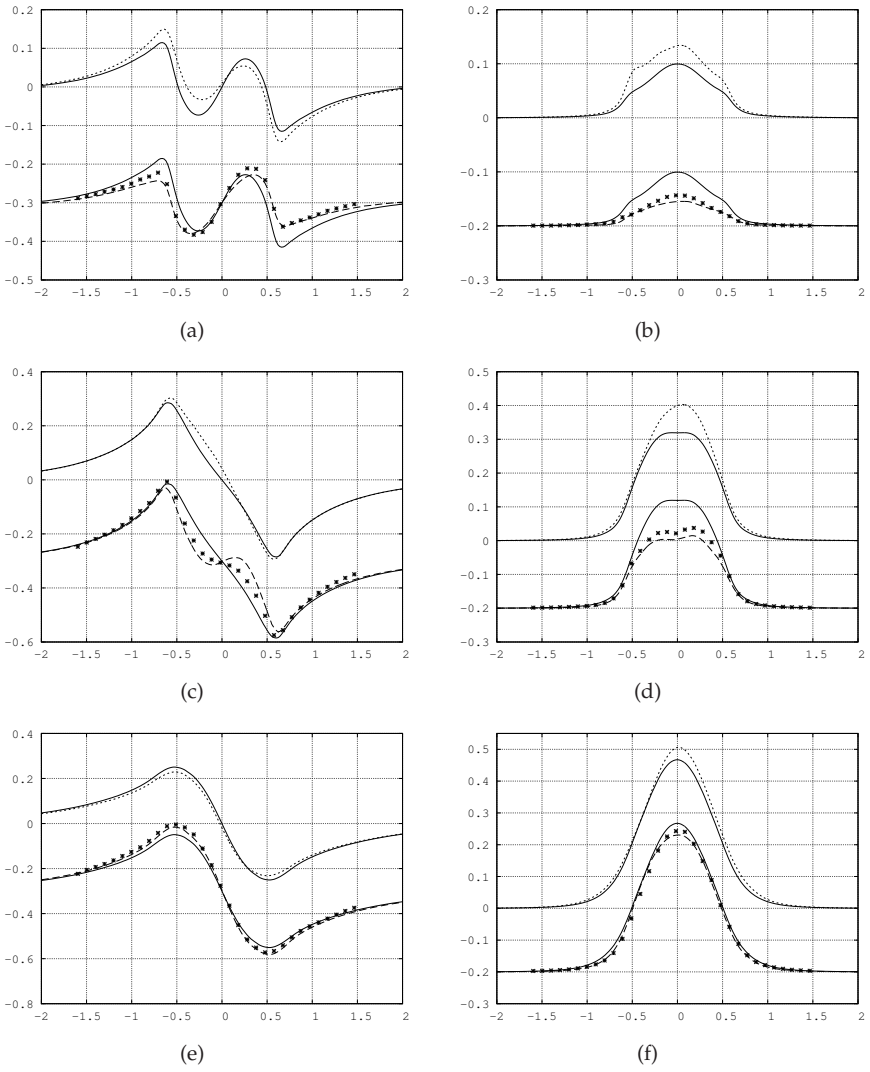

Figure 7.11: Effects of the recirculation in the wake configuration and comparison with literature results when possible. (left) Averaged cross-flow velocity profile and (right) its fluctuation at different stream-wise locations. (a,b) $x/D = 1.06$; (c,d) $x/D = 1.54$ and; (e,f) $x/D = 2.02$. (solid line) long-term averaged solution, (dotted line) Mode H; (dashed line) Mode L; (*) Experimental results from Parnaudeau et al. [6]

core.

Phase angle 90° shows the vortex completely formed near the top shear layer. Streamwise fluctuations are maximum near the vortex core and due to the entrainment of the turbulent shear layer in the recirculation zone, cross-stream normal Reynolds stress experiences an increase near the closure of the recirculation bubble. The two last phases of the vortex shedding describe a similar situation, but now the new vortex is forming in the bottom shear layer. A noticeable difference between both modes is that while in Mode H the transition to turbulence occurs close to the cylinder, Reynolds stresses in the turbulent wake are the highest for Mode L, but located at a larger distance from the cylinder than in Mode H.

7.5 Concluding remarks

A study of the wake configuration of the flow past a circular cylinder has been carried out by means of the DNS at $Re_D = 3900$. The analysis of the spectra of the velocity at different locations in the vortex formation zone, suggests that together with the vortex-shedding frequency and the small-scale Kelvin-Helmholtz instabilities frequency, there is also a low-frequency which can be attributed to the shrinkage and enlargement of the recirculation region. This low-frequency, measured from the analysis of several probes in the vortex formation region, is of $f_m = 0.0064$. This modulation of the recirculation zone can be seen as two alternating wake configurations which have been identified as i) a high-energy mode with larger fluctuations in the shear-layer (Mode H) and ii) a low-energy mode with weaker fluctuations in the shear layer (Mode L).

The large-amplitude fluctuations in the shear layers are accompanied with a shrinkage of the recirculation region, while when weaker fluctuations are observed there is also an enlargement of the recirculation region behind the cylinder. Furthermore, from the cross-correlation analysis between the pressure at the base of the cylinder and the streamwise velocity at the wake centreline has been shown that both variables are negative correlated. As the suction base pressure gets more negative, the streamwise velocity increases and as a consequence, the vortex formation zone decreases. This unsteady motion of the vortex formation has a direct influence in the near wake statistics as a long integration time is required for obtaining converged statistics, if it is considered that alternating modes of the wake occurs every 156 time-units on average. This is the main cause of the large scattering of solutions registered in the literature. As has been shown, by accommodating the averaging period to each mode, it is possible to obtain partial statistics which compares quite well with previous experiments and DNS results.

In order to gain insight into the wake topology for each mode, phase average statistics have been also computed. Although the vortex shedding period of each

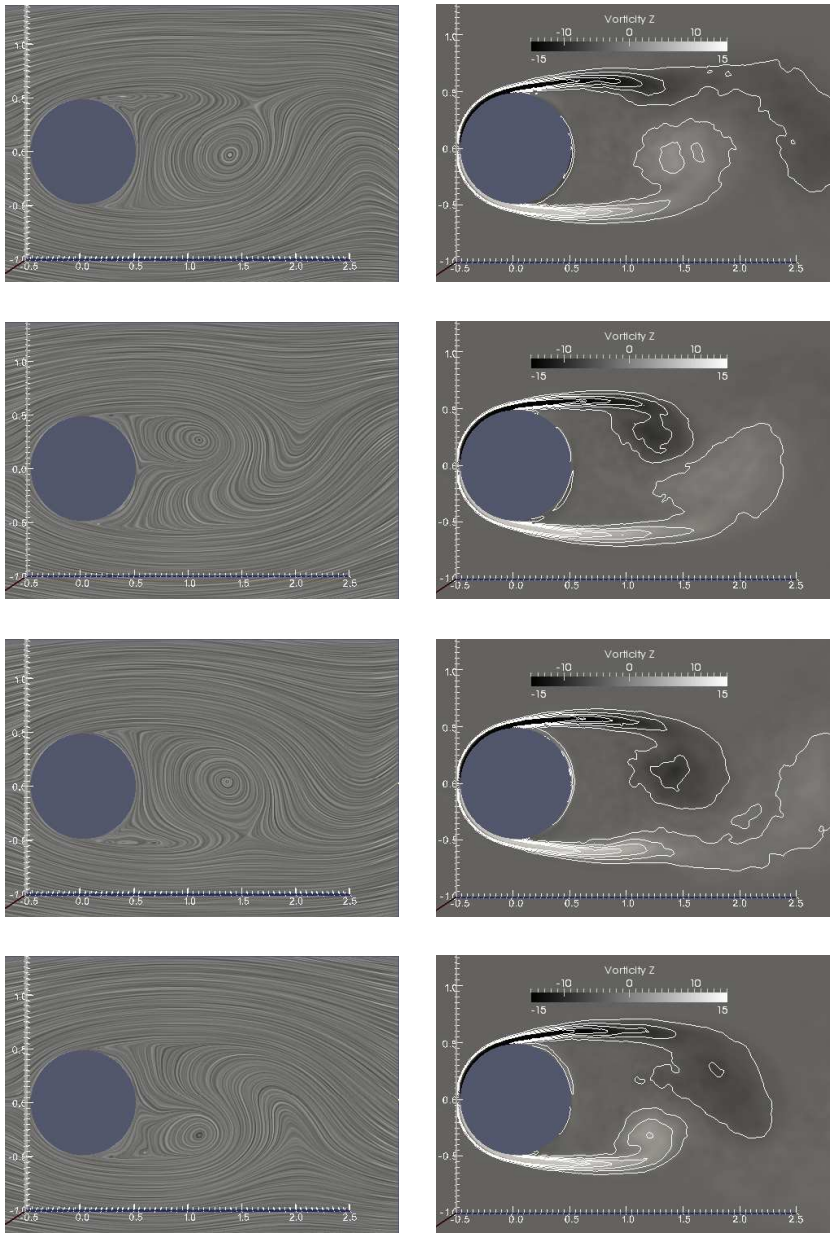

Figure 7.12: Phase-average during Mode H. (left) Streamlines; (right) Span-wise vorticity contours.

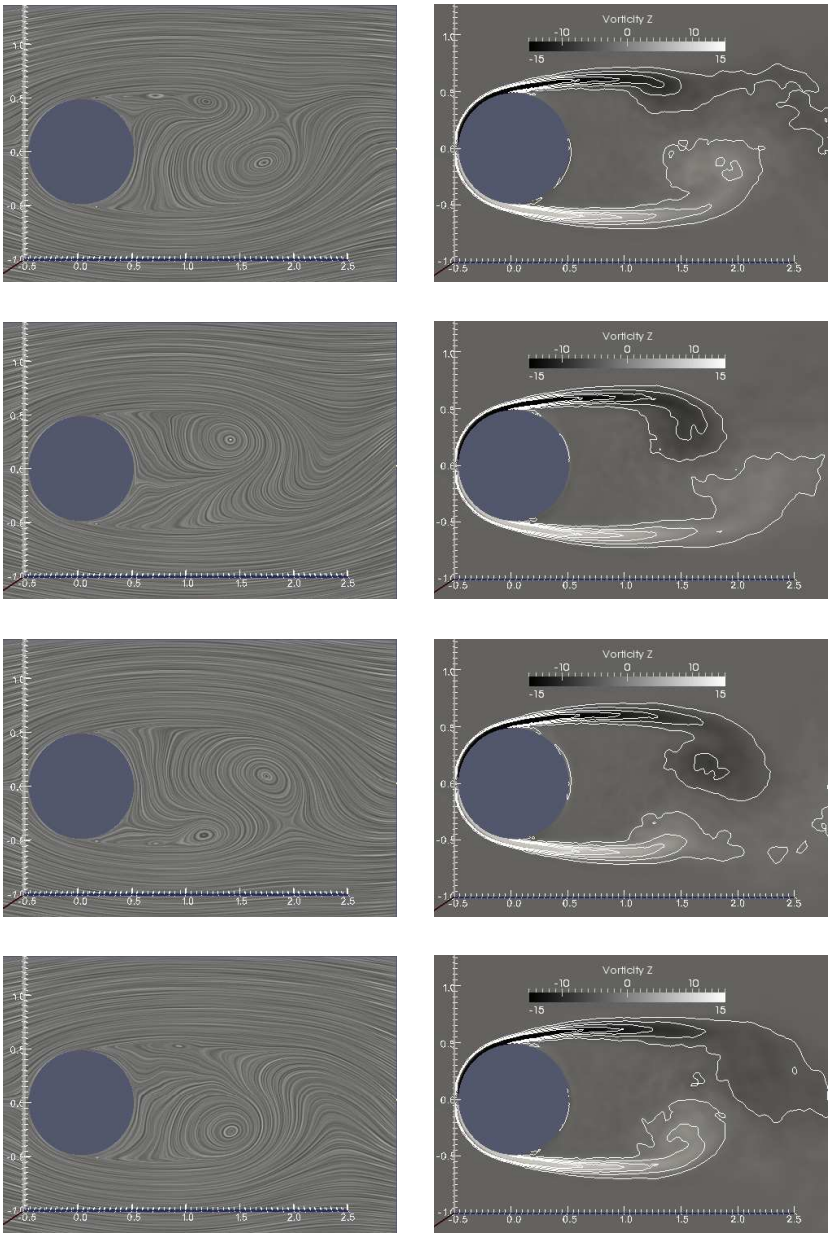

Figure 7.13: Phase-average during Mode L. (left) Streamlines; (right) Span-wise vorticity contours.

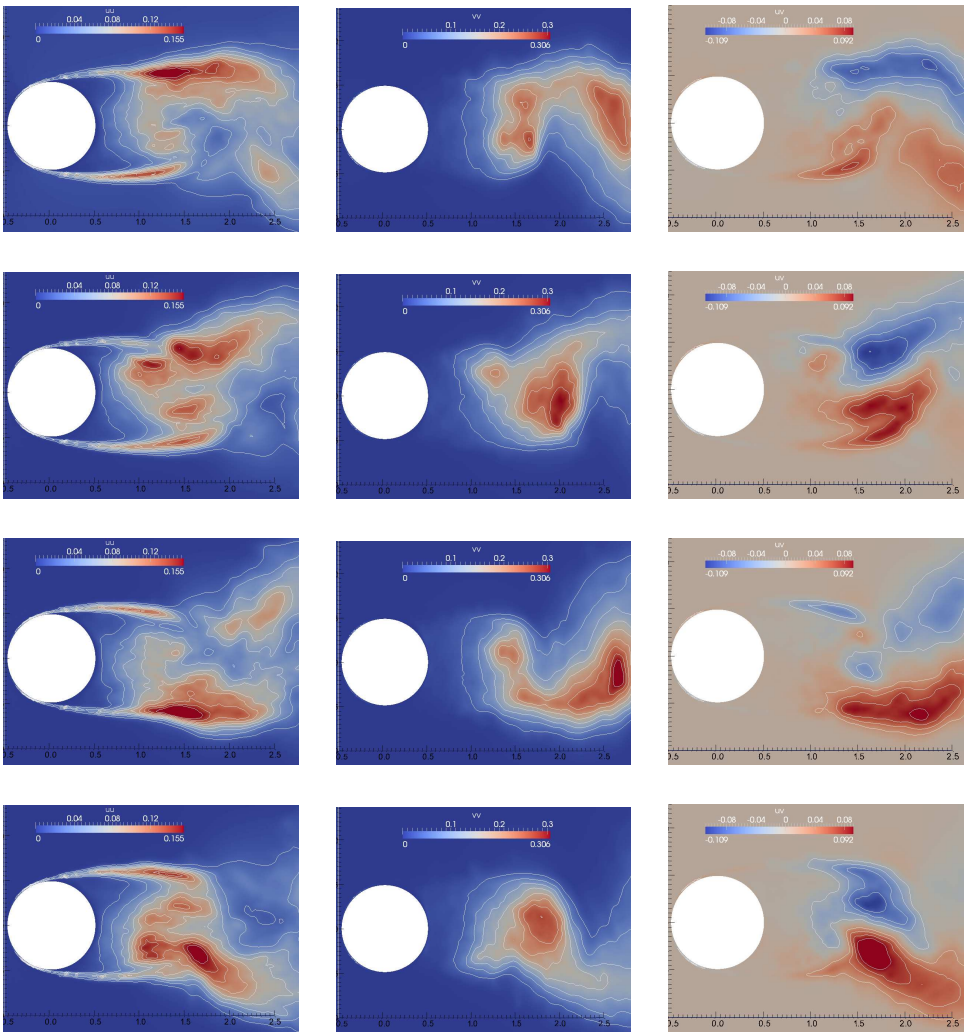

Figure 7.14: Phase-average during Mode S. (left) Streamwise normal Reynolds stress, (middle) Cross-stream normal Reynolds stress, (right) Shear Reynolds stress

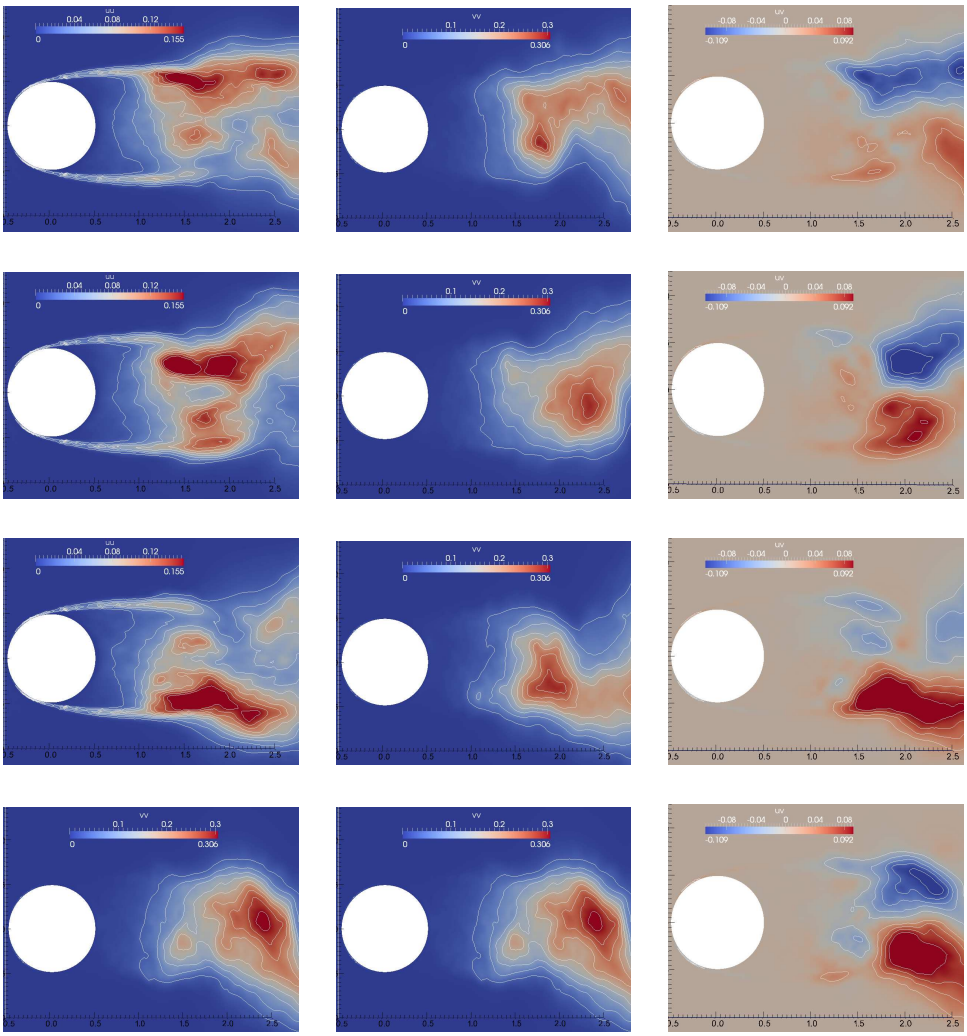

Figure 7.15: Phase-average during Mode L. (left) Streamwise normal Reynolds stress, (middle) Cross-stream normal Reynolds stress, (right) Shear Reynolds stress

mode is quite similar, important differences have been also pointed out. During Mode H, not only transition to turbulence occurs closer to the cylinder and vortex formation zone is shorted, but also vortices shed enters into the wake centreline, whereas in Mode L, the formed vortices remains slightly off the wake centreline. There are also differences in the normal and shear Reynolds stresses, being shown that although further downstream than in Mode H, their magnitude is higher in Mode L and the location of such maxima are more coherent.

References

[1] C H K Williamson. Vortex Dynamics in the Cylinder Wake. *Annual Review of Fluid Mechanics*, 28(1):477–539, 1996.

[2] A. Prasad and C. H. K. Williamson. The instability of the separated shear layer from a bluff body. *Phys. Fluids*, 8:1347, 1996.

[3] A. Prasad and C.H.K. Williamson. Three-dimensional effects in turbulent bluff body wakes. *Journal of Fluid Mechanics*, pages 235–265, 1997.

[4] Anatol Roshko. Experiments on the flow past a circular cylinder at very high Reynolds number. *Journal of Fluid Mechanics*, 10(03):345, March 1960.

[5] X. Ma, G.S. Karamanos, and G.E. Karniadakis. Dynamics and low-dimensionality of a turbulent wake. *J. Fluid Mechanics*, 410:29–65, 2000.

[6] P. Parnaudeau, J. Carlier, D. Heithz, and E. Lamballais. Experimental and numerical studies of the flow over a circular cylinder at Reynolds number 3900. *Physics of Fluids*, 20(8):085101, 2008.

[7] A.G. Kravchenko and P. Moin. Numerical studies of flow over a circular cylinder at $Re_D = 3900$. *Physics of fluids*, 12(2):403–417, 2000.

[8] C. Norberg. Ldv measurements in the near wake of a circular cylinder. In *Bearman PW, Williamson CHK (eds) Proceedings of the ASME conference on advances in the understanding of bluff body wakes and vortex induced vibration. Washington, DC*, 1998.

[9] J. Franke and W. Frank. Large eddy simulation of the flow past a circular cylinder at ReD=3900. *Journal of Wind Engineering and Industrial Aerodynamics*, 90(10):1191–1206, 2002.

[10] F. Tremblay, M. Manhart, and R. Friedrich. LES of flow around a circular cylinder at a high subcritical Reynolds Number. *Fluids Mechanics and its applications*, 65(3):133–150, 2004.

[11] E. Berger, D. Cholz, and M. Schumm. Coherent vortex structures in the wake of a sphere and a circular disk at rest and under forced vibrations. *Journal of Fluids and Structures*, 4(3):231–257, 1990.

[12] F M. Najjar and S. Balachandar. Low-frequency unsteadiness in the wake of a normal flat plate. *Journal of Fluid Mechanics*, 370:101–147, September 1998.

[13] J.J.Miau, J.T. Wang, J.H. Chou, and C.Y.Wei. Characteristics of the low-frequency variations embedded in vortex shedding process. *Journal of Fluids and Structures*, 13:339–359, 1999.

[14] S. J. Wu, J. J. Miau, C. C. Hu, and J. H. Chou. On low-frequency modulations and three-dimensionality in vortex shedding behind a normal plate. *Journal of Fluid Mechanics*, 526:117–146, 2005.

[15] I. Rodríguez, R. Borrell, O. Lehmkuhl, C.D. Pérez-Segarra, and A. Oliva. Direct Numerical Simulation of the Flow Over a Sphere at Re = 3700. *Journal of Fluids Mechanics*, 679:263–287, 2011.

[16] R. W. C. P. Verstappen and A. E. P. Veldman. Symmetry-Preserving Discretization of Turbulent Flow. *Journal of Computational Physics*, 187:343–368, May 2003.

[17] F.X. Trias and O. Lehmkuhl. A self-adaptive strategy for the time integration of navier-stokes equations. *Numerical Heat Transfer. Part B*, 60(2):116–134, 2011.

[18] O. Lehmkuhl, R. Borrell, J. Chivas, and C.D. Perez-Segarra. Direct numerical simulations and symmetry-preserving regularization simulations of the flow over a circular cylinder at Reynolds number 3900. In *Turbulence, Heat and Mass Transfer*, 2009.

[19] R. Borrell, O. Lehmkuhl, F.X. Trias, and A. Oliva. Parallel direct poisson solver for discretisations with one fourier diagonalisable direction. *Computational Physics*, 230(12):4723–4741, 2011.

[20] J.C.R. Hunt, A.A. Wray, and P. Moin. Eddies, stream and convergence zones in turbulent flows. Technical Report CTR-S88, Center for turbulent research, 1988.

[21] R. Mittal and S. Balachandar. Generation of streamwise vortical structures in bluff body wakes. *Physical review letters*, 75(7):1300–1303, 1995.

[22] A. Prasad and C.H.K. Williamson. The instability of the shear layer separating from a bluff body. *Journal of Fluid Mechanics*, pages 375–492, 1997.

[23] S. Dong, G. E. Karniadakis, a. Ekmekci, and D. Rockwell. A combined direct numerical simulation-particle image velocimetry study of the turbulent near wake. *Journal of Fluid Mechanics*, 569:185, 2006.

[24] Frederic Tremblay. *Direct and large-eddy simulation of flow around a circular cylinder at subcritical Reynolds numbers*. PhD thesis, Technische Universität München, 2002.

[25] K Mahesh, G Constantinescu, and P. Moin. A numerical method for large-eddy simulation in complex geometries. *Journal of Computational Physics*, 197(1):215–240, 2004.

[26] R. Mittal. Large eddy simulation of flow past a circular cylinder. *CTR Annual Research Briefs*, pages 107–116, 1995.

[27] M. F. Unal and D. Rockwell. On vortex formation from a cylinder. part 1. the initial instability. *Journal of Fluid Mechanics*, 190:491–512, 1988.

[28] C. Norberg. Effects of reynolds number and low-intensity freestream turbulence on the flow around a circular cylinder. Technical Report Rep. 87 (2), Department of Applied Thermodynamics and Fluid Mechanics, Chalmer University of Technology, Sweden, 1987.

[29] L. Ong and J. Wallace. The velocity field of the turbulent very near wake of a circular cylinder. *Experiments in Fluids*, 20(6):441–453, 1996.

[30] C. Norberg. Fluctuating lift on a circular cylinder: review and new measurements. *Journal of Fluids and Structures*, 17(1):57–96, January 2003.

[31] C. Norberg. Effects of reynolds number and a low intensity free-stream turbulence on the flow around a circular cylinder. publication no. 87/2. Technical report, Chalmers University of Technology, Sweden, 1987.

[32] W. C. Reynolds and a. K. M. F. Hussain. The mechanics of an organized wave in turbulent shear flow. Part 3. Theoretical models and comparisons with experiments. *Journal of Fluid Mechanics*, 54(02):263–288, 1972.

Chapter 8

Direct and Large-Eddy Simulations of the turbulent flow around a NACA-0012 airfoil

Most of the contents of this chapter have been published as:

O. Lehmkuhl, I. Rodríguez, A. Baez, A. Oliva and C.D. Pérez-Segarra (2012). Assessment of large-eddy simulations for the flow around aerodynamics profiles using unstructured grids. *Submitted to AIAA Journal*

Abstract. This chapter investigates the capabilities of two subgrid-scale (SGS) models suitable for unstructured grids for predicting the complex flow in transitional separated bubbles. We consider here the flow over a NACA 0012 airfoil at Reynolds number $Re = 5 \times 10^4$ and angles of attack (AOA) $AOA = 5^\circ$ and 8°. The SGS models investigated are: the wall-adapting eddy viscosity model within a variational multiscale method (VMS-WALE) and the QR eddy-viscosity model. Both are well suited for LES in complex geometries with unstructured grids. The models are assessed and compared to the results of direct numerical simulations (DNS) on the basis of first and second order statistics. Based on the good results obtained, challenging simulations at high Reynolds numbers and various AOA are also performed. It has been found that predictions of the lift and drag coefficients agree reasonably well with experimental data.

8.1 Introduction

The flow past aerodynamics structures at low-to-moderate Reynolds numbers (defined in terms of the free stream velocity and the chord length $Re = U_{ref}C/\nu$) is of great interest for many unmanned aerial vehicles (UAVs) designers, but also for small-scale wind turbines designers. The flow at these Reynolds numbers (specially in thin airfoils) is characterised by the laminar separation with transition to turbulence in the separated shear-layer. After separation, at low angles-of-attack (AOA) the flow reattaches to the airfoil surface forming a bubble (known as laminar separation bubble, LSB), which directly affects the airfoil efficiency. The greater the separation bubble, the higher the loss of lift and the increase of drag. At a certain AOA, the flow fails to reattach yielding to a complete separation (stall condition).

The study of the separation mechanism and the correct prediction of the transition from laminar to turbulent flow in the detached shear-layer are both key aspects for improving engineering designs. In this sense, the advances in computational fluid dynamics (CFD) together with the increasing capacity of parallel computers have made possible to tackle complex turbulent problems by using high-performance numerical techniques such as Direct Numerical Simulation (DNS) and the development of modelling techniques such as Large-Eddy Simulation (LES) methods. DNS has a key role for improving the understanding of the turbulence phenomena and for the simulation of transitional flows in complex geometries. However, to date few DNS studies of the flow around aerodynamics profiles have been performed. Can be cited the study performed by Hoarau et. al. [1] which investigated the transition to turbulence at a high incidence angle of 20° in a NACA0012 and low Reynolds numbers of $Re = 800$. Shan et. al. [2] studied the flow separation and transition at a low angle-of-attack $AOA = 4°$ and Reynolds number of $Re = 10^5$. Jones et. al. [3] at $AOA = 5°$ and $Re = 5 \times 10^4$ investigated the influence of the flow forcing in the transition to turbulence. In their work, transition was triggered by adding volume forcing and then results compared to the unforced situation. They found that aerodynamic performance can be effectively improved via flow forcing. More recently, Baez et. al. [4] carried out DNS at angles-of-attack $AOA = 5°$ and $8°$ showing the capabilities of high performance computing using unstructured grids for simulating the flow past aerodynamics profiles.

In spite of these works, one of the limitations of DNS is the large range of instantaneous scales to be solved, which increase rapidly with Reynolds numbers, and require the use of very large computational resources. Therefore, DNS is still limited to low-to-moderate Reynolds numbers and relative simple geometries. An alternative to DNS is large-eddy simulation (LES), which are based on computing the large-scales of the flow while modelling of the smallest ones. However, when using LES, some difficulties have to be overcomed such as the near-wall behaviour, flows undergoing transition to turbulence, among others.

One of the first attempts of using LES for modelling the flow over aerodynamics surfaces was reported by Jansen [5]. He studied the NACA4412 at maximum lift at a Reynolds number of $Re = 1.64 \times 10^6$. He was also pioneer in the use of unstructured grids by implementing a parallel code based on the Galerkin/least-squares finite element method. Later in LESFOIL project [6], the feasibility of different LES techniques for the prediction of the separated flow in an Aerospatiale A-profile at $Re = 2.1 \times 10^6$ and $AOA = 13.3°$ was investigated. They shown that the correct prediction of laminar to turbulence transition is extremely dependent on the mesh resolution. Jovicic and Breuer [7] also studied the capabilities of LES modelling by comparing the behaviour of two subgrid-scale (SGS) models, the Smagorinsky and the dynamic eddy-viscosity [8] models, in a NACA4415 at $Re = 10^5$ and $AOA = 18°$. Moreover, for the same airfoil and conditions Eisenbach & Friedrich [9] used also LES with an immersed boundary method and compared their results with those of the literature in order to test the capabilities of the method for these kind of flows.

One of the most studies aerodynamic profiles by means of LES techniques has been the SD 7003 airfoil. Yuan et al. [10] using an incompressible solver based on the SIMPLE algorithm performed LES of the flow around this airfoil. For the simulations, the Smagorinsky models was used. Also, Galbraith and Visbal [11] using a high-order implicit LES computed the flow at $Re = 6 \times 10^4$ with a good prediction of the lift coefficient, although drag coefficient was over-predicted. More recently, Zhou and Wang [12] studied the transitional flow over a SD7003 profile at low-to-moderate Reynolds numbers capturing the main instantaneous features of the transitional flow.

In addition to these works, LES techniques have been also used for aeroacoustic applications. For instance, Oberai et al. [13] performed acoustic calculations using the results of a LES Smagorinsky model as an input for solving the far field acoustic in a Eppler 387 airfoil at $Re = 10^5$. Kim et. al. [14] computed the flow field around a NACA0018 under generation of noise. Also LES was used by Marsden et. al. [15] for studying the flow around a NACA0012 at $Re = 5 \times 10^5$ at zero incidence with good results. In addition, they computed the radiated acoustic field directly from the LES.

Although the large number of time-accurate numerical studies available, most of the aforementioned works have been carried out using structured grids by means of body-fitted or immerse boundary techniques and only a few have been performed using unstructured grids [5, 13]. Unstructured meshes can be used efficiently on complex geometries, as it is possible the use of local grid refinement for accurate solving the flow and, at the same time, there is no need of increasing the mesh in zones where laminar regime prevails. Thus, there is an effective reduction of the number of control volumes required for solving a determined problems. Considering the necessity of the use of LES techniques for studying engineering flows on complex geometries [16], which in general can not be described with structured grids, it

is advisable to test models which do not use the wall-unit coordinates in their definition. In this sense, the Wall-Adapting Local-Eddy viscosity model [17] within the variational multiscale method (VMS-WALE) [18] and the QR eddy-viscosity model (QR) [19] are two good recent choices which have not been sufficiently tested yet.

This work aims at assessing the performance of the aforementioned LES models for predicting the flow around a NACA 0012 airfoil with angle of attacks (AOA) of 5° and 8° at $Re = 5 \times 10^4$ based on the free-stream velocity (U_{ref}) and the chord length (C). This is relevant for the prediction of flows with massive separation which can be found in many engineering and industrial applications. As reference numerical or experimental results are not available for this configuration, we have first performed DNS at both AOA. After that, LES capabilities using the aforementioned subgrid-scale models (SGS) (VMS-WALE and QR models), are tested by direct comparison of the first- and second-order statistics at both AOA with DNS data. In addition, the performance of these models is tested in challenging situations at high Reynolds numbers and different angles of attack by comparison with experimental data.

8.2 Problem definition and computational domain

Numerical simulations of the flow around a NACA0012 extended to include sharp trailing edge at Reynolds numbers $Re = U_{ref}\ C/\nu = 5 \times 10^4$ (Reynolds number is defined in terms of the free-stream velocity U_{ref} and the airfoil chord C) and at $AOA = 5^\circ$ and 8° have been carried out. As has been commented before, detailed first- and second-order statistical data to be used in the assessment of LES models is scarce. Thus, we have first performed DNS at both $AOAs$ and statistical data have been compared with that of DNS at different locations in the suction side and in the wake of the airfoil.

Solutions are obtained in a computational domain of dimensions $40C \times 40C \times 0.2C$ with the leading edge of the airfoil placed at $(0, 0, 0)$ (see figure 8.1). All coordinates are referred to body axes unless remarked. The x axis is chord-wise, y is in the plane of the airfoil and z is spanwise direction. Distances from the profile to the domain boundaries have been chosen according to previous experiences and potential vortices notions [4, 20]. The boundary conditions at the inflow consist of a uniform velocity profile (u,v,w)=($U_{ref} \cos AOA,\ U_{ref} \sin AOA, 0$). At the outflow boundary, a pressure-based condition is imposed. No-slip conditions on the airfoil surface are prescribed. Periodic boundary conditions are used in the spanwise direction.

Flow around an airfoil at low AOA is mostly laminar with the exception of a zone close to the surface of the airfoil (suction side) and in the wake of it. In the turbulent zones the grid must be dense enough to capture all the flow scales. Within laminar zones, boundary layer must also be well-solved. Taking into account that the accuracy of the results in the region of the separated shear-layer where transition to

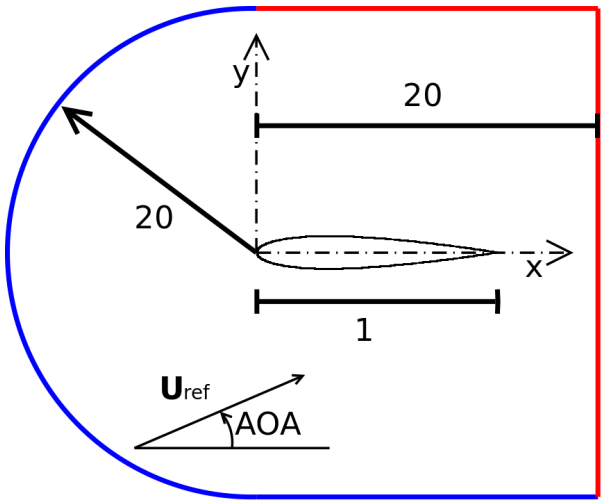

Figure 8.1: Computational domain. Blue boundary represents inflow conditions, with specified velocity and pressure. Red boundary represents outflow condition.

turbulence occurs is highly grid dependent [6], care must be taken when the computational grid is constructed by clustering more control volumes in this zone. Another critical region is the near wake of the airfoil, where a poor grid resolution may cause notable upstream flow distortions. With these criteria, the governing equations are discretised on an unstructured mesh generated by the constant-step extrusion of a two-dimensional unstructured grid.

Grids used for LES and DNS are shown in the table 8.1. Examples of the two-

Table 8.1: Computational meshes. N_{2D} number of control volumes in the plane; N_{planes} number of planes in the spanwise direction; $NCVs$ total number of control volumes

Name	N_{2D}	N_{planes}	$NCVs \times 10^{-6}$
$LES-M1$	46417	16	0.74
$LES-M2$	149355	32	4.78
$DNS-5$	263522	96	25.3
$DNS-8$	280876	96	26.9

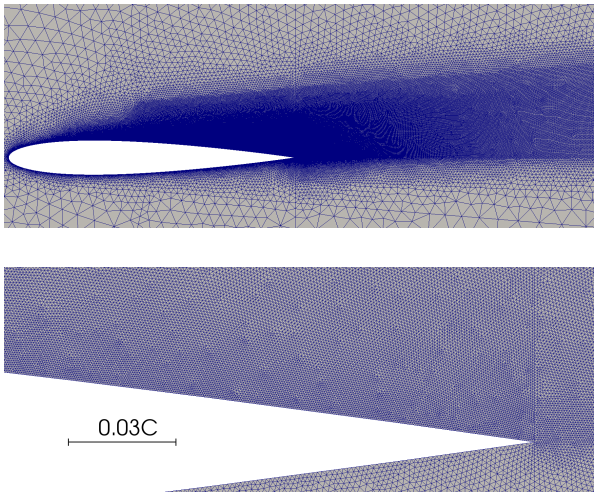

Figure 8.2: Detail of the 2D $DNS-8$ grid in the suction side and in the region near the airfoil surface.

dimensional grids and their refinement on the suction side of the airfoil at $AOA = 8°$ are depicted in figure 8.2. The presence of a laminar separation bubble (LSB) and detached shear-layer on the suction side makes LES computations highly dependent on the mesh resolution [6]. Hence, the behaviour of the two SGS models has been assessed on 2 different grids which have been constructed trying to set more resolution near the airfoil surface, while maintaining low the number of cells in the outer regions.

Meshes used in DNS computations have been further assessed in order to test if the grid resolution used is adequate for solving the smallest scales of the flow (Kolmogorov scale). To do this, the grid size h ($h \equiv (\Delta x \times \Delta y \times \Delta z)^{1/3}$) has been compared to the Kolmogorov length scale, which is evaluated from the dissipation rate ϵ as,

$$\eta = (\nu^3/\epsilon)^{1/4} \tag{8.1}$$

For the $DNS-5$ mesh, the average ratio between the grid size and the Kolmogorov length scale is of h/η=0.429, whereas in the near wake ($1 \leqslant x/C \leqslant 3$) this ratio is of $h/\eta = 0.675$. This value increases up to $h/\eta = 1.0364$ at a distance of $x/C = 5$. As for $DNS-8$ grid, similar quantities have been obtained. In the suction side of the airfoil mesh quality is of $h/\eta = 0.574$ on average, while in the region of $1 \leqslant x/C \leqslant 3$ it is of $h/\eta = 0.857$, increasing slightly up to $h/\eta = 1.879$ at a distance

of x/C. Profiles of the local values of h/η at different positions for both meshes is given in figure 8.3. With these ratios between grid-size and Kolmogorov scale, the grid density obtained for both meshes should be fine enough for solving the smallest flow scales in the suction side of the airfoil and in the near wake.

This analysis has been also performed for LES grids at both AOA. The ratio h/η is of the order of 7-12 in the suction side and increases up to 16 in the near wake ($1 \leqslant x/C \leqslant 5$). As shown by Pope [21], dissipation peak occurs at $h/\eta \sim 24$, being the motions responsible for the dissipation of a scale larger than that of the Kolmogorov and in the range $8 < h/\eta < 60$. Thus, considering the ratios obtained, the grid density used should be capable of solving a large part of the dissipation spectrum. It should also be pointed out that in all the turbulent zone, compressed in both the suction side and the near wake, the ratio of the subgrid-scale viscosity to the molecular viscosity ν_{sgs}/ν has been of $\mathcal{O}\ (0.5 - 0.7)$ which gives an idea of the influence of the turbulent viscosity compared to the molecular one.

The resolution of the grid in the near-wall region has also been assessed by evaluating the grid size in the cells adjacent to the airfoil surface in wall-units. Being the friction velocity $u_\tau = \sqrt(\tau_w/\rho)$, where τ_w is the wall shear-stress, the distance from the wall measured in viscous length can be evaluated as $y^+ = u_\tau y/\nu$. In a similar manner the streamwise Δx^+ and spanwise Δz^+ cell sizes can be obtained. According to Piomelli & Chasnov [22], the accurate representation of the near-wall structures requires grids fine-enough for solving the near-wall gradients. Thus, the distance from the wall of the first control volume must be at $y^+ < 2$, and the grid spacings for the streamwise and spanwise directions of order $\Delta x^+ \simeq 50 - 150$ and $\Delta z^+ \simeq 15 - 40$, respectively. The near-wall grid resolution obtained with $LES - M2$ and for $AOA = 8°$ is plotted in figure 8.4. As can be seen from the figure, these requirements are well accomplished for the turbulent region $x/C > 0.4$.

8.3 Results

For obtaining the numerical results presented, simulations have been advanced in time until statistical stationary flow conditions have been achieved. According to the observations of several probes located in the suction side and in the near wake of the airfoil, this occurs after about 15 time-units ($TU = tU_ref/C$). Once the initial transient has been washed out, results have been obtained based on the integration of instantaneous data over a sufficiently long-time period. It has been found, that to achieve well-converged first and second order statistics in the different zones, at least 60 TU must be integrated for $AOA = 5°$. However, as the physics at $AOA = 8°$ is more complex, with a larger detached zone, for this AOA it has been necessary to integrated 100 TU. For all LES computations, statistics have been averaged over 200 TU.

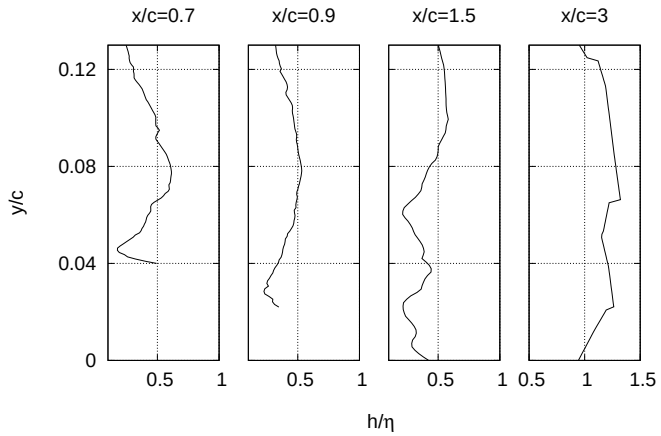

(a)

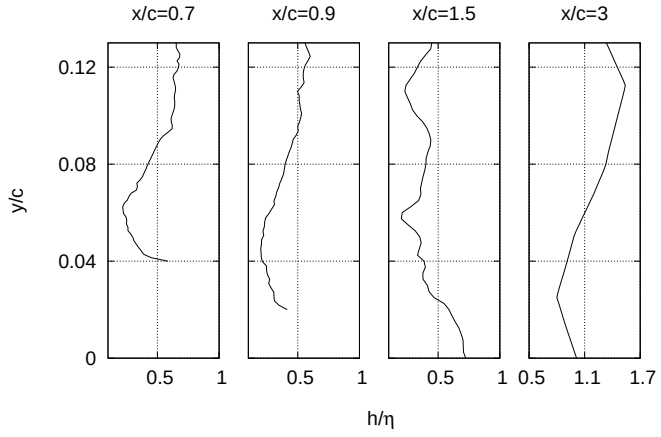

(b)

Figure 8.3: Ratio of h/η at different positions. a) mesh $DNS-5$; b) mesh $DNS-8$

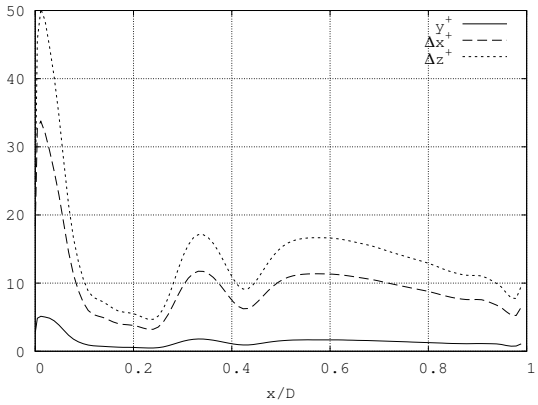

Figure 8.4: Mesh resolution near the wall obtained with mesh $LES - M2$ and for $AOA = 8^{\circ}$

8.3.1 Flow structure

In order to gain insight into the coherent structures developed in the separated zone, these structures have been identified. There are several techniques for their identification (see for instance [23, 24]). In this paper, the Q-criterion proposed by Hunt et al. [23] has been used. This method is based on the second invariant of the velocity gradient tensor $\nabla \mathbf{u}$. Definition and interpretations of the $\nabla \mathbf{u}$ invariants can be found in Chong et. al. [25]. The velocity gradient tensor can be decomposed into a symmetric (rate-of-strain, $\mathbf{S}$) and a skew-symmetric (rate-of-rotation, $\mathbf{\Omega}$) components. The second invariant of $\nabla \mathbf{u}$ is,

$$Q = \frac{1}{2}(\| \mathbf{\Omega} \|^2 - \| \mathbf{S} \|^2) \tag{8.2}$$

where $\| \mathbf{\Omega} \|^2$ and $\| \mathbf{S} \|^2$ are the trace of the skew-symmetric and symmetric components of $\nabla \mathbf{u}$. The Q-criterion defines an eddy structure as a region with positive second invariant (Q), i.e. regions where rotation dominates over strain.

Instantaneous Q-isocontours for DNS and LES data at both angles-of-attack are depicted in figure 8.5. A first inspection to the figures reveal the large quantity of small scales in the separated zone captured by DNS at both AOA. As expected, the flow separates laminarly from the leading edge of the airfoil and, transition to turbulence occurs in the separated shear-layer. Flow separation occurs as a consequence of the adverse pressure gradient on the suction side of the airfoil which leads to the formation of a LSB. Due to the strong pressure gradient, disturbances in the laminar separated shear-layer get amplified as the flow moves downstream triggering

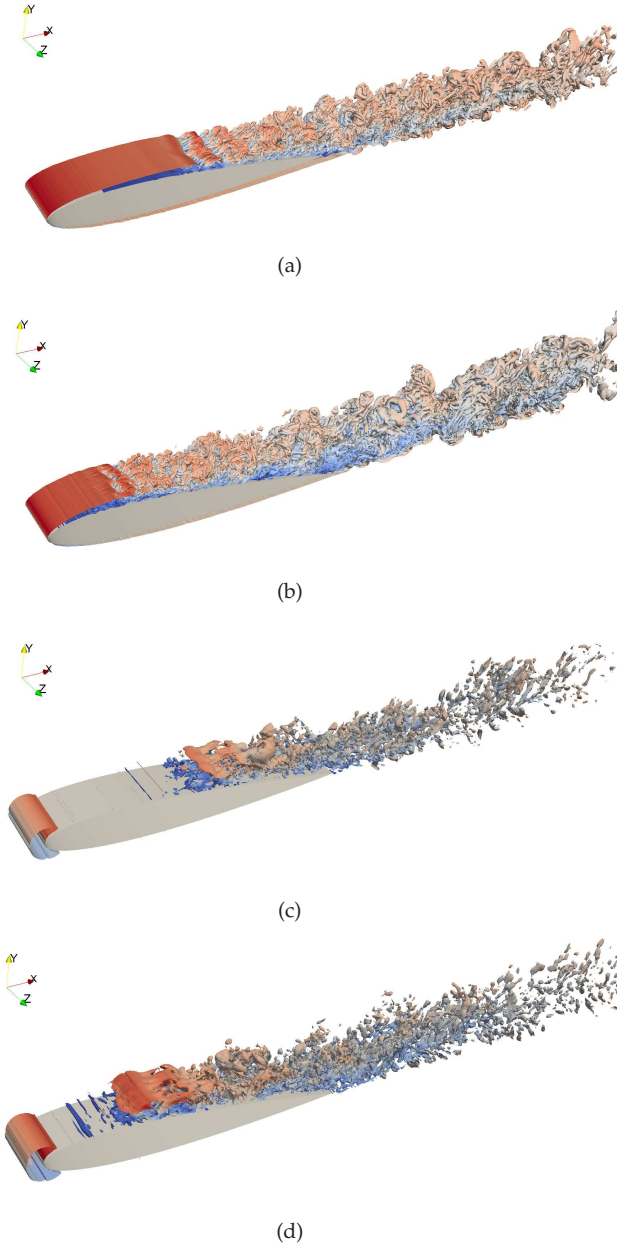

(a)

(b)

(c)

(d)

Figure 8.5: Isocontours of the second invariant of the velocity gradient. (a) DNS results, $AOA = 5°$; (b) DNS results, $AOA = 8°$; (c) LES results, $AOA = 5°$; (d) LES results, $AOA = 8°$.

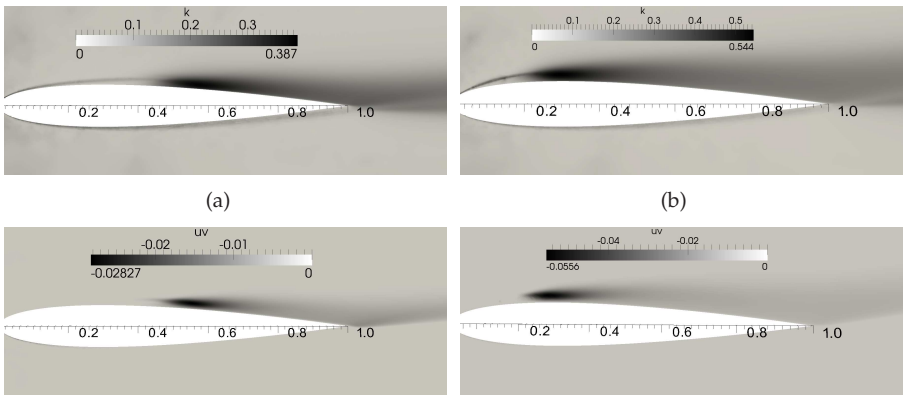

Figure 8.6: Results from DNS simulations: (left) for $AOA = 5°$; (right) for $AOA = 8°$. (a,b) Average turbulent kinetic energy and (c,d) Turbulent shear-stresses in the suction side.

the transition to turbulence. At the end of the laminar shear-layer, the instabilities are clearly observed, forming corrugated structures which interact with small-scale structures within the recirculation region. These corrugated structures, when separate from the shear-layer, can be seen as streamwise vortices which feed the detached zone. As the flow moves downstream into the separated zone and the wake, streamwise structures are distorted by the interaction with spanwise vorticity evolving into complicated structures as can be observed at both AOA.

As the AOA increases, the adverse pressure-gradient increases and the flow is decelerated, which results in a movement of the laminar separation point toward the leading-edge increasing the height of the separated bubble, while at the same time, the turbulent separated region moves forward from the trailing edge. Due to the increase in the turbulent shear stress after transition, the flow reattaches to the airfoil surface with the decrease in the pressure coefficient after reattachment. In the figures can also be observed, that with the increase in the AOA the bubble length decreases.

This can also be observed in the profiles of the turbulent shear stresses and turbulent kinetic energy from our simulations (see figure 8.6). In the figure the average turbulent kinetic energy and the turbulent shear-stresses for both AOA are depicted. The turbulent shear stress, which causes the transport of momentum in the boundary layer, is also responsible for the closure of the laminar separation bubble. The high values of turbulent shear stresses and turbulent kinetic energy in the region near the reattachment are strongly related with the vortex breakdown and theturbu-

Case	c_L	c_D	x_{sep}	x_{reat}
	$AOA = 5°$			
DNS	0.569	0.0291	0.0645	0.566
VMS-LES-M1	0.582	0.0248	0.140	0.571
VMS-LES-M2	0.561	0.0242	0.117	0.548
QR-LES-M1	0.586	0.0369	0.156	0.700
QR-LES-M2	0.565	0.0252	0.117	0.607
	$AOA = 8°$			
DNS	0.759	0.0497	0.0241	0.320
VMS-LES-M1	0.784	0.0536	0.0847	0.392
VMS-LES-M2	0.750	0.0460	0.0546	0.386
QR-LES-M1	0.805	0.0510	0.119	0.490
QR-LES-M2	0.760	0.0517	0.0833	0.418

Table 8.2: Aerodynamic coefficients for the DNS and LES cases. $Re = 5 \cdot 10^4$.

lent transport.

In addition, in figures 8.5c and 8.5 Q-isocontours obtained with QR-model are plotted. As can be seen, LES models are also capable of capturing the transition to turbulence and the large number of turbulent scales in both, the separated region and the airfoil wake.

8.3.2 LES results

In table 8.2 the main flow characteristics obtained with both models are compared with DNS results. As can be observed, both models predicts drag and lift coefficients with reasonable agreement even with the coarse grid. In the case of the length of the recirculation bubble, a closer prediction is obtained with the finest grid, as expected. Although both models predict a separation bubble slightly larger than DNS, in both cases this value decreases with the mesh refinement. In fact, for the finest grid the prediction of the LSB and the transition to turbulence compared reasonably well to the DNS data. This is mainly due to the resolution of the grid en the laminar zone close to the detachment point, where a fine grid is required in order to well predict the position of this point. This behaviour can be attributed to the fact that models give $\nu_{sgs} = 0$ in the laminar zone, thus being necessary a near DNS grid.

The detailed comparison of the local data should allow to the evaluation of how both SGS models are performing. In figures 8.7 and 8.8 a comparison of the streamwise velocity profiles at different positions of the airfoil surface and wake are plotted for both models and AOAs. Although for both models a very good prediction of this

quantity compared to the DNS results is achieved, it is observed that VMS-WALE model presents a better trend as the mesh is refined. Largest differences are observed in the transitional region specially at $x/C = 0.4$ for $AOA = 8°$, as both models over-predict the reattachment location. However, both models recover the velocity profile of the DNS in the fully turbulent zone where the fluid is detached.

In figures 8.9 and 8.10, Reynolds streamwise normal and shear stresses at different position in the suction side and in the near wake are compared to the DNS data for $AOA = 8°$. For the sake of brevity we are only presenting the comparison for $AOA = 8°$ as this case is more challenging than $AOA = 5°$, with a largest vortex breakdown region and higher turbulence intensities.

In the figures can be seen that, contrary to first-order statistics which are well predicted even with the coarse grid, the finest grid is required for a better prediction of the velocity fluctuations and Reynolds shear-stresses. Again, as for the streamwise velocity, VMS-WALE behaves better and its trend to predict DNS results as the grid is refined is better than QR-model. Yet, it might be said that both models are good choices for predicting the flow with massive separation which is specially true for the fiest grid.

Considering both, the integral quantities of table 8.2 and the local profiles of first- and second-order statistics, QR model is slightly less accurate than VMS-WALE with the coarser mesh. This behaviour may be related to an excessive dissipation at the large scales of the flow. This dissipation is always present but it is more apparent on coarser meshes. On the other hand, the scale separation of the VMS methodology prevents the model to alter the larger scales of the flow, allowing the VMS-WALE to predict quite accurately the general behaviour of the flow even with very coarse meshes. However, with finer grids both models yield quite similar results.

8.3.3 Challenging LES

As have been shown, both models are capable of predicting the behaviour of the flow, specially in the separated zones. The key success can be attributed to the use of a conservative formulation, which preserves well the kinetic energy balance even on coarse grids. After these encouraging results, it would be desirable to further test both SGS models in more challenging situations at higher Reynolds numbers. Hereafter two cases have been studied: i) the flow past a NACA 0012 at $Re = 1.44 \times 10^6$ for different AOAs and ii) the flow past a DU-93-W-210 dedicated airfoil for wind turbines at 3×10^6 and AOAs up to $16°$. In both cases, numerical results have been compared with experimental results from the literature.

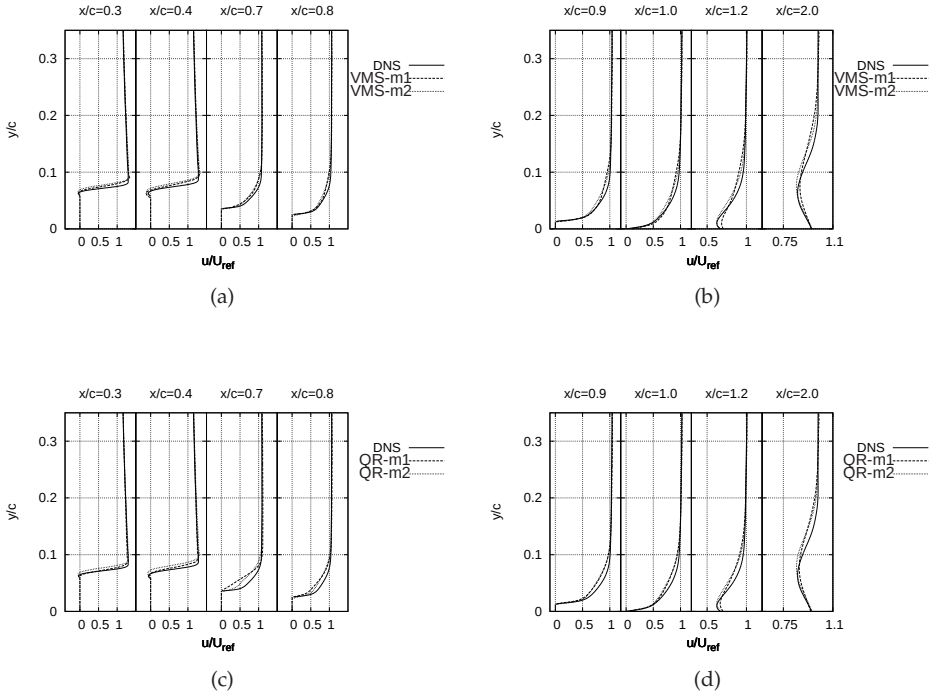

Figure 8.7: LES results for the streamwise velocity at different positions of the airfoil surface and wake compared with DNS data at $AOA = 5^{\circ}$. (a,b) VMS-WALE; (c,d) QR-model

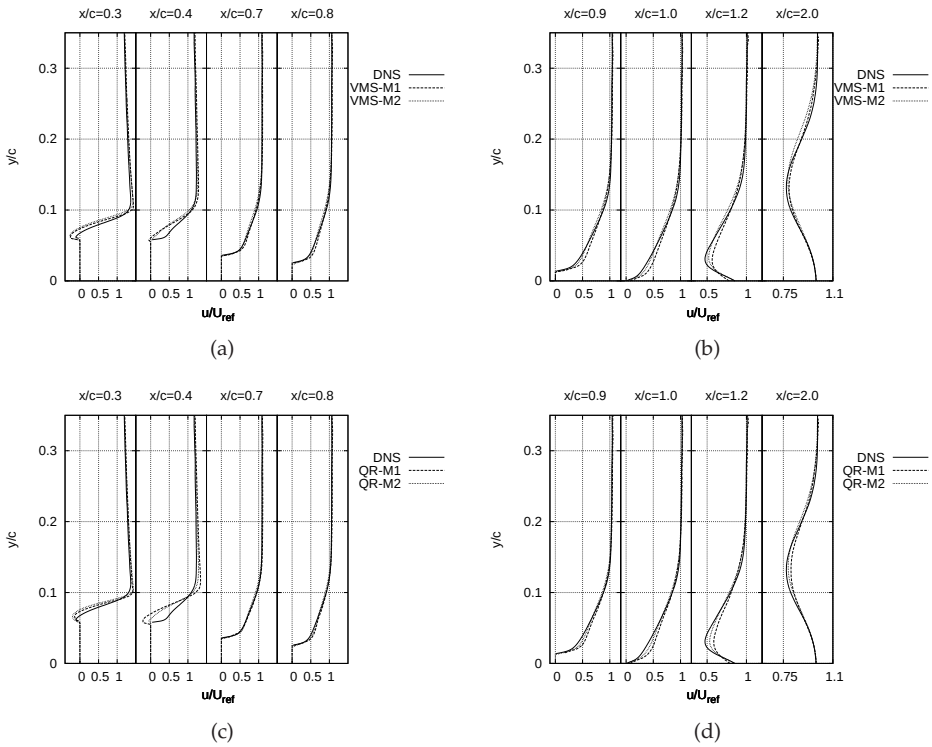

Figure 8.8: LES results for the streamwise velocity at different positions of the airfoil surface and wake compared with DNS data at $AOA = 8°$. (a,b) VMS-WALE; (c,d) QR-model

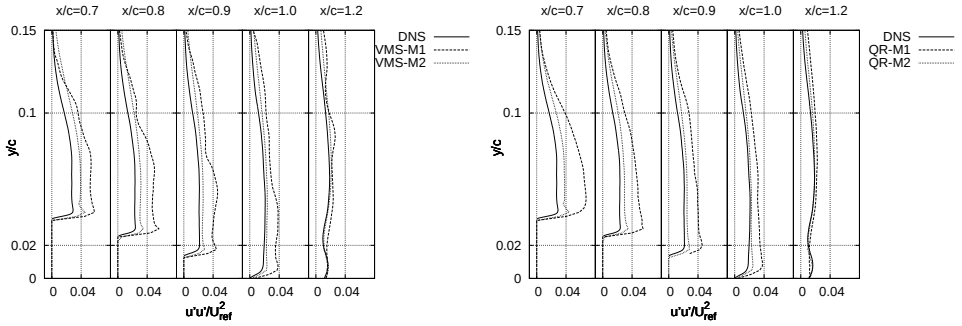

(a) (b)

Figure 8.9: LES results for the Reynolds streamwise normal stress at different positions of the airfoil surface and wake compared with DNS data at $AOA = 8°$.

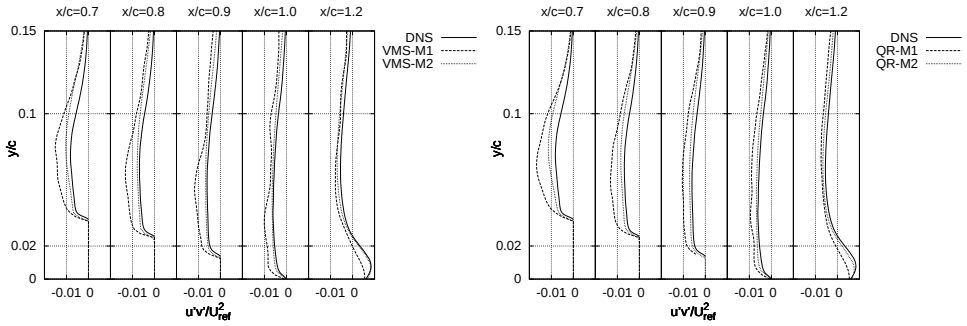

(a) (b)

Figure 8.10: LES results for the Reynolds shear-stress at different positions of the airfoil surface and wake compared with DNS data at $AOA = 8°$.

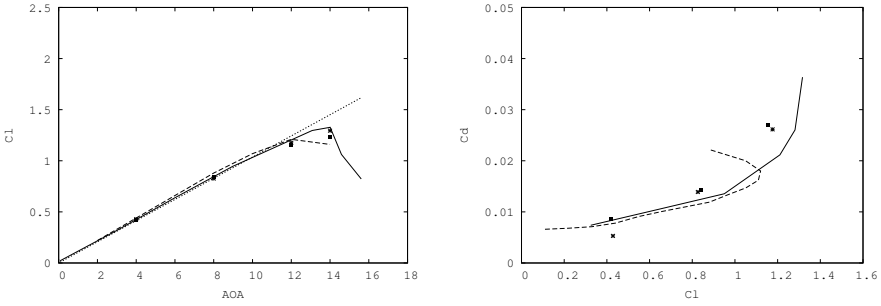

(a) (b)

Figure 8.11: Drag and lift coefficients at different AOAs. Comparison with experimental data from different sources: solid line: experiments from Gregory and O'Reilly [27]; dotted line: experiments from McCorskey [26]; dashed line: experiments from Sheldahl and Klimas [28]; solid squares: VMS-WALE; stars QR-model. a) Drag coefficient. b)Lift vs. drag coefficient.

Flow past a NACA 0012 at $Re = 1.44 \times 10^6$

Stall on airfoils is caused by massive separation of the flow leading to a sharp drop in the lift and an increase in the drag over the airfoil surface. NACA 0012 airfoil exhibits two types of stall. A trailing-edge stall at all Reynolds numbers and a combined leading-edge/trailing-edge stall at intermediate Reynolds number [26]. The latter shows the combined presence at stall of a turbulent boundary layer separation moving forward from the trailing-edge and a small laminar bubble in the leading-edge region failing to reattach which complete the flow breakdown. Thus, it is of interest to test the capability of SGS models to deal with these complex physics.

The selected Reynolds number to asses the performance of SGS models is $Re = 1.44 \times 10^6$ with $AOA = 4°, 8°, 12°, 14°$. Similar to the previous section, the three-dimensional (3D) physical domain of the simulation consist of $40C \times 40C \times 0.2C$ with the airfoil at its center. Simulations have been performed on unstructured grids of 149355×32 planes (about 4.8MCVs). Notice that the same mesh have been used for all the different AOA.

LES results have been compared with correlated experimental data which was obtained in more than 40 wind tunnels [26]. However, these correlations are not suitable when laminar separation bubble are presented in the profile. Thus, for these cases experimental data from Gregory and C. L. O'Reilly at $Re = 1.44 \times 10^6$ [27] and Sheldahl and Klimas at $Re = 2 \times 10^6$ [28] have been used in the assessment of the models.

Lift and drag coefficients at different AOA obtained with both models are de-

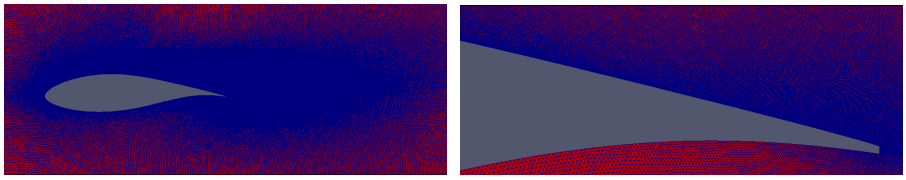

(a) (b)

Figure 8.12: Detail of the mesh for LES simulations of DU-93-W-210 airfoil.

picted in figure 8.11. These results are quite satisfactory considering the grid used which is quite coarse for the Reynolds number under study. For the higher AOA, errors in the drag coefficient prediction near stall and in stall, are the largest. At this point, it should be pointed out that concerning the comparison with experimental measurements, there are different facts such as free-stream turbulence in experiments or end-conditions, surface roughness, among others, which might lead to the scattering in the results, specially when drag coefficient is compared. The magnitude of this aerodynamic coefficient is quite low (if compared to lift) and thus, difficult to measure accurately. Thus, it might be kept in mind that although comparisons between numerical and experimental results are helpful in order to provide a good estimation of how a model behaves, differences obtained might also be attributed to the different conditions between experiments and numerics, in especial related to the turbulence level of the inlet flow.

Flow past a DU-93-W-210 at $Re = 3 \times 10^6$

This case corresponds with an aerodynamic profile designed at Delft University for wind energy applications. It was designed so as to achieve a high lift-to-drag ratio. As reported in [29], the airfoil exhibits a high lift-to-drag ratio of 143 at $Re = 3 \times 10^6$ and a maximum lift of 1.35. The Reynolds number studied in this case has been $Re = 3 \times 10^6$, which corresponds with the maximum high-to-lift ratio for this profile. Two different grids of 73086×16 planes ($\sim$ 1.2MCVs) and 594088×32 planes ($\sim$ 19MCVs) has been considered. It should be pointed out, that in the process of mesh generation, grids have been optimized for AOAs between 2 and 16 $^\circ$. In figure 8.12 a detail of the mesh of the plane in the region of the airfoil is depicted. As can be seen, control volumes have been clustered near the airfoil surface, in particular in the suction side.

With the finest mesh, LES results show that the maximum lift coefficient is obtained at an AOA of 8 degrees with a value of 1.32, which is only a 2.2% smaller than the value measured in experiments. In figure 8.13, the flow configuration at

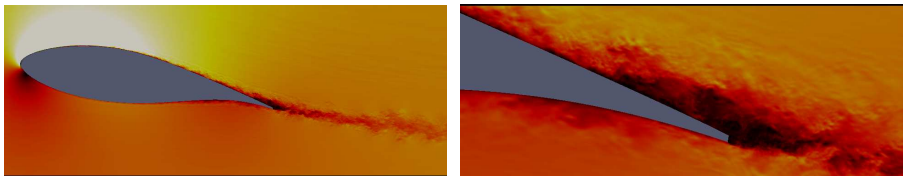

(a) (b)

Figure 8.13: Flow configuration for DU-93-W-210 airfoil. Velocity magnitude.

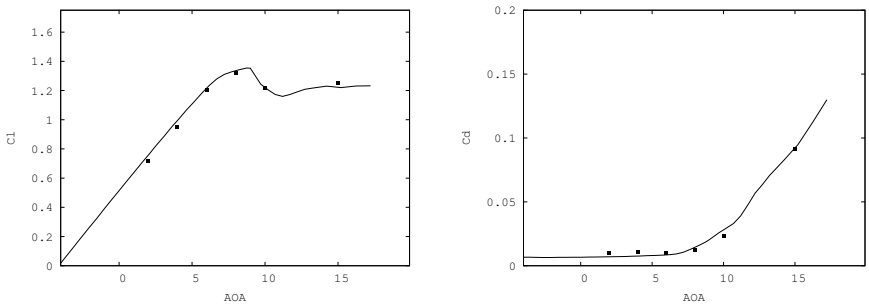

(a) (b)

Figure 8.14: Drag and lift coefficients at different AOAs. Comparison with experimental data from Timmer and van Rooij [29] (solid lines); VMS-WALE solid squares. a) Lift coefficient. b) Drag coefficient

this AOA is plotted. The stall region is present for AOAs larger than $10°$. A complete comparison of aerodynamic coefficients against experimental data from Timmer and van Rooij [29] is depicted in figures 8.14(a) and 8.14(b). A very good agreement between the calculated results and the experimental ones has been achieved, specially at angles of attack with important boundary layer detachment i.e. near stall and post-stall zones. It should be noted, that a fair agreement between the coarse mesh and the fine mesh has been obtained for AOAs larger than $8°$ (not shown here). This agreement was expected since our LES models are very accurate on detached flow regions. However, for the lineal and pre-stall region the coarse mesh clearly underpredicts the values of the lift coefficient.

8.4 Conclusions

The capabilities of two sub-grid scale models for predicting the flow past aerodynamic profiles using unstructured grids have been investigated. The models studied are: the wall-adapting eddy-viscosity model within a variational multiscale framework (VMS-WALE) and the QR-model based on the invariants of the rate-of-strain tensor. These models are well suited for working with unstructured grids as they do not use the wall-units coordinates in their formulation. In addition, one of their advantages is that the eddy-viscosity vanishes in any laminar or two-dimensional flow, or in the near wall region.

A second-order spectro-consistent scheme for collocated and unstructured grids has been used in the discretisation of the governing equations. The conservation properties ensure good stability and conservation of the kinetic-energy balance with coarse meshes even at high Reynolds numbers. All the results have been computed on unstructured grids generated by the constant-step extrusion of a two-dimensional unstructured grid. For solving the Poisson equation, which arises from the incompressibility constrain a Fourier diagonalization method which takes advantage of the homogeneity of our discretisation in the spanwise direction has been used. The methodology developed for solving bluff bodies using unstructured grids has allowed to accurately solve the flow with very good results.

In order to assess the performance of these models, the flow past a NACA 0012 airfoil at $Re = 5 \times 10^4$ and angles of attack of $AOA = 5°,\ 8°$ have been studied. Both cases exhibit laminar separation and transition to turbulence in the separated shear-layer. Direct comparisons of the first- and second-order statistics against direct numerical simulations (DNS) results have been done. This DNS data has also been computed at the same AOAs considered. Both models perform quite well being capable of predicting separation and transition to turbulence, as well as the fully developed turbulence in the wake. Yet, in coarser grids the VMS-WALE presents a better behaviour than QR-model. This behaviour is attributed to an excessive dissipation of the QR-model at the largest scales of the flow. This extra dissipation is prevented by the VMS methodology as by means of the scale separation, the model does not alter the largest scales. However as has been shown, as the grid is refined both models yield similar results and converge to DNS solution.

In addition, two more challenging cases at higher Reynolds numbers and different AOA have been also carried out. The cases considered are: i) the flow past a NACA 0012 at $Re = 1.44 \times 10^6$ for different AOAs and ii) the flow past a DU-93-W-210 dedicated airfoil for wind turbines at 3×10^6 and AOAs up to $16°$. In both cases, numerical results have been compared with experimental results from the literature. Lift coefficient is predicted within an acceptable error considering the grids used. For the higher AOAs, errors in the drag coefficient prediction are the largest, specially in the flow past a NACA 0012 airfoil, but differences might be attributed

not only to the numerical results, but also to the differences in conditions with the experimental data.

As a final remark, it should be pointed out that the good results obtained with both models should in part be attributed to the non-dissipative formulation used. This conservative formulation which preserves well the kinetic energy balance even on coarse grids, is the key success of the SGS models used and together with the use of unstructured grids might be a step towards the use of LES models for solving industrial flows on complex geometries at high Reynolds numbers.

References

[1] Y. Hoarau, D. Faghani, M. Braza, R. Perrin, Anne-Archard, and Ruiz. Direct numerical simulation of the three-dimensional transition to turbulence in the incompressible flow around a wing. *Flow, Turbulence and Combustion*, 71:119–132, 2003.

[2] H. Shan, L. Jiang, and C. Liu. Direct numerical simulation of flow separation around a naca 0012 airfoil. *Computers & Fluids*, 34(9):1096–1114, 2005.

[3] L.E. Jones, R.D. Sandberg, and N.D. Sandham. Direct numerical simulations of forced and unforced separation bubbles on an airfoil at incidence. *Journal of Fluid Mechanics*, 602:175–207, 2008.

[4] A Baez, Lehmkuhl O., I. Rodriguez, and C.D. Perez-Segarra. Direct Numerical Simulation of the turbulent flow around a NACA 0012 airfoil at different angles of attack. In *Parallel CFD 2011*, 2011.

[5] R.J.A. Janssen and R.A.W.M. Henkes. Influence of prandtl number on instability mechanisms and transition in a differentially heated square cavity. *Journal of Fluid Mechanics*, pages 319–344, 1995.

[6] L. Davidson, D. Cokljat, J. Frohlich, M.A. Leschziner, C. Mellen, and W. Rodi. *Lesfoil Large Eddy Simulation of Flow Around a High Lift Airfoil: Results of the Project Lesfoil Supported by the European Union 1998 - 2001*. Notes on Numerical Fluid Mechanics and Multidisciplinary Design Series. Springer, 2003.

[7] N. Jovicic and M. Breuerf. *High-Performance computing in turbulence research: Separated flow past an airfoil at high angle of attack*. Springer, 2004.

[8] M. Germano, U. Piomelli, P. Moin, and W. Cabot. A Dynamic Subgrid-Scale Eddy Viscosity Model. *Physics of Fluids A*, 7(3):1760–1765, 1991.

[9] Sven Eisenbach and Rainer Friedrich. Large-eddy simulation of flow separation on an airfoil at a high angle of attack and ReÂ =Â 105 using Cartesian grids. *Theoretical and Computational Fluid Dynamics*, 22(3-4):213–225, December 2007.

[10] Weixing Yuan, Mahmood Khalid, Jan Windte, Ulrich Scholz, and Rolf Radespiel. An investigation of low-reynolds-number flows past airfoils. In *Proceedings of the 23rd AIAA Applied Aerodynamics Conference, Canada*, 2005.

[11] M. C. Galbraith and M. R. Visbal. Implicit large eddy simulation of low reynolds number flow past the SD 7003 airfoil. In *Proceedings of the 46 AIAA Aerospace Sciences Meeting and Exhibit, Reno*, pages AIAA paper 2008–225, 2008.

[12] Ying Zhou and ZJ Wang. Implicit Large Eddy Simulation of Transitional Flow over a SD7003 Wing Using High-order Spectral Difference Method. *AIAA Paper*, 4442(July):2010, 2010.

[13] Assad a. Oberai, Thomas J. R. Hughes, and Farzam Roknaldin. Computation of Trailing-Edge Noise Due to Turbulent Flow over an Airfoil. *AIAA Journal*, 40(11):2206–2216, November 2002.

[14] H Kim, S Lee, and N Fujisawa. Computation of unsteady flow and aerodynamic noise of NACA0018 airfoil using large-eddy simulation. *International Journal of Heat and Fluid Flow*, 27(2):229–242, April 2006.

[15] Olivier Marsden, Christophe Bogey, and Christophe Bailly. Direct Noise Computation of the Turbulent Flow Around a Zero-Incidence Airfoil. *AIAA Journal*, 46(4):874–883, April 2008.

[16] K Mahesh, G Constantinescu, and P. Moin. A numerical method for large-eddy simulation in complex geometries. *Journal of Computational Physics*, 197(1):215–240, June 2004.

[17] F. Nicoud and F. Ducros. Subgrid-scale stress modelling based on the square of the velocity gradient tensor. *Flow, Turbulence and Combustion*, 62:183–200, 1999.

[18] T.J.R. Hughes, L. Mazzei, and K.E. Jansen. Large eddy simulation and the variational multiscale method. *Computing and Visualization in Science*, 3:47–59, 2000.

[19] R. Verstappen. When does eddy viscosity damp subfilter scales sufficiently? In ERCOFTAC Series, editor, *Quality and Reliability of Large-Eddy Simulations II*, volume 16, pages 421–430, 2011.

[20] O. Lehmkuhl, A. Baez, I. Rodríguez, and C. D. Perez-Segarra. Direct numerical simulation and Large-Eddy simulations of the turbulent flow around a NACA-0012 airfoil. In *7th International Conference on Computational Heat and Mass Transfer*, pages 1–8, 2011.

[21] S.B. Pope. *Turbulent Flows*. Cambridge University Press, 2000.

[22] U. Piomelli and J. R Chasnov. *Transition and turbulence modelling*, chapter Large-eddy simulations and applications, pages 269–331. Kluwer Academic Publishers, Dordrecht, 1996.

[23] J.C.R. Hunt, A.A. Wray, and P. Moin. Eddies, stream and convergence zones in turbulent flows. Technical Report CTR-S88, Center for turbulent research, 1988.

[24] J. Jeong and Hussain Fazle. On the identification of a vortex. *Journal of Fluids Mechanics*, 285(69–94), 1995.

[25] M. S. Chong, a. E. Perry, and B. J. Cantwell. A general classification of three-dimensional flow fields. *Physics of Fluids A: Fluid Dynamics*, 2(5):765, 1990.

[26] W.J. McCroskey. A critical assessment of wind tunnel results for the NACA 0012 airfoil. Technical report, National Aeronautics and Space Administration, 1987.

[27] N. Gregory and C.L. O'Reilly. Loww-speed aerodynamic characteristics of a naca 0012 airfoil section, including the effects of upper-surface roughness simulating hoar frost. Technical report, Ministry of Defence. Aeronautical Research council, London, 1973.

[28] R.E. Sheldahl and P.C. Klimas. Aerodynamics characteristics of seven symmetrical airfoil sections through 180-degrees angle of attack for use in aerodynamic analysis of vertical axis turbines. Technical report, Sandia National laboratories, 1980.

[29] W. a. Timmer and R. P. J. O. M. van Rooij. Summary of the Delft University Wind Turbine Dedicated Airfoils. *Journal of Solar Energy Engineering*, 125(4):488, 2003.

Chapter 9

Conclusions and further work

A conservative discretization for unstructured meshes together with an efficient self-adaptive strategy for the explicit time-integration of Navier-Stokes equations have been presented in Chapter 2. The spatial discretization preserves the symmetry properties of the continuous differential operator and ensure both, stability and conservation of the global kinetic energy balance on any grid. Together with the advantages of the conservative formulation, the time-integration proposed has an advantage respect standard approaches in terms of computational cost. The advantage of the proposed method becomes more significant for highly skewed meshes where the CFL-based criteria tend to under-predict the eigenvalues of the dynamical system. Such effect becomes even more relevant on unstructured formulations. In practice, the method has been successfully tested on both a Cartesian staggered and an unstructured collocated codes leading to CPU cost reductions of of up to 2.9 and 4.3, respectively. Therefore, it constitutes a robust and easy-to-implement approach for the time-integration of incompressible turbulent flows.

In Chapter 3, different LES model which are suitable for unstructured grids have been presented. In addition, regularization models have been also presented. This kind of models are directly dependent on the filtering procedure. Thus, the influence of the filter on the modelling has been analysed by means of a detailed study of the properties of standard filters for unstructured grids. It has been shown, that filters based on least-squares minimization procedures are not suitable for regularization models since they are not symmetrical. Furthermore, it has also been proven that it is not possible to force their symmetry because this operation breaks the local properties of the original least-squares reconstruction filter.

Following the presentation of the different LES models, their assessment have been carried out. First, in Chapter 4, regularization models have been tested by means of the simulation of different cases with different level of complexity of the mesh. From a structured grid to a very complex mesh, with zones a hybrid mesh of prism and tetrahedral control volumes. It has been shown, that regularization models are very dependent on the quality of the filtering process. Although good results can be obtained with structured or smooth unstructured meshes, their performance

is affected under fully irregular unstructured grids. Due to the bad quality of the filtering, first- and second-order statistics diverge from the expected results. As a possible remedy to this issue, the $\mathcal{C}_4$ model has been formulated within a LES template. Results obtained with this new approach seems very promising but further research is still required.

Closing the first part of the thesis, the assessment of LES models have been carried out in a natural convection case in Chapter 5. The Rayleigh-Benard convection in a cylindrical enclosure. For the study, first a DNS has been performed with a large integration time and then LES have been computed. Comparison with the different SGS models show that in general as the grid is refined all models behave quite well, in special at the core of the cavity where the turbulence is almost homogeneous. Largest differences are observed off the center of the cavity. Although even without model a good approach to reference data is observed, QR and DEV models predictions are in better agreement even with the coarser grid. However, if CPU time is considered, then QR model is the best alternative as it is essentially not more complicated to implement in a LES-code than the standard Smagorinsky model (with $\mathcal{C}_s$ constant) and is faster than DEV model. The comparison of the average Nusselt number shows that this quantity is quite well predicted even for the coarse grid and without model. These good results can be attributed to the use of a conservative formulation, which preserves the kinetic-energy balance, together with the large integration time used, ensuring converged temporal statistics.

In Chapter 6 direct numerical simulations of the turbulent flow past a sphere at Reynolds numbers of 3700 and 10000 have been carried out. Computations have allowed to analyse the influence of shear-layer vortices and vortex shedding process in the wake configuration at these subcritical Reynolds numbers. The instantaneous analysis of the wake has revealed that its structure is quite similar at both Reynolds numbers, i.e. it exhibits a helical-like configuration due to the instabilities in the shear layer which occur at random azimuthal positions. However, significant differences in the flow dynamics have also been observed. At $Re = 3700$, the onset of the vortex roll-up due to instabilities in the shear layer occurs locally which determines the position where the vortex are shed, but at $Re = 10000$, shear-layer instabilities evolve as corrugated structures along the azimuthal direction which separate from the shear-layer as vortex rings. With the increase in the Reynolds number, these instabilities move closer to the separation point with the consequent shrinkage of the vortex formation region. It has been observed, that similar to the wake behind a cylinder, variations in the vortex formation region are related to the base-suction coefficient C_{pb}, i.e., as the base-suction increases the formation region is shortened. In the analysis of the spectra of both flows has been identified a mechanism through which low-frequency large-scale flow affects the underlying turbulence and consequently, the wake characteristics. As a result of the wake modulation, large inte-

gration times are required to capture properly the shrinkage and enlargement of the recirculation region and hence, to achieve well converged statistics in the wake zone.

The study of the wake configuration of the flow past a circular cylinder has been carried out by means of the DNS at $Re_D = 3900$ has been done in Chapter 7. The analysis of the spectra of the velocity at different locations in the vortex formation zone, suggests that together with the vortex-shedding frequency and the small-scale Kelvin-Helmholtz instabilities frequency, there is also a low-frequency which can be attributed to the shrinkage and enlargement of the recirculation region. This low-frequency, measured from the analysis of several probes in the vortex formation region, is of $f_m = 0.0064$. This modulation of the recirculation zone can be seen as two alternating wake configurations which have been identified as i) a high-energy mode with larger fluctuations in the shear-layer (Mode H) and ii) a low-energy mode with weaker fluctuations in the shear layer (Mode L). This low-frequency has been shown to be the main cause of the large scattering of solutions registered in the literature. Thus, in order to gain insight into the configuration of the wake, partial statistics in each mode have been computed revealing the main differences between them, which are due to the difference in fluctuations in the near wake. Mode H has been shown to be more energetic than mode L, and as as a consequence of such strong vortex-shedding the vortex formation region decreases. Furthermore, by means of cross-correlation between the base pressure and the stream-wise velocity in the wake centreline, it has been shown that both variables are negative correlated. As the suction base pressure gets more negative, the stream-wise velocity increases and as a consequence, the vortex formation zone decreases.

The capabilities of two sub-grid scale models for predicting the flow past aerodynamic profiles using unstructured grids have been investigated in Chapter 8 . The models studied are: the wall-adapting eddy-viscosity model within a variational multiscale framework (VMS-WALE) and the QR-model based on the invariants of the rate-of-strain tensor. In order to assess the performance of these models, the flow past a NACA 0012 airfoil at $Re = 5 \times 10^4$ and angles of attack of $AOA = 5^\circ, 8^\circ$ have been studied. Both cases exhibit laminar separation and transition to turbulence in the separated shear-layer. Direct comparisons of the first- and second-order statistics against direct numerical simulations (DNS) results have been done. This DNS data has also been computed at the same AOAs considered. Both models perform quite well being capable of predicting separation and transition to turbulence, as well as the fully developed turbulence in the wake. Yet, in coarser grids the VMS-WALE presents a better behaviour than QR-model. This behaviour is attributed to an excessive dissipation of the QR-model at the largest scales of the flow. In addition, two more challenging cases at higher Reynolds numbers and different AOA have been also carried out. The cases considered are: i) the flow past a NACA 0012 at $Re = 1.44 \times 10^6$ for different AOAs and ii) the flow past a DU-93-W-210 dedicated

airfoil for wind turbines at 3×10^6 and AOAs up to $16°$. It should be pointed out that the good results obtained with both models should in part be attributed to the non-dissipative formulation used. This conservative formulation which preserves well the kinetic energy balance even on coarse grids, is the key success of the SGS models used and together with the use of unstructured grids might be a step towards the use of LES models for solving industrial flows on complex geometries at high Reynolds numbers.

Further Work

The main result of the present Ph.D. is a robust kernel to simulate turbulent flows on complex geometries. This methodology has been tested in several turbulent flows going from more canonical DNS cases to industrial complex configurations using the same CFD code. Now this kernel has been extended to include multi-physics by others researchers of CTTC and Termo Fluids S.L. with my collaboration. This work in some cases is at its beginning stage and in others is quite finished. Some of the topics we are currently working on are: Multiphase flow [1, 2], Reactive flow [3], Compressible flow [4], Dynamic mesh methods [5], Fluid and Structure Interaction [6], Non-Newtonian Fluids [7] and Simulations of Multi-physics Multiscale Systems [8].

References

[1] Ll. Jofre, N. Balcazar, O. Lehmkuhl, J. Castro, and A. Oliva. Numerical study of the incompressible Richtmyer-Meshkov instability. Interface traking methods on general meshes. *Conference on Modelling Fluid Flow. The 15th International Conference on Fluid Flow Technologies.*, September 2012.

[2] N. Balcazar, Ll. Jofre, O. Lehmkuhl, J. Rigola, and J. Castro. Numerical simulation of incompressible two phase flow by conservative level set method. *Conference on Modelling Fluid Flow. The 15th International Conference on Fluid Flow Technologies.*, September 2012.

[3] J. Ventosa, J. Chiva, O. Lehmkuhl, C. D. Pérez-Segarra, and A. Oliva. Low Mach Navier-Stokes equations on unstructured meshes. *Conference on Modelling Fluid Flow. The 15th International Conference on Fluid Flow Technologies.*, September 2012.

[4] A. Baez-Vidal, O. Lehmkuhl, C. D. Pérez-Segarra, and A. Oliva. A filtred kinetic energy preserving finite volume scheme for compressible fliows. *Conference on Modelling Fluid Flow. The 15th International Conference on Fluid Flow Technologies.*, September 2012.

[5] O. Estruch, R. Borell, O. Lehmkuhl, and C. D. Pérez-Segarra. A parallel radial basis function method for unstructured dynamic meshes. *24th International Conference on Parallell CFD 2012*, May 2012.

[6] O. Estruch, O. Lehmkuhl, R. Borell, and C. D. Pérez-Segarra. Large-eddy simulation of turbulent FSI. *7th Symposium on Turbulence, Heat and Mass Transfer*, September 2012.

[7] A. Carmona, C. D. Pérez-Segarra, O. Lehmkuhl, and A. Oliva. Benchmark solutions for the fluid flow and the heat transfer of viscoplastic-type non-Newtonian fluids. *6th European Thermal Sciences Conference*, September 2012.

[8] J. Lopez, O. Lehmkuhl, R. Damle, and J. Rigola. A parallel and object-oriented general purpose code for Simulation of Multiphysics and Multiscale Systems. *24th International Conference on Parallell CFD 2012*, May 2012.

Appendix A

Determining the region of stability for the 1D test problem

The problem under consideration reads

$$\left(\kappa+\frac{1}{2}\right)u^{n+1}-2\kappa u^{n}+\left(\kappa-\frac{1}{2}\right)u^{n-1}=\Delta t f\left((1+\kappa)u^{n}-\kappa u^{n-1}\right). \tag{A.1}$$

Assuming that Δt is small enough, the non-linear function $f(\cdot)$ can be linearized, *i.e.* $f(x)\approx\lambda x$ where $\lambda\in\mathbb{C}$. In this way, the problem becomes

$$\left(\kappa+\frac{1}{2}\right)u^{n+1}-2\kappa u^{n}+\left(\kappa-\frac{1}{2}\right)u^{n-1}=-e^{-i\varphi}\widetilde{\Delta t}\left((1+\kappa)u^{n}-\kappa u^{n-1}\right), \tag{A.2}$$

where $-e^{-i\varphi}$ is the unitary vector $-e^{-i\varphi}=\lambda/\|\lambda\|\in\mathbb{C}$ with $\varphi\in[-\pi/2,\pi/2]$ and $\widetilde{\Delta t}=\Delta t\|\lambda\|\in\mathbb{R}^{+}$. Then, to keep the time-integration method stable, we need that the eigenvalues, $\lambda^{\pm}$, of the amplification matrix T

$$\begin{pmatrix} u^{n+1}\\ u^{n}\end{pmatrix}=T\begin{pmatrix} u^{n}\\ u^{n-1}\end{pmatrix}\quad\text{with}\quad T=\begin{pmatrix} A(\kappa,-e^{-i\varphi}\widetilde{\Delta t}) & B(\kappa,-e^{-i\varphi}\widetilde{\Delta t})\\ 1 & 0\end{pmatrix}, \tag{A.3}$$

to be smaller than unity, $\|\lambda^{\pm}\|\leq 1$. The complex functions A and B are given by $A(x,y)=(2x+xy+y)/(x+1/2)$ and $B(x,y)=-(x+xy-1/2)/(x+1/2)$, respectively. Therefore, the two eigenvalues of the linear system are given by

$$\lambda^{\pm}=\frac{1}{2}\left(A\pm\sqrt{A^{2}+4B}\right). \tag{A.4}$$

Hence, the idea of the method is: given a φ to determine which is the κ that leads to the maximum $\widetilde{\Delta t}$ possible. In summary, the algorithm is:

i Determine φ, where $-e^{-i\varphi} = \lambda/\|\lambda\|$ and λ is given by (2.51).

ii Find $\kappa = K_{opt}(\varphi)$ and $\widetilde{\Delta t} = T_{opt}(\varphi)$.

iii Solve the problem (A.1) with $\Delta t = \widetilde{\Delta t}/\|\lambda\|$ and κ.

Note that since the stability domain is always symmetric respect the real axis we can restrict the analysis to the range $\varphi \in [0, \pi/2]$. Thus, the only thing that remains is to determine the exact form of the functions $K_{opt}(\cdot)$ and $T_{opt}(\cdot)$. However, the stability region cannot be given by a simple formula. Instead, it can be numerically found (Figure A.1 displays the form of these functions). In order to provide an easy-to-implement method, they can be approximated by means of piecewise polynomial functions. For $T_{opt}(\varphi)$, we propose the following approximation

$$T_{opt}(\varphi) \approx \begin{cases} G(\varphi, 0\ , c_1, c_2, 0, \varphi_1, 4/3, t_1) & \text{if} \quad 0 \le \varphi < \varphi_1 \\ G(\varphi, c_3, c_4, c_5, \varphi_1, \pi/2, t_1, 1) & \text{if} \quad \varphi_1 \le \varphi \le \pi/2 \end{cases} \tag{A.5}$$

where $\varphi_1 = \tan^{-1}(164/99)$, $t_1 = 0.9302468$, and the function G is a piecewise quartic interpolation of the form

$$G(x, a, b, c, x_0, x_1, f_0, f_1) = (ax^2 + bx + c)Q\left(x, x_0, x_1\right) + L\left(x, x_0, x_1, f_0, f_1\right), \tag{A.6}$$

where $L(x, x_0, x_1, f_0, f_1) = f_0 + (x - x_0)(f_1 - f_0)/(x_1 - x_0)$ is a piecewise linear interpolation and $Q(x, x_0, x_1) = (x - x_0)(x - x_1)$, respectively. In this way, we can guarantee the continuity of the resulting expression of $T_{opt}(\varphi)$. Then, using least squares criterion the set of constants follows: $c_1 = 0.0647998$, $c_2 = -0.386022$, $c_3 = 3.72945$, $c_4 = -9.38143$ and $c_5 = 7.06574$. Similarly, we propose to approximate $K_{opt}(\varphi)$ as follows

$$K_{opt}(\varphi) \approx \begin{cases} 1 & 0 \ \le \varphi \le \varphi_1 \\ G(\varphi, c_6\ , c_7\ , c_8\ , \varphi_1, \varphi_2, 1, k_1) & \varphi_1 < \varphi \le \varphi_2 \\ G(\varphi, c_9\ , c_{10}, c_{11}, \varphi_2, \varphi_3, k_1, k_2) & \varphi_2 < \varphi \le \varphi_3 \\ G(\varphi, c_{12}, c_{13}, c_{14}, \varphi_3, \pi/2, k_2, 0) & \varphi_3 < \varphi \le \pi/2 \end{cases} \tag{A.7}$$

where $\varphi_2 = \pi/3$, $\varphi_3 = (3/5)^2\pi$, $k_1 = 0.73782212$ and $k_2 = 0.44660387$. Then, least square minimization leads to the following values: $c_6 = 2403400$, $c_7 = -5018490$, $c_8 = 2620140$, $c_9 = 2945$, $c_{10} = -6665.76$, $c_{11} = 3790.54$, $c_{12} = 4.80513$, $c_{13} = -16.9473$ and $c_{14} = 15.0155$, respectively. The maximum errors for $T_{opt}(\varphi)$ and $K_{opt}(\varphi)$ are around 0.08% and 0.25%, respectively.

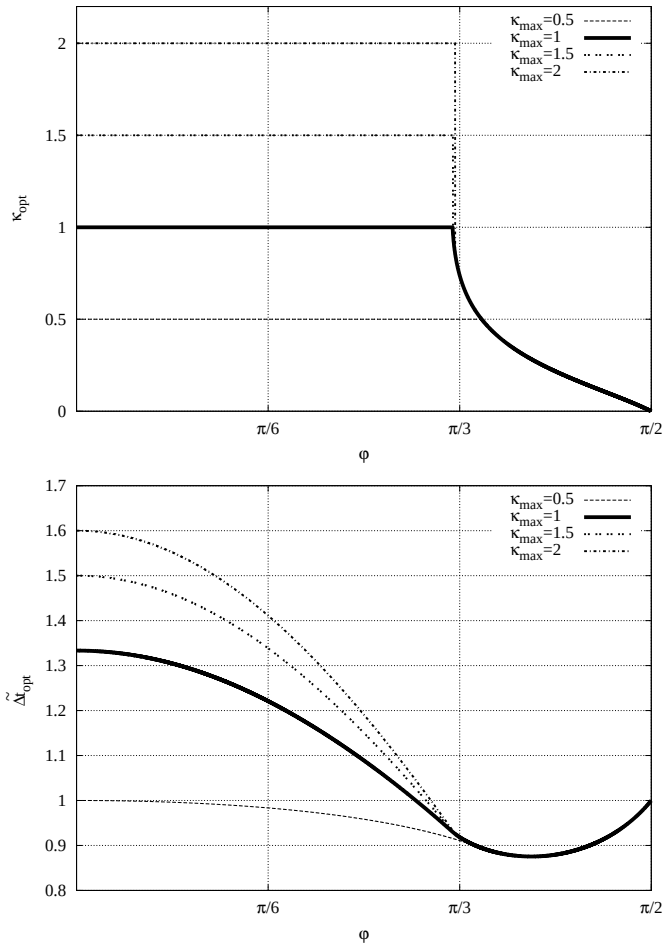

Figure A.1: Functions K_{opt} (top) and T_{opt} (bottom) as a function of $\varphi \in [0, \pi/2]$ for different values of κ_{max} from 0.5 to 2. The chosen option is $\kappa_{max} = 1$ (solid line). Note that for values $\kappa_{max} \gtrsim 1$, $K_{opt}(\varphi)$ is not a continuous function.

Appendix A. Determining the region of stability for the 1D test problem

Appendix B

Grid resolution studies. Flow past a sphere at $Re = 3700$

We performed simulations with different resolutions on both, the 2D plane (x,r) and the azimuthal direction. The coarser mesh solved was of 1.8 million CVs (28168×64 planes). In all cases a minimum number of control volumes within the boundary layer have been considered (4 CVs for the coarse grid and 12 CVs for the finest one). Mesh refinement has been carried out taking advantage of the unstructured grids used. Thus, more control volumes have been clustered within the near wake region than in the outer zones where the flow is laminar. Table B.1 summarises the details about each computational grid considered.

Table B.1: Main parameters for the different computations. N_t total number of CVs; $N_{CVplane}$ number of CVs in the plane; N_{planes} number of planes in the azimuthal direction; N_{BL} number of points in the viscous boundary layer

Case	$N_t[MCV]$	$N_{CVplane}$	N_{planes}	N_{BL}
I	9.48	74041	128	12
II	5.45	56787	96	10
III	3.63	56787	64	8
IV	1.8	28168	64	4

Flow features resulting from the different simulations are given in Table B.2. In all cases, statistical data have been obtained by averaging 350 D/U time units. The drag coefficient $\overline{C_d}$, base pressure coefficient $\overline{C_{pb}}$, the vortex-shedding frequency St and the separation angle φ_s, agree quite well with the experimental data for all resolutions. On the other hand, recirculation length shows a higher sensitivity to the grid resolution. These differences are also reflected in the mean streamwise velocity profiles in the near wake (see fig. B.1). A good agreement is obtained at $x/D = 0.2$

Table B.2: Statistical flow parameters for the different grids. Experimental measurements from [1]; [2] and numerical results from LES computations by [3]

	St	φ_s (°)	$\overline{C_d}$	$\overline{C_{pb}}$	L/D
Case I (9.48 MCV)	0.215	89.4	0.394	-0.207	2.28
Case II (5.45 MCV)	0.215	89.4	0.399	-0.209	2.18
Case III (3.63 MCV)	0.21	89.35	0.390	-0.238	2.08
Case IV (1.8 MCV)	0.215	89.5	0.378	-0.234	2.35
Kim & Durbin (exp)	0.225	-	-	-0.224	-
Sakamoto & Haniu (exp)	0.204	-	-		-
Yun et. al. (LES)	0.21	90	0.355	-0.194	2.622

and $x/D = 1.6$, but some differences are observed when it is compared at a distance $x/D = 3$. As this station is located at the outer limit of the recirculation zone, these differences might be due to the fluctuations of the recirculation bubble. Largest differences in the mean flow variables when comparing with the high-resolution mesh are obtained in the downstream region, specially for the two coarser grids, for downstream distances from the sphere of $x/D > 5$ (not shown in the image). These differences are mainly due to the coarsening of these grids further downstream, being not capable of capturing all flow scales.

Figure B.2 shows the mean pressure coefficient on the sphere surface as a function of the angle (measured from the stagnation point) for the low- and high-resolution grids (Cases IV and I, respectively), together with the experimental data by [1] at Re=4200. The low-resolution mesh captures quite well the pressure distribution with some differences in the front surface of the sphere and also it slightly under-predict the pressure in the base of the sphere. However, the position of the minimum pressure and its value are predicted satisfactorily.

References

[1] H.J. Kim and P.A. Durbin. Observations of the frequencies in a sphere wake and of drag increase by acoustic excitation. *Physics of Fluids*, 31(11):3260–3265, 1988.

[2] H. Sakamoto and H. Haniu. A study on vortex sheding from spheres in an uniform flow. *Journal of Fluids Engineering*, 112:386–392, 1990.

[3] G. Yun, D. Kim, and H. Choi. Vortical structures behind a sphere at subcritical Reynolds numbers. *Physics of Fluids*, 18, 2006.

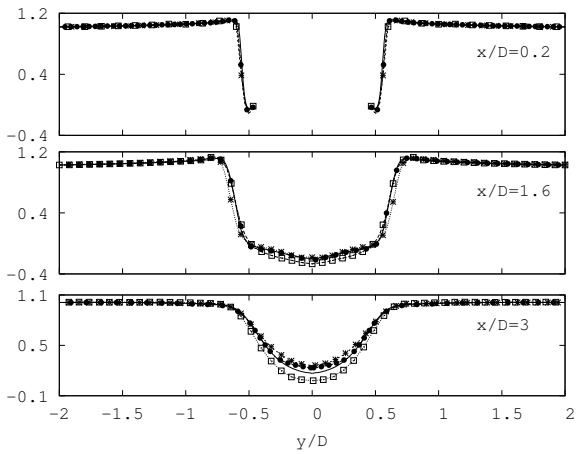

Figure B.1: Streamwise velocity profiles at different locations in the near-wake of the sphere for different grids resolutions: (⁻) case I; (•) case II; (∗) case III; (□) case IV

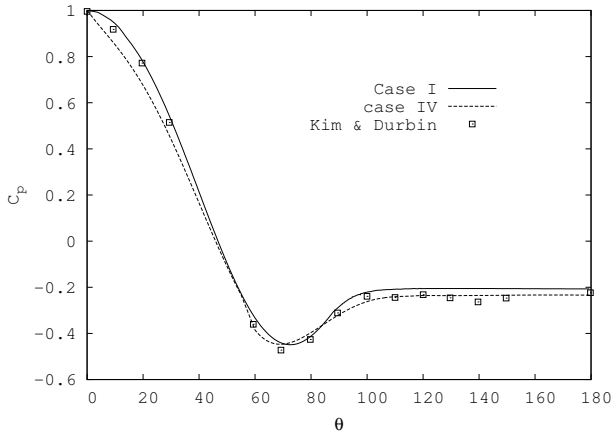

Figure B.2: Comparison of the pressure coefficient on the sphere surface: (solid line) case I; (dashed line) case IV; (□) experimental data by [1]

Appendix C

Statistic treatment of DNS and LES data

Turbulent flows are disordered, random and chaotic. To completely characterise a random process, it is necessary to know the joint Probability Density Function (PDF) for all instants of time, which is an impossible task. However, considerable simplification takes place if this random process is statistically stationary.

A process can be defined as statistically stationary if all multi-time statistics are invariant under a shift in time, i.e., for all positive time intervals s, and all the choices of $\{t_1, t_2, t_n\}$ we have:

$$f(v_1, t_1 + s; v_2, t_2 + s; ...; v_n, t_n + s) = f(v_1, t_1; v_2, t_2; ...; v_n, t_n) \tag{C.1}$$

In fact, a turbulent flow, after the initial transient period can reach a statistically stationary state in which the time statistics of all flow variables remain independent on time.

But, when we are collecting data in time, a question that must be solved is in what extent will the next measurement dependent on the time history? Or in other words, how long should this time integration be, in order to obtain flow variables independent on time?

Let's consider a process with a test probe x_1 at a location (x, y, z) measuring the variable ϕ. The reading of the probe x_1 is represented in figure C.1. Thus, if the process is statistically stationary, the variable ϕ can be represented as:

$$\phi(t) = \phi'(t) + \overline{\phi(t)} \qquad \text{for } 0 \leq t \leq T \tag{C.2}$$

where $\overline{\phi(t)}$ is the average of ϕ over the time integration T, and $\phi'(t)$ is the fluctuation of $\phi(t)$. The fluctuation of $\phi(t)'$ has a spectral representation as a weighted sum of Fourier modes of different frequencies ω, i.e., $e^{i\omega_n t} = cos(\omega_n t) + isin(\omega_n t)$. Then, it is possible to express the signal $\phi(t)$ as a Fourier series

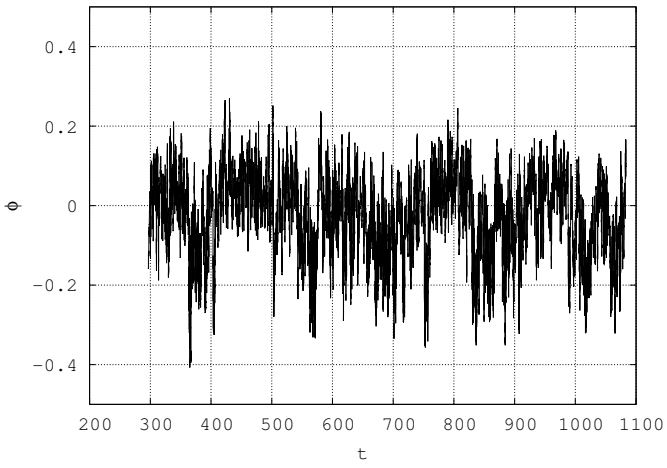

Figure C.1: Instantaneous data of ϕ

$$\phi(t) = \sum_{n=-\infty}^{\infty} (a_n + ib_n)e^{i\omega_n t} \tag{C.3}$$

and the frequency $\omega_n = \pi\, n/T$.

The coefficients $(a_n + ib_n)$ of the Fourier series satisfy the conjugate symmetry , the Fourier series becomes,

$$\phi(t) = 2\sum_{n=1}^{\infty} |c_n| cos(\omega_n t + \theta_n)] \tag{C.4}$$

where the amplitude of the nth Fourier mode is $|c_n| = (a_n^2 + b_n^2)^{1/2}$ and its phase $\theta_n = tan^{-1}(b_n/a_n)$.

For a statistically stationary process, the simplest multi-time statistic that can be considered for the variable $\phi(t)$ is the auto-covariance:

$$\Re_{ii}(s) \equiv \lim_{T\to\infty} \frac{1}{T} \int_0^T \phi(t)'\phi(t+s)' dt \tag{C.5}$$

or in normalised form, the auto-correlation function:

$$\rho(s) \equiv \frac{\Re_{ii}(s)}{\Re_{ii}(0)} \tag{C.6}$$

This function gives information about the time dependence of the turbulent process. To understand what the auto-covariance means, we can use the instantaneous data of the variable ϕ represented in figure C.1. The data corresponds to the instantaneous variation of a statistically stationary process. The auto-correlation of this variable as a function of the time lag is represented in the Figure C.2. The first thing to notice is the maximum value of the auto-correlation is at initial time. After that, the number decreases until it is zero. This point is known as decorrelation time. In this case, as the function exhibits an strong periodicity, it drops to zero and continues decreasing until a minimum. Thus, there is a negative correspondence, if the minimum occurs at about $s = 82.8$, then the function will reach a maximum in about $s = 82.8$. Notice also that the distance between two maximum values is also about $\tau = 165.6$. This is the indicator of periodicity. In addition, at lag zero ($s = 0$), the auto-covariance function returns the variance of the variable ($\overline{\phi'^2}$).

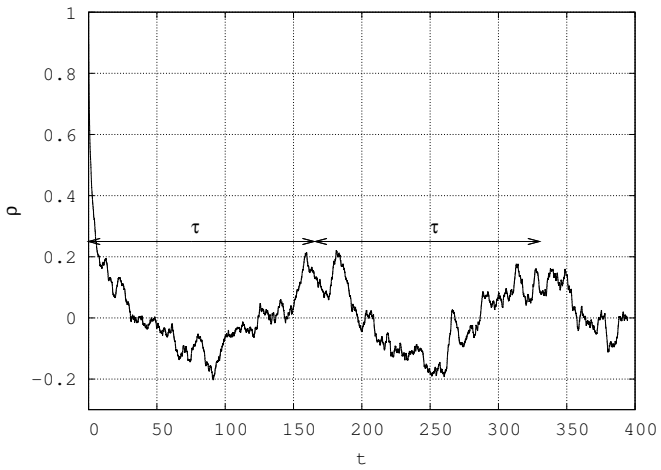

Figure C.2: Auto-correlation of ϕ

The Fourier transformation of the auto-covariance $\Re(s)$ gives information about the frequency contents of process, that is, auto-covariance and twice the frequency spectrum $E(\omega)$ form a Fourier-transform pair which is:

$$E(\omega) \equiv \int_{-\infty}^{\infty} R(s)e^{-i\omega s} = \frac{2}{\pi}\int_{o}^{\infty} R(s)cos(\omega s)ds \tag{C.7}$$

and

$$R(s) = \frac{1}{s}\int_{\infty}^{\infty} E(\omega)e^{i\omega s}d\omega = \int_{0}^{\infty} E(\omega)cos(\omega s)d\omega \tag{C.8}$$

The characteristic time-scale for the dynamics of measured quantities in a turbulent flow is defined by the integral time scale $\overline{\tau}$. It is a measure for the correlation length of a process and is given by:

$$\overline{\tau} = \int_{0}^{\infty} \rho(s)ds \tag{C.9}$$

Most of the time, auto-correlation or spectrum, together with $\overline{\phi}$ and its variance $\overline{\phi'\phi'}$, are the only quantities available to characterise the time properties of a process.

Thus, for data obtained at uniformly spaced intervals, Fast Fourier Transform (FFT) can be used to obtain the power spectrum of a signal. Unfortunately, in most LES and DNS computations, evenly sampled data is impossible to achieve. In those cases, the most commonly used method of calculating the spectrum of a non-uniformly spaced data is the periodogram analysis. It ignores the non-equal spacing and involves calculating Fourier power spectrum as if the data were evenly spaced, though without use the FFT algorithm.

However, periodogram is not invariant to time translations. Lomb [1] modified the definition of periodogram for a zero-mean time series. The Lomb periodogram provides a good approximation to the spectrum obtained by fitting sinus waves by least-squares to the data. This least-squares spectrum provides the best measure of the power contributed by the different frequencies to the overall variance of the data and can be regarded as the natural extension of Fourier methods to non-uniform data. It reduces to Fourier spectrum in the limit of equal spacing. A fast algorithm for the Lomb periodogram was proposed by Press and Ribicki [2] and can be found in Numerical Recipes [3].

The power spectrum of the signal represented in figure C.1 calculated using the Lomb Periodogram is plotted in figure C.3. Observe that the peak in the spectra occurs at a frequency $f = 6.04 \times 10^{-3}$ which corresponds with the time period of the signal $\tau = 165.6$ calculated by means of the auto-correlation (see figure C.2).

References

[1] N.R. Lomb. Least-squares frequency analysis of unequally spaced data. *Astrophysics and space science*, 36:447–462, 1976.

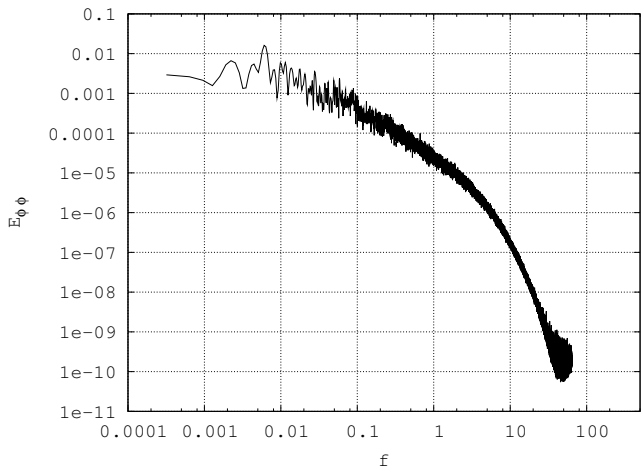

Figure C.3: Power spectrum of the signal ϕ

[2] W.H. Press and G.B. Rybicki. Fast algorithm for spectral analysis of unevenly sampled data. *The astrophysical journal*, pages 277–280, 1989.

[3] W. H. Press, S. A. Teukolsky, W. T. Vetterling, and B. P. Flannery. *Numerical Recipes: The Art of Scientific Computing*. Cambridge University Press, 3rd edition edition, 2007.

Appendix D

Ensemble average

The instantaneous flow can be represented by the contributions of a time-averaged component $\overline{\phi_i}$, a periodic fluctuation $\tilde{\phi}_i$ and a random fluctuation ϕ'_i, i.e. [1]

$$\phi_i = \overline{\phi_i} + \tilde{\phi}_i + \phi'_i \tag{D.1}$$

The phase-average can be defined as the average value of the variable ϕ_i over an ensemble of signals which have the same phase with respect to a reference signal. It can be evaluated as:

$$\langle \phi_i \rangle = \overline{\phi_i} + \tilde{\phi}_i \tag{D.2}$$

This decomposition opens the possibility of analysing the periodic motion flows which exhibits quasi-periodic components by resolving its dominant frequency.

Measurements of the phase-averaged quantities need a reference signal from which the phase of the flow is determined. The reference signal can be obtained from the direct measurement in a region of the flow dominated by the periodic wave and not too affected by the turbulent effects. In the case of the flow past a circular cylinder, it can be taken from the laminar region, near the cylinder surface. In this zone, the pressure signal exhibits clearly a strong periodic component and it is not affected by the turbulence developed downstream (see figure D.1(a)). In the figure, it is represented a piecewise of the pressure sampled near the cylinder surface at $\varphi = 70^\circ$ measured from the stagnation point. As can be seen, the signal is quasi-periodic fluctuating at the vortex-shedding frequency which can almost be measured directly from the instantaneous data. However, in order to extract the dominant frequency from the periodic oscillator, the FFT method has been used (see figure D.1(b)). As can be seen from the figure, the energy spectrum exhibits a dominant peak at the frequency $f = 0.2145$. Thus, taking this frequency as reference, the length of each period has been determined.

The flow field is then classified according to its phase-angle, by dividing each period into windows of $2\pi/128$. The phase-average at any of this windows (phases) can

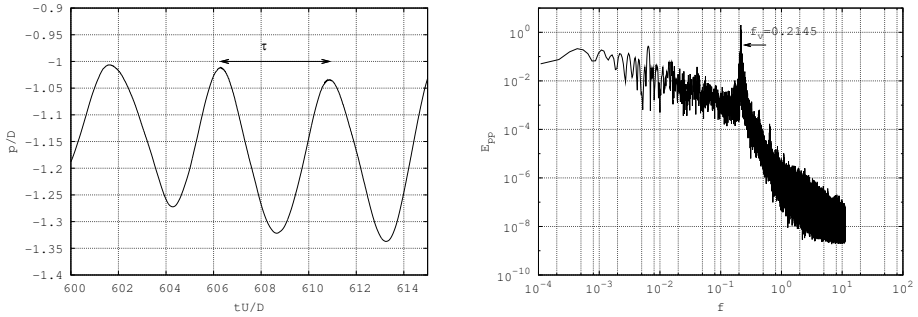

Figure D.1: a) Reference signal used as periodic oscillator. b) Power spectra of the reference oscillator signal.

be ensembled by averaging over a certain number of periods. In the case analysed in Chapter 7, a total number of 10 cycles were considered to ensemble each phase.

However, this procedure would require a large storage capacity, thus instead of the 128 phase-angles, only 4 equidistant phases were recorded (i.e. $\phi = 0°$, $90°$, $180°$, $270°$). The resulting phase-average for each of these phases can be seen in Figures 7.12 and 7.13

References

[1] W. C. Reynolds and a. K. M. F. Hussain. The mechanics of an organized wave in turbulent shear flow. Part 3. Theoretical models and comparisons with experiments. *Journal of Fluid Mechanics*, 54(02):263–288, 1972.

Appendix E

Related projects

The Heat and Mass Transfer Technological Center (CTTC) of the Technical University of Catalonia (UPC) is a research group dedicated to academic, research, innovation and technology transfer in the heat and mass transfer and fluid dynamic field, together with their application to thermal systems and equipments. The laboratory is composed by 47 professors and researchers, with all the members of the staff working full time.

Termo Fluids S.L. is a spin-off which was born 6 years ago from members of the CTTC and, together with CTTC, have a high capacity of simulating thermal systems and equipment.

The CTTC research activities are focused on one basic research line dedicated to the mathematical formulation, numerical resolution and experimental validation of heat and mass transfer phenomena. Some issues in this line are: natural and forced convection, turbulence modeling (RANS, LES and DNS), combustion, two-phase flow, solid-liquid phase change, radiation, porous media, numerical algorithms and solvers, general purpose CFD codes, high performance computing HPC (parallelization), aerodynamics, etc.

A second research line involves the application of the acquired know-how from the basic studies mentioned above to the thermal and fluid dynamic optimization of thermal system and equipment (maximum efficiency with a minimum environmental impact).

The present phd thesis is focused on the basic research side of the CTTC but the applied side of our center have been the real driving force of all my work. The first users of the presented unstructured methodology and LES models have always been others researchers of CTTC or Termo Fluids S.L. company interested on the simulation of complex industrial applications. As a general rule the industrial needs are to much ambitious for the current state of your possibilities, independently of how advanced is your software. Thus, work in a close relation with these necessities is positive since the only way to succeed is to find better models, algorithms or to improve implementations.

In what follows, some of these applications are summarized. The main work in order to clean up the geometry, mesh, simulate and post-process the results have been done by CTTC and Termo Fluids S.L. colleagues.

Numerical simulation of the thermal and fluid dynamic analysis of nacelle and wind turbines

The CTTC, in collaboration with Termo Fluids, S.L., has performed for Economical-ALSTOM a thermo-fluidic analysis of the behavior of a wind turbine generator (WTG) nacelle. Such a nacelle contains several compartments and devices responsible of the good functioning of the whole system, and the temperature in the different zones of the domain must be estimated. The thermal behavior of such devices and enclosing walls falls into three categories: 1) adiabatic, 2) isothermal, and 3) heat generators. Only one element belongs to 3): a finned transformer that delivers the electric output of the WTG. In the simulation, the heat flux at the transformer's surface is set to match a prescribed heat dissipation. Outside cold air enters through the upper section of the tower, at high speed, and interacts heavily with the elements present in the nacelle. It is intended to refrigerate the devices by the circulation of this air circulating between them. The air then is pumped out by a set of fans in the transformer zone. Given the complexity of the flow, with concurrent forced and natural convection, RANS models have been discarded in favor of the more robust, less parameter-dependent, well tested LES models.

Project publications

Colomer, G.; Lehmkuhl, O.; Borrell, R.; Oliva, A. CFD simulation of the thermal behavior of a wind mill power generator nacelle. A: VI International Symposium on Turbulence, Heat and Mass Transfer. "Proceedings of the VI International Symposium on Turbulence, Heat and Mass Transfer". 2009, p. 1075-1078.

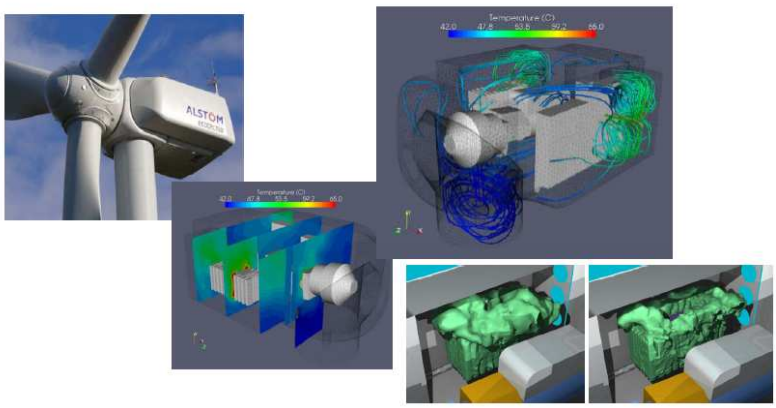

Figure E.1: Illustrative results of numerical simulation of the thermal and fluid dynamic analysis of nacelle and wind turbines.

Numerical simulation of wind turbine dedicated airfoils

The flow around aerodynamic profiles in pre- or full-stall at high Reynolds numbers is a problem of increasing interest since it is a normal operation state for wind turbine blades. In the past years, it has been subject of many experimental and numerical investigations. Most of the numerical studies performed since now have been carried out using RANS modeling, but it is well-known that such models fails in predicting the flow at angles of attack (AoA) near or after stall, mainly due to the highly unsteady and three-dimensionality nature of the flow. Under these situations, large-eddy simulations (LES) can be a good alternative for simulating such complex flows.

This R&D project between the CTTC and others European research centers and universities aims at modeling the flow behavior past airfoils used for wind turbine blades at high Reynolds number and large AoA. Three profiles have been selected: DU- 93-W-210, DU-91-W2-250 and FX77-W-500. The study has been carried out for Reynolds numbers up to $3 \cdot 10^6$ and AoA up to 16^o. Numerical results have been compared with experimental ones showing good agreement.

Project publications

O. Lehmkuhl, J. Calafell, I. Rodríguez, and A. Oliva. Large-Eddy Simulations of wind turbine dedicated airfoils at high Reynolds numbers. In Wind Energy and

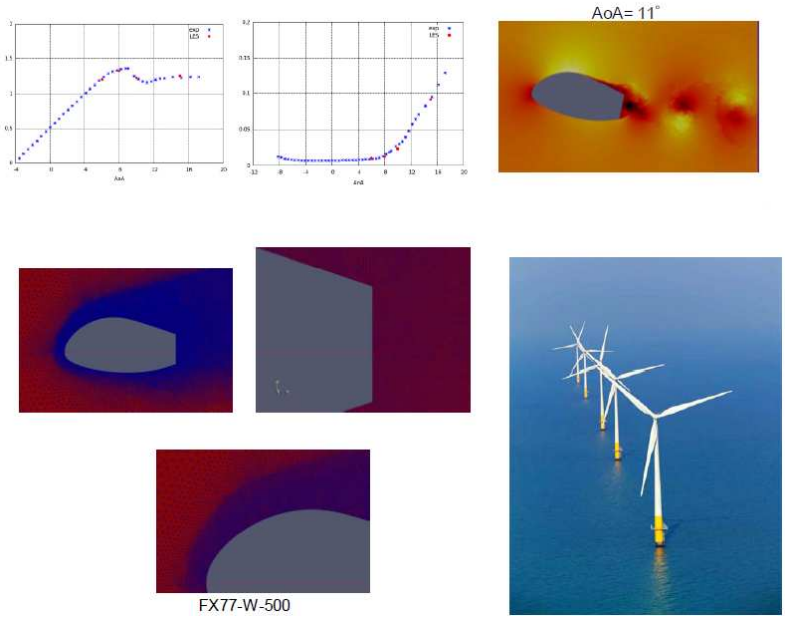

Figure E.2: Illustrative results for the FX77-W-500 airfoil: mesh design, instantaneous snapshots and C_d and C_l distributions.

the impact of turbulence on the conversion process. EUROMECH Colloquium 528. Oldenburg, 2012.

Research and development of vapor efficient solar receptors

High concentration solar thermal power plants are based solar energy concentration incident to a large number of reflectors. This energy is directed to a receiver, that is hundreds or thousands of times smaller than the reflectors where it is transferred to a working fluid. This working fluids is used to drive a conventional power cycle. The design of the receiver is critical for the performance of the solar plant. The higher its temperature, the better the performance of the power cycle. However, as the solar radiation is non uniform (in space and in time), the receiver is exposed to sudden changes in the solar radiation flux that induce changes in its temperature and therefore thermal tensions

CTTC has been working in the framework Project CONSOLIDA, coodirnated by Abengoa Solar in collaboration with Termo Fluids, S.L., in the development of advanced numerical models for the solar receivers, that include several phenomena such as: conduction in the metals and insulation materials, thermal radiation heat transfer, fluid flow and heat transfer in the ducts (one or two-phase flows), turbulent natural convection in the receiver chamber air, etc.

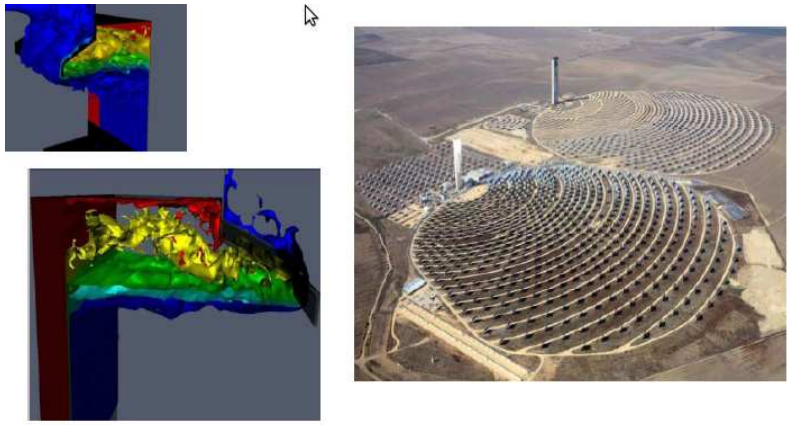

Figure E.3: Solar power plant receptor tower (PS10) of Abengoa Solar and instantaneous snapshots of differents LES simulations of the receptor.

Project publications

J. Chiva, O. Lehmkuhl, M. Soria, A. Oliva. Modelization of heat transfer and fluid dynamics in solar power towers. Proceedings of ISES Solar World Congress 2011. pp. 629 - 634. Kassel, Alemanya, 2011.

Domestic refrigerator analysis

This R&D project between Fagor and the CTTC was focused on the study of the temperature and air distribution inside household frost-free refrigerators. It is well known that the correct air and temperature distribution inside the refrigerated chamber is the most important factor that affects refrigerator efficiency. In frost-free refrigerators the cooled air is supplied directly inside the fresh food and vegetable cabinets. Therefore, studies intended to establish the actual air flow and tempera-

ture distributions inside these cabinets are relevant in order to improve temperature homogeneity and to reduce energy consumption.

Unsteady three-dimensional numerical studies were carried out, simulating the cooling process starting from a uniform warm temperature inside the refrigerator. Furthermore, the influence of inlet and outlet ports location was also investigated.

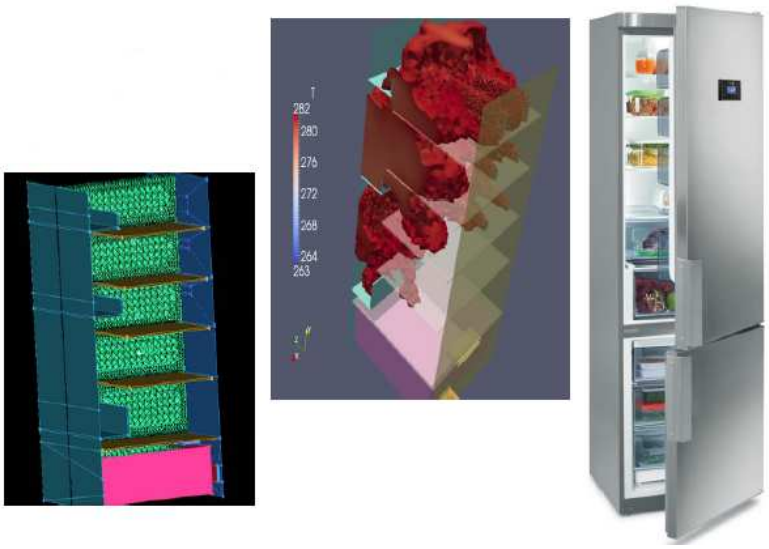

Figure E.4: Schematics of the household frost-free refrigerator modeled, mesh details and instantaneous snapshot.

Project publications

J. Jaramillo, J. Rigola, C.D. Pérez-Segarra, C. Oliet. Numerical Study of Air inside Refrigeration Compartment of Frost-Free Domestic Refrigerators. International Refrigeration and Air Conditioning Conference. Purdue, USA, 2010.

List of Publications

This is an exhaustive list of publications carried out within the framework of the present thesis.

On International Journals

O. Lehmkuhl, R. Borrell, I. Rodríguez, C.D. Pérez-Segarra and A. Oliva. Assessment of the Symmetry-Preserving Regularization model on complex flows using unstructured grids. *Computer & Fluids*, 60:108–116. 2012. doi:10.1016/j.compfluid.2012.02.030.

I. Rodríguez, O. Lehmkuhl, R. Borrell and A. Oliva (2012). Flow dynamics in the turbulent wake of a sphere at sub-critical Reynolds numbers. *Computers&Fluids*. doi:10.1016/j.compfluid.2012.03.009. 2012.

R. Borrell, O. Lehmkuhl, F.X. Trias, and A. Oliva. Parallel direct poisson solver for discretisations with one Fourier diagonalisable direction. *Computational Physics*, 230(12):4723–4741, 2011.

I. Rodríguez, R. Borrell, O. Lehmkuhl, C.D. Pérez-Segarra, and A. Oliva. Direct numerical simulation of the flow over a sphere at Re = 3700. *Journal of Fluids Mechanics*, 670: 263–287, 2011.

F.X. Trias and O. Lehmkuhl. A self-adaptive strategy for the time-integration of Navier-Stokes equations *Numerical Heat Transfer. Part B*, 60(2): 116–134, 2011.

Jaramillo, J. and Perez-Segarra, C.D. Lehmkuhl, O. and Castro, J, Detailed Analysis of Turbulent Flows in Air Curtains. *Progress in Computational Fluid Dynamics, An International Journal* , 11(6): 350– 362, 2011.

Gorobets, A.; Trias, F. X.; Borrell, R.; Lehmkuhl, O.; Oliva, A. Hybrid MPI+OpenMP parallelization of an FFT-based 3D Poisson solver with one periodic direction. *Computers & fluids*, 49(1): 101 – 109. 2011

Papers submitted to International Journals

Lehmkuhl, O.; Rodríguez, I.; Baez, A.; Oliva, A.; Pérez-Segarra, C.D. Assessment of Large-Eddy Simulations for the flow around aerodynamic profiles using unstructured grids. *AIAA Journal*

Estruch, O.; Lehmkuhl, O.; Borrell, R.; Pérez-Segarra, C.D.; Oliva, A. A parallel radial basis function interpolation method for unstructured dynamic meshes *Computers & Fluids*

Damle, R.; Lehmkuhl, O.; Rigola, J.; Lopez, J.; Oliva, A. Building Energy Simulation With A Modular Object-Oriented Software *Building and Environment*

Jofre, Ll.; Lehmkuhl, O.; Castro, J.; Oliva, A. A Three-Dimensional Volume-of-Fluid Interface Tracking Algorithm for General Meshes *Computational Physics*

On Conferences Proceedings

I. Rodríguez, O. Lehmkuhl, A. Baez, R. Borrell and A. Oliva Direct numerical simulation of a NACA 0012 in full stall In Conference on Modeling Fluid Flow, Budapest, 2012

I. Rodríguez, A. Baez, O. Lehmkuhl and C.D. Pérez-Segarra. On LES assessment in massive separated flows: flow past a NACA airfoil at $Re = 50000$. In Wind Energy and the impact of turbulence on the conversion process. EUROMECH Colloquium 528. Oldenburg, 2012.

O. Lehmkuhl, J. Calafell, I. Rodríguez, and A. Oliva. Large-Eddy Simulations of wind turbine dedicated airfoils at high Reynolds numbers. In Wind Energy and the impact of turbulence on the conversion process. EUROMECH Colloquium 528. Oldenburg, 2012.

P. A. Galione, O. Lehmkuhl, J. Rigola, A. Oliva and I. Rodríguez. Numerical simulations of energy storage with encapsulated phase change materials. Special emphasis on solid-liquid phase change CFD modelling. The 12th International Conference on Energy Storage. INNOSTOCK. Lleida, 2012.

A. Oliva, C. D. Pérez-Segarra, I. Rodríguez, O. Lehmkuhl, S. Torras. Modular object-oriented methodology for the resolution of molten salt storage tanks for CSP plants. The 12th International Conference on Energy Storage. INNOSTOCK. Lleida, 2012.

Lehmkuhl, A. Baez, I. Rodríguez, and A. Oliva. Direct numerical simulation and large-eddy simulations of the flow around a naca 0012.
In 7^{th} International Conference on Computational Heat and Mass Transfer, Istanbul, Turkey, 2011.

Jofre, L.; Lehmkuhl, O.; Castro, J.; Oliva, A. VOF/Navier-Stokes implementation

on 3D unstructured staggered meshes. Application to the Richtmyer-Meshkov instability In 7^{th} International Conference on Computational Heat and Mass Transfer, Istanbul, Turkey, 2011.

Damle, R.; Lehmkuhl, O.; Colomer, G. Mixed convection in a ventilated 3D cavity: comparison of different LES models with experimental data In 7^{th} International Conference on Computational Heat and Mass Transfer, Istanbul, Turkey, 2011.

Chiva, J.; Ventosa, J.; Lehmkuhl, O.; Pérez, C. Modelization of the Low-Mach Navier Stokes equations in unstructured meshes". In 7^{th} International Conference on Computational Heat and Mass Transfer, Istanbul, Turkey, 2011.

Capdevila, R.; Lehmkuhl, O.; Trias, F. X.; Colomer, G.; Pérez, C. Numerical simulations of turbulent natural convection coupled and uncoupled with radiation In 7^{th} International Conference on Computational Heat and Mass Transfer, Istanbul, Turkey, 2011.

O. Lehmkuhl, I. Rodríguez, R. Borrell, C.D. Pérez-Segarra and A. Oliva. Low-frequency variations in the wake of a circular cylinder at $Re = 3900$. Proceedings of the 13th European Turbulence Conference. Varsaw. 2011.

R. Capdevila, O. Lehmkuhl, F.X. Trias, C.D. Pérez-Segarra, G. Colomer. Turbulent natural convection in a differentially heated cavity of aspect ratio 5 filled with non-participating and participating grey media, Proceedings of the 13th European Turbulence Conference. Varsaw. 2011.

R. Damle, O. Lehmkuhl, G. Colomer, Modular simulation of buildings with an object-oriented tool, Proceedings of 23rd IIR International Congress of Refrigeration. ISBN 978-2-913-149-89-2, 2011.

S. Torras, O. Lehmkuhl, J. Rigola, A. Oliva. Numerical simulation of heat storage for domestic applications. Proceedings of 23rd IIR International Congress of Refrigeration. ISBN 978-2-913-149-89-2, 2011

J. Chiva, O. Lehmkuhl, M. Soria, A. Oliva. Modelization of heat transfer and fluid dynamics in solar power towers". Proceedings of ISES Solar World Congress 2011. pp. 629 - 634. Kassel, Alemanya, 2011.

P. Galione, O. Lehmkuhl, J. Rigola, A. Oliva, I. Rodriguez. Numerical simulations of thermal energy storage systems with phase change materials, Proceedings of ISES Solar World Congress 2011. pp. 1 - 12. Kassel, Alemanya, 2011.

R. Damle, O. Lehmkuhl, G. Colomer, I. Rodriguez. Energy simulation of build-

ings with a modular object-oriented tool. Proceedings of ISES Solar World Congress 2011. pp. 1 - 11. Kassel, Alemanya, 2011.

O. Estruch, O. Lehmkuhl, R. Borrell and C.D. Perez Segarra. A parallel three-dimensional radial basis function interpolation method for unstructured dynamic meshes. In Parallel CFD. 2011.

A. Baez, O. Lehmkuhl, I. Rodriguez and C. D. Perez-Segarra. Direct Numerical Simulation of the turbulent flow around a NACA 0012 airfoil at different angles of attack, In Parallel CFD. 2011.

R. Borrell, O. Lehmkuhl, F.X. Trias, G. Oyarzun and A. Oliva. FFT-based Poisson Solver for large scale numerical simulations of incompressible flows, In Parallel CFD. 2011.

I. Rodriguez, O. Lehmkuhl, R. Borrell and A. Oliva. Flow dynamics in the turbulent wake of a sphere at sub-critical Reynolds numbers, In Parallel CFD. 2011.

G. Colomer, R. Borrell, O. Lehmkuhl, C.D. Perez-Segarra. Parallel algorithm for the solution of the Boltzmann Transport Equation on unstructured meshes, In Parallel CFD. 2011.

L. Jofre, O. Lehmkuhl, R. Borrell, J. Castro and A. Oliva. Parallelization study of a VOF/Navier-Stokes model for 3D unstructured staggered meshes, In Parallel CFD. 2011.

Borrell, R.; Lehmkuhl, O.; Oliva, A. Parallelization of combined convection-radiation numerical simulations.. A: 14th International Heat Transfer Conference. "Abstracts of The 14th International Heat Transfer Conference". 2010, p. 46.

O. Lehmkuhl, R. Damle, J. Rigola, J.Lopez. Full numerical simulation of an object oriented program for hermetic reciprocating compressors: numerical verification and experimental validation.. A: 20th International Compressor Engineering Conference at Purdue. "Proceedings of 20th International Compressor Engineering Conference at Purdue". 2010

I. Rodríguez, O. Lehmkuhl, R. Borrell, A. Oliva, and C.D. P èrez Segarra. Direct numerical simulation of turbulent wakes: Flow past a sphere at Re= 5000. In V European Conference on Computational Fluid Dynamics ECCOMAS, Lisbon, Portugal, 2010.

I. Rodríguez, O. Lehmkuhl, R. Borrell and C.D. Pérez-Segarra. On DNS and LES of natural convection of wall-confined flows: Rayleigh-Bénard convection. *Direct*

and Large-Eddy Simulations 8 Eindhoven. 2010.

Lehmkuhl, O.; Borrell, R.; Pérez, C.; Oliva, A.; Verstappen, R.W.C.P. LES modeling of the turbulent flow over an Ahmed car *Direct and Large-Eddy Simulations 8* Eindhoven. 2010.

Lopez, J.; Rigola, J.; Lehmkuhl, O.; Oliva, A. Introduction of CFD&HT analysis into an object oriented one dimensional and transient program for numerically simulate hermetic refrigeration compressors. A: 20th International Compressor Engineering Conference at Purdue. "Proceedings of 20th International Compressor Engineering Conference at Purdue". 2010, p. 1-8.

Damle, R.; Soria, M.; Lehmkuhl, O.; Colomer, G.; Oliva, A. Large Eddy Simulation of airflow in a single family house. A: 1st International High Performance Buildings Conference at Purdue. "Proceedings of the 1st International High Performance Buildings Conference at Purdue". 2010, p. 1-8.

Capdevila, R.; Pérez, C.; Lehmkuhl, O.; Colomer, D. Numerical simulation of turbulent natural convection and gas radiation in differentially heated cavities using FVM, DOM and LES. A: Fifth European Conference on Computational Fluid Dynamics. "CFD 2010. Proceedings of Fifth European Conference on Computational Fluid Dynamics.". 2010.

Jaramillo, J.; Pérez, C.; Lehmkuhl, O.; Oliva, A. Detailed numerical study of turbulent flows in air curtains. A: Fifth European Conference on Computational Fluid Dynamics. "CFD 2010. Proceedings of Fifth European Conference on Computational Fluid Dynamics.". 2010, p. 1-19.

Lehmkuhl, O.; Borrell, R.; Rodriguez, I.; Pérez, C.; Oliva, A. On the symmetry-preserving regularization model on complex flows using unstructured grids. A: Fifth European Conference on Computational Fluid Dynamics. "Proceedings of the V European Conference on Computational Fluid Dynamics ECCOMAS CFD 2010". 2010, p. 1-18.

Jofre, L.; Lehmkuhl, O.; Castro, J.; Oliva, A. A PLIC-VOF implementation on parallel 3D unstructured meshes. A: Fifth European Conference on Computational Fluid Dynamics. "CFD 2010. Proceedings of Fifth European Conference on Computational Fluid Dynamics.". 2010, p. 1-15.

Capdevila, R.; Pérez, C.; Lehmkuhl, O.; Colomer, G. Numerical simulation of turbulent natural convention and gas radiation in diferentially heated cavities using FVM, DOM and LES. A: 6th International Symposium on Radiative Transfer. "Book

Abstracts for the 6th International Symposium on Radiative Transfer". 2010, p. 39-41.

O. Lehmkuhl, R. Borrell, J. Chivas, and C.D. Perez-Segarra. Direct numerical simulations and symmetry-preserving regularization simulations of the flow over a circular cylinder at Reynolds number 3900. In *Turbulence, Heat and Mass Transfer*, 2009.

I. Rodríguez, R. Borrell, O. Lehmkuhl, A. Oliva, and C.D. P èrez Segarra. Direct numerical simulation of the flow over a sphere at Re = 3700. In *Turbulence, Heat and Mass Transfer*, 2009.

Pérez-Segarra, C.D; Lehmkuhl, O.; Jaramillo, J.; Colomer, G.; Oliva, A. Turbulence modelling and numerical issues: from RANS to DNS and LES. A: III Conferencia Nacional em Mecanica de Fluidos, Termodinamica e Energia. "Actas da III Conferencia Nacional em Mecanica de Fluidos, Termodinamica e Energia (MEFTE - BRAGANCA 09), resumos.". 2009, p. 15-16.

Colomer, G.; Lehmkuhl, O.; Borrell, R.; Oliva, A. CFD simulation of the thermal behavior of a wind mill power generator nacelle. A: VI International Symposium on Turbulence, Heat and Mass Transfer. "Proceedings of the VI International Symposium on Turbulence, Heat and Mass Transfer". 2009, p. 1075-1078.

Rigola, J.; Lehmkuhl, O.; Pérez, C.; Colomer, G. Turbulent radial outflow between coaxial parallel disks. A: VI International Symposium on Turbulence, Heat and Mass Transfer. "Proceedings of the VI International Symposium on Turbulence, Heat and Mass Transfer". 2009, p. 371-374.

Chiva, J.; Soria, M.; Oliva, A.; Lehmkuhl, O.. Turbulent natural convection in an open cavity: a numerical study. A: VI International Symposium on Turbulence, Heat and Mass Transfer. "Proceedings of the VI International Symposium on Turbulence, Heat and Mass Transfer". 2009, p. 567-570.

Rigola, J.; Lehmkuhl, O.; Oliva, A.; Pérez-Segarra, C.D. Numerical simulation of the fluid flow though valves based on Large Eddy Simulation models. A: 2009 International Conference on Compressors and Their Systems. "Proceedings of the International Conference on Compressors and their Systems. 7-9 September 2009.". 2009, p. 137-145.

Lopez, J.; Lehmkuhl, O.; Rigola, J.; Pérez, C.; Oliva, A. Numerical study of suction gas flow in the shell of hermetic refrigeration compressors. A: 2009 International Conference on Compressors and Their Systems. "Proceedings of the International Conference on Compressors and their Systems. 7-9 September 2009.". 2009, p. 395-

404.

Borrell, R.; Lehmkuhl, O.; Rodriguez, I.; Pérez-Segarra, C.D; Oliva, A. Parallel Poisson solver for revolved unstructured grids. DNS of the flow around a sphere at Re = 3700.. A: 21st. International Conference on Parallel Computational Fluif Dynamics. "Parallel CFD 2009 : 21 th International Conference on Parallel Computational Fluid Dynamics". 2009, p. 332-336.

R. Borrell, O. Lehmkuhl, F.X. Trias, M. Soria, and A. Oliva. Parallel direct poisson solver for DNS of complex turbulent flows using unstructured meshes. In *Parallel Computational Fluid Dynamics*, Lyon, France, May 2008.

Lehmkuhl, O.; Trias, F. X.; Borrell, R.; Pérez-Segarra, C.D. Symmetry-preserving Regularization modelling of a turbulent plane impinging jet. A: "ERCOFTAC WORKSHOP Direct and Large-Eddy Simulations". V. Armenio, 2008, p. 1-6.

Rigola, J.; Lehmkuhl, O.; Pérez, C.; Oliva, A. Numerical simulation of fluid flow through valves reeds based on Large Eddy Simulation Models (LES). A: 19th International Compressor Engineering Conference at Purdue. "Proceedings of the 19th International Compressor Engineering Conference at Purdue". Douglas E. Adams, 2008, p. 1-8.

Lehmkuhl, O.; Borrell, R.; Trias, F. X.; Pérez-Segarra, C.D. Assessment of large-eddy simulation models in complex flows using unstructured meshes. A: "Proceedings of the Fifth European Congress on Computational Methods in Applied Sciences and Engineering". Schrefler, B. A. and Perego, U., 2008, p. 1-2.

Colomer, G.; Lehmkuhl, O.; Borrell, R.; Capdevila, R. Coupling radiation and convection: Effect of radiation mesh on both results and performance. A: "Proceedings of the Fifth European Congress on Computational Methods in Applied Sciences and Engineering". Schrefler, B. A. and Perego, U., 2008, p. 1-2.

Borrell, R.; Lehmkuhl, O.; Soria, M.; COLOMER, G. Parallel Schur-Forrier decomposition for the efficient solution of poisson equation on massive extruded unstructured meshes. A: "Proceedings of the Fifth European Congress on Computational Methods in Applied Sciences and Engineering". Schrefler, B. A. and Perego, U., 2008, p. 1-2.

Rodriguez, I.; Oliva, A.; Pérez-Segarra, C.D.; Lehmkuhl, O. On the turbulent natural convection in thermal storage tanks submitted to heat losses to the environment. A: "Proceedings of the Fifth European Congress on Computational Methods in Applied Sciences and Engineering". Schrefler, B. A. and Perego, U., 2008, p. 1-2.

Rigola, J. [et al.]. Numerical Analysis of CO2 trans-critical cycles using semi-hermetic reciprocating compressors for small cooling applications. Study of the internal heat exchanger influence under real working conditions. A: "Proceedings of the 22th International Congress of Refrigeration". International Institute of Refrigeration, 2007, p. 1-8.

Lehmkuhl, O. [et al.]. TERMOFLUIDS: A new Parallel unstructured CFD code for the simulation of turbulent industrial problems on low cost PC Cluster. A: "Proceedings of the Parallel CFD 2007 Conference". Ismail H. Tuncer, 2007, p. 1-8.

Borrell, R.; Lehmkuhl, O.; Trias, F. X.; Soria, M.; Oliva, In Parallel direct Poisson solver for DNS of complex turbulent flows using Unstructured Meshes".En: Proceedings of the Parallel CFD 2008 Conference.

Rigola, J.; Ablanque, N.; Pérez-Segarra, C.D; Lehmkuhl, O.; Oliva, Numerical Analysis of CO2 trans-critical cycles using semi-hermetic reciprocating compressors for small cooling applications. Study of the internal heat exchanger influence under real working conditions. Proceedings of the 22th International Congress of Refrigeration. 2007

R. Borrell, O. Lehmkuhl, M. Soria, and A. Colomer, Oliva. Schur complement methods for the solution of Poisson equation with unstructured meshes. In *Parallel Computational Fluid Dynamics*, 2007.

O. Lehmkuhl, C. D. Perez-Segarra, R. Borrell, M. Soria, and A. Oliva. TERMOFLUIDS: A new Parallel unstructured CFD code for the simulation of turbulent industrial problems on low cost PC Cluster. In *Proceedings of the 2005 Parallel Computational Fluid Dynamics Conference*, pages 1–8, 2007.